

# Geodätisch-geophysikalische Arbeiten in der Schweiz

(Fortsetzung der Publikationsreihe  
«Astronomisch-geodätische Arbeiten in der Schweiz»)

herausgegeben von der

Schweizerischen Geodätischen Kommission  
(Organ der Akademie der Naturwissenschaften Schweiz)

**Siebenundachtzigster Band  
Volume 87**

**Optical Survey Strategies and their  
Application to Space Surveillance**

Tim Flohrer

2012

Adresse der Schweizerischen Geodätischen Kommission:

Institut für Geodäsie und Photogrammetrie  
Eidg. Technische Hochschule Zürich  
ETH Zürich  
8093 Zürich  
Switzerland

Internet: <http://www.sgc.ethz.ch>

ISBN 978-3-908440-34-5

Redaktion des 87. Bandes:  
Dr. T. Flohrer, J. Müller-Gantenbein, A. Geiger  
Druck: Print-Atelier ADAG, Zürich

## VORWORT

Herr Tim Flohrer hat sich mit Strategien zur Suche und Überwachung von Raumschrott mittels optischer Beobachtungen beschäftigt. Die Thematik umfasst einen sehr weiten Bereich von Aspekten, beginnend mit der eigentlichen Detektion von Raumschrott-Objekten durch optische Teleskope bis hin zum Aufbau und Unterhalt eines Bahnkatalogs dieser Objekte.

Für eine optimale Suchstrategie sollen ausgehend von einer Referenzpopulation, gegeben durch die Abmessungen und Bahnparameter der Objekte, Beobachtungssequenzen von Teleskopen an einem oder mehreren Standorten so definiert werden, dass möglichst viele der Objekte beobachtet werden. Dabei sind geometrische Randbedingungen – die Objekte müssen vom Beobachtungsort aus gesehen sichtbar sein – und radiometrische Bedingungen – die Objekte müssen unter den gegebenen Hintergrundverhältnissen hell genug erscheinen, um detektiert zu werden – zu beachten.

Zum Aufbau und Unterhalt eines Bahnkatalogs müssen die Positionen der Objekte regelmässig gemessen werden, was entweder durch gezielte Nachfolgebeobachtungen oder, bei geeigneter Auslegung des Teleskopnetzwerkes, mittels zufälliger Beobachtungen im Suchmodus erfolgen kann.

Die vorliegende Arbeit setzt sich mit allen genannten Aspekten auseinander. Der Autor hat insbesondere eine Programmumgebung aufgebaut, die es erlaubt, eine gegebene Such- und Überwachungsstrategie von der Einzelbeobachtung bis zur Bahnbestimmung zu simulieren. Die Simulationen basieren auf einem umfassenden Modell des Sensors (Teleskop und Detektor) sowie einer voll ausgebauten Bahnbestimmung. Diese Kombination ist einzigartig und stellt den Schlüssel zum Erfolg der von Herrn Flohrer entwickelten Strategien dar.

Neben Strategien für bodengestützte Teleskopnetzwerke werden auch Konzepte zur Suche von kleinen Raumschrottteilen und zur Überwachung ganzer Bahnregionen mit raumgestützten optischen Sensoren untersucht.

Die in dieser Arbeit entwickelten Strategien zur Suche und Überwachung von Objekten im geostationären Ring und in den Bahnen der Navigationssatelliten-Konstellationen haben in der Fachwelt grosse Beachtung erfahren. Die neusten Konzepte in den Studien der ESA zum Aufbau eines europäischen Überwachungssystems basieren zu guten Teilen auf Herrn Flohrers Arbeiten.

Die Schweizerische Geodätische Kommission (SGK) bedankt sich bei der Akademie der Naturwissenschaften Schweiz (ScNAT) für die Übernahme der Druckkosten.

**Prof. Dr. Th. Schildknecht**  
Astronomisches Institut  
Universität Bern

**Prof. Dr. Alain Geiger**  
ETH Zürich  
Präsident der SGK

## PREFACE

Le travail de Tim Flohrer se concentre sur les stratégies de recherche de débris spatiaux sur la base de mesures optiques ainsi que l'application de ces stratégies à la veille spatiale. Un large spectre d'aspects sont traités, de la détection des débris spatiaux sur la base de clichés pris avec des télescopes optiques, jusqu'à la création et la mise à jour d'un catalogue d'orbites pour ces objets.

Une stratégie de recherche optimale a pour but de maximiser le nombre d'objets observés dans une population de référence définie par la taille et les éléments orbitaux de ces objets, en optimisant les périodes d'observation de télescopes à un ou plusieurs endroits. L'établissement d'une stratégie doit non seulement prendre en compte les aspects géométriques – les objets devant être visibles depuis le site considéré – mais aussi les contraintes radiométriques – les objets devant être suffisamment lumineux par rapport à la luminosité du ciel en arrière-plan.

L'établissement et la mise à jour d'un catalogue d'orbites nécessitent des mesures périodiques de la position astrométrique des objets répertoriés, soit via la mise en place d'observations de suivi, soit via l'établissement de stratégies qui permettent l'acquisition «alléatoire» de suffisamment de données pour chaque objet.

Tous ces aspects sont discutés dans la présente publication. L'auteur a développé un logiciel qui permet de simuler les stratégies de recherche et d'observation, en commençant par la synthèse d'observations individuelles en finissant avec la détermination de l'orbite complète. Cette combinaison inédite est à la clef du succès des stratégies développées par Tim Flohrer.

En plus des stratégies développées pour des réseaux terrestres de télescopes, cette thèse traite aussi de concepts pour la recherche de débris spatiaux de taille restreinte ainsi que de l'observation de régions orbitales entières en utilisant des capteurs optiques spatiaux.

Les stratégies pour rechercher et suivre des objets dans l'anneau géostationnaire et dans la région des satellites des systèmes de navigation élaborées dans ce travail sont désormais largement acceptées par la communauté scientifique. Les concepts en cours d'élaboration dans le cadre de l'initiative de l'ESA d'établir un système européen de veille et de suivi sont largement basés sur le travail de Tim Flohrer.

La Commission Géodésique Suisse (CGS) est reconnaissante envers l'Académie Suisse des Sciences Naturelles (ScNAT) pour avoir pris à sa charge les coûts d'impression du présent manuscrit.

**Prof. Dr. Th. Schildknecht**  
Institut d'astronomie  
Université de Berne

**Prof. Dr. Alain Geiger**  
ETH Zürich  
Président de la CGS

## FOREWORD

This publication of Tim Flohrer focuses on strategies to search for space debris using optical observations and on the application of these strategies for space surveillance. The topic covers a wide range of aspects, starting with the actual detection of space debris on frames acquired by optical telescopes, and ending with the build-up and maintenance of a catalogue of orbit of these objects.

An optimum search strategy aims at maximizing the number of observed objects of a reference population defined by the sizes and the orbital elements of the objects, by optimizing the observations sequences of telescopes at one or several sites. The design of the strategies must take into account geometrical boundary conditions – the objects must be visible from a given site – as well as radiometric constraints – the objects must be bright enough to be detected against the sky background.

The build-up and maintenance of an orbit catalogue require periodic acquisition of astrometric positions of the catalogue objects. This may be achieved either by scheduling dedicated follow-up observations or by designing survey strategies in a way that enough observations of all objects are gained “incidentally”.

All of the above-mentioned aspects are discussed in this publication. The author developed a software tool allowing to simulate search and observation strategies starting with the generation of individual observations and ending with a full orbit determination. This combination is rather unique and was a key element for the success of the strategies developed by Tim Flohrer.

In addition to strategies for ground-based networks of telescopes the paper discusses concepts for the search of small-size debris and for surveys of entire orbit regions using space-based optical sensors. The strategies to search for and monitor objects in the geostationary ring and the region of the global navigation satellite systems presented in this work became widely recognized in the scientific community. Concepts currently developed in the framework of the ESA initiative to establish an European space surveillance and tracking system are based to a great extent on Tim Flohrer’s work.

The Swiss Geodetic Commission (SGC) is grateful to the Swiss Academy of Sciences (ScNAT) for covering the printing costs of this volume.

**Prof. Dr. Th. Schildknecht**  
Astronomical Institute  
University of Bern

**Prof. Dr. A. Geiger**  
ETH Zurich  
President of SGC



# Contents

<b>Contents</b>	<b>i</b>
<b>List of figures</b>	<b>v</b>
<b>List of tables</b>	<b>xiii</b>
<b>1. Introduction and motivation</b>	<b>1</b>
<b>2. Space situational awareness, space debris, and space surveillance principles</b>	<b>3</b>
2.1 Space situational awareness . . . . .	3
2.2 Space surveillance . . . . .	4
2.3 Space debris and its lifecycle . . . . .	5
2.4 Space surveillance principles . . . . .	6
2.4.1 Surveying and tracking . . . . .	7
2.4.2 Correlation and catalogue maintenance . . . . .	11
2.4.3 Object identification and characterisation . . . . .	13
2.5 Sensors with space surveillance capabilities . . . . .	13
2.5.1 Ground-based sensors . . . . .	13
2.5.2 Space-based sensors . . . . .	26
<b>3. Observation fundamentals, data reduction, and orbit modelling</b>	<b>31</b>
3.1 Reference systems . . . . .	31
3.2 Orbital regimes . . . . .	32
3.2.1 LEO . . . . .	32
3.2.2 MEO . . . . .	33
3.2.3 GEO . . . . .	41
3.2.4 Highly eccentric orbits . . . . .	46
3.3 Observations . . . . .	46

3.3.1	Radar observations . . . . .	46
3.3.2	Optical observations . . . . .	47
3.4	Orbits of artificial satellites . . . . .	61
3.5	Two-line element (TLE) sets . . . . .	63
<b>4.</b>	<b>Simulation environment for optical observations</b>	<b>65</b>
4.1	PROOF . . . . .	65
4.2	CelMech . . . . .	66
4.2.1	Circular orbits . . . . .	67
4.2.2	Boundary value method . . . . .	68
4.3	Simulation environment . . . . .	77
4.4	Application of the simulation environment to a proposed space-based optical observation scenario . . . . .	79
4.4.1	Sensor baseline and proposed observation strategies . . . . .	79
4.4.2	Assessment of the observable objects using PROOF . . . . .	80
4.4.3	Performance of the image processing . . . . .	86
4.4.4	Performance of the orbit determination . . . . .	89
4.4.5	Combination of the performance simulation results . . . . .	92
4.5	Conclusions . . . . .	93
<b>5.</b>	<b>Ground-based optical observation strategies</b>	<b>95</b>
5.1	Population evolution . . . . .	95
5.2	Accessibility of population . . . . .	97
5.2.1	GEO . . . . .	99
5.2.2	MEO . . . . .	102
5.3	Proposed observation strategies . . . . .	103
5.3.1	Fundamentals for classification and evaluation of observation strategies . . . . .	103
5.3.2	GEO . . . . .	105
5.3.3	MEO . . . . .	115
5.3.4	Summary . . . . .	134

<b>6. A system proposal for space-based optical space surveillance</b>	<b>137</b>
6.1 SSA-related observation strategies with the SBO architecture . . . . .	137
6.2 Radiometric characteristics of the SBO observing high altitudes . . . . .	140
6.3 Coverage of reference populations . . . . .	144
6.4 Orbit determination based on simulations . . . . .	146
6.5 Conclusion . . . . .	147
<b>7. Conclusion and recommendations</b>	<b>149</b>
<b>A. Performance of initial orbit determination from space-based observations</b>	<b>153</b>
<b>B. Simulated orbit determination results for a system proposal for space-based optical space surveillance</b>	<b>161</b>



# List of Figures

2.1	Space debris spatial density according to MASTER-2005, analysis epoch May 2005, (a): fragments, (b): launch/mission-related objects, (c): NaK droplets, (d): SRM slag, (e): ejecta. Top-left: size threshold 1 dm, top-right: 1 cm, bottom-left: 1 mm, bottom-right: 100 $\mu\text{m}$ . . . . .	7
2.2	Assumed sensitivity and observation regions for US SSN and other sensors (modified from Krag (2003); Flury et al. (2000); Anonymous (1999b)); radar sensors are given by black, optical sensors by red curves. For comparison the requirements for ESA's SSA system (Krag et al., 2010) are provided in blue colour. . . . .	9
2.3	The US Space Surveillance Network (Source: (Klinkrad, 2011)) . . . . .	20
2.4	The ISON network (Agapov et al., 2010). . . . .	23
3.1	Classification of orbital regimes (not to scale), viewed from the celestial pole, modified from (Krag and Klinkrad, 2009), showing as examples transient upper-MEO orbits with a solid line and one resident upper-MEO orbit with a dashed line. . . . .	33
3.2	Inclination $i$ vs. right ascension $\Omega$ of the ascending node for catalogued MEO and GEO objects at the epoch 25 February 2011. . . . .	36
3.3	Eccentricity $e$ vs. the semi-major axis $a$ for catalogued MEO and GEO objects at the epoch 25 February 2011. . . . .	37
3.4	Apparent density and average dwell time in the J2000 frame for 332 MEO objects visible from the OGS on 25 February 2011, which are listed in the USSTRATCOM public TLE catalogue of that date per $1^\circ \times 1^\circ$ bin. The density is calculated from 120 s sampling of the objects' ephemerides. . . . .	38
3.5	Apparent density and average dwell time in the OGS topocentric frame for 332 MEO objects visible from the OGS on 25 February 2011, which are listed in the USSTRATCOM public TLE catalogue of that date per $1^\circ \times 1^\circ$ bin. The density is calculated from 120 s sampling of the objects' ephemerides. . . . .	39
3.6	Apparent density and average dwell time in the Earth-fixed rotating frame for 332 MEO objects visible from the OGS on 25 February 2011, which are listed in the USSTRATCOM public TLE catalogue of that date per $1^\circ \times 1^\circ$ bin. The density is calculated from 120 s sampling of the objects' ephemerides. . . . .	40
3.7	Apparent density and average dwell time in the J2000 frame for 462 GEO objects visible from the OGS on 25 February 2011, which are listed in the USSTRATCOM public TLE catalog of that date per $1^\circ \times 1^\circ$ bin. The density is calculated from 120 s sampling of the objects' ephemerides. . . . .	43

3.8	Apparent density and average dwell time in the OGS topocentric frame for 462 GEO objects visible from the OGS on 25 February 2011, which are listed in the USSTRAT-COM public TLE catalog of that date per $1^\circ \times 1^\circ$ bin. The density is calculated from 120 s sampling of the objects' ephemerides. . . . .	44
3.9	Apparent density and average dwell time in the Earth-fixed rotating frame for 462 GEO objects visible from the OGS on 25 February 2011, which are listed in the USSTRAT-COM public TLE catalog of that date per $1^\circ \times 1^\circ$ bin. The density is calculated from 120 s sampling of the objects' ephemerides. . . . .	45
3.10	Visibility and observability conditions of objects. . . . .	48
3.11	SNR as a function of the background brightness for different object brightness for $v_{rel}=15''/s$ and $t=2$ s. The sensor is characterised by $\tau=0.88$ , $\epsilon=0.60$ , $QE=0.80$ , $D=0.80$ m, $f=1.46$ m, $d_{pixel}=12.50 \mu\text{m}$ , diameter of $PSF=2.00$ pixels, $S_d=0.14 \text{ e}^-/\text{pixel/s}$ , no binning, and $\sqrt{S_r}=10.0 \text{ e}^-$ . . . . .	53
3.12	SNR as a function of the background brightness for different exposure times for $v_{rel}=15''/s$ and an object brightness of 18 mag. The sensor is characterised by $\tau=0.88$ , $\epsilon=0.60$ , $QE=0.80$ , $D=0.80$ m, $f=1.46$ m, $d_{pixel}=12.50 \mu\text{m}$ , diameter of $PSF=2.00$ pixels, $S_d=0.14 \text{ e}^-/\text{pixel/s}$ , no binning, and $\sqrt{S_r}=10.0 \text{ e}^-$ . . . . .	54
3.13	SNR as a function of the background brightness for different readout-noise levels for $v_{rel}=15''/s$ , $t=2$ s, and an object brightness of 18 mag. The sensor is characterised by $\tau=0.88$ , $\epsilon=0.60$ , $QE=0.80$ , $D=0.80$ m, $f=1.46$ m, $d_{pixel}=12.50 \mu\text{m}$ , diameter of $PSF=2.00$ pixels, $S_d=0.14 \text{ e}^-/\text{pixel/s}$ , no binning. . . . .	54
3.14	Apparent brightness for Lambert-scattering spherical objects following Eq. 3.18 assuming $\rho_{Bond}=0.1$ and $\theta=20^\circ$ (modified and extended from a classical figure by King-Hele (1983)). . . . .	57
3.15	Apparent brightness for Lambert-scattering spherical objects of 1 m diameter as a function of topocentric distance and phase angle $\theta$ following Eq. 3.18 and assuming $\rho_{Bond}=0.1$ . . . . .	57
3.16	Simplified mutual relationships and dependencies of user requirements on maintaining a catalogue (dark-grey), sensor design parameters (grey), and the main characteristics of observation strategies (white). . . . .	59
3.17	Orbital elements $a, e, i, \Omega, \omega, u_0$ and state $(\mathbf{r}, \dot{\mathbf{r}})$ . . . . .	63
4.1	Boundary value method - schematic view of the used quantities. . . . .	69
4.2	BNBN2D minimum search for $0''$ (left) and $2.5''$ (right) RMS of single observation. . . . .	71
4.3	Distribution of the observations acquired with ESA's 1-m telescope at the OGS at Tenerife, and with ZIMLAT, located at Zimmerwald (Switzerland). . . . .	72
4.4	Orbit determination for single arcs (blue) and combined arcs (yellow), and best (true) solution (red circle) in the $a-e$ (left column) and $\Omega-i$ space (right column); test objects (top to bottom lines): E07311A, E07343D, E08035A, E08061B, E08125C. . . . .	74
4.5	Obtained RMS as function of the arc length of the used short arc. Left: short arc formed from single observation unit; right: short arc formed from adding subsequent observation units. . . . .	75

4.6	Simulator data flow. . . . .	78
4.7	LEO operations concept: placed in a sun-synchronous orbit close to the terminator, the LOS of the sensor is slightly inclined to the normal of the orbital plane, ensuring a pointing into the densely populated regions in LEO. . . . .	80
4.8	SubGEO operations concept: a dedicated spacecraft in a near-circular, slightly inclined orbit below the GEO, the LOS of the sensor is pointing away from the Sun. . . . .	80
4.9	GEO operations concept: mounted as secondary payload on-board a GEO satellite, the LOS of the sensor points to the North or South, but slightly inclined towards the Earth by $15^\circ$ . . . . .	81
4.10	Peak SNR per pixel as a function of the object diameter in the LEO concept for five selected data subsets with different bands of the observation distance. The dashed lines indicate the average of the corresponding data subset. . . . .	82
4.11	FoV dwell times in the LEO concept for five selected data subsets with different bands of the observation distance. . . . .	82
4.12	Eccentricity vs. semi-major axis for objects larger than 5 mm crossing the FoV within the 576 h simulation for LEO400 top-left, LEO bottom-left, subGEO top-right, GEO bottom-right. . . . .	84
4.13	Inclination vs. right ascension for objects larger than 5 mm crossing the FoV within the 576 h simulation for LEO400 top-left, LEO bottom-left, subGEO top-right, GEO bottom-right. . . . .	85
4.14	Minimum distance vs. FoV dwell time for the simulated LEO, subGEO and GEO operational concepts considering objects larger than 5 mm diameter within 576 h simulated observation time; LEO400 top-left, LEO bottom-left, subGEO top-right, GEO bottom-right. . . . .	86
4.15	Brightness of the FoV crossing objects vs. the brightness of the sky background for all objects larger than 5 mm diameter within 576 h simulated observation time; LEO400 top-left, LEO bottom-left, subGEO top-right, GEO bottom-right. . . . .	87
4.16	Phase angle variations as function of the observation epoch; LEO400 top-left, LEO bottom-left, subGEO top-right, GEO bottom-right. . . . .	88
4.17	Peak SNR vs. diameter of the FoV crossing objects larger than 5 mm within the 576 h simulation for LEO400 top-left, LEO bottom-left, subGEO top-right, GEO bottom-right. . . . .	89
5.1	Long-term evolution of the GPS population from 2005 to 2059, from a numerical propagation considering luni-solar perturbations, the Earth's gravity field up to degree and order 30, Earth tides, general relativity, and the direct solar radiation pressure for an $A/m$ -ratio of $0.1 \text{ kg/m}^2$ . . . . .	98
5.2	Average night time for different twilight conditions as a function of site latitude, with Northern hemisphere as solid lines and Southern hemisphere as dashed lines. Modified from (Taff, 1981). . . . .	99
5.3	Variation of the length of the nautical night (time between nautical dusk and dawn) as function of the site's geographical latitude $\phi$ . Solid lines refer to Northern, dashed lines to Southern latitudes. Calculations are based on Seidelmann (1992). . . . .	99

5.4	Accessible longitude range for objects at GEO distance at declination of $0^\circ$ as a function of the geographical latitude for various elevation cut-off angles $e$ . . . . .	100
5.5	Ground-based infrastructure proposed for a European space surveillance system, modified from (Donath et al., 2005). . . . .	100
5.6	Coverage map for objects at GEO distance for different elevation angles in $10^\circ$ steps, top: $e = 0^\circ$ bottom: $e = 30^\circ$ . . . . .	101
5.7	Coverage map for objects at typical MEO geocentric distance of 25000 km for different elevation angles in $10^\circ$ steps, top: $e = 0^\circ$ bottom: $e = 30^\circ$ . . . . .	102
5.8	Topocentric distance to satellites as a function of the accessible longitude range, site's latitude for GEO objects at a geocentric distance of 40164 km (top) and 44164 km (bottom), with declination of $0^\circ$ (left) and $15^\circ$ (right). . . . .	106
5.9	SNR as a function of the background brightness for varying object brightness for the 1 m telescope (left) and the 0.5 m telescope (right), as defined in Table 5.3, for a velocity of $5''/s$ . . . . .	108
5.10	SNR of crossing and detected objects as a function of the object diameter from PROOF simulations for the 1 m telescope (left) and the 0.5 m telescope (right), as defined in Table 5.3. The one-stripe survey strategy was simulated (see Sect. 5.3.2.3). . . . .	109
5.11	Number of missed crossings and detections per $4^\circ$ longitude bins. The coverage map for GEO distances is included, as well. A network of 0.5 m sensors has been assumed. Fast drifters ( $>5^\circ/\text{day}$ in longitude) have been filtered out. . . . .	112
5.12	Angular velocities in the local horizon system of the OGS for GPS satellites. . . . .	117
5.13	Velocity in declination vs. declination of GPS satellites. . . . .	117
5.14	Topocentric observation distances for GPS satellites seen from the OGS for November 16, 2004. . . . .	118
5.15	Phase angles for GPS satellites seen from the OGS for November 16, 2004. . . . .	119
5.16	Apparent density of the upper MEO objects in the DISCOS catalogue projected onto the Earth for epoch 20 August 2004, highlighted are the declination stripe centred at $0^\circ$ declination and a "caustic" declination stripe at $65^\circ$ . . . . .	120
5.17	Total accessible area in right ascension of $0^\circ$ declination fields for Tenerife with elevation mask of $10^\circ$ and evolution of area over a one year period. . . . .	121
5.18	Possible observation duration of $0^\circ$ declination fields for Tenerife with elevation mask of $10^\circ$ and evolution over a one year period. . . . .	122
5.19	Implementation of the proposed MEO survey strategy in PROOF. . . . .	124
5.20	Coverage of the MEO reference population with the proposed $0^\circ$ declination MEO survey strategy. . . . .	125
5.21	Right ascension vs. declination of the two simulated caustic survey patterns at $t_0$ and $t_1$ and orbits of six objects. . . . .	127
5.22	Inclination $i$ vs. right ascension of ascending node $\Omega$ of the synthetic reference population based on explosion models, and the fraction of the population covered by the survey patterns $t_0$ and $t_1$ . . . . .	128

---

5.23	Differences in semi-major axis vs. eccentricity of the initially determined orbits w.r.t. the reference orbit as a function of the astrometric noise for test object 107. . . . .	128
5.24	Differences in right ascension of the ascending node vs. inclination of the initially determined orbits w.r.t. the reference orbit as a function of the astrometric noise for test object 107. . . . .	129
5.25	SNR as a function of MEO objects diameter during MEO survey. Red: average observing conditions. Green: worst observing conditions during full Moon. . . . .	129
5.26	Residuals of position differences between initial orbit determination results and the original synthetic MEO population. . . . .	131
5.27	Residuals of position differences between orbit determination results after the first follow-up observation ( $t_0+1$ h) and the original synthetic MEO population. . . . .	131
5.28	Residuals of position differences between orbit determination results after the second follow-up observation ( $t_0+2$ h) and the original synthetic MEO population. . . . .	132
5.29	Residuals of position differences between orbit determination results after the third follow-up observation ( $t_0+12$ h) and the original synthetic MEO population, assuming a simple model of the perturbing forces. . . . .	132
5.30	Residuals of position differences between orbit determination results after the third follow-up observation ( $t_0+12$ h) and the original synthetic MEO population, assuming a sophisticated model of the perturbing forces. . . . .	133
5.31	Residuals of position differences between orbit determination results after the fourth follow-up observation ( $t_0+24$ h) and the original synthetic MEO population, assuming a sophisticated model of the perturbing forces. . . . .	133
6.1	Covered regions in the GEO vicinity from a fix-mounted sensor with a $6^\circ$ FoV onboard a platform orbiting in an 800 km circular SSO. Pointing direction is orthogonal to the orbital plane with different elevation angles. Three different of the pointing direction are colour-coded. . . . .	140
6.2	Pointing centre directions intersecting GEO distance in an Earth-fixed frame during 24 hours, assuming a fix-mounted sensor onboard a platform orbiting in a 800 km circular SSO. Pointing is orthogonal to the orbital plane. . . . .	141
6.3	SNR of moving source with an apparent brightness of 14 mag as a function of the sky background brightness for different exposure times $t$ . . . . .	142
6.4	SNR of moving source of different apparent brightness as a function of the sky background brightness for exposure time $t=1$ s. . . . .	142
6.5	Angular velocities of TLE catalogue objects crossing the sensor's FoV as a function of the observation epoch for three elevation pointing scenarios. . . . .	143
6.6	Angular velocities of TLE catalogue objects crossing the sensor's FoV as a function of the phase angle at the observation epoch. Objects in the Earth shadow are excluded. . .	144
6.7	Reacquisition period compared to covered arc length, top row (red) $e=+5^\circ$ , middle row (blue) $e=0^\circ$ , bottom row (green) $e=-5^\circ$ . . . . .	145

6.8	First orbit determination of object 858 for ten subsequent days. The figures show the difference for selected orbital elements (semi-major axis, eccentricity, inclination, and right ascension of the ascending node) w.r.t the “truth” (i.e., the orbit determination without astrometric noise). . . . .	148
A.1	LEO case, percentage of ‘accepted’ IODs with respect to the total number of successful IODs (after filtering). . . . .	154
A.2	SubGEO case, percentage of ‘accepted’ IODs with respect to the total number of successful IODs (after filtering). . . . .	154
A.3	GEO case, percentage of ‘accepted’ IODs with respect to the total number of successful IODs (after filtering). . . . .	155
A.4	Relative frequency of the differences between the determined and reference orbital elements semi-major axis $a$ [km], eccentricity $e$ [-], inclination $i$ [°], and right ascension of ascending node $\Omega$ [°], grouped by the assumed astrometric noise [″], for the test object GEO1. . . . .	155
A.5	Relative frequency of the differences between the determined and reference orbital elements semi-major axis $a$ [km], eccentricity $e$ [-], inclination $i$ [°], and right ascension of ascending node $\Omega$ [°], grouped by the assumed astrometric noise [″], for the test object GEO2. . . . .	156
A.6	Relative frequency of the differences between the determined and reference orbital elements semi-major axis $a$ [km], eccentricity $e$ [-], inclination $i$ [°], and right ascension of ascending node $\Omega$ [°], grouped by the assumed astrometric noise [″], for the test object GEO3. . . . .	156
A.7	Relative frequency of the differences between the determined and reference orbital elements semi-major axis $a$ [km], eccentricity $e$ [-], inclination $i$ [°], and right ascension of ascending node $\Omega$ [°], grouped by the assumed astrometric noise [″], for the test object GEO4. . . . .	157
A.8	Relative frequency of the differences between the determined and reference orbital elements semi-major axis $a$ [km], eccentricity $e$ [-], inclination $i$ [°], and right ascension of ascending node $\Omega$ [°], grouped by the assumed astrometric noise [″], for the test object GEO5. . . . .	157
A.9	Relative frequency of the differences between the determined and reference orbital elements semi-major axis $a$ [km], eccentricity $e$ [-], inclination $i$ [°], and right ascension of ascending node $\Omega$ [°], grouped by the assumed astrometric noise [″], for the test object LEO1. . . . .	158
A.10	Relative frequency of the differences between the determined and reference orbital elements semi-major axis $a$ [km], eccentricity $e$ [-], inclination $i$ [°], and right ascension of ascending node $\Omega$ [°], grouped by the assumed astrometric noise [″], for the test object LEO2. . . . .	158
A.11	Relative frequency of the differences between the determined and reference orbital elements semi-major axis $a$ [km], eccentricity $e$ [-], inclination $i$ [°], and right ascension of ascending node $\Omega$ [°], grouped by the assumed astrometric noise [″], for the test object LEO3. . . . .	159

A.12 Relative frequency of the differences between the determined and reference orbital elements semi-major axis  $a$  [km], eccentricity  $e$  [-], inclination  $i$  [ $^{\circ}$ ], and right ascension of ascending node  $\Omega$  [ $^{\circ}$ ], grouped by the assumed astrometric noise [ $''$ ], for the test object LEO4. . . . . 159

A.13 Relative frequency of the differences between the determined and reference orbital elements semi-major axis  $a$  [km], eccentricity  $e$  [-], inclination  $i$  [ $^{\circ}$ ], and right ascension of ascending node  $\Omega$  [ $^{\circ}$ ], grouped by the assumed astrometric noise [ $''$ ], for the test object LEO5. . . . . 160

B.1 First orbit determination of object 33059 for subsequent passes. The individual subplots show the difference for selected orbital elements (semi-major axis, eccentricity, inclination, and right ascension of the ascending node) between the "truth" (i.e., the orbit determination without astrometric noise) and the orbit determination using noised observations. . . . . 162

B.2 First orbit determination of object 23192 for subsequent passes. The individual subplots show the difference for selected orbital elements (semi-major axis, eccentricity, inclination, and right ascension of the ascending node) between the "truth" (i.e., the orbit determination without astrometric noise) and the orbit determination using noised observations. . . . . 162

B.3 First orbit determination of object 22563 for subsequent passes. The individual subplots show the difference for selected orbital elements (semi-major axis, eccentricity, inclination, and right ascension of the ascending node) between the "truth" (i.e., the orbit determination without astrometric noise) and the orbit determination using noised observations. . . . . 163

B.4 First orbit determination of object 34710 for subsequent passes. The individual subplots show the difference for selected orbital elements (semi-major axis, eccentricity, inclination, and right ascension of the ascending node) between the "truth" (i.e., the orbit determination without astrometric noise) and the orbit determination using noised observations. . . . . 163

*List of Figures*

---

# List of Tables

2.1	Mean time [years] between collisions for different impactor diameters for 1 m <sup>2</sup> surface in several representative orbits for the reference epoch 1 May 2009, based on the most recent ESA MASTER-2009 model (Bastida, 2011). . . . .	6
2.2	Possible states of the catalogue maintenance process, depending on results of object reacquisition and detection tasks . . . . .	11
2.3	Ground-based sensors . . . . .	15
3.1	Catalogued objects in MEO orbit with $n < 6$ rev/day, sorted according to DISCOS identification. . . . .	36
3.2	Catalogued objects in GEO orbit sorted according class in DISCOS. . . . .	42
4.1	Test objects for the evaluation of BNB2D, with osculating elements referring to the latest available observation epoch per object. . . . .	72
4.2	Test objects for the evaluation of the space-based initial orbit determination capabilities of BNB2D. . . . .	75
4.3	Number of FoV crossing objects larger than 5 mm diameter within 576 h simulated observation time for the three considered operation concepts (LEO, subGEO, GEO). . . . .	83
4.4	Number of FoV crossing objects larger than 5 mm diameter within 576 h simulated observation time for various simulated SNR detection thresholds (peak values per FoV crossing event), together with the related minimum object diameter (in mm) in <i>italic</i> . . . . .	83
4.5	Centroiding accuracies (after the astrometric reduction step in the on-ground processing) in pixel units and maximum corresponding position error in arc seconds, assuming a SBO pixel scale of 9.041"/pixel. . . . .	90
4.6	Number of objects per day for which the initial orbit determination meets the acceptance criteria. . . . .	93
4.7	Capabilities of the SBO compared to existing ground-based sensors ((*): stare and chase for TIRA.) . . . . .	93
5.1	Relevant accelerations acting on a GPS-like satellite in MEO (modified from (Beutler, 2005)). . . . .	96
5.2	Summary of the assessed population evolution in MEO. . . . .	97
5.3	Preliminary system architecture used in performance estimation. . . . .	108

5.4	Catalogue coverage, number of objects crossing the FoV and being detected uniquely (one short arc generated) and several times (at least two short arcs, possibly by different sensors). Observing two fields in parallel is assumed (TF-Tenerife, PE-Perth, CY-Cyprus, MQ-Marquesas Islands). . . . .	111
5.5	Preliminary system architecture used in performance estimation. . . . .	119
5.6	Coverage of a reference population: Number of multiple crossing events and (in parentheses) unique crossing events, and the corresponding coverage of the reference population (TF-Tenerife, MQ-Marquesas Islands). . . . .	126
6.1	Simulation parameters using a TLE population of GEO objects. . . . .	143
6.2	Simulation results using deterministic (TLE) populations of the GEO regime obtained from PROOF-based analysis. Covered objects refer to objects crossing the FoV, while numbers of detected objects refer to covered objects illuminated at the observation epoch. 145	145
6.3	Summary of the simulation runs: average number of FoV crossing events, properly illuminated crossing events (“detections”), object-wise calculated mean, minimum, and maximum time between re-acquisitions, and mean, minimum, and maximum observation length per short arc. . . . .	146
6.4	Selected test objects for the simulation of the orbit determination. . . . .	147

# 1. Introduction and motivation

The uninterrupted availability of services provided through space systems is essential in today's daily life. The applications relying on space systems cover global navigation systems, global telecommunication services, support of disaster control through Earth observation, just to name some popular examples. The exploitation of the near-Earth space is indispensable and must be secured, as interruptions of the provided services would not only impose severe economical risks, they might also have security-related, possibly life-critical implications.

Space is "vastly hugely mindbogglingly big" in fact, quoting Douglas Adams. The near-Earth environment is, however, more and more populated with man-made objects. Since the advent of the space age more than fifty years ago, about 4800 launches were performed, placing more than 6400 payloads into orbit. But not only payloads form the population of man-made objects. Also rocket-bodies, mission-related objects, and fragments from in-orbit explosions and incidental or accidental collisions may be found. Space surveillance is the main technique to understand the population of Earth-orbiting man-made objects. It involves detecting, tracking, cataloguing, and identifying man-made objects orbiting Earth. As of today the U.S. Space Surveillance Network has collected orbital information for more than 37000 man-made objects, which are available in a published catalogue. Only roughly 21000 of the catalogued objects have decayed into the Earth's atmosphere yet. The vast majority of the man-made objects remaining in orbit, about 94%, are non-functional objects, or "space debris". Two major events led recently to a nearly 50% increase in the number of catalogued debris objects: the intentional destruction of Feng-Yun 1C by the Chinese government in January 2007, and the collision between the active Iridium-33 satellite and the non-functional Russian Cosmos-2251 communication satellite in February 2009.

The sensor systems searching for and tracking space debris in order to maintain a catalogue of orbital elements cannot track objects smaller than a few centimetres or decimetres, mainly depending on the object's altitude. Lower altitude bands (low Earth orbits, LEO) are mainly surveyed by ground-based radar sensors. High-altitude bands (medium Earth orbits, MEO, and geostationary orbits, GEO) are observed by electro-optical means from ground. Optimally, intermediate orbits and elliptical orbits would require the fusion of radar and optical data. Space-based sensors, such as the space-based visible (SBV) instrument on-board the midcourse space experiment (MSX) contributed significantly to space surveillance of high-altitude regions until MSX was decommissioned in 2008. Its successor, the Space Based Space Surveillance (SBSS) satellite, was launched in September 2010. A significant increase of space-based contributions to the U.S. Space Surveillance Network can be expected from the SBSS.

The population of smaller objects can only be described statistically, using space debris environment models. According to ESA's MASTER-2005 model, 600,000 objects larger than 1 cm are in orbit. One centimetre is the widely accepted limit for which a collision would be catastrophic, causing the destruction of the objects involved in the collision. In addition the energy-to-mass ratio of a catastrophic collision must exceed 40 J/g. Recent studies revealed that such collisions could lead to continuously growing debris population, which in turn steadily increases the collision risk for operational satellites.

Both, the complete and timely information on the orbital elements of the trackable population of objects in space, and the availability of maintained and validated space debris environment models, are of paramount importance for the future exploitation of space as an “enabling tool”. Catalogues of orbital elements, provided by space surveillance systems, are central to perform conjunction analysis and collision risk assessments for the operation of satellites - not only to secure the functioning of the satellites, but also as a main space debris mitigation practice. The space debris environment models are required during the design phase of missions and satellites, in particular to address the threat imposed by space debris.

In this context special attention must be paid to the formulation of efficient survey strategies for the sensor systems used to search for unknown, or newly generated, space debris objects. Such survey strategies are not only tightly bound to the capabilities of the utilised sensors, they are also strongly connected to the aimed use of the generated data - i. e., catalogue build-up and maintenance, model validation, or even a mixture of both. The various instrumental and processing-related, but also the financial and political constraints of potential implementations of the proposed survey strategies have to be considered during the formulation.

We study optical survey strategies in the framework of space surveillance. In Chapter 2 we start with addressing the needs set by space situational awareness (SSA), which we relate to the space surveillance principles, in particular to the passive optical observations of objects. We analyse the capabilities of optical sensors in existing and planned space surveillance networks, including these of complementary space-based sensors.

Chapter 3 introduces the relevant observation models and satellite orbit models of artificial Earth satellites. Furthermore, different observation types and the reduction process are described in detail for optical observations.

Chapter 4 is devoted to introducing the developed simulation environment. We review in particular methods for initial orbit determination and discuss a new alternative formulation for analysing optical observations. We use the simulation environment to assess the achievable performance for a system proposal to survey small-sized space debris in lower and higher altitude by space-based optical means.

Chapter 5 discusses several options for realising optical survey strategies, already used ones, as well as simulated ones. The discussion makes use of a classification scheme developed for considering performance-related aspects, such as the estimated orbit determination accuracy, the covered fraction of a population, and the achievable re-acquisition frequency of a particular object.

In Chapter 6 we investigate how the system proposal for space-based optical observations could be employed for space-based space surveillance of objects in high altitudes.

Finally, Chapter 7 summarises the achieved results and draws conclusions potentially leading to further investigations.

## 2. Space situational awareness, space debris, and space surveillance principles

In this chapter we present fundamental definitions relevant for this work and introduce techniques, which will be further refined in subsequent chapters. Special attention is paid to relate these basic definitions to the currently ongoing European initiatives, and European sensors, in particular the optical ones.

### 2.1 Space situational awareness

Space systems face several major threats. Collisions with space debris objects, malfunctioning due to space weather effects, or even deliberate attacks might endanger the space-segment. The concept of space situational awareness (SSA), originating from the United States, takes into account these threats. A commonly accepted definition of SSA does not exist. The US Air Force defines SSA as “characterizing, as completely as possible, the space capabilities operating within the terrestrial and space environments” (Weeden and Kelso, 2009). The US SSA system has the core components surveillance, intelligence, reconnaissance, command and control, and environmental monitoring. Widely, SSA is, understood as the combination of space surveillance data (see below) with other data from various heterogeneous sources, which allows the characterisation of known space objects as Space Object Identification (SOI), and aims at assessing the capabilities of the payloads, at identifying the owner and operator, and, finally, at determining and forecasting their intents. Observation technologies for SOI include narrow-band (variation of the reflected energy), wide-band (radar imaging), photometry (analysis of intensity, luminance, and illuminance), and optical imaging. Intelligence sources maybe included in SOI activities, as well.

SSA has received major and still growing interest in Europe in recent years. According to a definition used by ESA (Anonymous, 2008a), SSA comprises the awareness and understanding of the orbital population, the awareness of the space environment, and the awareness of threats to/by the orbital population, and addresses the related data policy, security and governance issues. A SSA preparatory programme (SSA-PP) was authorised at the 2008 ESA Ministerial Council for an initial period of three years, and was formally launched on January 1, 2009. The SSA-PP encompasses three segments: space surveillance and tracking (SST), space weather effects, and near-Earth objects. Considering the SST the customer requirements have been formulated (Krag et al., 2010) starting from the needs of the European user community. Currently, the system requirements are derived from these requirements. Potential architectural solutions for European SSA have been studied by European industry under ESA contracts (Donath et al., 2005, 2008, 2009) already. The SSA-PP also shall define the data and governance policy, and establish data centers and management processes, launch precursor services and develop a radar breadboard.

The existing SSA systems were clearly driven by military needs. While the newer European definition sees SSA as a dual use (harmonising and serving military and civil needs), there are also initiatives

for an International Civil SSA. These initiatives anticipate the importance of fully opening the access to SSA data for non-military users (Weeden and Kelso, 2009). All SSA activities are understood to require a careful trade-off between costs (mostly directly related to accuracy of the data) and system complexity. Civil SSA will require a limited set of functionalities compared to the full set of military SSA needs. The civil SSA users are not interested in all of the SOI, intelligence and reconnaissance capabilities. Civil needs are limited to identify an object and its operator, and to gather information on manoeuvring capabilities and manoeuvre plans, which are essential inputs for collision avoidance activities. Reducing the risk of accidental collisions in space is commonly understood as the driver for developing an international SSA architecture (Ferrazzani, 2010).

Weeden and Kelso (2009) expect that a civil SSA system is freed from political and military constraints by the intended open collaboration and data policy. Such a system may close some capability gaps existing today in (US) military SSA, in particular in population coverage. The interesting approach of civil SSA is rather new and significant technical, security, political, legal and diplomatic challenges lie ahead. Weeden and Kelso (2009) are confident that these challenges may be solved. International cooperation in SSA is also listed in the 2010 released US National Space Policy. The following “potential areas for international cooperation” are inter alia listed: space nuclear power to support space science and exploration; space transportation; space surveillance for debris monitoring and awareness; use of space for maritime domain awareness.

Taking into account that space is a unique resource and that the unavailability of space-based services would impose strong economical and social consequences the “Long Term Sustainability of Space Activities” has been put on the agenda of the major space agencies recently, and is promoted by the United Nations Committee on the Peaceful Uses of Outer Space (COPUOS). Ferrazzani (2010) expects that the establishment of SSA capabilities will have to link with the sustainability activities, e.g. by fostering comprehensive international exchange of SSA data.

## **2.2 Space surveillance**

The acquisition and monitoring of the orbital population is of central importance for most SSA tasks. Acquired and maintained object properties are the base for most products of a SSA system. They all require the precise knowledge of the orbital elements of the object. Acquiring and maintaining the orbital information is a key issue, and we may introduce the term “space surveillance” here. Klinkrad (2006) defines it as the “combined, routine tasks of operational detection, correlation with sources, characterisation and orbit determination of space objects”.

Here, we strictly limit to space surveillance techniques only, and thus focus on the population of artificial Earth-orbiting objects. We divide this population into so-called trackable and non-trackable objects. We define the trackable objects as the sub-population for which we may maintain a catalogue of orbital elements and other object properties utilising a given network of so-called space surveillance sensors. Search campaigns (“surveys”) carried out by this network will return information on the non-trackable object population, too, but for different reasons this information is not sufficient to be maintained in the catalogue. We may, however, use this information as input to describe the non-trackable object population by using (statistical) modelling techniques. Strictly speaking, the term space surveillance is, however, only applicable to trackable objects.

With more practical applications in mind, we use the term space surveillance as comprising the tasks of 1) systematically surveying and tracking all man-made objects above a certain size and 2) maintaining a

catalog with regularly updated orbital and physical characteristics for these objects.

## 2.3 Space debris and its lifecycle

The entire population of artificial Earth-orbiting objects may not only be grouped into trackable and non-trackable objects. We may use very different classification schemes. For example we may use the orbital regions as criteria, or we may distinguish active, i.e., transmitting and/or controlled, and non-functional objects. With a share of less than approximately 6% of the entire mass placed in orbit, the about 1100 active objects are minor in number and mass compared to the non-functional objects.

Non-functional objects are commonly denoted as “space debris”, or, by an equivalent term, as “orbital debris”. While “space debris” is mainly used in Europe, in particular promoted by ESA, the expression “orbital debris” is commonly used in the United States. Irrespective of the term there is only a technical, but no legal definition available. A definition agreed upon at international level is the following (Anonymous, 1999c): “Space debris are all man-made objects, including their fragments and parts, whether their owners can be identified or not, in Earth orbit or re-entering the dense layers of the atmosphere that are non-functional with no reasonable expectation of their being able to assume or resume their intended functions or any other functions for which they are or can be authorized.” By the International Academy of Aeronautics (Anonymous, 1999b), space debris is defined as follows: “Orbital debris is herein defined as any man-made Earth-orbiting object which is non-functional with no reasonable expectation of assuming or resuming its intended function or any other function for which it is or can be expected to be authorised, including fragments and parts thereof”. The mitigation guidelines of the Inter-Agency Space Debris Coordination Committee (Anonymous, 2007) define space debris as “all man made objects including fragments and elements thereof, in Earth orbit or re-entering the atmosphere, that are non functional”.

Major sources of space debris are launches and on-orbit operations. Space debris objects are non-operational spacecraft, spent upper rocket stages, and mission related objects. Secondly, a rapidly growing share of space debris objects is produced by or from the primary objects through fragmentation events (either deliberate or accidental collisions or explosions, or low-energy break-ups), through release events, particle impacts, or surface degradation. More than 250 fragmentation events have taken place till today (Johnson et al., 2008). Space debris objects also include solid rocket motor (SRM) combustion residues ( $\text{Al}_2\text{O}_3$  dust with sizes around 1 to 10  $\mu\text{m}$ , and slag, reaching cm sizes), NaK droplets (sodium-potassium coolant liquids) released from ejected reactor cores of Soviet radar ocean reconnaissance satellites, with sizes up to 5.6 cm, and copper wire dipoles (product of the deliberate release during the “Westford” experiment). Furthermore, up to millimetre-sized paint flakes produced by surface erosion and ejecta generated by particle impacts (debris and meteoroid) contribute to the space debris environment.

Figure 2.1 gives the spatial density of the space debris classes as a function of the altitude. The spatial densities for different diameter thresholds are obtained from ESA’s Meteoroid And Space debris Terrestrial Environment Reference (MASTER) model in the version 2005 (Oswald et al., 2005) for the reference epoch May 1, 2005. The population larger than 1 cm is dominated by fragments, while the main contributor to the mm-sized population is SRM slag, and for the 100  $\mu\text{m}$  population ejecta play a major role. NaK droplets are absent in the dm-size population, and, due to their origin, above 1000 km altitude. Space debris accumulates mainly in areas interesting for space operations and in orbital regimes required to reach these interesting areas. The highest densities are found in the low-Earth orbits (LEO), while

Perigee height	Apogee height	Inclination	0.1 mm	1 mm	1 cm	1 dm
356 km	364.1 km	51.6°	8.95	636	41102	942507
773.5 km	789.2 km	98.6°	0.68	42.52	1252	43783
1400 km	1400 km	52°	1.72	102	9208	126550
20000 km	20000 km	55°	244.80	10794	1.14E+07	7.20E+08
560 km	35786 km	7°	36.76	2627	241546	4.41E+06
35786 km	35786 km	0.1°	676.30	18674	6.46E+06	1.40E+08

Table 2.1: Mean time [years] between collisions for different impactor diameters for 1 m<sup>2</sup> surface in several representative orbits for the reference epoch 1 May 2009, based on the most recent ESA MASTER-2009 model (Bastida, 2011).

other peaks of the density can be found in the geostationary orbits (GEO) and the semi-synchronous orbits in the medium Earth orbits (MEO). The characteristics of these orbital regimes are further specified in Sect. 3.2. In addition Table 2.1 lists the mean time between collisions for different size thresholds and for several representative orbits based on the most recent ESA MASTER-2009 model for the reference epoch 1 May 2009.

Space debris objects are removed from the Earth-orbiting population either by natural forces (atmospheric drag and third body perturbations, forcing the object to re-enter into the atmosphere of the Earth), or by an active removal. Most of the space debris objects have a long orbital lifetime (see also Sect. 3.2). During the recent years the consensus emerged that not only continuing a business-as-usual approach will lead to a growing population of space debris. This effect was first described by Kessler and Cour-Palais (1978). Today it is widely accepted that even without additional launches the very uncomfortable situation of a continuously growing space debris population would emerge (see, e.g. analyses by Bastida and Krag (2009), who used ESA's long-time evolution forecast tool DELTA).

An expected 50% increase of close approaches in the next 10 years and a 250% increase in the next 50 years (Lewis et al., 2009) will have a strong impact on operating spacecraft. The operational costs will increase due to an increasing effort for conjunction event analyses and the performance of collision avoidance manoeuvres (see, e.g., recent results by Flohrer et al. (2009) for ESA missions). In addition, the performance of avoidance manoeuvres shortens the mission lifetime and potentially degrades the quality of the generated data products. Last, but not least, the costs for operating spacecraft in densely populated regimes will become unaffordably high. Cascading collision events within the existing population will make the situation even worse with time.

Strategies for space debris remediation, which is the effective and cost-efficient active removal of large space debris objects, have to be identified soon. The first step, mitigating the release of new debris objects, has become a widely accepted practice. National and international guidelines and regulations exist and are widely followed.

## 2.4 Space surveillance principles

Three major space surveillance principles may be identified, namely surveying and tracking, correlation and catalogue maintenance, object identification and characterisation. The following paragraphs will look at each principle in more detail, in particular from the perspective of passive optical observations of objects.

### 2.4.1 Surveying and tracking

Surveying and tracking are the two primary tasks of space surveillance. Surveying denotes the systematic search for unknown objects in defined spatial volumes. Tracking, on the other hand stands for the re-observation of already known objects based on a-priori information. Accomplishing these two tasks requires a network of sensors, formed by radars and optical telescopes, either operated on ground or in space. At high-altitude regions (MEO and GEO), ground-based optical telescopes are preferred over ground-based radars. This is mainly due to the higher sensitivity of telescopes at higher regions: the sensitivity of optical telescopes only decreases proportionally to the distance with the power of two, the sensitivity of radar decreases proportionally to the distance with the power of four. The optical technique also has some disadvantages. The objects have to be in the sunlight in front of a dark sky background to observe them by optical means. For lower LEO objects, the observation time therefore is limited to one or two hours before sunrise and after sunset. For higher orbits observations may be acquired during the entire night.

Figure 2.2 gives the sensitivity of radar and optical sensors as a function of the object's altitude, based on assumptions and on publicly available sensitivity information. For objects in the GEO region it is assumed that the most advanced space surveillance networks provide sufficient capabilities to routinely track and catalogue objects down to about 1 m (mostly through optical means), in LEO down to 10 cm (mostly through radars) (Klinkrad, 2006; Stansberry, 2010). There are, however, some solitary sensors, which are not part in a network, but have a higher sensitivity, such as the Haystack radars in Westford, Massachusetts, or ESA's 1-m telescope at the Optical Ground Station (OGS) at Izaña, Tenerife, Spain.

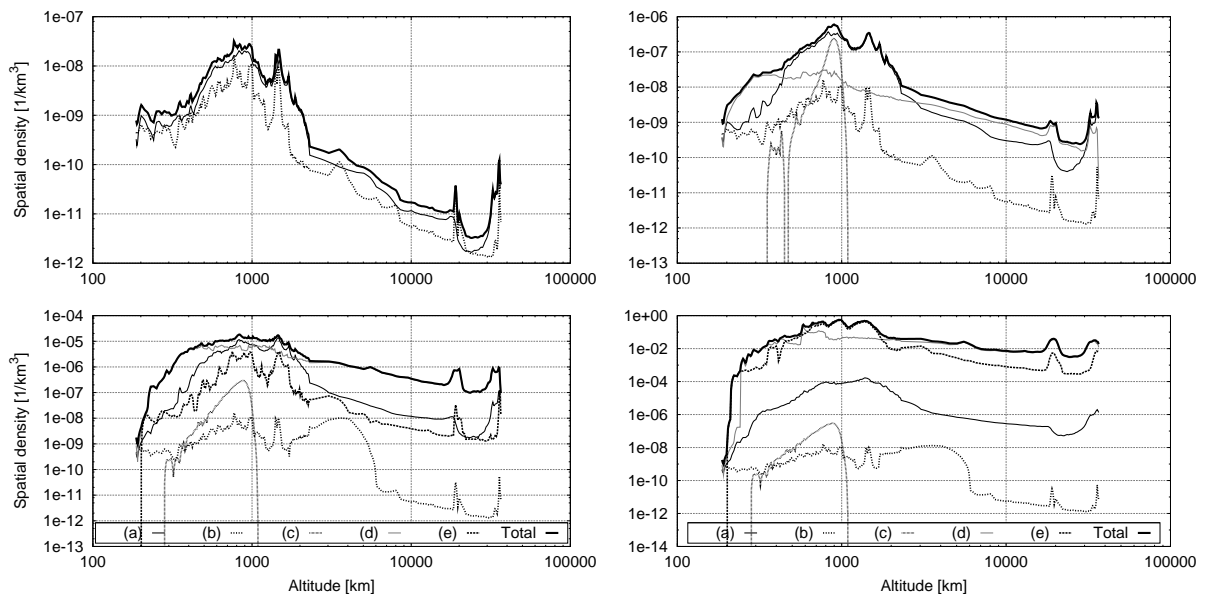


Figure 2.1: Space debris spatial density according to MASTER-2005, analysis epoch May 2005, (a): fragments, (b): launch/mission-related objects, (c): NaK droplets, (d): SRM slag, (e): ejecta. Top-left: size threshold 1 dm, top-right: 1 cm, bottom-left: 1 mm, bottom-right: 100  $\mu\text{m}$ .

Typical detection limits for optical telescopes (see Sect. 2.5) are down to about 5 cm diameter in LEO with the (no longer operational) Liquid Mirror Telescope (LMT), 0.6 m diameter object with albedo 0.2 at 36000 km using the (no longer available) CCD Debris Telescope (CDT), or about 20 mag for ESA's Zeiss 1-m-Telescope at Tenerife. These values correspond to objects of 0.1 to 0.2 m in diameter at GEO. Cost-efficient, robotic small aperture sensors, such as the Zimmerwald Small Aperture Robotic Telescope (ZimSMART/ZimSMART2), are able to detect metre-size objects in GEO. A knowledge gap exists in the centimetre regime at higher altitude (see Fig. 2.2). More details of the most important sensor installations will be provided in Sect. 2.5.

Smaller, non-trackable, particles of space debris are not in the focus of our work. Information on such objects can be retrieved from in-situ measurements, i. e., from surfaces that have been exposed in the space region of interest and brought back to ground. This method is mainly used for the LEO region. Some examples are the Long Duration Exposure Facility (LDEF), the European Retrieval Carrier (EuReCa), the Standard in Situ Impact Detector (DEBIE), surfaces of the space shuttle and components (mainly the solar arrays) from the Hubble Space Telescope. These surfaces provide knowledge of objects smaller than 0.1 cm. The distinction between impacts from debris and from meteoroids is a problem. From the impact craters (and calibration experiments on ground) the flux of space debris (and meteoroids) may be deduced as a function of particle size.

#### 2.4.1.1 Radar observation of space objects

A radar (radio detection and ranging) is always an active sensor that does not require illumination of the target object. At all weather conditions a radar provides range measurements by registering the time difference between the emission of energy (the "signal") towards the target and the reception of the reflected signal at the radar sensor.

Mono-static, bi-static, or even multi-static radars can be designed, depending on the co-location of transmitter and receiver antenna. We may distinguish furthermore between continuous-wave and pulsed radars according to the modulation of the amplitude of the transmitted signal. If a traditional radar system (that is basically a large dish-shaped antenna) is equipped with encoders on the antenna mount, the system may also provide angular information (e.g., azimuth and elevation) on the direction of the reflected energy. Range-rate information can be derived from the Doppler shift between the frequency of the received signal and frequency of the transmitted signal.

So-called phased-array radars, where the phases of the emitted signals are differentially shifted within an antenna array, are an alternative to the mechanically complex dish antennas. These type of radar allows it to control the shift of the maximum of the emitted signal to a different direction. This technique, also known as digital beam steering, allows for very flexible beam steering patterns and very short delays between different pointing directions of the emitted signal. Even multiple parallel pointing directions can be realised. Phased-array radars are of great importance for surveying large volumes efficiently (such as the French GRAVES, or the Cobra Dane radar (see Sect. 2.5.1)).

While most phased-array radars operate survey-oriented, we may distinguish survey and tracking operations for the traditional (dish) radars. In order to conduct surveys, the dish radar may be operated in a beampark mode, where the antenna points to a fixed elevation and azimuth. The acquired measurement data is only sufficient for providing statistical information, such as number and size of the objects crossing the field-of-view (FoV), as well as deducing coarse orbits. Operating the radar in tracking mode helps to acquire more precise data, which allows the determination of precise orbits. In tracking mode,

the radar usually follows previously (a-priori) objects for a certain period and registers epoch, angular direction, range, range-rate, amplitude and phase of the radar echoes, so that measurements distributed over a longer arc may be correlated with a particular object. Some radars can autonomously track in a closed-loop mode.

More information about radar are provided in Sect. 3.3.1.

### 2.4.1.2 Optical observations of space objects

We focus on optical observations of objects in space, in particular at Earth-orbiting satellites. In this section we focus on space surveillance applications of optical observations, the surveys and tracking techniques introduced in Sect. 2.4.1, but also touch “non-space surveillance” applications.

Position and apparent brightness of objects can be measured directly with optical means. Other interesting information is derived later on from these direct measurements, as, e.g., orbital elements (if more

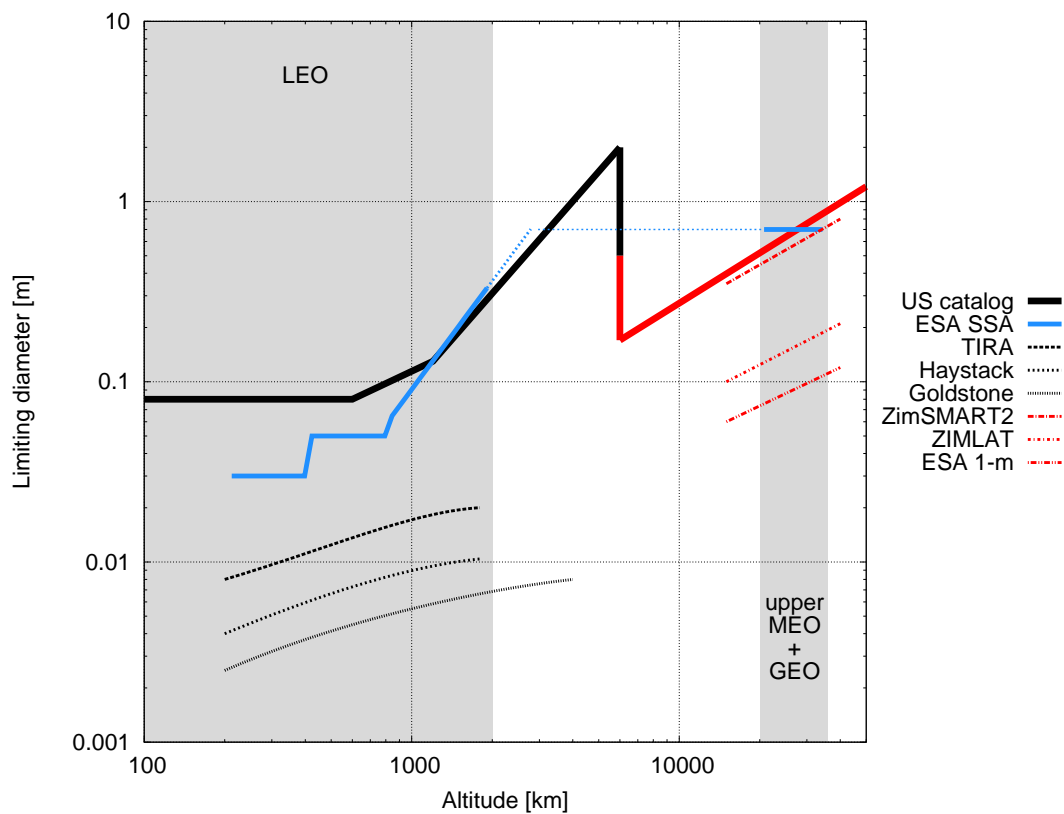


Figure 2.2: Assumed sensitivity and observation regions for US SSN and other sensors (modified from Krag (2003); Flury et al. (2000); Anonymous (1999b)); radar sensors are given by black, optical sensors by red curves. For comparison the requirements for ESA’s SSA system (Krag et al., 2010) are provided in blue colour.

than one observation is available), or the size of the object (from the phase angle at the observation epoch, and by making assumptions concerning the object's albedo and shape).

Optical observations of artificial satellites boomed in space geodesy before the 1970's. At that time optical observations were the primary tool to determine the orbits of satellites. The principles and techniques developed, e.g. by King-Hele (1983) are still valid today, but of course we need to take into account technological innovations, too. The major technological break-through is the digitalisation of the observation process. Efficient electro-optical detectors, such as charge-coupled devices (CCD), have been developed together with cost-efficient capabilities for handling the generated digital data. Optical observations only play, however, a minor role in modern space geodesy, because the achievable accuracy of the data is inferior to that of other space-geodetic observation techniques. Combining optical observations with data from other techniques is thus limited to some selected applications, such as the calibration of observing systems, or the validation of reference star catalogues (Flohrer, 2008). As Flohrer (2008) pointed out, an improvement by one order of magnitude of today's accuracy provided by optical observations might lead to a new type of coupling celestial and terrestrial reference systems. This so-called CQSSP (Coupled Quasar, Satellite and Star Positioning) was proposed by Baueršima (1984) and further refined by Schildknecht et al. (1991). The CQSSP proposal makes use of the fact that a satellite orbit may be well determined in both, the stellar and the terrestrial reference frame. The latter is linked to the quasar-based reference frame via the Earth orientation parameters (EOP). Thus, optical observations of satellites would enable the monitoring of transformation parameters between the quasar-based and the stellar-based reference frames.

Optical observations face the problem that the star background and the moving objects need to be segmented in the acquired exposures. Applying a specific tracking scheme when acquiring the exposure may help to solve this problem. Depending on whether star (sidereal) tracking or ephemeris tracking was applied, either the stars or the object are (nearly) point-shaped, and either the object or the stars are short streaks. It is, however, possible that both may appear as streaks if a different tracking scheme is applied. This streak-vs-streak segmentation is very challenging.

The segmentation may either use single exposures or series of exposures to identify moving objects in front of a star background. Several filter techniques may be applied in order to remove false detections or detector failures from the list of detected moving objects. In a next step all remaining candidate objects are subject to the so-called astrometric reduction. The measured centroid positions of the object pixel coordinates are transformed into a standard reference system, either a celestial or a terrestrial one, by applying corrections applicable to the observing system (mount/mapping), and, if necessary, station coordinates and Earth-orientation parameters as functions of the observation epoch.

The next step of data processing consists of the orbit determination using these astrometrically reduced observations. Objects found during surveys are usually unknown, implying that no a-priori orbital information is available. It is thus necessary to proceed with initial orbit determination algorithms. Initial orbit determination using the usually short observed arc will result in an orbit of limited accuracy and requires later improvement by additional further observations. The relevant definitions of detector parameters, reference frames, astrometric reduction, and (initial) orbit determination are provided in Sect. 3.3.2.8.

The short observed arc, either represented by a set of initial orbital elements, or by a list of observations, is the output of the survey and tracking tasks based on optical or radar observations. It is important to point out that all subsequently presented space surveillance principles (correlation and catalogue maintenance (see Sect. 2.4.2), and object identification and characterisation (see Sect. 2.4.3)) rely on short observation arcs.

### 2.4.2 Correlation and catalogue maintenance

The orbits and other properties of space debris objects are collected in a catalogue. These properties may include: shape and size, mass, albedo, and launch information. The most relevant catalogues, which are updated regularly, are the catalogue from the US Strategic Command (USSTRATCOM) and the catalogue from the Russian Federation. Both catalogues include information on active satellites and on space debris objects.

A catalogue contains at least the orbital elements of a certain number of objects at either a common reference epoch, or at known individual reference epochs per object. From these orbital elements an ephemeris can be generated through orbit propagation, where the same force model as for the orbit determination should be applied. The catalogue may also contain the individual observations of each object, which were used for orbit determination. Other observations, which were not used yet, are then treated as so-called un-correlated observations in a separate data pool.

The aim of correlation is the identification of observations of already known objects, which have already been observed or may already have been catalogued, and to generate correlated observations. This implies to decide whether or not an object detection is related to a “new” (i. e., a previously unknown or newly generated) object.

Catalogue maintenance goes a step beyond correlation. Starting from a given catalogue performance or quality criteria (like accuracy and timeliness of the stored data) certain rules for the re-acquisition of catalogued objects are defined. The definition and update of the observation schedule of the survey and tracking sensors takes these rules into account. The correlation of the resulting observations then helps to maintain (i. e., to refine and update) the catalogued data, but also to identify so-called “no-shows”. The latter are objects for which no new data could be correlated with the catalogue. In most cases “no-shows” are due to manoeuvring spacecraft, and hopefully not so often due to fragmentation events. In any case no-shows will trigger special observation patterns in order to restart the catalogue maintenance process for these objects. Table 2.2 summarises the four possible states of catalogue maintenance for a certain object as a function of object detection and object re-acquisition.

We treat correlation and catalogue maintenance as a single task, but these tasks are often discriminated in the literature. It is, however, difficult to clearly draw the borderline between correlation (of observations) and catalogue maintenance, because knowledge gained in the correlation of observations is useful for catalogue maintenance and both processes use similar, if not identical, techniques. Even if only short arcs are correlated with short arcs, our pragmatic definition of a catalogue supports that one may still

	Object detection	
Object reacquisition	true	false
true	correct reacquisition	miss-tag (wrong orbit determination)
false	missed re-acquisition, potentially leads to double object in catalogue, delayed catalogue update	new object

Table 2.2: Possible states of the catalogue maintenance process, depending on results of object reacquisition and detection tasks

see this correlation as a catalogue maintenance task, if one short arc is treated as representing catalogue containing only one object.

Algorithms and techniques for correlation of observations and catalogue maintenance are not well documented in the open literature. No generic approach is known, if existing at all. All solutions and algorithms that are available today are derived from specific problems. Some of them have been extended to a broader range of applications later on.

Relevant aspects for correlating optical observations at observation level are, e.g., studied by Früh et al. (2008). A similar brute force strategy is used in the widely used software package Apex by Koupryanov (2010). Früh et al. (2009a) and Früh et al. (2009b) discuss how short arcs can be mapped on a given ephemeris, which is one frequently used catalogue correlation technique. Correlation approaches based on initial orbit determination algorithms are, e.g., presented by Olmedo et al. (2008) and Olmedo et al. (2009).

Techniques and conceptual considerations for maintaining a catalog of specific near-GEO objects are discussed by Musci et al. (2010). The authors apply the presented technique successfully to observational arcs of several months. The underlying observation concept covers also catalogue build-up and is outlined by Musci et al. (2005) and further refined by Schildknecht et al. (2007). With that technique it is possible to build-up and to routinely maintain a catalogue of the visible GEO region making use of highly automated observation acquisition and processing systems (Herzog et al., 2010).

It has been shown recently that, as a principle, initial orbit determination and short arc formation, i.e., correlation of observations, can be combined into a common process (Farnocchia et al., 2010). This approach has been developed originally for heliocentric orbits and has been first introduced to Earth-bound orbits by Tommei et al. (2007). The concept makes use of so-called admissible regions of the topocentric distance and range-rate plane that contain all possible, i.e., physically meaningful, orbits, which could be associated with a given short arc. Experimentally, the concept was applied to a set of optical GEO observations by Milani et al. (2010). Its applicability to optical observations of LEO has been established by simulations. Maruskin et al. (2009) introduced a method of searching the admissible region more efficiently using Delaunay elements. Fujimoto and Scheeres (2010) use probability distributions in the Poincaré orbit element space to improve the mapping within the admissible region.

Taking into account the specific output of the survey and tracking tasks we may introduce in a more general manner the following correlation and catalogue maintenance approaches:

- Correlation of orbital elements (orbital elements of short arcs with catalogued orbital elements)
- Correlation of ephemerides (propagated ephemerides of uncorrelated objects with propagated ephemerides of the catalogued objects)
- Correlation of observations (observations of short arcs with catalogued observations of objects)
- Correlation of orbital elements with ephemerides (orbital elements of short arcs with propagated ephemerides of catalogued objects, propagated ephemerides of uncorrelated objects with catalogued orbital elements)
- Correlation of orbital elements with observations (orbital elements of short arcs with catalogued observations of objects, observations of short arcs with catalogued orbital elements)

- Correlation of ephemerides with observations (propagated ephemerides of uncorrelated objects with catalogued observations of objects, observations of short arcs with propagated ephemerides of catalogued objects).

### 2.4.3 Object identification and characterisation

Space object identification and characterisation is per definition more an SSA task rather than part of space surveillance. SSA requires the identification of objects that goes beyond the orbital elements and the object size. Catalogued object data in SSA are not limited to orbital elements, they may also include a subset of (at least) the following quantities: attitude parameters, object type (S/C, R/B, others and fragments), sensor/antenna pointing, physical parameters (e.g., shape, size, mass, material composition, optical & radar parameters), launching data (nation, if possible launch time, launch site), owner, operator, status (operational for S/C, non operational for all others), object function(s) or mission type and manoeuvre data. For all of these additional information the data source, the data history and (if possible) the degree of confidence in that information (i.e., the covariance) are also included. Typical problems of space object identification and characterisation are the required technological effort and the associated costs for acquiring the additional information, and the definition of an appropriate (i.e., a commonly accepted) data policy for accessing the generated data.

For the core task “space surveillance” a clear launch identification (COSPAR-ID) is, however, considered to be sufficient. The interest of civil SSA users is driven by collision avoidance activities and thus limited to status and manoeuvring capabilities and owner/operator identification of a conjuncting space object.

Space object characterisation can only be achieved through fusing data from heterogeneous techniques and multiple sensors. Efficient and reliable methods for sensor fusion are understood to impose a key problem today (see, e.g., recent work by Abbot and Wallace (2007) and Stansberry (2010)).

## 2.5 Sensors with space surveillance capabilities

Based on the introduction of space surveillance principles we now discuss observation systems providing space surveillance capabilities. The focus is on optical observing systems. Radars are only briefly considered. Where applicable, we discuss the image acquisition and orbit determination algorithms. We start with the ground-based optical observing systems, followed by a review of space-based observing systems.

Compared to a ground-based optical instrumentation, a higher number of observations – with increased accuracy – is possible from a space-based optical sensor, due to the absence of weather constraints. Furthermore the whole longitude band is in principle accessible from a single space-based sensor, and observations might not be limited by daylight conditions, as on ground. The big disadvantages are the costs and development time of a space mission and the limited operation lifetime. In addition, there is often no possibility to access space-based observation data in real-time due to limited data downlink or relaying opportunities.

### 2.5.1 Ground-based sensors

The most successful ground-based systems are currently operated in the United States, in Russia and in Europe. Other sensor systems exist in Japan, China, and Australia. We already mentioned the fact,

## *2 Space situational awareness, space debris, and space surveillance principles*

---

that for carrying out space surveillance, a network of space surveillance sensors is required. Today, only the United States and Russia operate such a network, and only the United States make a part of their resulting data products available to registered users.

Table 2.5.1 lists the characteristics of the ground-based sensors provided in this section.

Table 2.3: Ground-based sensors

Sensor name	Abbreviation	Observation technique	Location	Note
<i>Ground-based sensors of US Space Surveillance Network</i>				
Air Force Space Surveillance System (dedicated)	AFSSS	continuous-wave fully multi-static VHF radar interferometer	along 33° latitude in the continental US	
Eglin (dedicated)	AN/FPS85	single-side phased-array radar		
Ballistic Missile Early Warning System (collateral)	BMEWS	two-side phased array radars (except three-sided phases array radar at Fylingdales)	Thule (Greenland), Clear (Alaska), Fylingdales (UK)	
Phased Array Warning System (collateral)	PAVE PAWS	two-side phased array radars	Cape Cod (Massachusetts), Beale (California)	
Perimeter Acquisition Radar and Attack Characterization System (collateral)	PARCS	single-sided phased array radar	Cavalier (North Dakota)	
Antigua and Ascension radar (collateral)				
Cobra Dane (contributing)	AN/FPS108	single-side phased array radar	Shemya (Alaska)	
Millstone and Haystack radars (contributing)		dish radars	Westford (Massachusetts), operated by MIT	
ARPA Lincoln C-band Observable Radar (contributing)	ALCOR		Kwajalein Atoll, operated by the US Army	
ARPA Long-range Tracking and Identification Radar (contributing)	ALTAIR		Kwajalein Atoll	
Maui Space Surveillance System (collateral)	MSSS with MO-TIF	several telescopes, and spectrograph	Maui (Hawaii) operated by Air Force Maui Optical and Supercomputing Site (AMOS)	
Ground-Based Electro-Optical Deep Space Surveillance network (dedicated)	GEODSS	electro-optical telescopes	Socorro (New Mexico), White Sands Missile Range (WSMR), Mt. Haleakala at Maui (Hawaii), Diego Garcia (British Indian Ocean Territory), mobile site (MOSS) in Moron (Spain)	
<i>Other US sensors</i>				
NASA CCD Debris Telescope	CDT	mobile 32 cm telescope	Maui and Cloudcroft (New Mexico)	no longer operational
NASA liquid mirror telescope	LMT	3 m aperture telescope	Cloudcroft (New Mexico)	operated from 1996 to 2002
Meter-Class Autonomous Telescope	MCAT	1.3 m telescope	Kwajalein Atoll (Pacific)	operations to start 2011
Michigan Orbital Debris Survey System	MODEST	0.6/0.9 m telescope	Cerro Tolo Inter-American Observatory (CTIO), Chile	
Panoramic Survey Telescope and Rapid Response System	Pan-STARRS	1.8 m telescope		
Goldstone radar		bistatic dish radar		
<i>Russian Space Surveillance System</i>				
Volga radars		Tracking and phased-array radars	Nurek site (Tadshikistan)	operational since 1980
Okno system		Several telescopes		
<i>Other Russian sensors</i>				
International Scientific Optical Network	ISON	Numerous 0.4 m to 2.6 m telescopes	30 telescopes of 20 observatories in 8 states	operated by Keldysh Institute of Applied Mathematics of the Russian Academy of Science (RAS)
<i>European optical sensors</i>				

Continued on next page

Table 2.3 – continued from previous page

Sensor name	Abbreviation	Technique	Location	Note
Optical Ground Station	OGS	1 m telescope	Tenerife	operated by ESA
Zimmerwald Laser and Astrometry Telescope	ZIMLAT	1 m telescope	Zimmerwald Observatory, Switzerland	operated by the Astronomical Institute of the University of Bern (AIUB)
Zimmerwald Small Aperture Robotic Telescope	ZimSMART	20 cm telescope	Zimmerwald Observatory, Switzerland	operated by the Astronomical Institute of the University of Bern (AIUB)
Télescope à Action Rapide pour les Objets Transitoires	TAROT	25 cm telescope	Calern, France	operated by CNES
Starbrook wide-field telescope	TAROT-S	10 cm telescope	La Silla, Chile Troodos/Cyprus	sponsored by the British National Space Centre (BNSC)
Starbrook North		15 cm telescope	Herstmonceux, UK	
Colleparado Automatic Telescope		40 cm telescope	Colleparado, Italy	
Observatori Astronòmic de Mallorca		40 cm telescope	Mallorca, Spain	
Gautier astrograph		33 cm telescope	San Fernando, Spain	operated by the Real Instituto y Observatorio de la Armada (ROA)
Baker-Nunn camera		50 cm telescope	Montsec d' Ares, Spain	
"Pi of the sky" project		8 cm telescope	Las Campanas Observatory, Chile and Mazagn near Huelva, Spain	working prototype
<i>European radar sensors</i>				
Grand Réseau Adapté à la Veille Spatiale	GRAVES	bistatic radar, using VHF transmitters	near Dijon and Apt, France	operated by the French air force
Tracking and Imaging Radar	mono-pulse radar, parabolic dish antenna	TIRA	Wachtberg, Germany	belongs to the Fraunhofer Institute for High Frequency Physics and Radar Techniques (FHR)
Effelsberg		100 m radio telescope		operated with TIRA
Armor		radar	vessel Monge, France	operated by the Systems Evaluation and Test Directorate of the French Ministry of Defence (DGA/DCE)
Bearn, Provence, Gascogne		radars	France	operated by DGA/DCE
Chilbolton radar		monopulse radar operating in S-band	Winchester, UK	operated by the Rutherford Appleton Laboratory (RAL)
European Incoherent Scatter Radars	EISCAT	radar	Tromsø(Norway), Kiruna (Sweden), Sodankylä (Finland), Longyearbyen (Svalbard)	
Fylingdales		high-performance 3-face, phased-array radar, operating in the UHF-band	Fylingdales (UK)	US SSN sensor, operated by the British armed forces
Globus-II		X-band mono-pulse radar, parabolic dish antenna	Vardø, Norway	US SSN sensor
<i>Japanese sensors</i>				
Bisei SpaceGuard Center	BSGC	1 m optical telescope	Bisei SpaceGuard Center (BSGC)	operated by the Japan Aerospace Exploration Agency (JAXA)
Kamisaibara SpaceGuard Center	KSGC	S-band radar	Okayama prefecture	operated by JAXA

Continued on next page

Table 2.3 – continued from previous page

Sensor name	Abbreviation	Technique	Location	Note
<i>Australian sensors</i>				
Zadko		1 m telescope	90 km North of Perth	owned by the University of Western Australia
<i>Chinese sensors</i>				
Purple Mountain Observatory		1 m-telescope and 0.65 m telescope	Xuyi (Jiangsu province)	operated by the China National Space Administration (CNSA)

### 2.5.1.1 The US space surveillance network

The US Space Surveillance Network (SSN) of the US Strategic Command (USSTRATCOM) comprises more than 20 ground-based optical and radar sensors and from 1998 until 2007 and again from 2010 onwards it also has space-based observation capabilities. Currently, it tracks about 16500 man-made objects in the publicly available catalogue, and, in addition, an unknown number of objects in the so-called analysts catalogue.

The US space surveillance distinguishes between deep-space surveillance (more than 225 minutes revolution period) and low-altitude surveillance (fewer than 225 minutes revolution period).

The sensitivity limits of the SSN are not published. It is widely assumed that 10 cm objects in LEO and objects larger than 1 m in GEO (see Sect. 2.4.1) are covered. This sensitivity no longer meets future needs of the US. Spencer et al. (2000) report on a study of cataloguing 1 cm objects at 1000 km altitude by optical means. Schumacher (2009) expects a total catalogue size of more than 100,000 objects if 5 cm objects in LEO are catalogued. He reports on the planned and ongoing sensitivity upgrades of a central radar sensor of the SSN to achieve this enhanced sensitivity.

According to Chatters and Crothers (2009) three groups of sensors are distinguished in the US SSN (for the global distribution see Fig. 2.3):

- Dedicated sensors (military sensors fully available for space surveillance): GEODSS, MOSS, AFSSS and AN/FPS 85 at Eglin,
- Collateral sensors (the primary mission is not space surveillance): MOTIF, MSSS, BMEWS, PAVE PAWS, PARCS, the Antigua and Ascension radars,
- Contributing sensors (owned and operated by others, providing data on request of the US SSN): Millstone/Haystack, ALCOR, ALTAIR, and AN/FPS108 at Cobra Dane.

Klinkrad et al. (2008) mentions that the Globus-II X-band tracking radar located at Vardø, Norway, is connected to the US SSN.

The Air Force Space Surveillance System (AFSSS) was initially built-up and operated by the US Navy (NAVSPASUR or NSSS at that time) in the early 1960s. The system is commonly denoted as “the fence”. It is a continuous-wave fully multi-static Very High Frequency (VHF) radar interferometer that now consists of 3 triplets of 1 emitter and 2 receivers with all sites distributed along 33° latitude in continental US. This sensor provides most of the LEO observations for the US catalogue. An upgrade of the fence to S-band aiming to detect 90% of 5 cm objects at 1000 km distance is ongoing (Schumacher, 2009). This upgrade potentially involves new sites, e.g., on the Southern hemisphere. The new number of sites is unknown yet. Various design options are considered. The final system development is expected to start in 2012.

AN/FPS85 Eglin is a single-side phased-array radar. The ballistic missile early warning system BMEWS has sites in Thule, Greenland, in Clear, Alaska, and in Fylingdales, UK. All radars (except Fylingdales) has two-side phased array radars. The phased array warning system PAVE PAWS are two-side phased array radars, too, with sites in Cape Cod, Massachusetts, and Beale, California. The Perimeter Acquisition Radar and Attack Characterization System (PARCS) is a single-side phased array radar located at Cavalier, North Dakota, and points northwards over Hudson Bay. The Antigua and Ascension radars are used for telemetry tracking to support space control operations.

The AN/FPS108 Cobra Dane in Shemya, Alaska is a single-side phased array radar. Millstone and Haystack radars are dish radars, operated by MIT in Westford, Massachusetts. The MIT radars and the Cobra Dane sensor are also used for space debris observations (Stansbery and Foster, 2005). The ARPA Lincoln C-band Observable Radar (ALCOR) is a radar located on the Kwajalein Atoll, operated by the US Army. ALTAIR (ARPA Long-range Tracking and Identification Radar) is closely located to ALCOR, and is able to track GEO objects. Imaging capabilities are provided by Haystack and ALCOR.

An overview status of US optical observations of debris is given by Africano et al. (2001) and Africano et al. (2004). Results from debris observations from the Air Force Maui Optical and Supercomputing Site (AMOS) operating the MSSS (Maui Space Surveillance System with the Maui Optical Tracking and Identification Facility MOTIF) are presented. The MSSS comprises the large 3.7 m electro-optical telescope (AEOS), a recently renovated Baker-Nunn system, a spectrograph and, of lower complexity, the RAVEN telescope farm. The RAVEN telescopes are remarkable by using commercially available hardware and software to perform space surveillance tasks. With these telescopes of 0.36 m aperture,  $0.6^\circ$  FoV, and a moderate pixel scale of  $4''/\text{pixel}$  objects as faint as 17 mag could be detected with 20 s exposure time. The RAVEN telescopes are designed to work absolutely autonomously. The results include radiometric and spectroscopic observations in several passbands acquired by several telescopes, as well as imaging. Automatic observations using COTS equipment (so-called RAVEN-Class) are introduced, as well, as wide FoV applications (NEAT, GEODSS and Phoenix).

The backbone of the ground-based US Space Surveillance sensors observing high-altitude orbits is the Ground-Based Electro-Optical Deep Space Surveillance (GEODSS) network. GEODSS sites are at Socorro, New Mexico, on White Sands Missile Range (WSMR); Mt. Haleakala on the island of Maui, Hawaii; Diego Garcia, British Indian Ocean Territory. A mobile site (MOSS) located in Moron, Spain, is operated in addition. Observations are acquired with telescopes of basically Ritchey-Chrétien design equipped with CCDs. Each site operates four telescopes, three main telescopes (102 cm aperture,  $2^\circ$  FoV,  $f/2.15$ ) and one auxiliary telescope (38 cm aperture,  $6^\circ$  FoV), with the exception of Diego Garcia (three main telescopes), and the Moron Optical Space Surveillance System (0.5 m CCD telescope). A brief outline of the original GEODSS instrumentation is given by Schefter (1982). The pixel scale of the first main and auxiliary GEODSS telescopes was comparatively large:  $15''/\text{pixel}$  and  $40''/\text{pixel}$ . After 1999 the astrometric accuracy of GEODSS sensors was about  $4''$  (Faccenda, 2000).

The GEODSS network covers all altitude regions, from LEO up to GEO. The smaller aperture GEODSS telescopes are used to survey lower altitudes, searching objects with higher relative velocities. Details on sensor architecture and observation strategy are not available. It is known, however, that the observation and analysis concept was developed by the Lincoln Lab of the MIT: the telescopes perform sidereal tracking, taking very rapid exposures. Consecutive observations are combined. In these combined images, stars can be removed and objects - appearing as streaks can be extracted. Multiple objects in the same frame can be processed (Faccenda, 2000). GEODSS currently undergoes a refurbishment, a significant increase in the performance by 2-2.5 mag can be expected from the use of CCD detectors. Faccenda (2000) describes the CCD as MIT/LL CCID-16 device, a monolithic back-illuminated array of 1960 by 2560 pixels with  $24\ \mu\text{m}$ , covering nearly 60% of the focal plane. With 8 readout channels a readout rate of 3 frames per second should be achieved.

### 2.5.1.2 Other US sensors

In this section we discuss the capabilities of non-SSN sensors in the US. These sensors may provide either a higher measurement accuracy or a higher sensitivity compared to SSN sensors, but the acquired

data is only used for statistical analysis and these sensors are not meant to contribute to the maintenance of the US catalogue. It is important to note that several industry research and developing facilities exist in the US (which are not listed explicitly by Johnson (2001)) carrying out a major part of the space surveillance and space debris related research.

The most detailed description of the results, search strategy, system design and operation of the NASA CCD Debris Telescope (CDT) system is presented in a series of papers (Hebert et al., 2001; Jarvis et al., 2001b; Matney et al., 2004; Barker et al., 2005). Talent et al. (1997) give a description of the search strategy, focussing on high altitude regimes. The CDT was a mobile 32 cm aperture Schmidt telescope equipped with a CCD providing a  $1.7^\circ$  FoV. The CDT had been operated at Maui and Cloudcroft, New Mexico. The detection limit was reported at a visual magnitude of about 17.5. The CDT is no longer operational.

From 1996 until 2002 NASA also operated the LMT. The LMT had a primary mirror of 3 m aperture formed by a spinning dish of liquid mercury. The FoV was  $0.34^\circ$ . A video camera served as detector (Stansbery and Foster, 2005). Descriptions of the telescope and of the attempts to use the LMT for the detection of space debris in LEO and GEO from the telescope location in Cloudcroft, New Mexico are given by Potter and Mulrooney (1997) and by Hebert et al. (2001). Results of LMT observations are also presented by Potter and Mulrooney (1997) and, especially for a 1999/2000 LEO campaign, by Jarvis et al. (2001a). Due to the special configuration of this telescope only zenith-fixed observations were possible. The LMT mainly contributed statistical information on the orbital population, with a limiting object diameter of down to 0.05 m objects in LEO. A comparison of CDT and LMT results and their operation is provided by Africano et al. (1999).

NASA now designs and is about to install in 2011 a 1.3-m class telescope (Stansbery et al., 2010) on the Kwajalein Atoll in the Pacific for space debris research (the Meter-Class Autonomous Telescope MCAT).

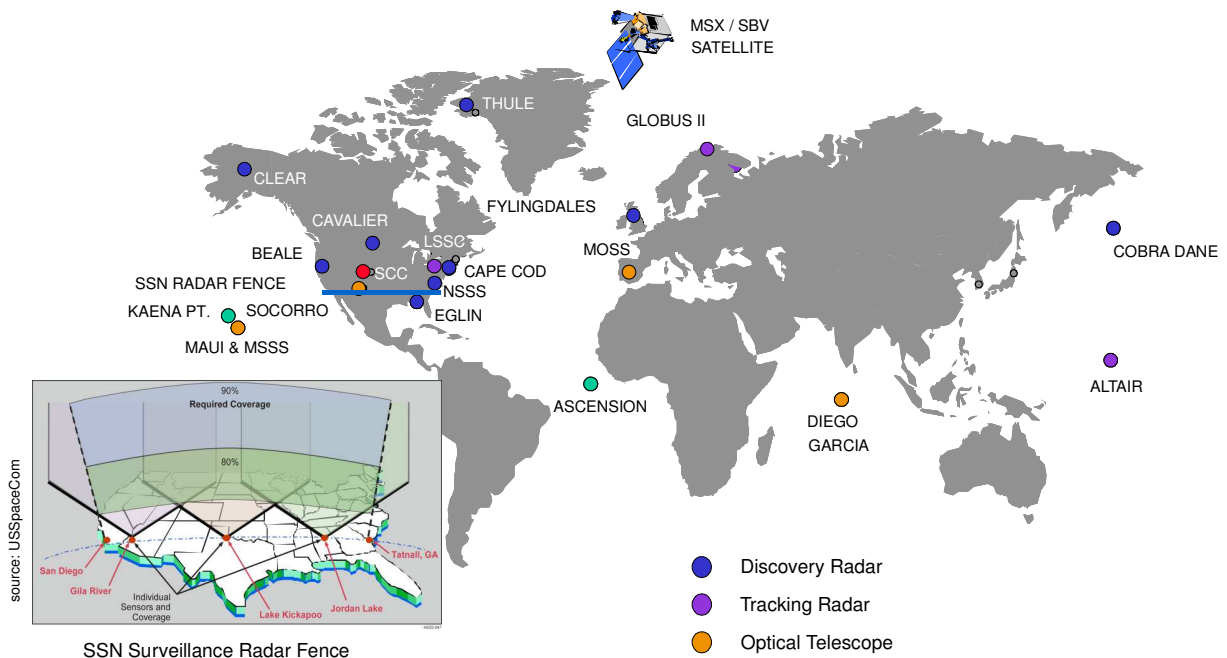


Figure 2.3: The US Space Surveillance Network (Source: (Klinkrad, 2011))

The FoV of the  $f/4$  modified Ritchey-Chrétien will be  $0.7^\circ \times 0.7^\circ$  ( $0.96^\circ$  in diagonal). A  $4k \times 4k$  CCD camera will be attached. For exposure times of 5 s it should be possible to detect 10 cm objects at GEO. A double horseshoe mount allows to operate at low latitude. Two operating modes are foreseen: a “track before detect” mode during twilight hours at low inclination and a more conventional GEO search elsewhere. Coordinated operation with the Kwajalein radars is planned with the goal to improve the estimation of object sizes from optical observations.

The Michigan Orbital Debris Survey System (MODEST) is the most important operational optical sensor for NASA today. The NASA program for ground-based optical observation of space debris has the focus on the use of MODEST. MODEST is a 0.6/0.9 m Schmidt telescope located at the Cerro Tolo Inter-American Observatory (CTIO), Chile, owned and operated by the University of Michigan. MODEST with  $f/3.5$  has a FoV of  $1.3^\circ$ . The detection limit is at a visual magnitude of +18. More details about MODEST, its survey campaigns, and the applied search strategy are provided by Seitzer et al. (2004). MODEST can apply a follow-up strategy (for MODEST the term “survey and chase” is common) when it is used in conjunction with the 0.9 m Small- and Medium-Aperture Research Telescope System (SMARTS) telescope that is also located at CTIO. MODEST is usually in survey mode while SMARTS is used to follow-up new detections.

The large optical synoptic survey telescope system Pan-STARRS (Panoramic Survey Telescope and Rapid Response System) will, after completion, consist of an array of four 1.8 m optical subsystems, which provide a very large FoV of 7 square degrees. Each of the four telescopes will be equipped with a 1.4 billion pixel CCD camera (Kaiser, 2006). This system is designed to search for Minor Planets, but its moving objects detection pipeline can be expected to detect, in principle, also objects in Earth-bound orbits. This pipeline is expected to operate with a detection threshold of 3 (Jedicke, 2006).

Looking to non-SSN radars, the Goldstone radar, a bistatic dish radar, has demonstrated the detection of 3 mm diameter objects in LEO (Matney et al., 1999).

### 2.5.1.3 The Russian space surveillance system

While the Russian Space Agency is responsible for all Russian space activities, the Russian Space Surveillance System (RSSS) is operated by the Russian Space Forces. Dicky et al. (1993) introduces the structure of the network and mentions that radar and optical observation means are available. Additional public information reveals that the RSSS consists of tracking and phased array radar systems (“Volga”), passive (and potentially also active) optical tracking facilities, as well as R/F sensors (Anonymous, 2008b).

A catalogue based on radar measurements conducted by the RSSS includes objects of a minimum size of 0.2 to 0.3 m up to altitudes of several thousand kilometers. A catalogue based on optical observations in the geostationary ring contains data of about 700 objects, including about 230 active spacecraft (Blagun et al., 1999). Klinkrad (2006) states that the catalogue maintained by Russian sensors is about 30% smaller than its US counterpart, which might be due to the higher latitude of the sensors of the Russian network preventing the cataloguing of low inclination orbits, or due to a lower sensitivity or reduced availability of the individual sensors.

Not too much is known about the currently used optical instrumentation. Blagun et al. (2001) and in more detail Batyr et al. (1993), later updated by Khutorovsky et al. (2001), give an overview, from which we conclude that optical observations of the Russian Space Surveillance System focus on the GEO region. The Okno system is the main optical sensor with 9 domes at the Nurek site in the Pamir mountains of

Tadshikistan (Anonymous, 2008b), which presumably is operational since 1980. No sensor and operating details are known.

Aksenov et al. (2003) give an overview about catalogued data. The results show that the Russian catalogues contain only a few MEO objects (compared to the American catalogue). However, the source of the data remains unclear. The optical part of the Russian Space Surveillance Network is assumed to consist of up to 14 sites with heterogeneous instruments up to 2 m apertures, partly equipped with CCDs. Considering that the sites are distributed over the former Soviet Union no full coverage of the Earth's near space environment is possible. The observations are limited to 30° up to 160° in longitude in the GEO. All sensors operate with significant availability gaps.

### 2.5.1.4 Other Russian sensors

The Keldysh Institute of Applied Mathematics of the Russian Academy of Science (RAS) conducts a very successful project on monitoring and surveying high-altitude orbits through the International Scientific Optical Network (ISON) (Molotov et al., 2008).

Since 2004 ISON has partnered with the Astronomical Institute of the University of Bern (AIUB) to track faint space debris objects mainly discovered with ESA's 1 m telescope at the OGS and with the Crimean observatory in Nauchniy. The tracking network covers more than 340° in longitude and consists of telescopes between 0.4 m and 2.6 m aperture. A total of more than 30 telescopes of 20 observatories in 8 states is organised in ISON (Molotov and Agapov, 2009). ISON is able to maintain orbits of presumably all larger objects that are not present in the US catalog, and to identify most of them (see the list of 235 identified objects provided by Flohrer et al. (2011b) based on ISON data). In addition, more than 500 faint space debris fragments, of which more than 200 are continuously tracked, were discovered (Molotov and Agapov, 2009). ISON now is in the process of adding dedicated, automated, 22 cm telescopes with a large FoV to the network, as well as designing 60 cm telescopes that will be added later on. Independently of the military data ISON data is used for conjunction assessment of operational spacecraft at high altitudes. Figure 2.4 illustrates the status of the ISON as of 2010.

ISON uses the identical open software package Apex-II (Kouprianov, 2010) at all core sites .

### 2.5.1.5 European sensors

A comprehensive overview on European capabilities is provided by Klinkrad (2006) and Klinkrad et al. (2008). Optical and radar sensors are available as in the US and the Russian systems, but there is no coordinated or integrated space surveillance system. All sensors operate independently, but there are as well some limited coordinated observations.

**Optical sensors** The most successful optical search program in Europe is run by ESA using the 1 m telescope at the Optical Ground Station (OGS) at Tenerife (Flury et al., 2000). This  $f/4.47$  sensor covers a sector of 120° of the GEO ring. The telescope has a FoV of 0.7°, which maps onto a 2×2 mosaic of CCDs of 2048 by 2048 pixels each. The detection threshold is at +19 to +21 visual magnitude (corresponding to 15 cm objects at GEO altitudes). The continuous update and validation of ESA's statistical space debris environment model MASTER using the PROOF tool is the key application for ESA. Schildknecht et al. (1995) outline the core detection technique, and Schildknecht et al. (1999) describe the observation strategy in detail. The common search strategy and the required use of follow-up

techniques to refine the determined orbits from the surveys are discussed by Schildknecht et al. (2001). In essence, initial orbits are derived from short observed arcs. These orbits are in general of adequate quality to ensure the re-acquisition of the object within the same night, which allows successive improvement of the orbit. This “follow-up” observation technique was applied to highly eccentric orbits and allowed it to detect objects with high area-to-mass ratio originating from GEO (see works by Schildknecht et al. (2004a) and Schildknecht (2007)). This long time series of now more than 12 years of observations allows statistical analyses of the GEO environment (Schildknecht et al., 2008).

ESA’s observation program is connected to the Zimmerwald Observatory of the AIUB. The core facilities at Zimmerwald are the Zimmerwald Laser and Astrometry Telescope ZIMLAT (see Schildknecht et al. (1997)) and the smaller ZimSMART/ZimSMART2. The operation scenario and the applied detection techniques for survey and follow-up observations are presented by Flohrer et al. (2007a). From its location in Zimmerwald, the telescopes cover a sector of  $100^\circ$  of the GEO ring. The primary applications of ZIMLAT are astrometry and satellite laser ranging, while ZimSMART/ZimSMART2 is dedicated to monitor objects at high altitudes. A significant share of the observation time is used for follow-ups of GEO objects discovered by the ESA telescope, or by the ISON network. ZIMLAT has been designed as a multi-purpose instrument and has an aperture of 1 m and a FoV of  $0.5^\circ$ . A CCD of 2048 by 2048 pixels allows the detection of objects up to visual magnitude +19. The 20 cm ZimSMART telescope complements ZIMLAT since 2006, and uses a CCD of 3056 by 3056 pixels with a FoV of  $4.2^\circ \times 4.2^\circ$ . With ZimSMART2 the optics of ZimSMART was replaced by the end of 2009. ZimSMART2 is a 30 cm aperture  $f/3$  telescope with an effective FoV of  $2^\circ \times 2^\circ$ . The pixel scale is  $1.8''/\text{pixel}$  and the limiting magnitude is +15 (Herzog et al., 2010). Herzog et al. (2010) were also able to show that a sensor like ZimSMART/ZimSMART2 is sufficient to cover a significant portion of the GEO objects in the USSTRATCOM catalogue, and to detect and catalogue a large number of previously uncatalogued

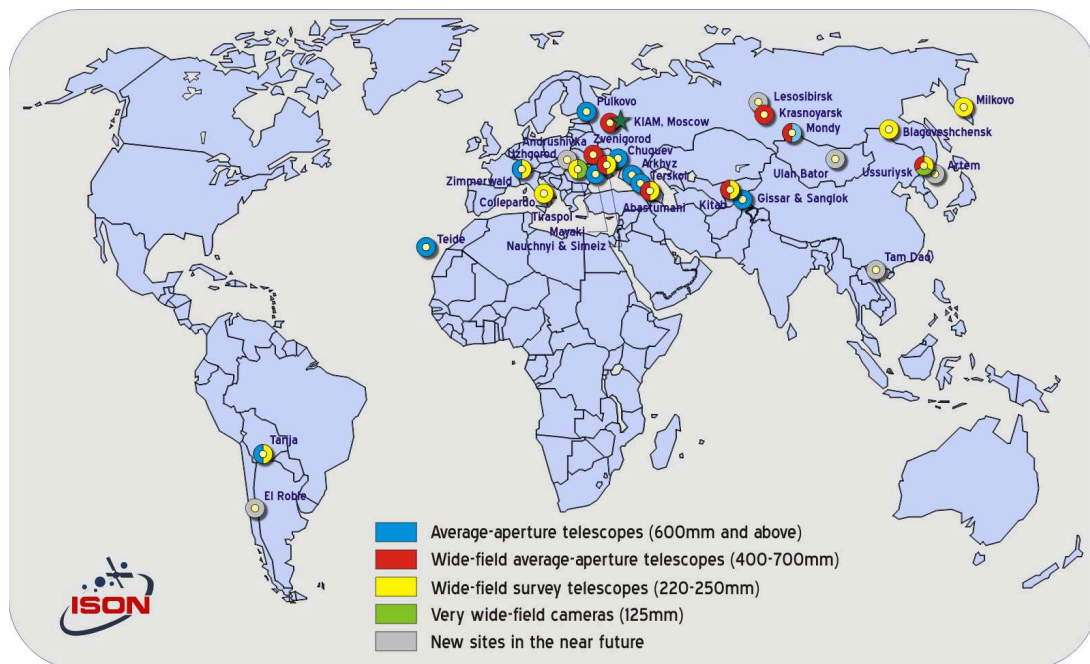


Figure 2.4: The ISON network (Agapov et al., 2010).

objects.

The French Space Agency CNES uses observation time of the TAROT telescope (Télescope à Action Rapide pour les Objets Transitoires) to survey and follow-up objects in GEO. The fully robotic TAROT is located at the plateau de Calern, France. The observation principles and strategies of TAROT and other (deactivated) French optical sensors are presented by Alby et al. (2004). A companion telescope, TAROT-S, has been deployed to La Silla, Chile. TAROT's primary mission is, however, the detection of the optical afterglow of gamma-ray bursts. The  $f/3.5$  TAROT has a 25 cm aperture, and a FoV of  $2^\circ \times 2^\circ$ . Equipped with a CCD of 2048 by 2048 pixels, the detection limit is at a visual magnitude of +18.2 for 30 s exposures. In 2009 both TAROT were connected with the Zadko 1 m telescope located in Western Australia to form a network that covering nearly the full longitude range (Laas-Bourez et al., 2011). All three telescopes use the identical software for observation scheduling and image processing.

The British National Space Centre (BNSC) has sponsored the Starbrook wide-field telescope as an experimental survey sensor for high-altitude debris search since 2006. The telescope is located at Troodos/Cyprus. It is able to detect objects down to a visual magnitude of +14. The telescope has an aperture of 10 cm, and a wide FoV of  $10^\circ \times 6^\circ$ . Starbrook is equipped with a CCD of 4008 by 2672 pixels. Starbrook North is located at Herstmonceux, UK, and provides an aperture of 15 cm and a  $4^\circ \times 4^\circ$  FoV. Both sensors operate independently but use identical software. Dick et al. (2009) introduce the sensors and survey results for the MEO region.

In 2002 an Italian group started to gather optical observations of space debris (Porfilio et al., 2002), which later on were extended to coordinated trial observations. The telescopes used were both of the Ritchey-Chrétien design: the 40 cm aperture,  $0.43^\circ$  FoV  $f/7.5$  "Colleparado Automatic Telescope" located in Colleparado, Italy, and the 40 cm aperture,  $0.3^\circ$  FoV  $f/5$  telescope of the "Observatori Astronòmic de Mallorca", located in Mallorca, Spain (Porfilio et al., 2006). More optical observations are carried out in Spain by the Real Instituto y Observatorio de la Armada (ROA) that observed satellites in GEO using ROAs 33 cm aperture Gautier astrograph with a FoV of  $0.45^\circ \times 0.3^\circ$ , located in San Fernando, Spain in the frame of the PASAGE project (Montejo et al., 2010). ROA is also involved in an ongoing upgrade of a Baker-Nunn camera (50 cm aperture,  $f/1.5^\circ \times 5^\circ$ ) at the summit of the Montsec d'Ares, Spain, promising efficient survey capabilities.

The "Pi of the sky" project (Nalezty et al., 2010), which performs an all-sky monitoring for gamma-ray bursts, is one example for an observing system that uses space debris observation and space population monitoring as a secondary mission goal. Since 2004 a working prototype is installed at the Las Campanas Observatory, Chile. The individual cameras provide 8 mm aperture with  $f/1.2$  and a FoV of  $20^\circ \times 20^\circ$ . The robotic installation combines 4 CCD cameras on one parallactic mount, so such a way that  $40^\circ \times 40^\circ$  can be covered. A second sensor has been installed at Mazagn near Huelva, Spain.

**Radar sensors** GRAVES (Grand Réseau Adapté à la Veille Spatiale) is a French military sensor, operated by the French air force. GRAVES has the capability to autonomously build-up and maintain a catalogue of orbital elements of LEO objects from scratch (Michal et al., 2005). Together with Fylingsdales it belongs to the few space surveillance sensors in the classical sense in Europe. GRAVES is able to maintain a catalogue of 2500 objects larger than 1 m with inclinations higher than  $28^\circ$  (Klinkrad, 2006). It is a bistatic radar, using VHF transmitters located near Dijon and receivers located near Apt, some 380 km south of Dijon. GRAVES carries out continuous surveys and is able to acquire simultaneous observation data (angles, Doppler shifts, and Doppler rates) for several objects.

The German mono-pulse TIRA (Tracking and Imaging Radar) belongs to the Fraunhofer Institute for High Frequency Physics and Radar Techniques (FHR) at Wachtberg, Germany. TIRA has a parabolic dish antenna of 34 m diameter, housed in a 49 m diameter radome. The radar uses L-band for tracking at 1.333 GHz, with 1 MW peak power, and Ku-band for Inverted Synthetic Aperture Radar (ISAR) imaging at 16.7 GHz, with 13 kW peak power. In its tracking mode, the TIRA system determines orbits from angles, ranges, and Doppler shifts for single targets. The detection size threshold is about 2 cm at 1000 km distance. This sensitivity can be enhanced to about 1 cm, when operating TIRA and the nearby Effelsberg 100 m radio telescope in a bistatic beam-park mode with TIRA as transmitter and Effelsberg as receiver. In this case only statistical data can be acquired. Details on the observation capabilities of TIRA are provided by Jehn (2001) and Mehrholz et al. (2002).

DGA/DCE, the Systems Evaluation and Test Directorate of the French Ministry of Defence, is operating several radar and optical sensors throughout France. Four types of radars are available: Armor, Bearn, Provence, and Gascogne. Normandie type radars will be put in service in the future. The most powerful of these systems, Armor, is located on the vessel Monge. The two Armor radars operate in C-band with 5.5 GHz, at 1 MW peak power. They are dedicated to tracking tasks, based on high resolution angular and range data.

The Chilbolton radar is located in Winchester, UK, and is operated by the Rutherford Appleton Laboratory (RAL). It is a monopulse radar operating in S-band at 3 GHz, transmitted through a 25 m parabolic dish antenna. Chilbolton is mainly used for atmospheric and ionospheric research. With a planned upgrade the radar would be able to track LEO objects down to 10 cm in size at 600 km altitude.

EISCAT is a network of European Incoherent Scatter Radars, with sites in Tromsø, Norway, (a transmitter/receiver site with a 32 m dish antenna), in Kiruna, Sweden (receiver only), Sodankylä, Finland (receiver only), and Longyearbyen, Svalbard (transmitter and receiver). The EISCAT system is mainly used for high-latitude ionospheric research. Its radar echoes, however, also contain information on LEO space objects. EISCAT has shown its capability to detect objects down to 2 cm sizes at altitudes of 500 to 1500 km (Markkanen, 2005). As these measurements are not sufficient to determine complete orbits, EISCAT is of lesser importance for space surveillance tasks.

Two US SSN sensors (see Sect. 2.5.1.1) are located in Europe. Fylingdales (UK) is a high-performance three-face, phased-array radar operating in the UHF-band. It is operated by the British armed forces and is associated with and feeds data into the SSN. No technical details are available. Globus II is located in Vardø, Norway. It is an X-band mono-pulse radar with a 27 m parabolic dish antenna housed in a 35 m radome.

### 2.5.1.6 Japanese sensors

Nakajima and Kurosaki (2007) introduce space debris observations performed by the Japan Aerospace Exploration Agency (JAXA). Both, radar and optical systems are used. The optical systems are located at the Bisei SpaceGuard Center (BSGC), while the radar is called Kamisaibara SpaceGuard Center (KSGC), located in the Okayama prefecture.

The S-band KSGC is remotely controlled and can be operated daily. It is able to track up to 10 targets simultaneously, with a range accuracy of 30 m, and accuracies of  $0.2^\circ$  and  $0.3^\circ$  in azimuth and elevation, respectively. It can observe objects up to 1350 km range. Spherical objects of about 1 m at distances of about 580 km may be detected.

The “Large Optical Telescope” at BSGC, a 1 m telescope with a  $3^\circ \times 3^\circ$  FoV, observes NEO, GEO and GTO objects. The CCD is remarkably large with a mosaic of 10  $2k \times 4k$  pixel sensors. Objects with velocities of up to  $5^\circ/s$  can be tracked. Two smaller telescopes of 0.25 m and 0.5 m aperture sharing the mount are used for tracking purposes. Both tracking sensors are wide-field telescopes with  $5^\circ \times 5^\circ$  and  $2^\circ \times 5^\circ$ , respectively. The 0.5 m instrument has a  $4k \times 4k$  pixel CCD detector, while the 0.25 m instrument uses a  $2k \times 2k$  pixel detector.

Recently, JAXA has added two sensors at Nyukasa highland, namely a 0.35 m telescope with a  $2k \times 2k$  CCD camera and a 0.25 m telescope with a  $2k \times 2k$  or  $4k \times 4k$  CCD camera in 2006. A stacking method for detecting faint objects in GEO has been developed, which accumulates the signals from an exposure series (Yanagisawa et al., 2005).

### 2.5.1.7 Australian sensors

Laas-Bourez et al. (2011) describe an optical observation capability in Australia, which started operations in 2009. The 1 m Zadko telescope is located 90 km North of Perth and is owned by the University of Western Australia. The  $f/4$  telescope has a FoV of  $0.39^\circ \times 0.39^\circ$ . The limiting magnitude is +21 for 180 s exposures. The control and processing software of the French TAROT is used. The Zadko telescope is also connected to the TAROT central scheduler. The current focus is on the GEO region, but concepts for LEO observations are under development, as well.

Newsam (2008) announces that Australia may host sensors of the US SSN in the future, such as a radar fence or optical telescopes. A surveillance and tracking system based on lasers already exists through Electro-Optical Systems (EOS). Their system is capable of detecting and tracking objects smaller than 10 cm at a distance of 1000 km.

### 2.5.1.8 Chinese sensors

Only very limited information is available on Chinese sensors or activities on space surveillance and space situational awareness. China develops space surveillance capabilities and investigates radar and optical sensor technologies. Zhao et al. (2010) report on a catalogue of 100 defunct Chinese satellites and spent upper stages, which is maintained by the Purple Mountain Observatory. In addition, a 1 m-telescope located in Xuyi (Jiangsu province) has been reported to perform a recent GEO survey (Zhao et al., 2010). MEO and LEO space surveillance capabilities also seem to exist at Xuyi. Back in 2002 the China National Space Administration (CNSA) operated a 0.65 m aperture  $3^\circ \times 3^\circ$  FoV telescope for GEO surveys. The limiting magnitude was around magnitude +18. Furthermore, two mobile 0.25 m aperture telescopes with  $4^\circ \times 4^\circ$  FoV telescopes with a limiting magnitude of +9.5 (Zhang, 2002) are in use.

## 2.5.2 Space-based sensors

In this section we focus on examples and studies for space-based optical sensors. We group the available information by origin, starting with the US, followed by Russia, Canada, Europe, and others.

A space-based sensor generates a higher number of observations than a ground-based sensor, and usually with a higher accuracy. Furthermore, the whole longitude band is accessible from a single space-based sensor. Costs and development time of a space mission and the limited operation lifetime, are, however, important disadvantages. Often is no possibility to access space-based observation data in real-time.

### 2.5.2.1 US sensors

Reports on space-based optical observations in the US are mostly related to the Space-based Visible (SBV) instrument onboard the Midcourse Space Experiment (MSX) satellite. The SBV instrument had been the only dedicated space-based space surveillance payload in orbit until 2010. It acquired space-based optical observations between 1996 and 2008 (Gaposchkin et al., 2000; Harrison and Chow, 1996; Butler, 2008).

After launch the MSX was placed in a sun-synchronous orbit at 898 km altitude. MSX is a  $1.5\text{ m} \times 1.5\text{ m} \times 5.1\text{ m}$  satellite with a mass of 2.7 tons. The goals of MSX with its four electro-optical sensors were not only to observe man-made objects, but also to measure the atmospheric and celestial backgrounds around Earth in a wide range of spectral bands, along with other technology exploration (Price et al., 2001). The SBV became primary payload in October 1997 after the cryogen was depleted and also the observations in the UV ended.

The SBV instrument is a 0.15 m aperture  $f/2.32$  three mirror off-axis anastigmat. The camera has 420 pixels by 1680 pixels ( $27\text{ }\mu\text{m}$  pixel size). The resulting rectangular FoV is  $1.4^\circ \times 6.6^\circ$ . The telescope was designed to allow very close pointing to the Earth, which requires efficient reduction of straylight. To ensure a high thermal stability the telescope was made of aluminium (Wang et al., 1991). The detection limit of SBV was equivalent to a 22 cm-diameter sphere at a distance of 3000 km (Stokes et al., 1998).

Stokes et al. (1998) and Harrison and Chow (1996) provide a review on the SBV project, covering technology and operational demonstration, radiation issues, metric and photometric data collection and cataloguing issues, and outline the hardware. Gaposchkin et al. (2000); Von Braun (1999); Von Braun et al. (2000) focus on space surveillance issues of the SBV and present two observation strategies with some implementation details, ephemeris and sidereal tracking. Updates to the observation strategy (which increased significantly the detection performance so that now the GEO is very efficiently covered) are given by Sharma et al. (2001). First orbit determination, orbit improvement and precise orbit determination for objects in GEO are discussed by Sharma (2000). These observations substantially contributed to cataloguing objects at high altitudes by USSTRATCOM (Miller and Schick, 1999). The achieved astrometric accuracy for GEO objects is 10 to  $20''$  (Faccenda, 2000).

The SBV could also have been used to observe the MEO region. The total observational error of the SBV was in fact determined by comparing the SBV-based orbits of GPS satellites with the known precise orbits from ground-based tracking networks.

The upcoming constellation of space-based space surveillance satellites (SBSS) can be viewed as the successor of the SBV and is reported to have capabilities for quick tasking due to slewable telescopes mounted on each satellite. The first SBSS was launched on September 25, 2010. SBSS is also expected to provide higher resolution data.

Not much information is available on the SBSS. A factsheet released by the manufacturer Ball Aerospace reveals that the first SBSS is designed for 5.5 years mission time. From a photograph the size of the satellite is roughly estimated to be  $4\text{ m} \times 2\text{ m} \times 2\text{ m}$ . The launch mass is below 1.1 tons. The telescope is introduced as a three mirror anastigmat mounted on a two-axis gimbal allowing to access  $3\pi$  sr. The aperture is 0.3 m and the camera has 2.4 megapixels.

Reynolds et al. (1989) outline a search scenario based on a telescope using the Space Shuttle as a platform. It is interesting that the authors considered debris in LEO with sizes as small as 1 mm in the discussion.

### 2.5.2.2 Canadian sensors

Canada has a long tradition in space-based optical observations. The observation of space debris is investigated as a secondary application of space-based observations of Near-Earth Objects (NEOs) in the NEOSAT mission and was scheduled for launch in 2010 (Wallace et al., 2004). Canadian researchers also have shown that tasked space-based observations of satellites can be extracted from other missions, e.g., from the first Canadian space telescope MOST (Microvariability and Oscillation Of Stars) launched in 2003 (Scott et al., 2006).

Reported to be of a similar design as the SBV the future Canadian Sapphire mission will be capable to provide observations of high-altitude (in particular GEO) objects from a sun-synchronous dusk-dawn orbit (Maskell and Oram, 2008). After its launch scheduled for 2011 Sapphire will become a key element of the Canadian Space Surveillance System. Sapphire is expected to become a contributing sensor to the US Space Surveillance Network.

### 2.5.2.3 European sensor studies

There are no past or current operational capabilities of space-based optical observations in Europe. Active research and conceptual studies are, however, performed by European researchers, supported in particular by ESA and the national space agencies.

A first theoretical study on how to choose and design an optical space debris search system for LEO and GEO was made by Lobb (1992). Based on signal-to-noise estimations, detection probabilities for different optical observation designs are discussed for ground-based and space-based systems.

Alby et al. (2000) discuss space-based optical observations for a 10 cm telescope with a  $1024 \times 1024$  passive pixel detector and conclude that space based observations are feasible and that for the size range of 0.1 mm-10 cm space-based passive optical observations are best suited.

A study made by CNES (Thillot et al., 2001) presents the results of a theoretical feasibility study about micro-satellites for detection and classification of small debris. The authors compare an active (pulsed micro laser) and a passive sensor, both using a 10 cm space-based optical telescope. The spatial and temporal coverage of the space debris environment are discussed, the sensor optics is outlined and finally a preliminary design proposal is made.

The use of small satellites in constellations is further studied by Vanwijck and Flohrer (2008), in particular in the context of a preliminary analysis of the benefits for SSA activities.

Interestingly, it was found that space-based sensors observing or searching for NEOs may also provide observations of artificial satellites in Earth-bound orbits, such as space debris. DLR's AsteroidFinder mission (Mottola et al., 2008) may serve as an example.

As already stated, optical observations may help to close the knowledge gap in the space debris population in the millimetre and centimetre regime by means of a passive optical instrument. Bendisch et al. (1993) focus on the observation of small-sized space debris environment in the 1 cm to 10 cm regime. The authors formulate requirements for optical space based debris observation missions, propose mission parameters and propose a mission concept. Based on that work Krag et al. (2001) focus on a specific passive optical in-orbit system. Various simulations using the PROOF tool were carried out. A deterministic approach to model the observations is introduced. We will make extensive use of that approach in Sect. 4. Oswald et al. (2004b) elaborates on space-based optical observations for the Robotic Geostationary Orbit

Restorer (ROGER) study. A part of the ROGER study dealt with a space-based telescope to observe the small-sized geostationary orbit debris population. It has been shown that even small telescopes are able to provide promising results, compared to the capabilities of ground-based radar systems. Again, ESA's PROOF tool was used to simulate different mission scenarios (in terms of telescope mounts, viewing direction and attitude stabilisation). The operational scenario for the ROGER telescope is a piggy-back GTO launch for GEO observation. Instrument configuration and parameters are then optimised for a 24 month operations scenario.

In 2005 a Finnish/Dutch/Swiss consortium under ESA contract formulated the user requirements and derived a suitable observation and processing strategy for space-based optical (SBO) observation of small-sized space debris. In parallel, the team developed a suitable sensor architecture, described the corresponding ground support system architecture, and defined the instrument operations, as well as the data processing concept together with the necessary calibration procedures. An end-to-end approach was chosen to assess the performance of the instrumentation.

The primary goal of the SBO study was to analyse how the mentioned knowledge gap can be closed. The SBO instrument was requested to provide statistical information on the space debris population, in particular number of objects and their size distribution. The SBO architecture and the key characteristics of the performance assessment have been published, see reports by Flohrer et al. (2005a, 2006); Wokke et al. (2006).

The proposed SBO is a small, low-cost space-based mission concept. It considers a cost-efficient instrumentation with flexible integration requirements. Therefore, the integration of the SBO as a secondary payload on satellites launched into low-Earth orbits (LEO) or into a geostationary orbit (GEO) was envisaged. A generic instrument architecture was found feasible for both. The platform was assumed to be a 3-axis stabilised spacecraft, which shall accommodate the telescope (a 20 cm aperture, 6° FoV, 45° folded Schmidt design with  $f/2.05$  and a field flattener), the camera (either a CCD or a hybrid CMOS detector with  $2k \times 2k$  pixels), electronics, and radiators. The overall dimensions of the instrument in nominal observation mode were found to be approximately  $105 \text{ cm} \times 70 \text{ cm} \times 35 \text{ cm}$ , with the estimated mass (without radiators) of 33 kg.

The particular mission concept only allows for fix-mounted SBO components. The study team assumed that the fixed pointing direction could be requested freely. The performance analysis showed that the statistical information on small-sized space debris can only be collected if the observation distances are comparatively small. Two regions of space debris populations were considered, the GEO and the LEO regions. The two most promising concepts are the observation of objects in LEO from a sensor placed into a Sun-synchronous LEO close to the terminator plane with the sensor pointing away from the Earth, but slightly inclined, while objects in GEO should be observed from a GEO satellite, with the sensor pointing to the North (or South). Another promising option to observe the GEO region with the sensor pointing "away from the Sun" would require the satellite to be placed in a low inclination orbit with an altitude below the GEO in order to achieve full GEO coverage, which was found only to be feasible in the frame of a dedicated mission.

The instrument is designed for autonomous operation. Observations and data processing shall be controlled by on-board software without the requirement of ground real-time commanding or specific spacecraft operations. Only subframes containing either reference stars or debris objects shall be downlinked due to the proposed "dynamic masking" image processing approach using series of exposures. Astrometric reduction, object identification and orbit determination shall then be carried out on ground. This approach keeps the downlink rate moderate.

The SBO feasibility study concluded that the capabilities of ground-based radar are theoretically superior in terms of sensitivity, but due to their limited availability an optical space-based system could still contribute significantly to the monitoring of the space debris environment. At higher altitudes (GEO) the SBO system is found to clearly exceed the capabilities of 1-m telescopes on ground by enhancing the knowledge about space debris from 10 cm diameter objects down to about 2 cm.

The performance of the SBO system proposal for observing small-sized space debris objects will be discussed in Sect. 4.4 (Flohrer et al., 2006), while Sect. 6 will analyse in detail the application of this instrument architecture for space surveillance tasks (Flohrer et al., 2011a).

#### **2.5.2.4 Other sensors**

The National Space Development Agency of Japan announced a Japanese “on-orbit debris observation system” in collaboration with the Japan Society for Aeronautical and Space Sciences (Takano and Imagawa, 1997). The feasibility of a Space Debris Observation Satellite (SDOS) was studied by Tajima and Takano (2001) in 1995. Different mission scenarios were considered for surveying the geostationary region either by a secondary payload onboard a GEO satellite or by a dual-launch. The two options comprise a drift orbit near the GEO and a so-called HERO (High Eccentricity Elliptical Recurrent Orbit) with a fixed line of apsides.

## 3. Observation fundamentals, data reduction, and orbit modelling

In this chapter we introduce the fundamental concepts and quantities required to describe, simulate and assess observation strategies and processing concepts. We start with defining the relevant reference systems, as well as the transformation parameters to connect the systems. We cover the orbital regimes. We also describe how measurements can be modeled with the focus on optical observations and show how the acquired data can be reduced. The most important quantities used to discuss the optical observation conditions of given objects (illumination conditions, signal-to-noise ratio (SNR), and apparent brightness) are introduced. We conclude with a brief outline of the relevant models of the orbit of artificial Earth satellites, also covering the frequently used two-line elements (TLE).

### 3.1 Reference systems

Subsequently, we will need an Earth-fixed and a celestial geocentric Cartesian coordinate system and the transformation between them. The former system is the natural choice to describe the station positions and motions, the latter to describe the satellite motion (via the equations of motion). A time-scale is needed to describe the evolution of satellite orbits and station coordinates as a function of time  $t$ . For a general discussion of time scales, reference systems, and reference frames we refer to Beutler (2005), for precise definitions of the reference systems actually used today, namely the International Terrestrial Reference Frame / International Terrestrial Reference System (ITRF/ITRS) and the International Celestial Reference Frame / International Celestial Reference System (ICRF/ICRS), we refer to the IERS conventions (Petit and Luzum, 2010) as issued by the International Earth Rotation and Reference Systems Service (IERS). The geocentric inertial coordinate system should be called quasi-inertial, because its origin is in accelerated orbital motion (of the Earth) around the Sun.

The transformation between the celestial and the terrestrial geocentric reference frames is governed by three Euler angles, which are functions of time (Beutler, 2005). Subsequently, we will use the transformation equations as provided by Petit and Luzum (2010) to describe the transformation between the two coordinate systems:

$$\mathbf{X}_C = \mathbf{P}(t)\mathbf{N}(t)\mathbf{R}(t)\mathbf{W}(t)\mathbf{X}_T \quad (3.1)$$

where  $\mathbf{X}_C \dots$  Vector in the ICRF  
 $\mathbf{X}_T \dots$  Vector in the ITRF  
 $\mathbf{P} \dots$  Transformation matrix containing precession parameters  
 $\mathbf{N} \dots$  Transformation matrix containing nutation parameters

- R** ... Transformation matrix containing the Earth rotation angle
- W** ... Transformation matrix containing the polar coordinates .

We will also need a detector coordinate system, which is a two-dimensional Cartesian coordinate system rigidly attached to the detector and that assigns each pixel of an electro-optical detector array (see Sect. 3.3.2.2) to two planar Cartesian coordinates  $x_p$  and  $y_p$ . During the detector readout the current per pixel is converted into its digital representation  $F(x_p, y_p)$ . The astrometric reduction (see Sect. 3.3.2.8) maps object positions  $x_p$  and  $y_p$  to the associated apparent topocentric direction in the celestial coordinate system.

The transformation of the observed apparent topocentric places into Earth-fixed coordinates consists of the following steps:

1. Correction for parallactic refraction
2. Correction for light travel time
3. Correction for geocentric parallax
4. Application of the inverse of Eq. 3.1.

## 3.2 Orbital regimes

Orbital regimes are used to classify objects, mainly by the altitude and eccentricity of their orbits. It is possible that an orbit crosses different regimes, which is why “resident” and “transient” orbits may be distinguished. For a resident orbit the boundaries of the orbital regime are not violated. For a transient orbit only a part of the orbit is inside the boundaries. Figure 3.1 illustrates the most important orbital regimes LEO, MEO, and GEO and shows two transient and one resident upper MEO orbits as examples.

### 3.2.1 LEO

The Low Earth Orbit (LEO) region goes up to 2000 km altitude. The majority of the LEO objects are in near-circular orbits. The revolution period of these objects is below 127 minutes. Due to atmospheric drag the lifetime of LEO objects ranges from days to hundreds of years, strongly depending on the selected altitude. The entire LEO region is a protected region where the generation of space debris should be limited.

Due to the small distance to the Earth’s surface but also due to sun-synchronous orbits (the orbital plane maintains always the same orientation relative to the Sun) the LEO regime is of particular interest to communication, meteorological, remote sensing, or reconnaissance missions. The vast majority of all catalogued objects (nearly 80%) and also the vast majority of all operational spacecraft resides in the LEO.

Optical observations of LEO objects not only have to cope with the high velocities of LEO objects with respect to the sensor, but also with the illumination conditions, in particular the Earth’s shadow. Observations are limited to a few hours during dusk and dawn periods and strongly depend on the altitude of the objects. Below 1000 km altitude optical observations are extremely difficult.

### 3.2.2 MEO

The MEO is implicitly defined as lying “between LEO and GEO” (Liou et al., 2004), roughly between altitudes of 2000 km and to 35586 km. This region is sparsely populated. Only about 4% of the catalogued objects reside in MEO. The orbital lifetime of MEO objects ranges from several centuries to some million years. Presently, there is no protected region in MEO. Johnson (2010) concludes that establishing such a region in MEO currently is neither justified nor necessary.

In order to focus on the most densely populated MEO part, which is used for navigation satellite constellations, Flohrer et al. (2008b) used a preliminary work definition of MEO with the perigee altitude above 2000 km and the apogee altitude below 34000 km and a mean motion between 1.5 and 2.5 revolutions per day. Some other references use the term “semi-synchronous orbits” for orbits with a revolution period of 12 h in an equivalent manner to MEO, and, at times, the term ICO (Intermediate Circular Orbits) is used, too. Figure 3.1 shows that ESA (Krag and Klinkrad, 2009) divides the MEO for practical reasons into a “lower MEO” regime with perigee above 2000 km and apogee below 12846 km altitude, and an “upper MEO” with perigee above 12846 km and apogee below 33786 km altitude.

In the MEO most of the active satellites are part of a satellite network or a satellite constellation. Most networks are used for communication and for navigation. Other use of the MEO region is relatively limited. Two exceptions are the passive geodetic satellites ETALON-1 and ETALON-2, which are observed by Satellite Laser Ranging (SLR).

The lower MEO region is well suited for establishing global communication networks. However, none of the networks planned in the early 1990s became reality: Odyssey, ICO, and Ellipso. The Odyssey system was planned to consist of 15 MEO satellites (four satellites evenly spaced in three orbital planes plus spares) in near-circular orbits at 10350 km altitude with 50° inclination. ICO (Inmarsat, then ICO, now ICO-Teledesic) planned to have a constellation of 10 MEO satellites at 10390 km altitude in two orthogonal planes with 45° inclination. One successful launch took place on 19 June 2001. Ellipso was designed to have four plus three satellites at 8050 km altitude, zero inclination orbits (“Concordia”) and in elliptical, highly inclined sun-synchronous orbits at 116.6° inclination with the apogee at 7605 km

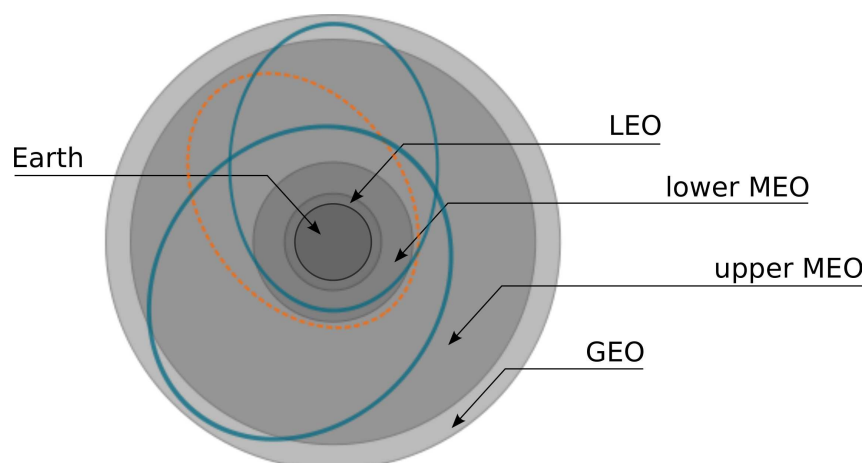


Figure 3.1: Classification of orbital regimes (not to scale), viewed from the celestial pole, modified from (Krag and Klinkrad, 2009), showing as examples transient upper-MEO orbits with a solid line and one resident upper-MEO orbit with a dashed line.

and the perigee at 633 km (“Borealis”). The later Ellipso 2G constellation had a system of three orbital planes housing five satellites each in inclined elliptical orbits. A fourth plane with six satellites in a circular equatorial orbit, and a fifth plane with five satellites in an elliptical equatorial orbit.

The GNSS (Global Navigation Satellite System) are the most prominent parts of the current active MEO population: the US-owned GPS (Global Positioning System) and the Russian GLONASS (Global'naya Navigatsionnaya Sputnikovaya Sistema). The European GNSS Galileo is under development, as well as the Chinese Compass/Beidou.

Deactivated satellites will drift with respect to the operational satellites of the constellation and therefore impose a risk. No end-of-life manoeuvring has been observed for GLONASS satellites, while GPS satellites are manoeuvred into higher graveyard orbits. Similar debris mitigation measures are discussed for Galileo (Jehn et al., 2009).

**GPS** The first GPS satellite was launched in 1978. After that the nominal constellation changed several times. Since about ten years more than 30 satellites are in orbit. In February 2011 32 satellites are active, implying that in general six satellites are simultaneously observable with elevations above  $15^\circ$  anywhere on Earth. The GPS constellation consists of 6 orbital planes, separated by  $60^\circ$  in longitude in the equator, with an inclination of  $55^\circ$ . Each plane nominally holds four unequally spaced satellites in circular orbits. The nominal altitude is 20200 km, thus the revolution time is about 11h58min, giving rise to a deep 2:1 resonance with Earth rotation.

The first class of GPS satellites, the so-called Block-I satellites formed a test constellation optimised for the coverage of North America. Block-I satellites had an inclination of  $63.4^\circ$ . No Block-I satellites are operational today. In 1989, Block-I was followed by the Block-II/IIA satellites. Since 1997 Block-IIR satellites are launched. By February 2011 a total of 59 GPS satellites are in orbit: 10 belong to Block-I, 28 to Block-II/IIA, 20 to Block-IIR, and 1 to Block-IIF.

GPS satellites are moved into graveyard orbits at the end of their mission (Jenkin and Gick, 2001; Jehn et al., 2009), as the current US guidelines require to clear the “semi-synchronous” orbit by  $\approx 500$  km (Anonymous, 1999a). GPS IIF satellites shall be put into a graveyard orbits 832 km above the nominal orbit (Chao and Gick, 2004).

**GLONASS** The GLONASS started operation as a Soviet system in 1982 and is now operated by the Russian Federation’s Ministry of Defense. The GLONASS satellites orbit at an altitude of about 19130 km, 1000 km below the GPS orbital height. The revolution time is 11h16min or  $8/17$  of a sidereal day, i.e., the configuration repeats after eight sidereal days. The nominal GLONASS configuration consists of three orbital planes, separated by  $120^\circ$  in longitude. The nominal inclination is  $64.8^\circ$ . In the nominal configuration eight satellites are equally spaced in each orbital plane, spaced by  $45^\circ$ . The system reached its full nominal configuration in 1995. The average lifetime of a GLONASS satellite used to be relatively short, only about three years, which is why Russia was not able to maintain the complete configuration. During recent years the constellation has been restored. As of 5 December 2010 the University of New Brunswick’s GLONASS Constellation Status report lists 19 operational satellites, two satellites in reserve, and five unhealthy but active satellites. Due to the short lifetime of the GLONASS satellites, there are a higher number of inactive satellites. DISCOS logs 92 inactive satellites in orbit.

**GALILEO** Europe develops its own GNSS named Galileo. The Galileo Program is a joint initiative of the European Commission (EC) and the European Space Agency (ESA). The goal is to provide Europe

with its own independent global satellite navigation system under civil control. Galileo will have a nominal configuration of 30 satellites in three orbital planes with  $56^\circ$  inclination in a Walker-type (Walker, 1971) configuration 27/3/1, including three in-orbit spare satellites. The orbital planes will be spaced by  $120^\circ$  in longitude. All orbits shall be nearly circular with a nominal altitude of 23616 km. The orbital period is thus about 14h04min. The satellites shall be placed equally distributed in the orbital plane.

Two experimental satellites are already in orbit: GIOVE-A launched in 2005, followed by GIOVE-B launched in 2008. The first IOV (in orbit validation) satellites were launched in 2011.

**Compass/Beidou** Compass is the second phase of the Chinese Beidou satellite navigation system. Compass will consist 30 satellites in MEO, and will have five satellites in inclined orbits near the GEO.

In 2007 the first Compass test satellite has been launched into a MEO orbit with an altitude of about 21150 km and an inclination of about  $55.5^\circ$ . Two more Compass satellites were launched into highly-inclined geosynchronous orbits. The system is currently under rapid development.

**Population assessment** No fragmentation events are known in the MEO region, which is why only few debris objects are catalogued (see Table 3.2.2). The statistical knowledge on space debris in MEO is illustrated by Fig. 2.1. Debris objects in super LEO and sub-GEO dominate the resident MEO population. A peak is visible at the altitude of the GNSS. The largest part of the population results from solid rocket motor slag particles, which are too small to be detected with ground-based optical observations. Further assessment also shows that debris objects are distributed over the whole inclination range, with a clear peak below an inclination of  $70^\circ$ .

The existence of small debris in resident or transient MEO orbits is still somewhat uncertain. Elliptical and circular MEO orbit regions have not been subject to intense search campaigns yet. Breiter and G. Métris (1998) estimate that the lifetime of GPS transfer orbits with the perigee at an altitude of about 190 km is between 1.8 and 32 years, depending on the initial right ascension of the Sun and the right ascension of the ascending node, with a mean lifetime of about 5.5 years. GLONASS transfer orbits have a higher perigee altitude of 400-500 km. Objects in GLONASS transfer orbits may have a lifetime of hundreds of years. Considering the lifetime of MEO objects in circular and elliptical orbits and the launch activities to MEO, we conclude that the debris population in MEO will continue to grow significantly, but will stay below the population density in LEO and GEO.

In the USSTRATCOM TLE catalogue of 25 February 2011 351 objects have the perigee altitude above 2000 km and the apogee altitude below 34000 km. The majority of these 257 objects performs fewer than 6 revolutions per day. A breakdown of that population according to their origin is given in Table 3.2.2.

Figure 3.2 and Fig. 3.3 show the distribution of the orbital elements w.r.t. inclination and ascending node, eccentricity and semi-major axis for the lower (indicated by circles) and upper (indicated by squares) catalogued MEO objects. Most of the MEO population is in near-circular orbits, only a smaller fraction of the upper MEO is found in highly-eccentric transfer orbits. In the inclination-node diagram (Fig. 3.2) the highly-inclined lower MEO in sun-synchronous orbits are visible in the centre of the figure, as well as the constellation design of GPS (six equally distributed orbital planes at  $\approx 55^\circ$  inclination) and GLONASS (three equally distributed orbital planes at  $\approx 64^\circ$  inclination). Figure 3.3 shows that a large part of the upper MEO objects are in near-circular orbits, while the lower MEO objects have slightly higher eccentricities. Figure 3.3 also indicates the presence of some objects in highly eccentric orbits meeting our MEO definition.

Identification in DISCOS	Number
NAVSTAR	59
GLONASS	118
Other COSMOS	3
GIOVE	2
BEIDOU	1
Rocket bodies	52
Debris	7
Others payloads	15
<b>Total</b>	<b>257</b>

Table 3.1: Catalogued objects in MEO orbit with  $n < 6$  rev/day, sorted according to DISCOS identification.

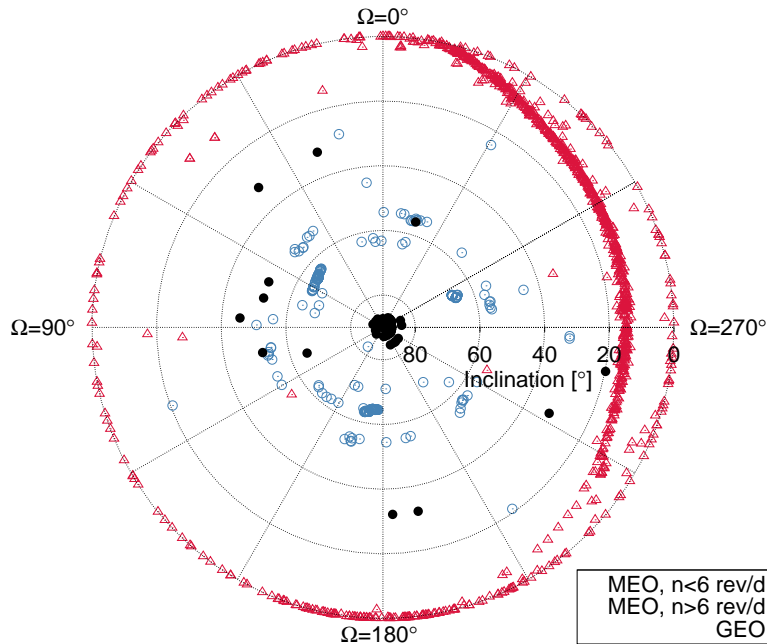


Figure 3.2: Inclination  $i$  vs. right ascension  $\Omega$  of the ascending node for catalogued MEO and GEO objects at the epoch 25 February 2011.

At a typical mid latitude observation site a large fraction of the MEO population is visible within 24 h. For the OGS a total of 332 objects out of 351 objects is above the horizon during 24 h, 237 of these objects complete fewer than six revolutions per day.

Figures 3.4, 3.5, and 3.6 give the apparent density and average dwell time for visible MEO objects per  $1^\circ \times 1^\circ$  bin in different coordinate systems averaged for a 24 h interval for the OGS site for the analysis epoch 25 February 2011.

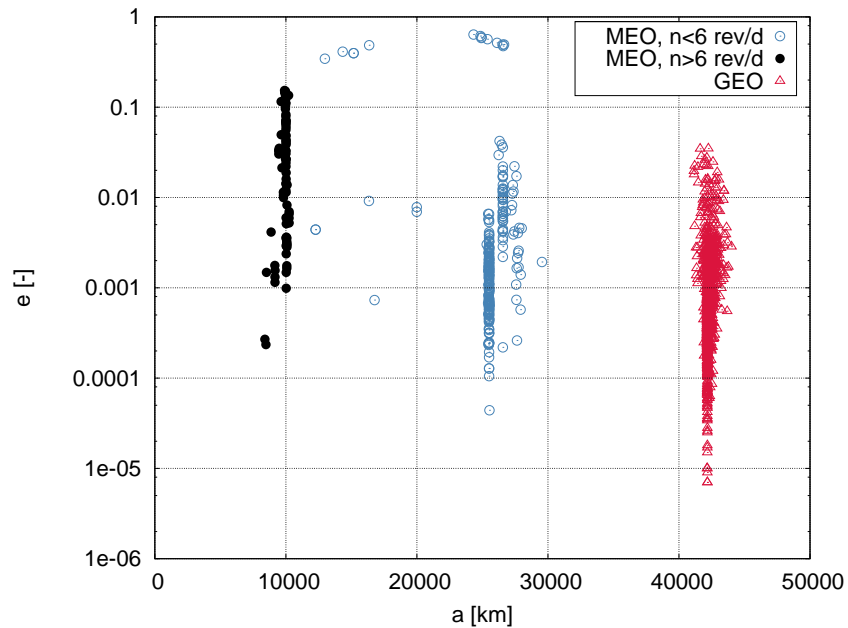


Figure 3.3: Eccentricity  $e$  vs. the semi-major axis  $a$  for catalogued MEO and GEO objects at the epoch 25 February 2011.

Figure 3.4 shows the predominant objects belonging to different GNSS, in particular to the GLONASS constellation. The apparent MEO density shows that most GNSS use Walker-type constellation designs, and therefore all satellites are placed into a limited number of specific orbital planes. The dwell time per bin varies more in the equatorial frame than in the local topocentric frame (Fig. 3.5).

The preferred GNSS constellation design in MEO is visible in Fig. 3.5 in the local topocentric frame. The apparent object density is low in the topocentric North direction around the celestial pole. GNSS objects are not expected in this area. Around this sparsely populated region, a 'caustic' around the culmination is prominent for azimuth angles between  $320^\circ$  and  $40^\circ$  and for elevation angles up to  $45^\circ$ . This caustic corresponds to the highest possible declination, where the highest spatial density is expected. The dwell time does not vary much around 170 s per  $1^\circ \times 1^\circ$  bin. The s-shaped features in the figure are due to single objects in highly-eccentric orbits.

No relevant structures can be seen apart from the GNSS-driven latitude cut-off in the rotating earth-fixed coordinate frame (latitude/longitude). The average dwell time for the GNSS objects per bin is about 220 s. In both pictures of Figure 3.6 one can see the equally distributed background scatter from the lower-MEO objects.

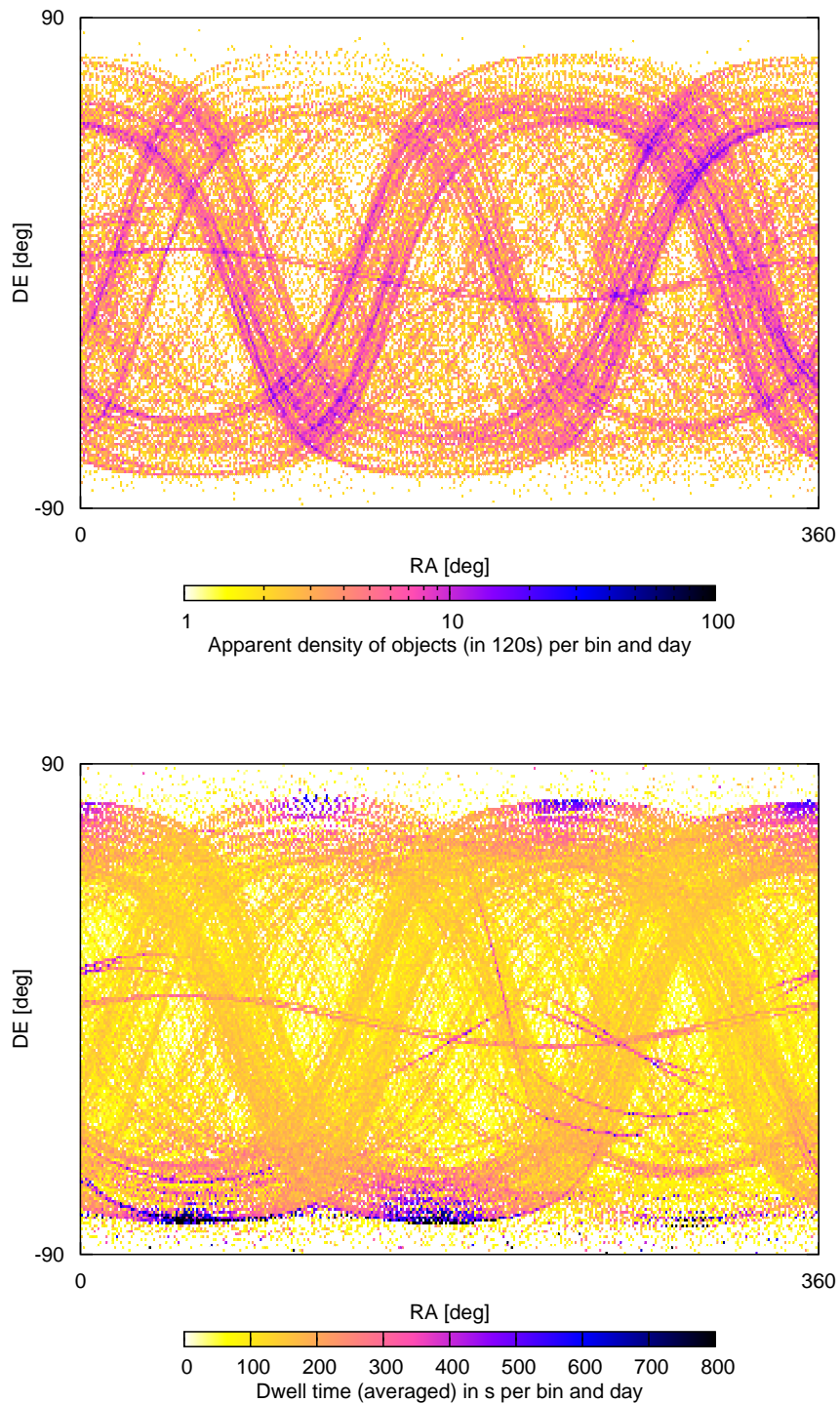


Figure 3.4: Apparent density and average dwell time in the J2000 frame for 332 MEO objects visible from the OGS on 25 February 2011, which are listed in the USSTRATCOM public TLE catalogue of that date per  $1^\circ \times 1^\circ$  bin. The density is calculated from 120 s sampling of the objects' ephemerides.

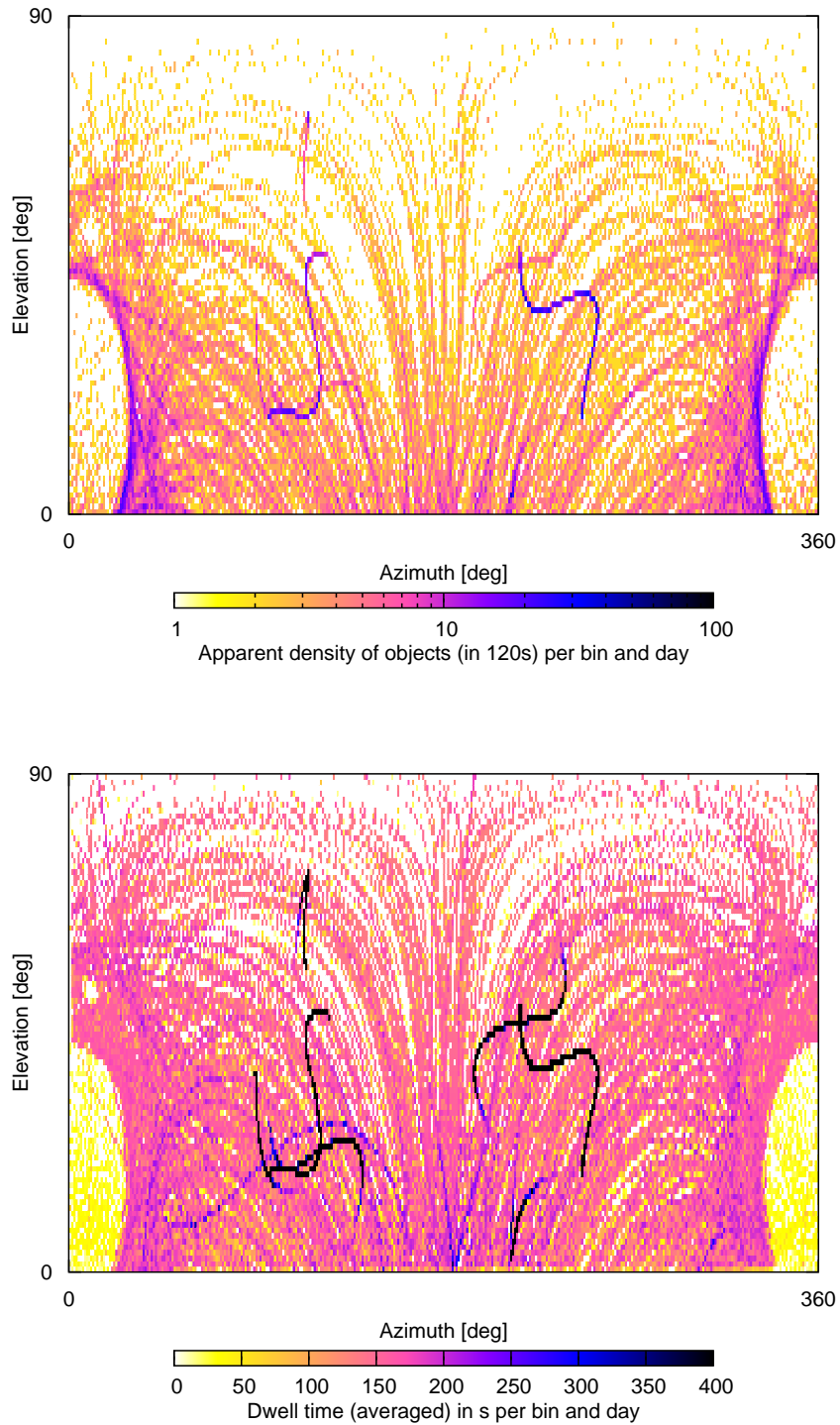


Figure 3.5: Apparent density and average dwell time in the OGS topocentric frame for 332 MEO objects visible from the OGS on 25 February 2011, which are listed in the USSTRATCOM public TLE catalogue of that date per  $1^\circ \times 1^\circ$  bin. The density is calculated from 120 s sampling of the objects' ephemerides.

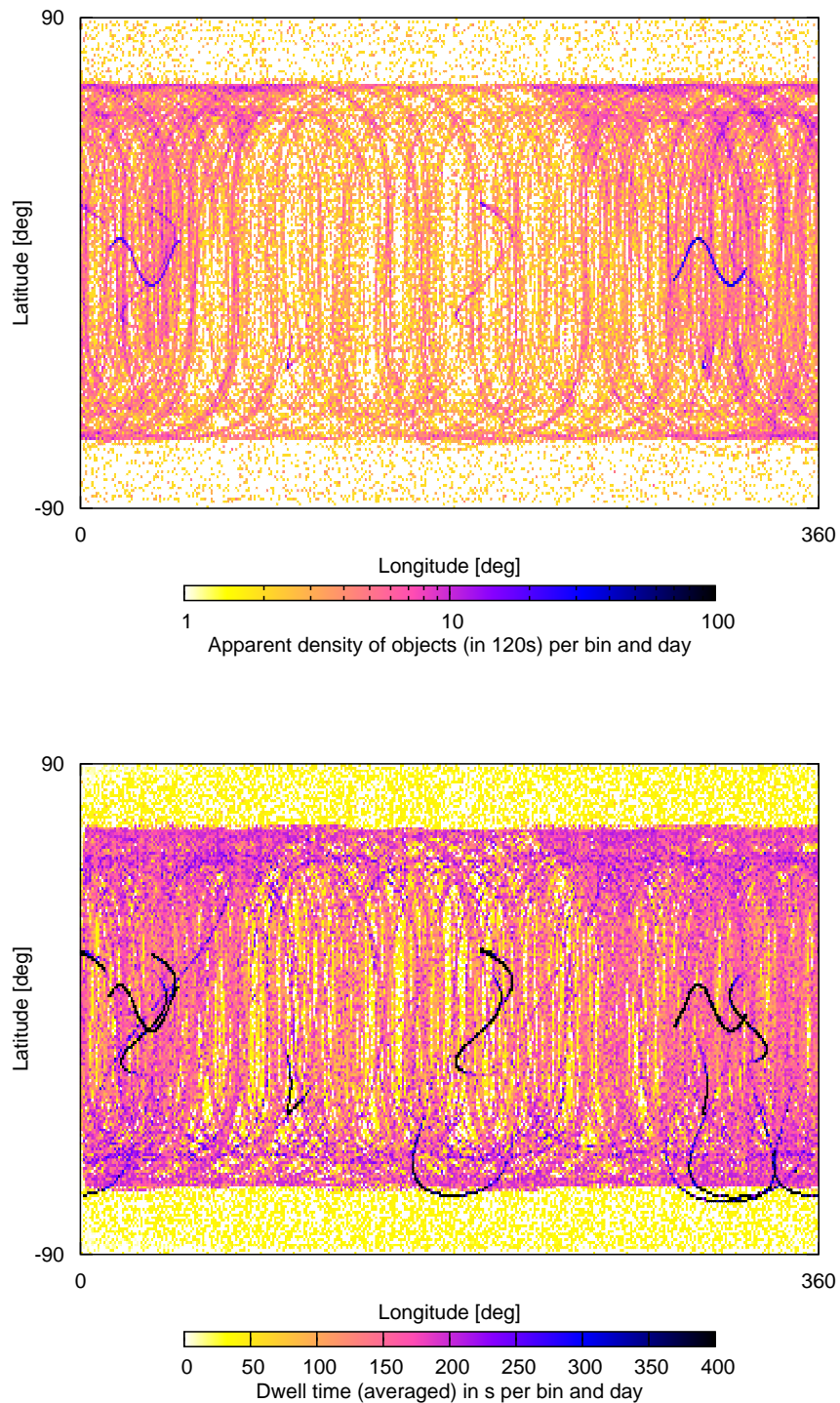


Figure 3.6: Apparent density and average dwell time in the Earth-fixed rotating frame for 332 MEO objects visible from the OGS on 25 February 2011, which are listed in the USSTRATCOM public TLE catalogue of that date per  $1^\circ \times 1^\circ$  bin. The density is calculated from 120 s sampling of the objects' ephemerides.

### 3.2.3 GEO

Satellites with an inclination of  $0^\circ$  and an altitude of 35 786 km have a revolution period of 23h56min and appear stationary in an Earth-fixed reference frame. This characterisation makes the GEO an unique resource, in particular for Earth observation, communication and broadcasting purposes.

Usually satellites are not directly launched into GEO, but are injected from a Geostationary Transfer Orbit (GTO). As objects will remain in GEO for millions of years, it is of paramount importance to remove retired satellites from the GEO, which is achieved by re-orbiting satellites to a graveyard orbit at least 235 km above the nominal GEO altitude, outside of the protected GEO region. This region is defined for the altitudes of  $35\,786 \pm 200$  km and inclination between  $0^\circ$  and  $15^\circ$ . This definition corresponds to an circular orbits with an orbital period of 1425.6 to 1446.7 min.

The motion of the orbital planes of GEO objects can be described as a precession around the Laplacian plane with a period of about 53 years. The inclination of  $7.3^\circ$  of the Laplacian plane (the plane normal to the vector of total angular momentum) remains approximately constant during the precession, so that the inclination of the orbital planes of the GEO objects increases from 0 to  $14.6^\circ$  during 26.5 years and then decreases to 0 over the next 26.5 years. Other perturbing forces, in particular induced by solar radiation pressure, may add more periodic variations of the inclination. Therefore, most objects in that altitude band have a low inclination below  $17^\circ$  (Flohrer et al., 2006) to  $20^\circ$  (Krag and Klinkrad, 2009).

Due to the non-circularity of the Earth's equator (no-zero  $J_{22}$ -term of the Earth's gravitational potential), satellites at nominal GEO altitude are subject to periodic longitude variations usually around one of two stable equilibrium points at longitudes  $75.3^\circ$  East and  $104.7^\circ$  West. Therefore a classification scheme for GEO objects can be defined distinguishing controlled, drifting and librating objects (Flohrer et al., 2011b).

Often a band of  $\pm 2000$  km around GEO is referred to as "the GEO region" to cover also graveyard objects and fragments. Space debris from fragmentation events exists in GEO, although they are not listed in the catalogue. Two explosions in the GEO region are confirmed. Johnson et al. (2008) list a Titan 3C Transtage, which fragmented in 1992 and an EKARAN 2 satellite that fragmented at an unknown epoch. The existence of small-sized space debris objects could be confirmed later by optical observations from ESA surveys (Schildknecht et al., 1999; Schildknecht, 2007). Statistical analysis from observing space debris clouds in GEO by Schildknecht et al. (2008) indicate that more fragmentation events in GEO have occurred. With modelling techniques ESA's MASTER model introduces several (eight to nine) synthetic fragmentation events to explain the observational data.

Flohrer et al. (2011b) use a working definition of GEO, which limits the eccentricity to 0.2 and the mean motion to between 0.9 and 1.1 rev/day, corresponding to a semi-major axis between 39 664 km and 45 314 km, and the inclination to  $30^\circ$ . As recently more objects have been launched into high inclination, near circular orbits, ISON proposes to define the GEO inclination between  $0^\circ$  and  $30^\circ$ , the eccentricity below 0.2, and the mean motion between 0.7 and 1.3 revolutions per day.

The distribution of the orbital elements of the catalogued GEO population is given in addition to the catalogued MEO population in Figs. 3.2 and Fig. 3.3, and is indicated by triangles. Figure 3.3 shows that GEO objects are in near-circular orbits, for some of the controlled objects the eccentricity is kept at very low values. The precession of the orbital planes around the Laplacian plane is visible in Fig. 3.2. The first objects in GEO, which ended operational life during the 1960s, are about to finish their first revolution around the pole of the Laplacian plane.

As of 25 February 2011 985 objects in the USSTRATCOM TLE catalogue meet the common GEO definition with an altitude band of  $\pm 2000$  km (Table 3.2.3). Flohrer et al. (2011b) state that 397 of

Identification in DISCOS	Number
Payloads	809
Rocket bodies	160
Debris	16
<b>Total</b>	<b>985</b>

Table 3.2: Catalogued objects in GEO orbit sorted according class in DISCOS.

the catalogued objects in GEO are controlled objects of which 268 are under longitude and inclination control. Flohrer et al. (2011b) also provide information based on ISON observations on 235 additional controlled and uncontrolled objects in GEO. For 163 of these additional objects orbital elements are available and 157 objects can be correlated with a launch. The total number of known objects in the geostationary region exceeds the catalogued population by about 23%.

Only a certain part of the GEO population is, in principle, observable for a given site. The fraction strongly depends on the latitude and on the number of station-keeping satellites in the accessible longitude band. For a low-latitude site, as, e.g., the OGS, the accessible longitude band is about  $120^\circ$  for a  $10^\circ$  elevation mask. At the OGS 462 of the 985 catalogued objects are above the horizon during 24 h.

Figures 3.7, 3.8, and 3.9 show the apparent density and average dwell time of catalogued GEO objects observable from the OGS per  $1^\circ \times 1^\circ$  bin averaged over 24 h for epoch 25 February 2011.

Figure 3.7 gives the apparent density and dwell times for GEO objects in the inertial frame. The highest density is visible for the large group of station keeping low-inclination satellites with a declination close to  $0^\circ$ . The motion of the orbital planes of uncontrolled objects is reflected by a region with higher densities forming a 'caustic'. This caustic region starts at  $\alpha=90^\circ$  towards the maximum declination, as well as heads from  $\alpha=270^\circ$  towards the minimum declination. This properly indicates how the orbital pole starts to drift towards the vernal equinox when the satellites are no longer controlled. One can also see that the oldest objects in GEO are about to finish their first rotation around the pole of the Laplacian plane. In the most densely populated regions of the caustic up to 120 objects can be counted per  $1^\circ \times 1^\circ$  bin during one day. The average dwell time is about 340 s per bin, slightly longer in the maximum and minimum declination areas.

Figure 3.8 shows the density and dwell time in the local horizon of the OGS. GEO objects culminate in the South direction while they cross the local meridian. The highest density of objects in the nominal GEO ( $0^\circ$  declination) is visible, which, due to inclination and longitude control, leads to infinite dwell times for some objects. Objects with non-zero inclination angles follow an eight-shaped curve closing after about 24 h. Longest dwell times of objects without inclination control are expected at the maximum distance from the nominal GEO, where it can reach about 3600 seconds, while in the other  $1^\circ \times 1^\circ$  bins the average dwell time is about 1800 seconds.

Figure 3.9 also illustrates that only part of the full longitude band can be accessed from a single site. The highest density is again associated with the controlled satellites. These satellites are skipped in the dwell-time picture of Fig. 3.9. The shortest dwell times can be expected at the maximum distance from the GEO with about 600 seconds in this frame, while the average is about 3000 seconds per  $1^\circ \times 1^\circ$  bin and object.

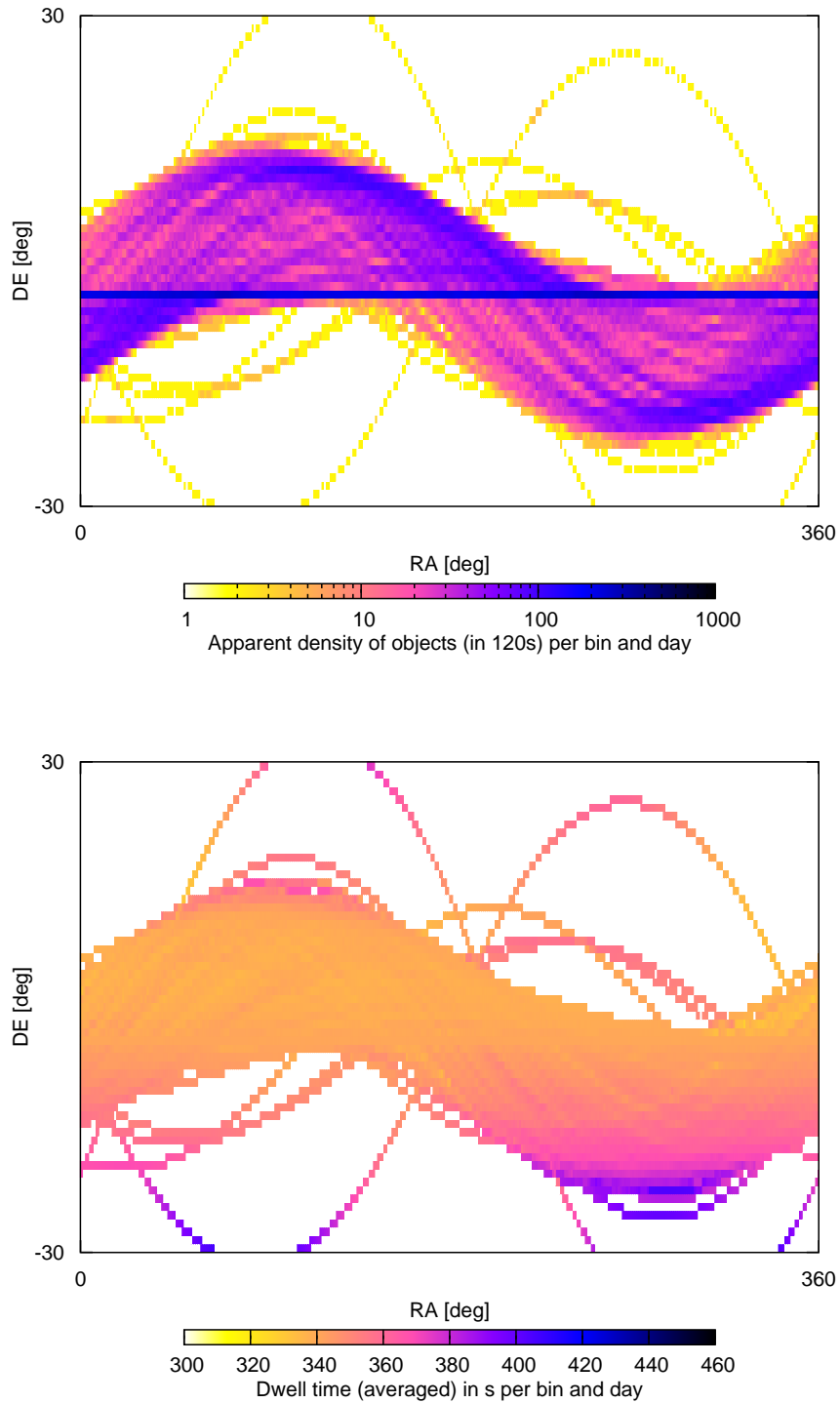


Figure 3.7: Apparent density and average dwell time in the J2000 frame for 462 GEO objects visible from the OGS on 25 February 2011, which are listed in the USSTRATCOM public TLE catalog of that date per  $1^\circ \times 1^\circ$  bin. The density is calculated from 120 s sampling of the objects' ephemerides.

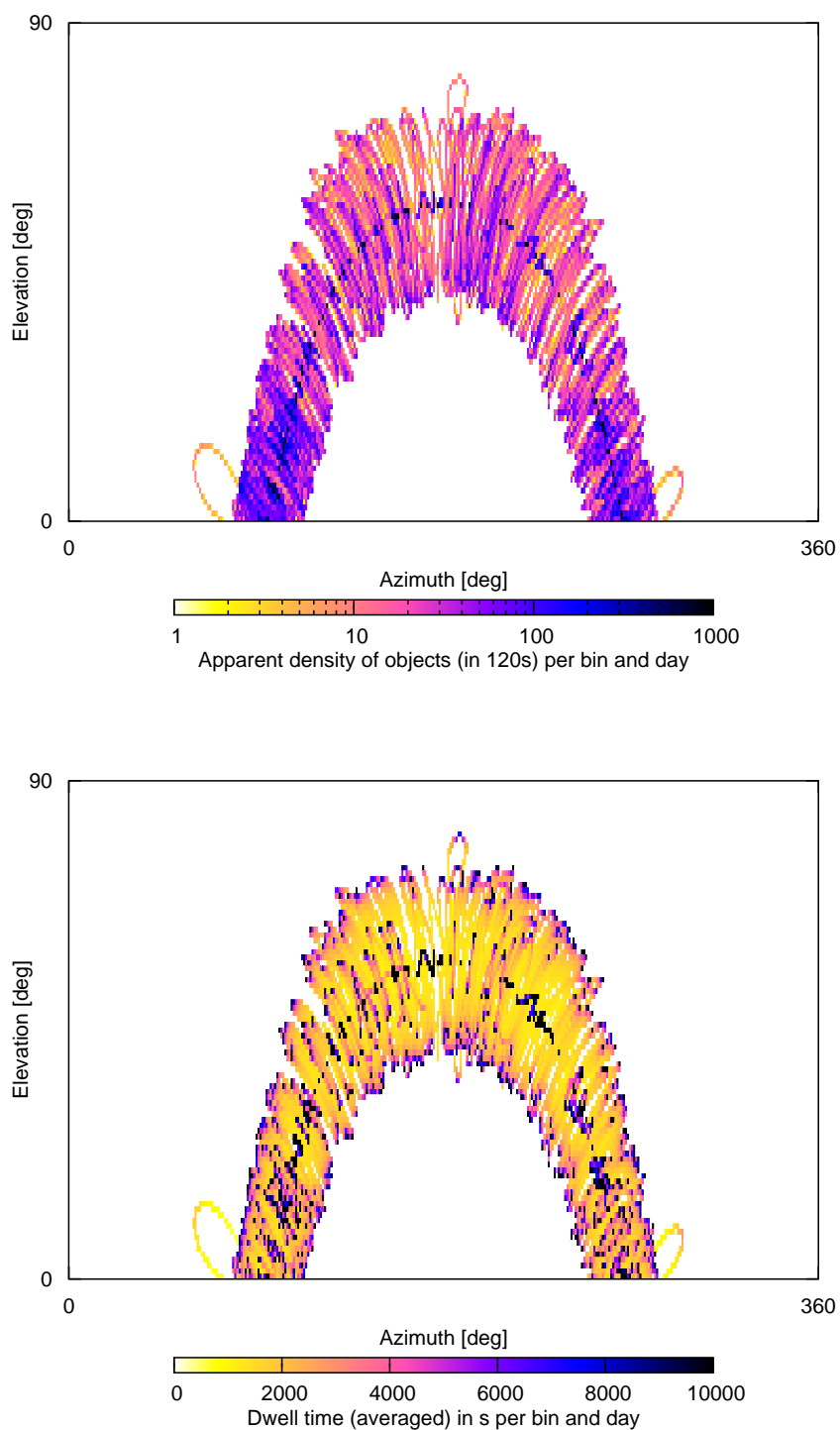


Figure 3.8: Apparent density and average dwell time in the OGS topocentric frame for 462 GEO objects visible from the OGS on 25 February 2011, which are listed in the USSTRATCOM public TLE catalog of that date per  $1^\circ \times 1^\circ$  bin. The density is calculated from 120 s sampling of the objects' ephemerides.

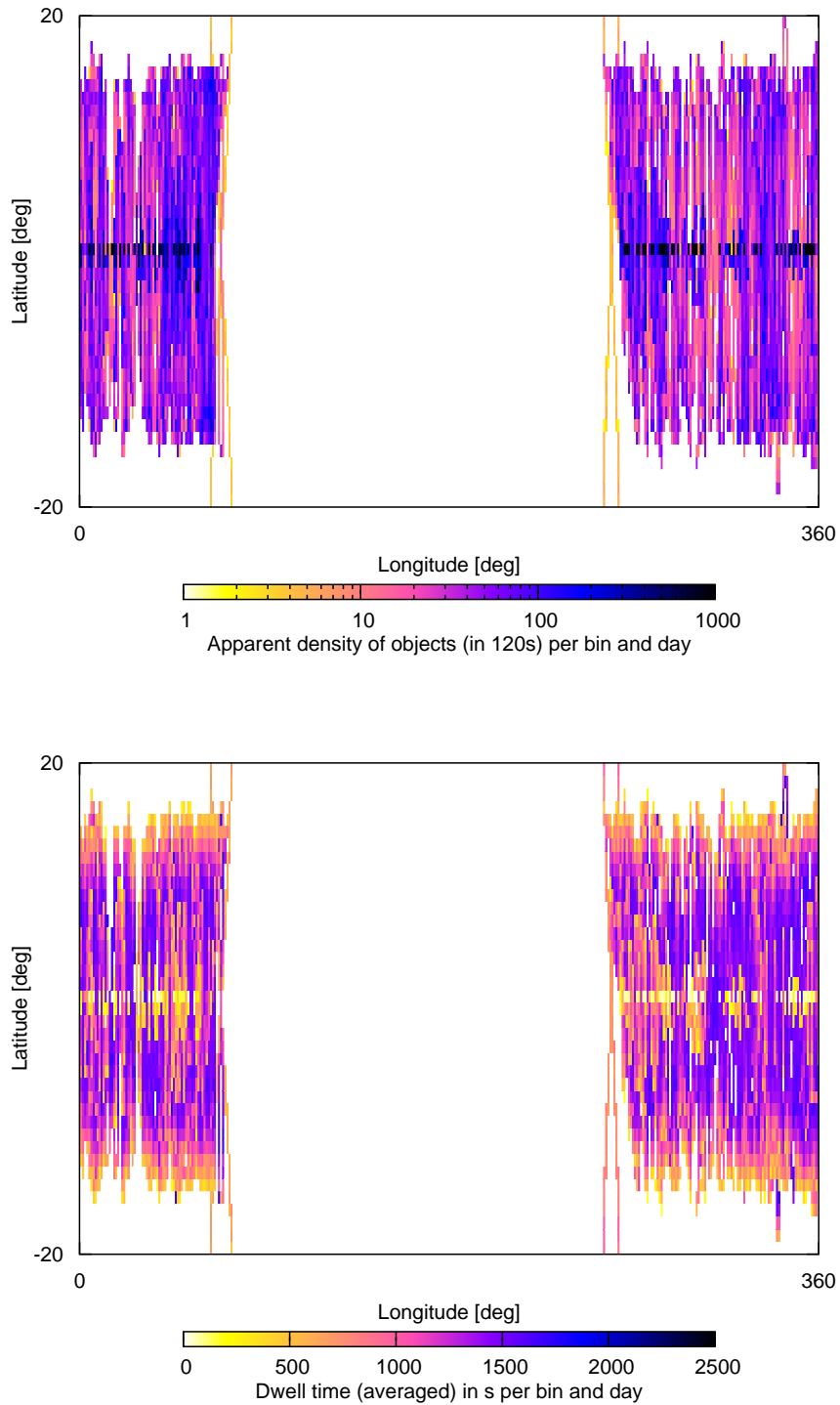


Figure 3.9: Apparent density and average dwell time in the Earth-fixed rotating frame for 462 GEO objects visible from the OGS on 25 February 2011, which are listed in the USSTRATCOM public TLE catalog of that date per  $1^\circ \times 1^\circ$  bin. The density is calculated from 120 s sampling of the objects' ephemerides.

### 3.2.4 Highly eccentric orbits

The three regimes LEO, MEO and GEO are mostly populated with near-circular orbits. Highly eccentric orbits are often transient. One example are GTOs, which are used for the transportation of satellites to the GEO region. GTOs usually have a low inclination, their perigee is at LEO altitude and their apogee at GEO altitude. The revolution period of GTOs is about 10.5 to 12 h, and the orbital velocity varies from about 10 km/s at perigee to about 1.5 km/s at apogee. Highly-inclined Molniya and Tundra orbits, used for communication constellations covering higher latitudes, are other examples for highly-eccentric orbits.

## 3.3 Observations

Figure 2.2 introduced the primary observation regions for radar and optical sensors. We present in this section the observation principles for both observing techniques. Section 3.3.1 covers the radar observations, while Sect. 3.3.2 discusses the principles of passive optical observations of objects in Earth-bound orbits.

### 3.3.1 Radar observations

The primary observables of radar are range measurements and angular measurements, the latter are typically in the local horizon frame. The two-way range  $R$  from the radar to the target is

$$R = c \frac{\Delta t}{2} \quad (3.2)$$

with the time of flight  $\Delta t$  and assuming that the radar pulse travels at the speed of light  $c$ .

Radars can also acquire range-rate information, if the Doppler shift of the frequency of the received signal  $f_r$  with respect to the frequency of the transmitted signal  $f_t$  is measured:

$$f_r - f_t = f_d = 2\dot{R} \frac{f_t}{c - \dot{R}} \approx 2\dot{R} \frac{f_t}{c} \quad (3.3)$$

The radar power budget, also called the link budget, allows assessing the sensitivity of a radar, and is the fundamental equation for all radar systems. According to Krag (2003) the relevant equation reads as:

$$P_r = \frac{P_t G_t}{4\pi R^2} A_r \frac{\sigma}{4\pi R^2} \frac{1}{L_{transmitter}} \frac{1}{L_{radome}^2} \frac{1}{L_{atmos}^2} \frac{1}{L_{receiver}} \frac{1}{L_{polarisation}} \quad (3.4)$$

where

- $P_r$  ... the received power
- $P_t$  ... the transmitting power
- $G_t$  ... the antenna gain
- $R$  ... the distance to the target
- $A_r$  ... the receiver antenna area
- $\sigma$  ... the radar cross section (RCS) of the target
- $L_i$  ... the losses

The signal-to-noise ratio (SNR) is given in the formulation by Krag (2003) as:

$$SNR = \frac{P_r}{kT_0F_NB} \quad (3.5)$$

where  $k$  ... Boltzmann constant  
 $T_0$  ... noise temperature of the ideal receiver  
 $F_N$  ... noise figure of the internal receiver noise  
 $B$  ... receiver bandwidth

### 3.3.2 Optical observations

There are three visibility constraints (see Sect. 3.3.2.1) that are relevant for the detection of an object. The detector parameters limiting the observation possibilities are outlined in Sect. 3.3.2.2.

Two more quantities that are related to the observation conditions have to be introduced: the angular velocity of the object  $v_{rel}$  and the apparent magnitude are also needed to characterise the source signal of an object received in a pixel. This will be discussed in Sect. 3.3.2.3 and Sect. 3.3.2.4. After that we are able to develop the SNR equations in Sect. 3.3.2.5 where we only consider passive approaches starting from the received irradiation at the telescope aperture. This SNR is the major criterion governing the detection of an object by optical observations.

In Sect. 3.3.2.6 we link the size of objects to a certain apparent magnitude by introducing and discussing the albedo as an object property.

With these fundamentals we can now relate design parameters of optical sensors to observation strategies, which is a complex multi-dimensional optimisation process. In Sect. 3.3.2.7 we try to outline the basics of this process.

The astrometric reduction process of optical observations, transforming acquired exposures into measured and epoch-related object positions, is presented in Sect. 3.3.2.8.

#### 3.3.2.1 Visibility constraints

An object is considered as “observable”, if it is illuminated by the Sun and the ground-based observer is in the Earth’s shadow, or the space-based observer is not affected by the presence of the Earth or the Sun in the line-of-sight.

Based on these considerations we may formulate three conditions, which must be met for the successful optical observation of an object (see Fig. 3.10):

1. The angle observer-object-Sun (the phase angle  $\theta$ ) must meet the condition  $0^\circ \leq \theta < \theta_{max}$ . The maximum allowed phase angle  $\theta_{max}$  depends on instrumental and operational constraints. If we accept the presence of the Sun in the FoV,  $\theta$  may have values up to  $180^\circ$ , if fully reflecting spheres are assumed. In reality the reflected energy is significantly lower and any appearance of the Sun in the FoV will rule out optical observation.
2. The angular distance of the object to the edge of the Earth’s Shadow  $\zeta$  must meet the condition  $\zeta > 0^\circ$ .

3. For space-based observations the angular distance to the Earth  $\gamma$  must meet the condition

$$\gamma > \arcsin\left(\frac{r_{Earth}}{\|\mathbf{x}_{obs}\|}\right) + \xi \quad (3.6)$$

to avoid the presence of the Earth in the FoV. The parameter  $\xi$  depends on the diameter of the sensor's FoV and has to take into account the limb. Usually a distance of  $3^\circ$  is sufficient for moderate FoV sensors.

From Fig. 3.10 we can write  $\theta$ ,  $\zeta$ , and  $\gamma$  as functions of the object position  $\mathbf{x}_{obj}$ , the observer position  $\mathbf{x}_{obs}$ , the Sun's position  $\mathbf{x}_{Sun}$  relative to the geocentre, and the Earth's radius  $r_{Earth}$ :

$$\begin{aligned} \theta &= \arccos\left(\frac{(\mathbf{x}_{obj} - \mathbf{x}_{obs}) \cdot (\mathbf{x}_{obj} - \mathbf{x}_{Sun})}{\|\mathbf{x}_{obj} - \mathbf{x}_{obs}\| \|\mathbf{x}_{obj} - \mathbf{x}_{Sun}\|}\right) \\ \zeta &= \pi - \arccos\left(\frac{\mathbf{x}_{Sun} \cdot \mathbf{x}_{obj}}{\|\mathbf{x}_{Sun}\| \|\mathbf{x}_{obj}\|}\right) - \arcsin\left(\frac{r_{Earth}}{\|\mathbf{x}_{obj}\|}\right) \\ \gamma &= \arccos\left(\frac{\mathbf{x}_{obs} \cdot (\mathbf{x}_{obs} - \mathbf{x}_{obj})}{\|\mathbf{x}_{obs}\| \|\mathbf{x}_{obs} - \mathbf{x}_{obj}\|}\right) \end{aligned} \quad (3.7)$$

Crossings of the Moon shadow were not taken into account. Object crossings of the Moon core shadow will very rarely happen in the considered high-altitude regions, but crossing's of the Moon's penumbra region (possible around New Moon) may cause a loss of about 1 mag in the objects apparent brightness (see Schildknecht et al. (2004b)).

### 3.3.2.2 Detector parameters

There is a big variety of different image acquisition sensor designs. We limit the discussion to the most commonly used integrating silicon-based detector techniques, i.e. the analog charge-coupled devices

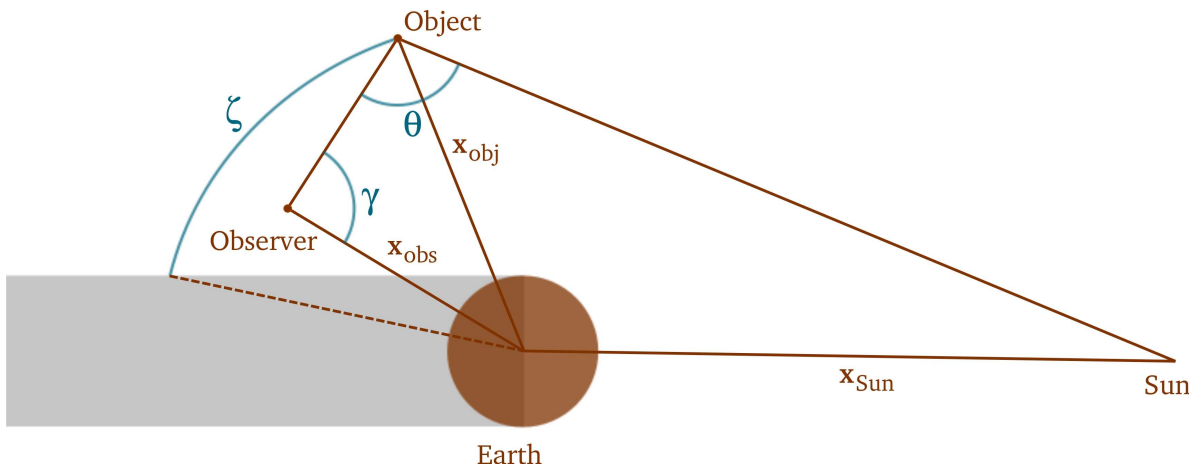


Figure 3.10: Visibility and observability conditions of objects.

(CCD), the active pixel sensors based on complementary metaloxidesemiconductor (CMOS) technology, and hybrids based on CCD or CMOS. For applications in astronomy CCD still dominate.

The photon counting technique is, in contrast to CCD or CMOS, a non-integrating technique. The use of image intensifiers makes this approach very sensitive to power supply and environmental variations (see Schildknecht (1994) for a detailed comparison of CCD and photon counting techniques). Furthermore, the dynamic range is limited by the readout rate and is therefore smaller than for integrating techniques. At present, photon counting devices are used for very low SNR and very short exposure times ( $<0.1$  s), but this is not typical for optical observations of space objects.

There are CCD detectors suitable for astronomical purposes with pixel sizes in the  $\mu\text{m}$ -range. Today, single chips up to  $4096 \times 4096$  pixel are available. Several single chips can be combined to build mosaic sensors with more pixels. For astronomical purposes mostly CCD detectors with 'Full Frame' architecture are used. The whole detector area is utilised to collect photons within the exposure time. After that the whole frame is read out. This concept can be extended to a 'Frame Transfer' CCD architecture, where the detector is divided into two identical arrays: the image array and the storage array. Technically speaking, the image is shifted to the storage array after the exposure. From there it can be read out, while the image array is available for the next exposure. Higher frame rates are possible With this procedure.

For the optical observation of space objects several CCD detector parameters are important:

- **Binning** combines a matrix of  $m \times n$  pixels (usually  $2 \times 2$  or  $4 \times 4$ ) into one logical 'binned pixel' during the readout prior to digitisation. The SNR is increased by binning for cases where the SNR is dominated by the readout noise. However, in order to limit the noise contributions from the background and the detector dark current, the size of the resulting binned pixel should not substantially exceed the diameter of the point-spread function of the source. Binning also increases the achievable frame rate, but lowers the spatial resolution.
- The **fullwell capacity** of a pixel can be defined as the total amount of electrons an individual pixel can hold before saturating. The fullwell capacity parameter may be given by the manufacturer or third parties doing calibrations. The fullwell capacity depends on the pixel size (the area) and on the operating voltages. Techniques used to reduce the dark current signal and to speed up the detector readout lower the fullwell capacity.
- **Dark current** originates from thermal energy within the silicon lattice of the CCD and is therefore independent from exposing. The detector signal is overlaid by the dark current signal, which only can be described by statistical methods. The aim should be to reduce the dark current signal so that its contribution to the error budget can be neglected. Obviously, the dark current signal decreases linearly with the extension of the exposure time. Cooling reduces the dark current exponentially.
- A **wide dynamic range** of a detector denotes the ability to detect very dim and very bright objects within the same exposure. Considering a given fullwell capacity, the readout noise and the dark current have to be minimised in order to get the desired maximum dynamic range. The dynamic range is defined as the ratio of the fullwell capacity and readout noise.
- The **nonlinearity** is a measure of the camera gain constant as a function of signal strength. Nonlinearity impacts the brightness/magnitude estimations and should therefore be as small as possible.
- The **quantum efficiency** (QE) is the probability of a photon of getting absorbed by the detector to produce electric charge. To indicate the effectiveness of a detector QE is given by the manufacturer

as a function of wavelength. As QE is directly proportional to the source signal, QE drives the achievable SNR of the observing system.

- The angular resolution (also known as **pixel scale**) depends on the telescope to which the detector is connected. For a given telescope the aperture and the focal length (or the focal ratio) are known. The pixel scale follows directly from pixel size and focal length.
- Detectors can be divided into **frontside-** and **backside-illuminated** detectors. Photons have to pass through a gate before they can interact with the resistance silicon for the front-side cases. These gates are made of very thin polysilicon, implying that the gate is opaque at wavelengths shorter than 400 nm and therefore the QE value for front-side illuminated detectors is degraded over a part of the working spectrum. As opposed to front-side illuminated detectors the back-side illuminated provide a much better QE performance due to the absence of the polysilicon gate in the path of the photons. The sensitivity is improved significantly in the blue part of the spectrum and ranges from soft x-ray to near-infrared regions of the spectrum. Back-side illuminated detectors are produced by thinning down the detector substrate to less than 10  $\mu\text{m}$ .
- The **detector duty cycle** specifies the time span during which the detector is not available to acquire exposures. For space surveillance one would like to keep the duty cycle as short as possible. The duty cycle is dominated by the readout time. The readout of CCD detectors is performed by shifting the accumulated charges along the detector columns to the top row. The current top row is read out by a shift towards the output amplifier. This process is repeated until the last row of the detector array has been transferred. The use of frame transfer detectors allows it to shorten the duty cycle. In order to get the full benefit from the frame transfer architecture the readout time should be shorter than the exposure time. An increase of the readout rate allows it to minimise the duty cycle, but this increase of the readout rate will also increase the readout noise depending on the quality of the used amplifier. From manufacturer data typical detectors can be read out at  $3 \dots 5e^-$  at 50 kHz up to  $20e^-$  at 20 MHz at typical operating temperatures.

### 3.3.2.3 Relative angular velocity

The angular velocity of a object crossing the FoV is the projection of the angular velocity perpendicular to the line-of-sight, therefore in the instrument-fixed coordinate frame. This relative angular velocity  $v_{rel}$  of the crossing object is identical to the velocity of the image of the crossing object at the detector plane. If this angular velocity is known, one easily can calculate the number  $m$  of pixels covered during an exposure time  $t$  from the pixel crossing time  $t_p$ , the number of pixels illuminated by the source at a given instant  $m_0$ , and the pixel scale  $PS$

$$m = m_0 + \frac{\sqrt{m_0} t_p}{t} = \frac{\sqrt{m_0} v_{rel}}{PS} t. \quad (3.8)$$

The quantity  $m_0$  depends on the instrumental point-spread function (PSF), the physical pixel size of the detector and on the detection algorithm.

Vice-versa, the definition of observation strategies has to take into account the resulting achievable relative velocity of targetted objects crossing the FoV.

### 3.3.2.4 Apparent magnitude

The apparent magnitude measures the brightness of a certain object. A difference of five magnitudes is equivalent to a factor of 100 in brightness. If the scattering is grey, meaning that the reflected radiation has the same spectral distribution as the incident solar radiation, the apparent magnitude  $m_{obj}$  of an object can be related directly to the solar irradiation outside the Earth's atmosphere  $E_{sol} = 1367 \text{ Wm}^{-2}$  and the irradiation received from the object at the telescopes' aperture  $E_{obj}$

$$m_{obj} = m_{Sun} - \sqrt[5]{100} \log_{10} \frac{E_{obj}}{E_{sol}} \approx m_{Sun} - 2.5 \log_{10} \frac{E_{obj}}{E_{sol}}. \quad (3.9)$$

It is assumed that the magnitude of the Sun in near-Earth space around 1 AU is  $m_{Sun} = -26.74$  mag and refers to  $E_{sol}$ .

A reference point of the relation between brightness and photo-electrons is obtained by using the relation  $E = hc/\lambda$  (Schildknecht, 1994), where  $h$  is the Planck constant ( $6.62606896 \times 10^{34}$  Js), and  $c$  the speed of light (299 792 458 m/s). This relation has to be integrated over the whole response spectrum of the optical system, considering the wavelength dependent losses due to the telescope optical efficiency  $\epsilon_\lambda$  and detector quantum efficiency  $q_\lambda$ . For a typical back-side illuminated CCD we may assume from this relation that 16 mag correspond to 8000 photo-electrons/s outside the Earth's atmosphere.

### 3.3.2.5 Signal-to-noise equations for optical detectors

The total object signal can be considered as the sum of the photon flux stemming from the source of interest  $S_0$ , the sky and atmospheric background  $S_s$ , and the detector dark current  $S_d$ . The source signal accumulated for an exposure time  $t$  for a circular aperture with diameter  $D$  can be estimated to be

$$S_0 = \frac{\pi}{4} D^2 t \int_{\lambda} E_\lambda \tau_\lambda \epsilon_\lambda q_\lambda d\lambda, \quad (3.10)$$

where  $E_\lambda$  denotes the irradiance of the object outside atmosphere and  $\tau_\lambda$  the atmospheric transmission.

The sky background signal  $S_s$  can be calculated in analogy to  $S_0$ . For space-based observations  $\tau_\lambda$  can be assumed as 1, and the atmospheric background signal does not exist. The estimation of the sky background signal is then limited by the fixed natural sky glow. Continuous sources, like the zodiacal light, light from faint stars and galaxies, and the light from discrete sources, as from bright stars and planets contribute to the natural sky glow outside the atmosphere. This corresponds to a magnitude of 21.8-22.0 mag/arcsec<sup>2</sup>. Apart from the natural background signal a part of the sky background signal depends on the observational strategy and varies with time and instrument pointing: visibility of the Moon in the FoV, Gegenschein, aurora effects, satellite flares, aeroplane strobe lights, meteors, planets. The Gegenschein becomes relevant if the instrument is pointing fixed away from the Sun (this would ensure small phase angles). Straylight from the Earth's atmosphere may also largely impact the background signal.

The noise to be considered in principle in the SNR equation consists of the photon noise of the source, the sky and atmospheric background noise, the detector dark current noise, the readout noise (due to readout signal amplification), and the flat-fielding noise. The photon noise (variation of the number of photons emitted by any source) cannot be avoided as this is a fundamental property of the light. A Poisson distribution is assumed, where the noise is the square root of the signal. The dark current noise is the noise of the dark current signal  $S_d$ . The amplifier noise  $S_r$  consists of reset noise, white noise,

flicker noise, shot noise, contact noise, and popcorn noise and depends on the readout frequency and on the quality of the amplifiers components. This readout noise is specified by the detector manufacturers and is measured in  $[e^-]$ .

Finally, the SNR per pixel can be calculated from the ratio of the objects signal to the accumulated noise as

$$SNR = \frac{\dot{S}_0 t}{\sqrt{m_0 S_r + \left( \dot{S}_0 + m_0 (\dot{S}_s + \dot{S}_d) + \sqrt{m_0} v_{rel} S_r \right) t + \sqrt{m_0} v_{rel} (\dot{S}_s + \dot{S}_d) t^2}}. \quad (3.11)$$

This formulation is used in a similar way in the PROOF environment (Krag et al., 2000; Krag, 2003). Note that the numerator  $\dot{S}_0 t$  is expressed in photo-electrons and the denominator is in “equivalent” photo-electrons.

Normally, even for sophisticated segmentation approaches, a SNR higher than 3 to 4 is required to discriminate objects from background in an exposure. We assume for the sake of simplicity that the background signal can be determined from object-free regions and that the individual noise sources are uncorrelated.

As shown by Schildknecht (1994) the SNR per streak can be calculated by replacing  $m_0$  by  $m$  as defined in Eq. 3.8:

$$SNR = \frac{\dot{S}_0 t}{\sqrt{m S_r + \left( \dot{S}_0 + m (\dot{S}_s + \dot{S}_d) + \sqrt{m} v_{rel} S_r \right) t + \sqrt{m} v_{rel} (\dot{S}_s + \dot{S}_d) t^2}}. \quad (3.12)$$

The photon flux  $\Phi$  is defined as the number of photons per second per unit area. The power density  $H$  for photons at a particular wavelength (the irradiance) can be calculated from the photon wavelength  $\lambda$  and the photon flux  $\Phi$  at that wavelength

$$H = \Phi \frac{hc}{\lambda} \approx \Phi \frac{1.24}{\lambda[\mu m]}. \quad (3.13)$$

Because the dark current and, predominantly, the sky-background signal grow with the exposure time, and because the read-out noise is independent of the exposure time, two typical cases for the SNR result. Schildknecht (1994) discusses the relation of the sky-background-dominated and the readout-dominated cases in detail. Here, we just revisit the two cases for a typical optical sensor proposal (Schildknecht et al., 2005; Flohrer et al., 2008b) making the following assumptions:  $v_{rel}=15''/s$ ,  $\tau=0.88$ ,  $\epsilon=0.60$ ,  $QE=0.80$ ,  $D=0.80$  m,  $f=1.46$  m,  $d_{pixel}=12.50$   $\mu$ m (this leads to a diameter of the FoV of  $2.5^\circ$ ), diameter of  $PSF=2.00$  pixels,  $S_d=0.14$   $e^-/pixel/s$ , and no binning during readout.

Figure 3.11 introduces the resulting SNR for a 2 second exposure as function of background values. A typical site in central Europe, such as Zimmerwald, will provide conditions around  $17$  mag/arcsec<sup>2</sup> on average (unpublished estimates by L. Ostini based on acquired routine observations), while astronomical sites, such as the OGS, may be expected to have values around  $19$  mag/arcsec<sup>2</sup>. Roughly, this difference relates to a gain of 1 mag object brightness if the darker site is selected.

The variation of the exposure time for a 18 mag object in Fig. 3.12 reveals that for exposure times shorter than  $\approx 1$  s a lower background signal does not significantly increase the SNR of a given object. For longer

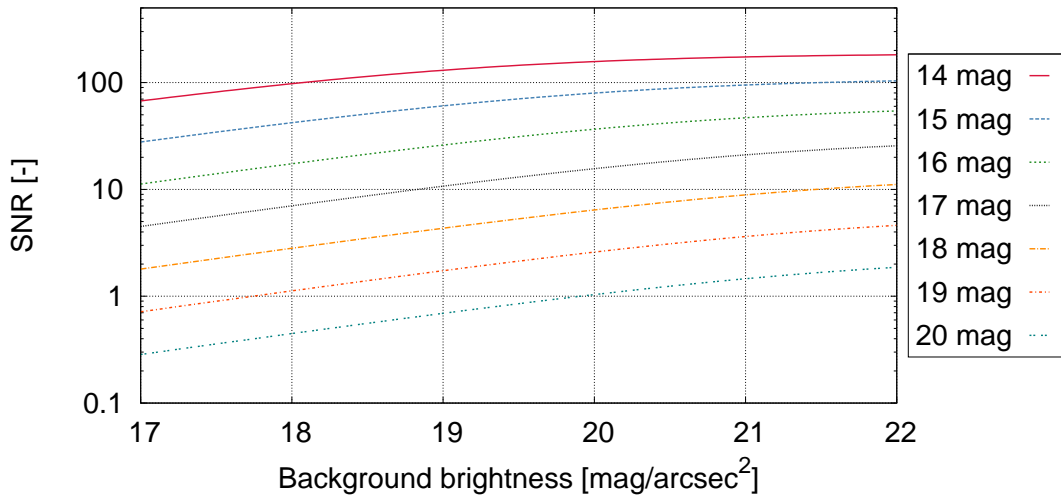


Figure 3.11: SNR as a function of the background brightness for different object brightness for  $v_{rel}=15''/s$  and  $t=2s$ . The sensor is characterised by  $\tau=0.88$ ,  $\epsilon=0.60$ ,  $QE=0.80$ ,  $D=0.80$  m,  $f=1.46$  m,  $d_{pixel}=12.50$   $\mu\text{m}$ , diameter of  $PSF=2.00$  pixels,  $S_d=0.14$   $e^-/\text{pixel}/s$ , no binning, and  $\sqrt{S_r}=10.0$   $e^-$ .

exposure times the effect of a lower background signal is eminent, but the relative velocity compensates in part for these improvements, so that exposure times longer than  $\approx 2$  s do not provide additional benefit.

Figure 3.13 varies the readout noise signal for a 18 mag object and 2 s exposure time. The figure shows that noise levels better than  $\sqrt{S_r}=10.0$   $e^-$  should be aimed at. Otherwise, the readout signal dominates the improvements from a reduced background signal.

From the above discussion of a single sensor scenario it becomes clear that the definition of an observation strategy has to consider the sensor design and vice versa. Sensor design parameters are mostly dependent or correlated. As the technical feasibility of the sensor design becomes a key issue, it is recommended that an optimal observation strategy should be defined together with the sensor developer in order not to compromise the achievable detection threshold. See Sect. 3.3.2.7 for more information.

### 3.3.2.6 Brightness-size relation

Optical observations do not directly measure the object size  $d_{deb}$ , which can only indirectly be deduced from brightness measurements. The most important quantity for relating the observed apparent magnitude to the object size is the albedo. Two types of albedo are frequently used, the Bond albedo and the geometric albedo.

The Bond albedo is the fraction of the total incident radiation and the radiation reflected by the object. It is an “effective reflection coefficient”.

The geometric albedo is the ratio between the incident intensity and the intensity of reflected radiation at  $\theta=0^\circ$  phase angle. It is a “resulting reflection coefficient”.

Specifying the shape and the scattering properties of an object allows to relate the geometric to the Bond albedo. Shape and scattering are important characteristics for the brightness estimation, in particular

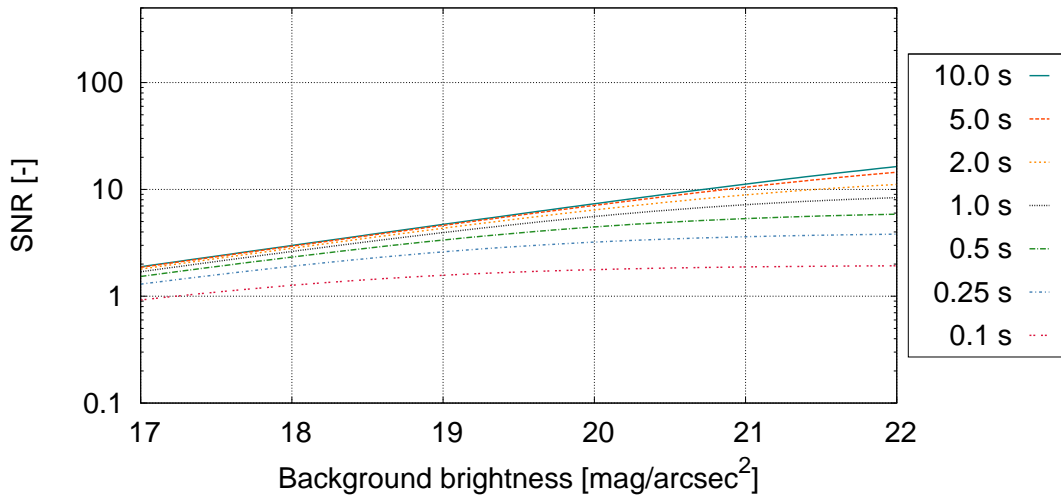


Figure 3.12: SNR as a function of the background brightness for different exposure times for  $v_{rel}=15''/s$  and an object brightness of 18 mag. The sensor is characterised by  $\tau=0.88$ ,  $\epsilon=0.60$ ,  $QE=0.80$ ,  $D=0.80$  m,  $f=1.46$  m,  $d_{pixel}=12.50 \mu\text{m}$ , diameter of  $PSF=2.00$  pixels,  $S_d=0.14 e^-$  /pixel/s, no binning, and  $\sqrt{S_r}=10.0 e^-$ .

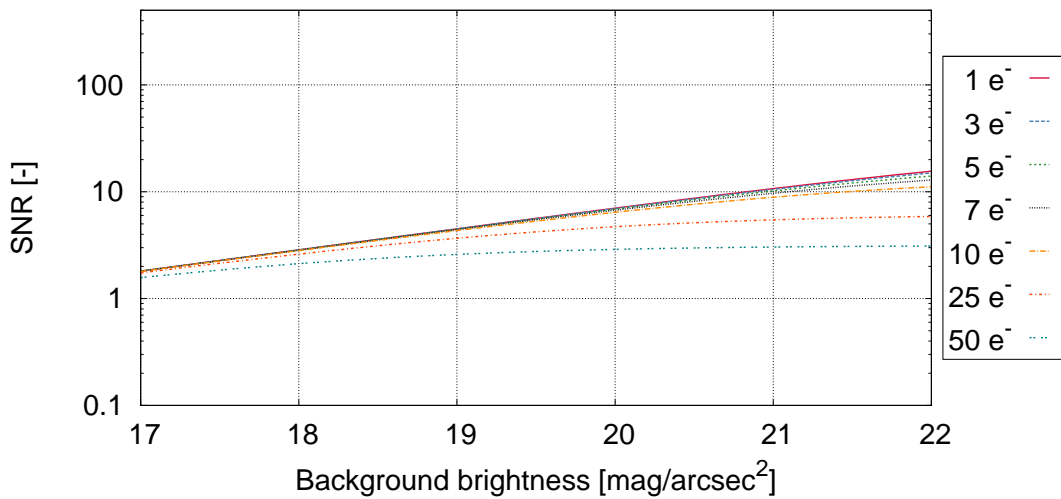


Figure 3.13: SNR as a function of the background brightness for different readout-noise levels for  $v_{rel}=15''/s$ ,  $t=2$  s, and an object brightness of 18 mag. The sensor is characterised by  $\tau=0.88$ ,  $\epsilon=0.60$ ,  $QE=0.80$ ,  $D=0.80$  m,  $f=1.46$  m,  $d_{pixel}=12.50 \mu\text{m}$ , diameter of  $PSF=2.00$  pixels,  $S_d=0.14 e^-$  /pixel/s, no binning.

for debris objects. Usually, objects of unknown shape are either assumed as spherical or as plates. Lambertian scattering properties are assumed (i.e., the radiance is independent of the viewing angle).

The irradiance  $H$  received at the telescope aperture can be written as the product of the following four quantities:

1. the total reflectable energy calculated from the solar irradiance outside the atmosphere  $E_{sol}$  per solid angle  $\Omega$  suspended by the object as

$$E_{sol} \frac{\Omega}{4\pi}. \quad (3.14)$$

The debris object seen by the observer defines a cone with the apex angle  $2\alpha$  that has the solid angle  $\Omega$ , which is

$$\Omega = 2\pi (1 - \cos \alpha) = 2\pi \left( 1 - \cos \left( \arcsin \left( \frac{d_{deb}}{2R} \right) \right) \right). \quad (3.15)$$

For typical  $d_{deb}$  and observing distances  $R$  this can be approximated better than 0.1% even for 10 m objects at 100 m distance to

$$E_{sol} \frac{\pi d_{deb}^2}{4R^2} \quad (3.16)$$

2. the phase function defined as (Schildknecht, 2003)

$$\varphi(\theta) = \frac{1}{\pi} (\sin \theta + (\pi - \theta) \cos \theta) \quad (3.17)$$

3. the Bond albedo  $\rho_{Bond}$

4. the reflectivity  $\alpha$  (for a perfect white diffuse (non-specular) reflecting sphere  $\alpha = \frac{8}{3}$ ).

We can finally write:

$$H = E_{sol} \frac{\pi d_{deb}^2}{16\pi R^2} \varphi(\theta) \rho_{Bond} \alpha = \frac{2}{3\pi^2} E_{sol} \frac{\pi d_{deb}^2}{4R^2} (\sin \theta + (\pi - \theta) \cos \theta) \rho_{Bond}. \quad (3.18)$$

We can use the geometric albedo  $\rho_{geom}$  instead of the Bond albedo  $\rho_{Bond}$ , following the definition  $\rho_{Bond} = q\rho_{geom}$  with  $q$  denoting the phase integral, which is defined as function of the incident intensity  $I(\theta, \phi)$  and the intensity of incident radiation normally reflected from a surface  $I(0)$ :

$$q = \frac{\int I(\theta, \phi) d\Omega}{\pi I(0)}. \quad (3.19)$$

For a sphere we have  $I(\theta, \phi) = I(\theta)$  and the phase integral becomes

$$q = \frac{2 \int_0^\pi I(\theta) \sin(\theta) d\theta}{I(0)} = 2 \int_0^\pi \varphi(\theta) \sin(\theta) d\theta = \frac{2}{\pi} \int_0^\pi (\sin \theta + (\pi - \theta) \cos \theta) \sin \theta d\theta. \quad (3.20)$$

Solving the integral gives

$$\begin{aligned}
 \int_0^{\pi} (\sin \theta + (\pi - \theta) \cos \theta) \sin \theta d\theta &= \int_0^{\pi} \sin^2 \theta d\theta + \pi \int_0^{\pi} \cos \theta \sin \theta d\theta - \int_0^{\pi} \theta \cos \theta \sin \theta d\theta \\
 &= \frac{\pi}{2} + 0 + \frac{\pi}{4} \\
 &= \frac{3\pi}{4},
 \end{aligned} \tag{3.21}$$

so that  $\rho_{Bond} = \frac{3}{2}\rho_{geom}$ .

The received irradiance  $H$  becomes

$$H = \frac{1}{\pi^2} E_{sol} \frac{\pi d_{deb}^2}{4R^2} (\sin \theta + (\pi - \theta) \cos \theta) \rho_{geom}. \tag{3.22}$$

Hejduk (2007) uses a similar formulation also assuming the diffuse sphere approximation for debris objects, which can be written by keeping the original symbols as

$$M_v = -26.74 - 2.5 \log_{10} \left( A \rho \frac{2}{3\pi^2} ((\pi - \theta) \cos \theta + \sin \theta) \right) + 5.0 \log_{10}(R) \tag{3.23}$$

with  $A$  denoting the cross-sectional area of the object,  $\rho$  the ‘‘targets albedo’’ (we understand that this refers to a Bond albedo) and the observing distance  $R$ .

We may now relate the apparent brightness to object diameters. In Fig. 3.14 we assume spherical objects with a constant albedo observed under a constant, small phase angle. With these assumptions Fig. 3.14 may be used to approximate the input required for a SNR assessment or more general as input for a sensor design starting from the minimum detectable object diameter. Vice versa Fig. 3.14 provides an easy look-up for the dependencies between topocentric distance and apparent brightness for objects of a given diameter.

If we consider a reference size and assume Lambertian scattering with a fixed albedo, the most important quantities for the apparent brightness are the topocentric distance and the phase angle at the observation epoch. For 1 m objects Fig. 3.15 allows it to estimate this important parameter for optical observation strategies and sensor design considerations.

From Fig. 3.15 we conclude that a 1 m object in GEO typically is observed with an apparent magnitude of 16, if the phase angle is small. For low phase angles an apparent magnitude of about 18 can be expected. A 1 m object in MEO typically may be observed with an apparent magnitude between 14 and 16.

### 3.3.2.7 Optical sensor design

Optical sensor design parameters are mutually dependent, and are closely linked to the planned observation strategy. The definition of an observation strategy is governed by the user requirements. For maintaining a catalogue the essential user requirements are population coverage, timeliness of the observations, and accuracy of the observations (Krag et al., 2010). The ability to cover a given object population is dominated by the limiting SNR of the sensors. We find that the timeliness of the observations can be related mainly to the re-visiting time of a particular survey field in the case of surveys. The

accuracy of the determined orbit is dominated by the SNR of a single observation and by the length of the formed short arc, which in turn is a function of the number of subsequent exposures of the object.

These parameters directly derived from the user requirements together with the parameters characterising an observation strategy can be related to parameters for the sensor design and selection. For an optical sensor we identify the diameter of the FoV, the pixel scale, the  $f$ -number, the aperture, and the general telescope design constraints. The general constraints comprise the detector parameters and the detector/optics interface.

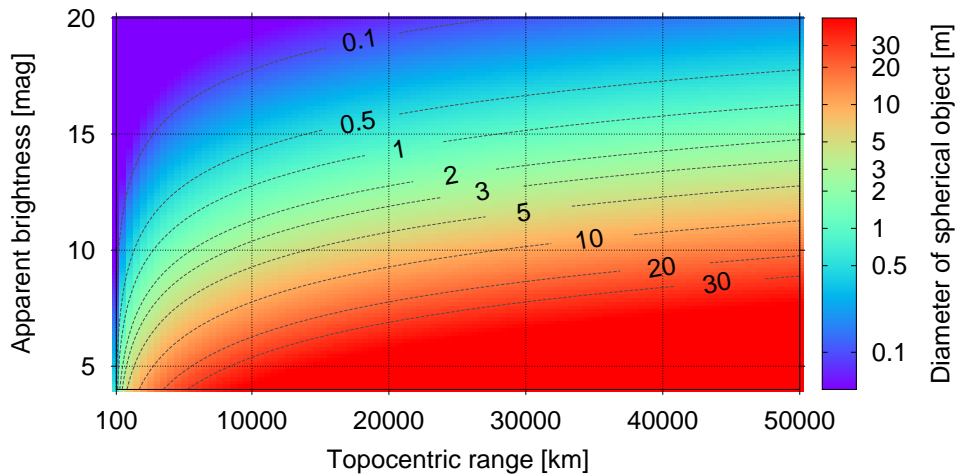


Figure 3.14: Apparent brightness for Lambert-scattering spherical objects following Eq. 3.18 assuming  $\rho_{Bond}=0.1$  and  $\theta=20^\circ$  (modified and extended from a classical figure by King-Hele (1983)).

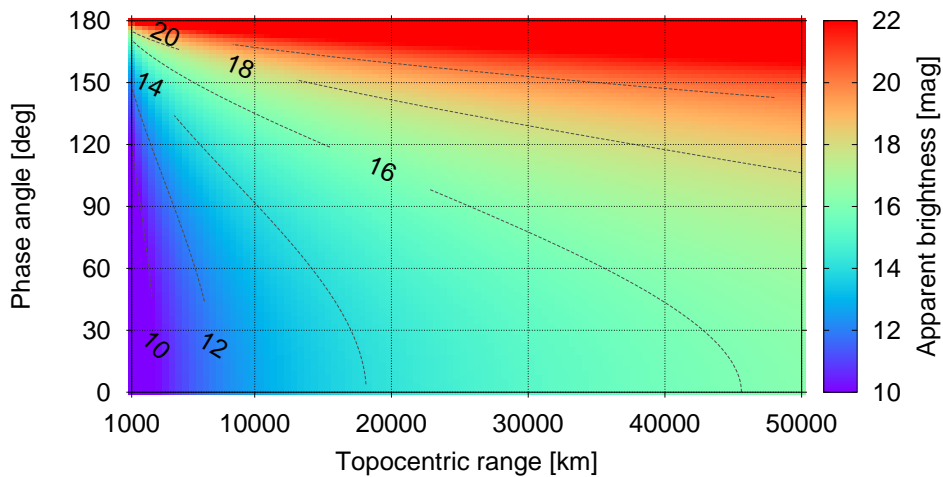


Figure 3.15: Apparent brightness for Lambert-scattering spherical objects of 1 m diameter as a function of topocentric distance and phase angle  $\theta$  following Eq. 3.18 and assuming  $\rho_{Bond}=0.1$

Figure 3.16 shows relations and dependencies of sensor parameters (grey), user requirements (dark-grey), and the parameters for the characterisation of observation strategies (white) simplified to the essential parameters and main relations. The pixel scale and the FoV diameter have most links to other parameters. A strict top-down or bottom-up design process for selecting or designing the optimal sensor is not possible without knowledge of the observation strategy and of the user requirements. In analogy, the formulation of an observation strategy without considering the feasibility of the assumed sensor is impossible. Usually, the design process is iterative, allowing it to re-visit the observation strategy definition and sensor design, respectively. Obviously a good initial guess is essential for the success of that iterative approach.

The relation between SNR and pixel size may be selected as one example for such a complex multi-parameter optimisation process. Large size pixels, resulting in a larger pixel scale, would significantly lower the SNR, because for a given exposure time, the background signal grows more rapidly while the source signal per pixel remains unchanged. As the astrometric position accuracy benefits from a smaller pixel scale and a higher accuracy is desirable, one might conclude that the pixel size should be chosen as small as possible to receive higher SNR and better orbit determination accuracy. Unfortunately, small pixel sizes also lead to a shorter pixel crossing time, which in turn, for a given exposure time, results in more pixels forming an object. Longer pixel trails require more sophisticated segmentation algorithms, which are more demanding in terms of computing power and could even be less sensitive. In addition, the readout noise becomes significant for small pixel sizes, as the detector has to provide more pixels to cover the given FoV and thus has to be read out faster, with higher noise, lowering the achievable SNR.

The design of an optical observing system dedicated to space surveillance is subject to a multi-dimensional optimisation process. A large FoV combined with a low  $f$ -number, high detector efficiency and capabilities for rapid and frequent repositioning are generally acknowledged to be good characteristics. Often, additional design goals are added, such as NEO observation capabilities, or SOI or imaging capabilities. The latter is, e.g., the case for DARPA's Space Surveillance Telescope (SST) program striving to combine multiple observation goals with an innovative telescope design, such as the use of detectors for a curved focal plane.

### 3.3.2.8 Astrometric reduction of optical observations

Through a process called "astrometric reduction" the direction from the observer to an object at the observation epoch may be derived. The observables eventually are right ascension  $\alpha$  and declination  $\delta$  describing the apparent topocentric place:

$$\rho \doteq |\mathbf{r}(t - \frac{\rho}{c}) - \mathbf{R}(t)| \quad (3.24)$$

$$\mathbf{e} \doteq \frac{\mathbf{r}(t - \frac{\rho}{c}) - \mathbf{R}(t)}{\rho} \quad (3.25)$$

$$\alpha = \arctan \frac{e_y}{e_z} \quad (3.26)$$

$$\delta = \arcsin e_z \quad (3.27)$$

- where
- $\rho$  ... Geometric distance between the observer at the epoch  $t$  and the object at the epoch  $t - \Delta t$  (slant range)
  - $\mathbf{e}$  ... Unit vector pointing from the observer to the object
  - $\mathbf{r}(t - \frac{\rho}{c})$  ... Position vector of the satellite at the epoch  $t - \Delta t \doteq t - \frac{\rho}{c}$
  - $\mathbf{R}(t)$  ... Position vector of the observer at the epoch  $t$

$t$	... Observation epoch
$c$	... Speed of light
$\alpha$	... Right ascension of the object
$\delta$	... Declination of the object
$\Delta t$	... One-way signal travel time.

The astrometric reduction of the raw data comprises three steps.

In a first step, the moving object must be identified in front of the reference star background. This task is sometimes called “segmentation”, as it identifies reference stars and moving objects, and provides their position in the detector coordinate frame. The correct estimation of the background signal to enable the detection of very faint objects is challenging. Several segmentation approaches are known. Some successful approaches use several sequential exposures (a “series”) (Schildknecht et al., 1995; Schildknecht, 2007). Alternatively, single exposures may be segmented by subsequently applying a global threshold, where the background is estimated from large kernels for a median filter, followed by a logical bit masking (Kouprianov, 2008).

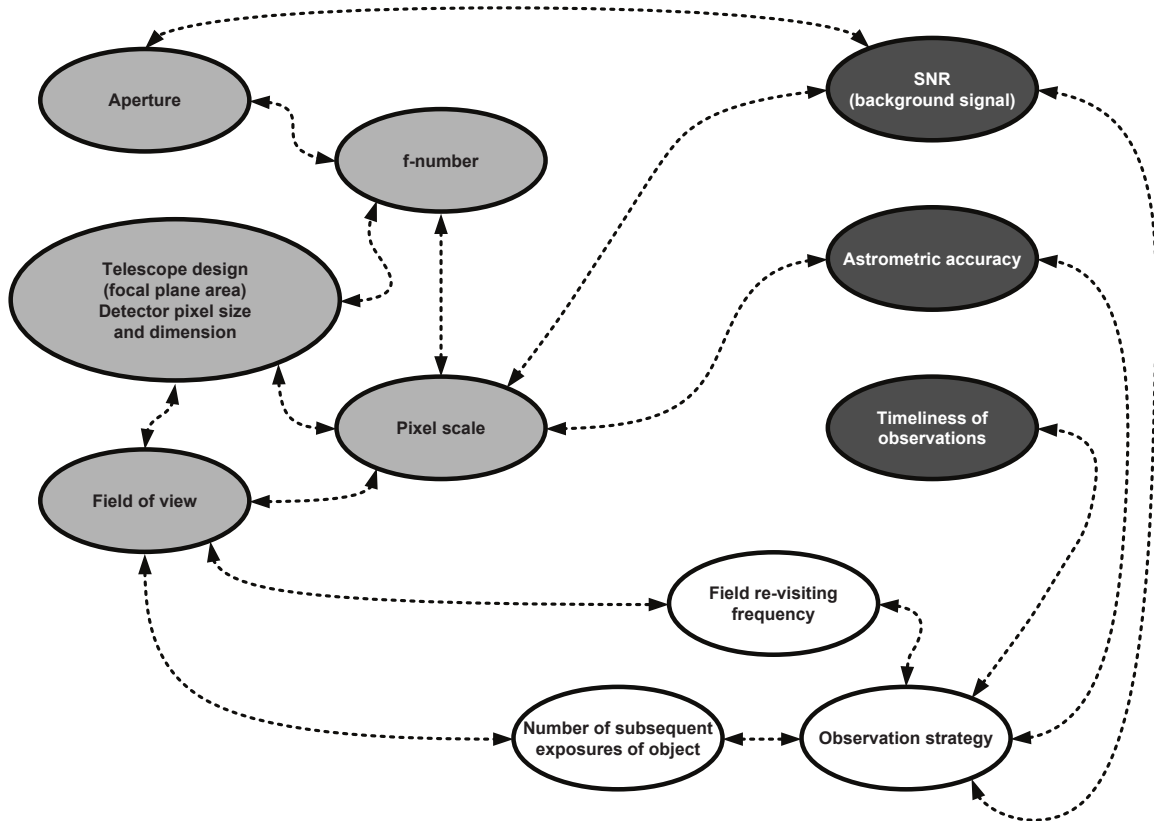


Figure 3.16: Simplified mutual relationships and dependencies of user requirements on maintaining a catalogue (dark-grey), sensor design parameters (grey), and the main characteristics of observation strategies (white).

In the next step, the identified stars and objects are subject to refined measurements, the so-called “centroiding”. This task, depending on the parameters of the observing system and on the observation strategy, results in the centres of the stars and objects (the “raw observations”) with sub-pixel precision in a detector coordinate system. The reference algorithm for centroiding is a fitting of a PSF, e.g., as described by Kouprianov (2008) and Kouprianov (2010). A PSF fitting has limits for very faint objects where the signal is not strong enough to allow the fitting of a PSF model.

Eventually, through a set of transformations, the centroid positions in the detector coordinate frame are mapped to the celestial reference system (see Sect. 3.1) in order to derive the observables.

The mapping of reference positions onto the focal plane is disturbed (at lower order there is, e.g., a tilt). This non-uniformity is described by a specific model, the so-called “mapping model”. The model takes into account the various characteristics of the observing system. The model may be rather complex and has to consider the orientation of the focal plane, the plate scale, and radial, typically non-linear, deformations stemming from imperfect optics. Therefore, a number of well distributed reference stars is commonly used in a least-squares adjustment process to determine the parameters of the mapping model. Mapping models need to be maintained regularly. They are a mandatory input to the astrometric reduction process.

The following specific relevant aspects of the astrometric reduction process are based on the work of Schildknecht (1994) and Flohrer (2008). The formal error of the transformation into the system defined by the star catalogue at the end of the astrometric reduction process should also give a first estimate for the total error, as the accuracy of a reference star catalogue usually is assumed not to contribute much to the overall error budget. However, some systematic effects in star positions or proper motions of some catalogues have been identified (Flohrer, 2008). As a reference we may assume the recently released UCAC3 (Zacharias et al., 2010) from the US Naval Observatory (USNO), with a claimed accuracy of about  $0.015''$  to  $0.1''$  per coordinate, depending on magnitude. The GEODSS system uses a modified USNO-B or UCAC catalogue to meet the requirement of  $0.3''$  for the astrometric position and 1 ms for the epoch (Faccenda, 2000).

Reference stars also allow it to determine the mount model (or pointing model) defining the system orientation (i.e., the nonorthogonalities) and the misalignment of optical axes. The mount model usually is characterised by a set of parameters that allow it to compensate for pointing deviations in the observation planning process.

In the previous section we have stated that the how achievable SNR dominates the detection process and the astrometric reduction process, where the pixel scale is a key parameter. We also need to consider seeing conditions and the quality of the observing system.

Seeing characterises the effect of turbulence within the airmass, which results in changes of the refraction index. Seeing is highly variable from site to site and is mainly a function of altitude and wavelength. Therefore, the received object signal and the observed colour of objects varies with moderate frequency (scintillation). As seeing leads to “smearing out” of the received object signal, the full width at half maximum (or FWHM) of the seeing disc is an important characteristic. Through the SNR degradation and the smearing out effect seeing directly impacts the achievable astrometric accuracy. Seeing can also vary significantly during the observation night, and even with pointing direction. Astronomical observatories, such as the OGS typically have a seeing around  $1''$ , while sites close to urban areas only have a seeing in the range of  $2''$ - $3''$ .

Differential atmospheric refraction reflects the fact that the refraction is a function of wavelength, thus is variable within the FoV, and needs to be modelled. Refraction is defined as the angle between the

apparent direction of an object as seen by the observer and the direction in the absence of the atmosphere. In the absence of atmospheric dispersion correctors the differential atmospheric refraction of a white point source is projected into short trails along the elevation angle.

Parallactic atmospheric refraction is important for the observation of non-stellar objects. This effect covers the differences in the refraction effect between an object observed at infinite and at finite distances, and needs to be considered in the astrometric reduction process.

Colour refraction may impact the astrometric reduction process if (some) reference stars and the observed object have different colours. This may lead to systematic offsets in the determined object position. The colour of stars may be known from the star catalogue, which allows it to reject such stars of exotic colours in the reduction process. In the case of an unknown object having an extreme colour such an approach may not work.

The motion of the observer caused by the rotation of the Earth and the finite speed of light  $c$  leads to the so-called “aberration”. Diurnal aberration is caused by the motion of the observer with respect to the geocentre. At the equator it reaches  $0.32''$ . Annual aberration is due to the motion with respect to the barycentre of the solar system. Secular aberration is due to the motion of the solar system, and can be neglected. The annual aberration has an amplitude of about  $20''$ , which has, e.g., been reported for the GEODSS processing by (Faccenda, 2000).

The accuracy of epoch registration that is introduced by the shutter timing technique and may introduce position errors of a stochastic or systematic nature. The effect may be a function of the object’s offset to the centre of the FoV, and should be modelled. Depending on the centroiding algorithm the registration of epoch marks of an object streak in the exposure may be more difficult.

Total measurement accuracy is obtained by a calibration using active satellites. The satellite position resulting from astrometric observations is compared to the satellite’s precise ephemeris, see (Flohrer, 2008) for GNSS.

### 3.4 Orbits of artificial satellites

Beutler (2005) gives the equations of motion in the quasi-inertial coordinate system in the following generic form:

$$\ddot{\mathbf{r}} = -GM \int_{V_{\oplus}} \rho_{pr} \frac{\mathbf{r} - \mathbf{r}_p}{|\mathbf{r} - \mathbf{r}_p|^3} dV_{\oplus} - G \sum_{j=1}^n m_j \left( \frac{\mathbf{r} - \mathbf{r}_j}{|\mathbf{r} - \mathbf{r}_j|^3} + \frac{\mathbf{r}_j}{r_j^3} \right) + \sum \mathbf{a}_{ng} \quad (3.28)$$

where  $GM$ ... product of the gravitational constant and the mass of the Earth,

$$GM = 398600.4418 \pm 0.0008 \text{ km}^3\text{s}^{-2}$$

$\mathbf{r}_j$  ... Geocentric position of the point mass  $j$

$\mathbf{r}_p$  ... Geocentric position of a discrete volume element  $dV_{\oplus}$  of the Earth

$V_{\oplus}$  ... Volume of the Earth

$\rho_{pr}$  ... Relative density function

$n$  ... number of perturbing solar system objects

$m_j$  ... Mass of the point mass  $j$

$\mathbf{a}_{ng}$ ... Non-gravitational accelerations .

The first term on the right-hand side may be written as the gradient of the Earth's gravitation potential  $V(r, \lambda, \phi)$ , which is usually specified in the Earth-fixed coordinate system as:

$$V(r, \lambda, \phi) = \frac{GM}{r} \sum_{n=0}^{\infty} \frac{R^n}{r^n} \sum_{m=0}^n P_{nm}(\sin \phi) \{C_{nm} \cos(m\lambda) + S_{nm} \sin(m\lambda)\}. \quad (3.29)$$

where  $\lambda, \phi$  ... Geocentric longitude and latitude  
 $R$  ... Mean equatorial radius of the Earth  
 $n, m$  ... Degree and order of the geopotential term  
 $P_{nm}$  ... Associated Legendre functions of degree  $n$  and order  $m$   
 $C_{nm}, S_{nm}$  ... Geopotential coefficients of degree  $n$  and order  $m$ .

As the potential is given in the Earth-fixed coordinate system, we first have to transform the satellite coordinates into the Earth-fixed system (using the inverse of transformation Eq. 3.1), then we have to calculate the gradient of the potential via Eq. 3.29. Eventually, we have to use the transformation equations Eq. 3.1 for back-transformation into the quasi-inertial coordinate system.

The second term on the right-hand side of Eq. 3.28 represents the sum of  $n$  gravitational point-mass attractions, those due to Moon and Sun being the most important ones. There are other accelerations of gravitational nature, which we do not consider here (e.g., the effects due to the tidal deformation of the solid Earth, the oceans and the atmosphere).

Two forces of non-gravitational origin have to be mentioned, namely solar radiation pressure and the drag due to the upper atmosphere (for LEOs only). For details we refer to Beutler (2005).

When solving the equations of motion (3.28) we have to provide the initial state vector consisting of the initial position and velocity vectors at the initial epoch  $t_0$ :

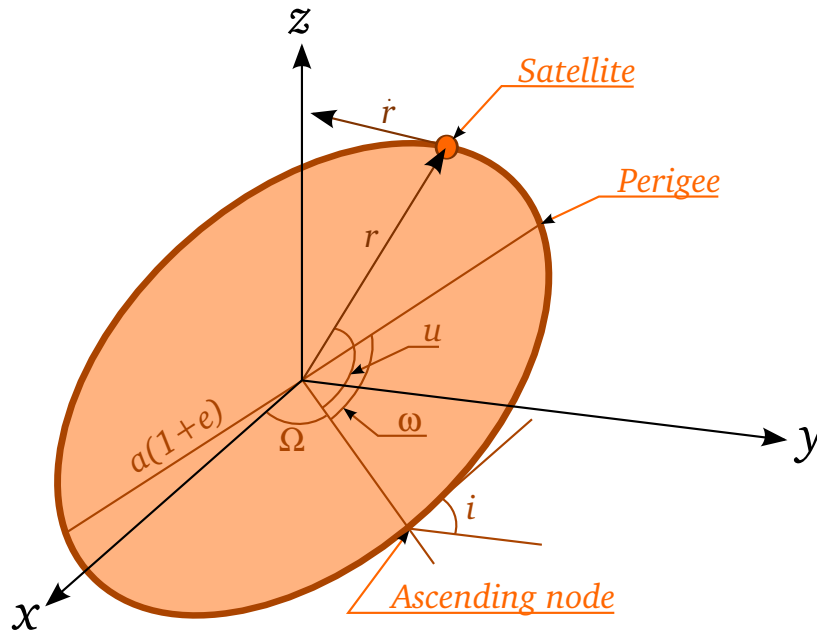
$$\begin{aligned} \mathbf{r}(t_0) &= \mathbf{r}_0 \doteq \mathbf{r}(a, e, i, \Omega, \omega, u_0) \\ \dot{\mathbf{r}}(t_0) &= \dot{\mathbf{r}}_0 \doteq \dot{\mathbf{r}}(a, e, i, \Omega, \omega, u_0). \end{aligned} \quad (3.30)$$

The second expression on the right-hand sides of Eq. (3.30) indicates that the initial position and velocity vectors may be expressed by the corresponding osculating elements:

$a$  ... Semi-major axis  
 $e$  ... Eccentricity  
 $i$  ... Inclination with respect to the equatorial plane  
 $\Omega$  ... Right ascension of the ascending node  
 $\omega$  ... Argument of perigee  
 $u_0$  ... Argument of latitude,

referring to the initial epoch  $t_0$  (see Fig. 3.17 for an illustration).

From the geometrical point of view  $a$  and  $e$  define the size and the shape of the orbit, while  $i$  and  $\Omega$  define the orientation of the orbital plane in the inertial system.  $\omega$  defines the orientation of the orbit in the orbital plane, and finally  $u_0$  defines the position of the satellite in the orbit at a certain time.

Figure 3.17: Orbital elements  $a, e, i, \Omega, \omega, u_0$  and state  $(\mathbf{r}, \dot{\mathbf{r}})$ 

### 3.5 Two-line element (TLE) sets

So-called two-line elements (TLEs) are commonly used in space surveillance applications to represent orbital information. The US space surveillance network provides TLEs, for example via the website [www.space-track.org](http://www.space-track.org). TLEs are not just a specific format for writing orbital elements, these data sets are mean elements and contain additional information. The modelling of the Earth's gravitational field and of the third-body perturbations is limited. Therefore, TLEs should only be used in connection with the underlying propagation theory. TLEs are given in a true equator-mean equinox (TEME) system.

The analytical theory to be used for propagating TLE sets from USSTRATCOM is the so-called Simplified General Perturbation 4 (SGP4/SDP4) model (Hoots and Roehrich, 1980). Objects with a revolution period longer above 225 min (or more than 6 rev/day), equivalent to a circular orbit above 5876 km altitude, are called deep-space objects.

The accuracy of TLEs is not known. Some attempts (as, e.g., by Laporte and Sasot (2008); Flohrer et al. (2008a); Levit and Marshall (2010) were made to assess the uncertainties associated with TLEs provided by USSTRATCOM. All studies conclude that in LEO the uncertainties are up to several hundred meters, and in GEO the uncertainties are several kilometres.

Listing 3.1 gives a standard example for a TLE set. Noted that in the TLEs the mean motion  $n = \sqrt{\frac{GM}{a^3}}$ , and not the semi-major axis  $a$  is not provided.

Listing 3.1: Sample TLE for ISS (source: space-track.org)

```
1 1_25544U_98067A_04236.56031392_00020137_00000-0_16538-3_0_5135
2 2_25544_51.6335_341.7760_0007976_126.2523_325.9359_15.70406856328903
```

where the columns refer to the following values:

Line 1

1 ... Line number  
3-7 ... Satellite catalogue number  
8 ... Classification  
10-17 ... COSPAR object identifier (year-launch-piece)  
19-32 ... Element set epoch (UTC), two-digit year, DoY, fraction of day  
34-43 ... First derivative of the mean motion  $\dot{n}$  (rev/day/2)  
45-52 ... Second derivative of the mean motion  $\ddot{n}$  (decimal point assumed)  
(rev/day<sup>2</sup>/6)  
54-61 ...  $B^*$  drag term (earth radii<sup>-1</sup>)  
63 ... Element set type  
65-68 ... Element number  
69 ... Checksum

Line 2

1 ... Line number  
3-7 ... Satellite catalog number  
9-16 ... Inclination  $i$  (deg)  
18-25 ... Right ascension of ascending node  $\Omega$  (deg)  
27-33 ... Eccentricity  $e$  (leading decimal point assumed)  
35-42 ... Argument of perigee  $\omega$  (deg)  
44-51 ... Mean anomaly  $M_0$  (deg)  
53-63 ... Mean motion  $n$  (rev/day)  
64-68 ... Revolution number at epoch  
69 ... Checksum

## 4. Simulation environment for optical observations

In this chapter we introduce an end-to-end simulation chain tailored for optical observations. This toolchain allows it to assess the performance of ground-based and space-based optical observation strategies.

The geometric and radiometric observation conditions are obtained from ESA's Program for Radar and Optical Observation Forecasting (PROOF) using modeled optical sensor means. PROOF supports different object reference populations (see Sect. 4.1). The initial orbit determination (IOD) based on measurements is a crucial step in the end-to-end simulation. For IOD we use a modified version of ORBDET from AIUB's program system CelMech supporting ground-based and space-based sensors (see Sect. 4.2). In Sect. 4.2.2 we describe an alternative formulation for IOD that has been implemented into ORBDET. We evaluate the capabilities of this approach using ground-based and space-based test scenarios. Section 4.3 shows how PROOF and ORBDET are linked through a measurement simulator module SIMOBS. Based on the work of Flohrer et al. (2006) we present the capabilities of the simulation environment for a proposed space-based optical observation scenario in Sect. 4.4.

### 4.1 PROOF

Originally, PROOF was developed as a tool for the validation of ESA's MASTER model through the comparison between observed detection rates of space objects and model predictions for given observation scenarios and sensors (Krag et al., 2000; Krag, 2003). This approach opens, however, also a wide range of applications beyond the original goal, ranging from the evaluation of sensor capabilities (see, e.g., the approaches chosen by Landgraf et al. (2004) or by Flohrer et al. (2005b)) to search for biases or selection effects in specific observation programs (Schildknecht et al., 2008). PROOF has extensively been used to discuss space-based optical observation capabilities. Krag et al. (2001) and later on Krag (2003), presented concepts for optical observations from a sensor in a sun-synchronous orbit (SSO), from a near-GEO drifting orbit, and from GTO. Oswald et al. (2004a) discuss orbit determination from optical observations via a space-based platform. These early studies introduced PROOF as an extremely valuable tool for observation forecasting and performance evaluation of space-based observations, but did not focus on the technical feasibility of the proposed system architecture and processing concept.

The first release of PROOF was associated with the MASTER model in the version 1999. Subsequent releases of MASTER were always accompanied with updated PROOF releases for the versions 2001, 2005, and 2009. Today, PROOF supports the simulation of optical and mono- or bistatic radar sensors, either on ground or in space. In addition to the main application based on statistical MASTER populations for selected reference epochs, PROOF may be used to forecast the observation conditions for

discrete population files that must be in TLE format (see Sect. 3.5). In the latter case an implementation of the SGP4/SDP4 theory (Hoots and Roehrich, 1980) is used to propagate the object positions. PROOF considers all relevant constraints of the observation conditions, and finally allows it to estimate the SNR for the observed object at the simulated observation epoch. The tabulated results are grouped into so-called crossing, detected, and gap objects. “Gap” objects are within the sensor FoV while the sensor is not able to perform measurements; “detected” objects are visible with a sufficiently high signal while the sensor acquires measurements. The term “crossing” refers to all objects that are in the sensor FoV irrespective of meeting the detection and operation constraints. The ESA PROOF tool, version 2005, was used here to study the various performance issues.

The major input parameters of PROOF for optical sensors include:

- sensor location or sensor orbit,
- optical instrument description and performance model,
- simulation settings (e.g., observation epoch and duration).

PROOF provides the following output parameters for each simulated observation epoch:

- geometrical observation conditions, such as, e. g., the time of closest approach (TCA) in the FoV, observation distance, angular velocity between object and sensor pointing, and the dwell time in the FoV,
- radiometric observation conditions, e.g., phase angle, object’s apparent magnitude, background brightness, estimated SNR per pixel,
- osculating elements of the object at the TCA,
- used object diameter for SNR estimation (derived either from the statistical model of the population or from deterministic settings for a TLE population).

## 4.2 CelMech

For the simulation of orbit determination we use CelMech, a program package for celestial mechanics applications developed by Beutler (2005). CelMech supports a broad range of applications from numerical integration to tools allowing it to assess the stability of the planetary system. The algorithms in CelMech and their application to ground-based orbit determination from short arcs using astrometric places of unknown objects are described in detail by Beutler et al. (2003). The modules used here are the program for initial orbit determination ORBDET and, to a lesser extent, the program for orbit propagation and orbit improvement SATORB.

ORBDET is used to determine a first orbit, and, subsequently, to improve the determined initial orbit using all observations available. ORBDET requires no a-priori information for first orbit determination. The only input information are the astrometric places of the object and the observation epochs. No dynamical parameters are determined in ORBDET.

ORBDET supports two different approaches for initial orbit determination based on angular measurements: one approach assuming a circular orbit, and another using a “boundary value” method. Two

measured astrometric places are required for the determination of a circular orbit. The boundary value method requires at least three astrometric places. The subsequent orbit improvement step may be invoked after both initial orbit determinations. We introduce the circular orbit and the boundary value method in Sect. 4.2.1 and Sect. 4.2.2, respectively.

In this work SATORB is only used to determine and propagate a reference ephemeris. As SATORB provides a sophisticated modelling of the perturbing forces acting on artificial Earth satellites, we consider ephemerides generated by SATORB being the “truth”, if a long arc of observations has been available for SATORB. In SATORB we include perturbations due to Sun and Moon, consider Earth tides, model the Earth’s gravity potential up to degree and order 12, apply corrections due to general relativity, use a simplified radiation pressure model (spherical satellite), and perform the numerical integration of order 10. The orbit determination epoch is set to the centre of all available observations. The created ephemeris data has a spacing of 10 min.

### 4.2.1 Circular orbits

For circular orbit determination the eccentricity  $e$  and argument of perigee  $\omega$  are 0. The determination of a circular orbit is interesting, if either only two observations are available, which is not sufficient for the determination of six orbital elements, or if the observed arc is very short. In the latter case typically the determination of the shape of the orbit ( $a$  and  $e$ ) is rather difficult, but the orientation of the orbit ( $i$  and  $\Omega$ ) may still be determined with sufficient accuracy.

The circular orbit can then be used to schedule follow-up observations. From the combination of initial and follow-up observations the full set of orbital elements can be determined, see, e. g., the process developed by Musci (2006).

An algorithm may be defined, which searches for the radius, as where the angle between the two position vectors is calculated from the observation geometry and from the known mean motion at the observation times. Limits for the semi-major axis need to be defined in the search process. We consider two observations at the epochs  $t_A$  and  $t_B$ , introduce the topocentric observer positions  $\mathbf{R}_A$  and  $\mathbf{R}_B$ , the two observed directions in the topocentric frame  $\mathbf{e}_A$  and  $\mathbf{e}_B$ , and the two topocentric distances  $\rho_A$  and  $\rho_B$ , so that (ignoring the light travel time)

$$\mathbf{r}_i = \mathbf{R}_i + \rho_i \mathbf{e}_i, \quad i = \{A, B\}. \quad (4.1)$$

To solve the circular IOD problem Beutler (2005) formulates two ways of estimating the difference between the arguments of latitude  $\Delta u$  at  $t_A$  and  $t_B$ :

- $\Delta u_g$ : determined directly from the angle enclosed by  $\mathbf{r}_A$  and  $\mathbf{r}_B$ , which requires an assumption on  $a$  that in turn fixes the distances  $\rho_A$  and  $\rho_B$ , and
- $\Delta u_d$ : determined from the uniform mean motion of the object on a circular orbit via

$$\Delta u_d = \sqrt{\frac{GM}{a^3}} \left( t_B - t_A - \left( \frac{\rho_B}{c} - \frac{\rho_A}{c} \right) \right), \quad (4.2)$$

which again requires an assumption on  $a$ .

As  $\Delta u_g$  and  $\Delta u_d$  have to be identical, we can search for the root of the nonlinear equation

$$B(a) = \Delta u_g - \Delta u_d \quad (4.3)$$

by varying  $a$  within the assumed ranges. Having found  $a$ , the remaining orbital elements of the circular orbit  $i$  and  $\Omega$  can be easily found with

$$\tilde{\mathbf{h}} = \mathbf{r}_A \times \mathbf{r}_B \quad (4.4)$$

$$\Omega = \arctan\left(\frac{\tilde{h}_1}{-\tilde{h}_2}\right) \quad (4.5)$$

$$i = \arccos\left(\frac{\tilde{h}_3}{|\tilde{\mathbf{h}}|}\right), \quad (4.6)$$

and for the argument of latitude, e.g., at  $t_A$  we obtain

$$u_A = \sqrt{\frac{GM}{a^3}} \left(t_A - \frac{\rho_A}{c}\right). \quad (4.7)$$

The solution may be ambiguous if  $B(a)$  has multiple roots, which occurs in particular for short arcs. Therefore, a reasonably defined search window for  $a$  is essential. If more than just two observations are available, and a boundary value approach cannot be used, it is often helpful to determine a circular orbit for all possible pairs of observations. This may help to resolve the ambiguities of multiple roots.

Note that all observations have to be within the same revolution of the orbit.

ORBDET allows it to execute an orbit improvement step after the IOD, which takes into account the major perturbing forces. Orbit improvement is based on a least squares adjustment using all given observations. An interpretation of the orbit determination results is therefore possible using the RMS a posteriori, and the obtained residuals.

## 4.2.2 Boundary value method

First orbit determination may be based on a boundary value problem, and not on an initial value problem. The particular boundary value problem used here may be solved by numerical integration. The method tries to identify a local minima of the residuals over all observations or, alternatively, over a selectable subset of all available observations within the considered arc. The sum of the residuals squares from a least-squares adjustment process is used to find the local minima. The particular solution of the equations of motion for satellites is used in this process, and may include perturbations.

Beutler et al. (2003) showed that this approach is applicable to determining orbits of GEO and GTO objects from ground-based observations. The approach is stable and fast. Usually, good results are achieved for short observation arcs, which is a typical case in surveys. The ORBDET approach may therefore be used for space-based observations as well, after some modifications of the original ORBDET code. The instrument's position (the orbital elements of the instrument) is introduced as input data.

Figure 4.1 illustrates the used quantities. The topocentric observer is located at  $\mathbf{R}(t)$ . The object  $S$  is observed in the direction  $\mathbf{e}(t)$ , and has the topocentric distance  $\rho$  of the observer at the observation epoch

$t$ . The direction  $e(t)$  can be approximately calculated from the equatorial coordinates  $\alpha$  and  $\delta$ . The light travel time  $\Delta t$  must be taken into account for the observation geometry. The observed short arc has the boundaries  $A$  and  $B$ .

The boundary value method has the advantage of being robust and highly flexible and may be used for both, ground-based and space-based applications. The method works for different arc lengths, but Beutler (2005) states that the best performance can be expected for arc lengths between  $10^\circ$  and  $30^\circ$ . Boundary value methods may deal with eccentric orbits - a significant advantage compared to assuming a circular orbit. As the implementation is comparably easy, even a use in on board software system seems feasible.

For the boundary value method the typical limits of any initial orbit determination applies. If the short arc is too short compared to the measurement accuracy, what may occur, e.g., for objects crossing a narrow FoV, or for poorly determined object positions, any initial orbit determination will fail.

In a space-based scenario several projection effects may also cause the algorithm to fail. Not enough information can be collected, e.g., for a pointing direction in-flight, which sees the observed object approaching from or departing into a head-on direction, or for co-planar fly-bys with the observed object.

Both boundary value approaches follow the idea that two boundary vectors  $r_A$  and  $r_B$  (geocentric positions of the unknown object at the boundary epochs  $t_A$  and  $t_B$ ) can be calculated from the observed direction between sensor and unknown object and the known sensor position, if the topocentric distances  $\rho_A$  and  $\rho_B$  are known (similar to Eq. 4.1). By systematically varying  $\rho_A$  and  $\rho_B$ , one will find the best fit of the observed directions  $\alpha$  and  $\delta$  on an orbit fixed by the boundary conditions by minimising the sum of the squared residuals. These residuals between observations and determined orbit are estimated in right ascension and declination. At least three observations (in fact astrometric position measurements) are required for the boundary value approach.

Two implementations of a boundary value method are discussed allowing for full-parameter orbit determination. The first approach (BNBNDV) is the original one used in ORBDET. The second one

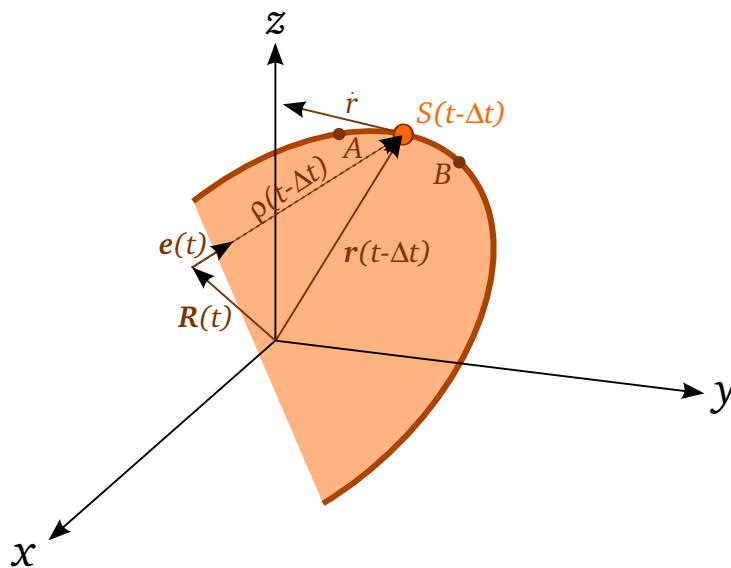


Figure 4.1: Boundary value method - schematic view of the used quantities.

(BNBN2D) is based on a newly developed 2D-search.

#### 4.2.2.1 BNBNDV

In particular for short arcs we can assume that the topocentric distances at the boundary epochs are similar ( $\rho_A \approx \rho_B$ ). This allows formulating an interesting approach for the majority of survey observations of MEO or GEO objects. Beutler (2005) demonstrates how in ORBDET a one-dimensional search over topocentric distances can be used for initial orbit determination.

The following steps are proposed:

- Variation of  $\rho_A$  within user-defined search limits with the given stepsize  $\Delta\rho$
- Re-computation of the geocentric distance at  $t_A$  via  $r_A^2 = (\mathbf{R}_A + \rho_A \mathbf{e}_A)^2$
- Approximation of  $\rho_B$  via  $r_A \approx r_B = (\mathbf{R}_B + \rho_B \mathbf{e}_B)^2 = R_B^2 + 2(\mathbf{R}_B \mathbf{e}_B) \rho_B + \rho_B^2$
- Fixing  $\rho_A$ ,  $\alpha_i$ , and  $\delta_i$  with  $i = \{A, B\}$  allows solving the linearised observation equations given by Beutler (2005) for only one remaining parameter  $\rho_B$
- A simple one-dimensional search criterion is defined by using the sum of the squared residuals  $\Delta\alpha$  and  $\Delta\delta$  as function of  $\rho_A$ , considering all  $n$  observations:

$$B(\rho_A) \doteq \sqrt{\frac{\sum_{i=1}^n (\cos^2 \delta_i \Delta\alpha_i^2(\rho_A) + \Delta\delta_i^2(\rho_A))}{n-1}}. \quad (4.8)$$

- The minima of  $B(\rho_A)$  give the best solutions in a least-squares sense, and from that the associated orbital elements can be calculated.

#### 4.2.2.2 BNBN2D

BNBN2D represents an alternative formulation to BNBNDV. This concept was originally developed by Beutler for his lectures on astrodynamics at the University of Bern and is briefly outlined in (Beutler, 2005), but, as opposed to the one-dimensional search algorithm BNBNDV, it has not been implemented into the released version of ORBDET.

If  $n$  observations are available in the interval  $(t_A, t_B)$  an approximation of the observed arc through a truncated Taylor series with the coefficients  $b_j$  can be formulated from these observations. This approximation around the epoch  $t$  and its second derivative are:

$$\mathbf{r}(t) = \sum_{j=0}^n (t_A - t)^j b_j \quad (4.9)$$

$$\ddot{\mathbf{r}}(t) = \sum_{j=2}^n j(j-1)(t_B - t)^{j-2} b_j. \quad (4.10)$$

For  $n = 3$  the equation system is linear and we can build a simple least-squares system, if we ask the solution to meet the equation of motion at the boundary epochs. In principle, an approximation up to order  $q = n$  is possible, if a system of  $q - 2$  differential equations is used.

$$\begin{aligned}
\mathbf{A}\mathbf{b} &= \mathbf{l} \\
\mathbf{A} &= \begin{pmatrix} 1 & t_A - t & (t_A - t)^2 & (t_A - t)^3 \\ 1 & t_B - t & (t_B - t)^2 & (t_B - t)^3 \\ 0 & 0 & 2 & 6(t_A - t) \\ 0 & 0 & 2 & 6(t_B - t) \end{pmatrix} \\
\mathbf{b} &= (b_0, b_1, b_2, b_3)^T \\
\mathbf{l} &= \left( r_A, r_B, -GM \frac{r_A}{r_A^3}, -GM \frac{r_B}{r_B^3} \right)^T
\end{aligned} \tag{4.11}$$

$\mathbf{A}$  is fixed for known  $t$ ,  $t_A$ , and  $t_B$  the  $4 \times 4$  matrix can be inverted directly. The equation system can be solved easily for  $\mathbf{b}$  as a function of systematically varied  $\rho_A$  and  $\rho_B$ . This variation searches for the best fit to the observed arc. A filtering mechanism may exclude all hyperbolic solutions ( $e > 1$ ).

A possible fit criterion  $B$  for observed ( $O$ ) and computed ( $C$ ) positions obtained from the reconstituted arc is :

$$B(\rho_A, \rho_B) \approx \sqrt{\frac{\sum_{k=1}^n \cos^2 \delta_k^O (\alpha_k^O - \alpha_k^C)^2 + (\delta_k^O - \delta_k^C)^2}{2n}}. \tag{4.12}$$

Varying both topocentric distances  $\rho_A$  and  $\rho_B$  at the boundary epochs of the observed arc allows it to perform a two-dimensional search.

Figure 4.2 illustrates a typical case of initial orbit determination using BNBN2D from a short arc observations. We consider a space-based observation scenario, where a sensor orbiting in the GEO observes other near-GEO objects. For this example we study a typical situation, where the observed arc contains 280 observations acquired in 280 s.

The left picture refers to a simulation without any measurement error, while in the right picture a random measurement error of  $2.5''$  is assumed. The major challenges are obvious: without a good initial values  $\rho_A$  and  $\rho_B$ , the search volume is large, and the minimum can be very sharp. Therefore, selecting an appropriate sampling width is essential. The implementation of BNBN2D foresees a fine-search within the gridpoint containing the found minima. On the other hand, if the noise level is high, the minimum is less prominent and “flat”, and searching for the minima becomes a cumbersome process.

In BNBN2D the minimum is sought for using either a brute-force method with a fine-search as a second step ensuring completeness, or using a gradient-step method, which is more rapid, but may run into numerical problems with very sharp or flat minima.

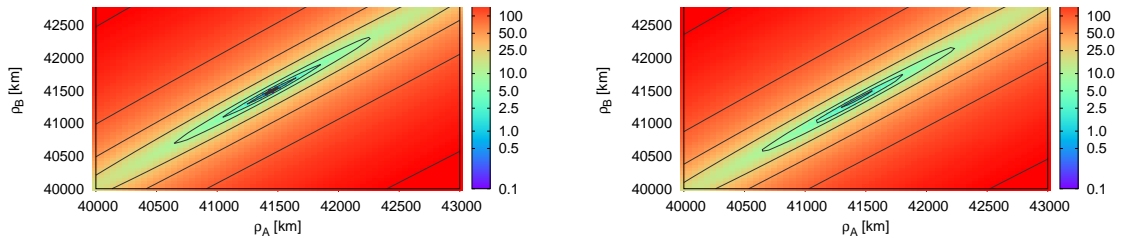


Figure 4.2: BNBN2D minimum search for  $0''$  (left) and  $2.5''$  (right) RMS of single observation.

Table 4.1: Test objects for the evaluation of BNB2D, with osculating elements referring to the latest available observation epoch per object.

Object	$a$ [km]	$e$ [-]	$i$ [°]	$\Omega$ [°]	Class
E07311A	41334	0.00	9.52	-32.45	GEO
E07343D	42026	0.49	11.23	3.55	HAMR
E08035A	41206	0.05	12.95	-0.14	GEO
E08061B	23162	0.71	7.30	23.23	GTO
E08125C	42302	0.21	6.65	-41.03	HAMR

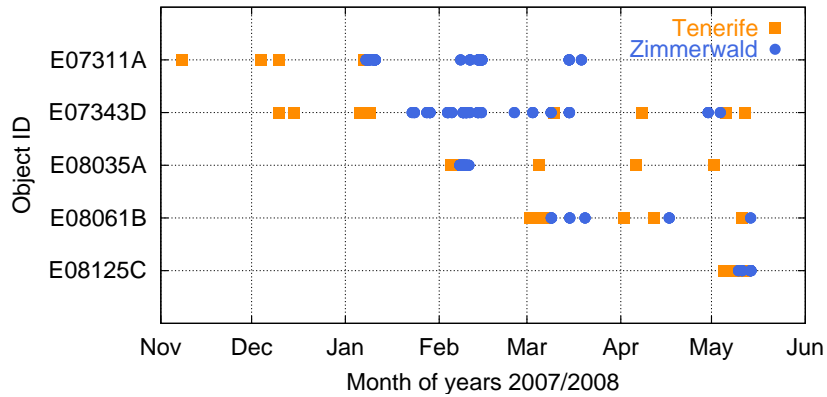


Figure 4.3: Distribution of the observations acquired with ESA’s 1-m telescope at the OGS at Tenerife, and with ZIMLAT, located at Zimmerwald (Switzerland).

**Evaluation of BNB2D** We will now demonstrate the capabilities of BNB2D for initial orbit determination. We use ground-based observations acquired with ESA’s 1-m telescope and with ZIMLAT, and we use simulated space-based observations for the SBO proposal. We assume that the astrometric accuracy of the observations is better than  $0.5''$  (RMS).

**Ground-based observations** Table 4.1 introduces the selected 5 test objects, which cover 5 classes of typical objects found in high altitudes. The class indicates whether a particular object belongs to GEO or GTO, or is an object with an extremely high ratio of area to mass (HAMR). HAMR objects originating from GEO are of certain interest as the solar radiation pressure leads to a comparably fast growth in eccentricity and inclination. The evolution of eccentricity and inclination of HAMR objects shows complex periodic patterns.

Figure 4.3 outlines the distribution of the available observations acquired in 2007/2008.

Figure 4.4 presents for all 5 test objects the result from the orbit determination using ORBDET with initial orbit determination through BNB2D, and a subsequent orbit improvement step. Each blue dot refers to one solution from a single short arc, which is formed by associating observations of one observing unit typically covering 3 to 5 observations within about 1-2 minutes. A yellow dot refers to the results of an orbit determination based two consecutive short arcs. Figure 4.5 shows the corresponding arc length for both cases, together with the resulting RMS a posteriori. We considered an orbit determination with a small RMS as successful. A small RMS a posteriori does not really imply that the determined orbit is

correct.

The left column of Fig. 4.4 gives orbit determination results in the  $a$ - $e$  space with error-bars indicating the results from the orbit improvement step. The right column shows the results in the  $\Omega$ - $i$  space. The indicator “Truth” refers to the best possible orbit determination result obtained from a long arc of all test observations via SATORB, with the orbit determination epoch set to the epoch closest to the middle of all available observations.

Figure 4.4 shows that in all test cases the solutions using a combination of subsequent arcs give significantly better results than the orbit results from a single short arc. The determination of  $a$  and  $e$  from short arcs is often difficult and returns wrong results of high eccentricity, while the determination of  $\Omega$  and  $i$  is more robust in all cases. The orientation of the orbital plane seems to be determined better in cases where the eccentricity is low (E07311A and E08035A).

**Space-based observations** We apply ORBDET with the BNB2D algorithm to a set of selected test cases simulating a space-based optical observation scenario. Here, we focus on capabilities of the initial orbit determination algorithm. We will discuss the simulation environment combining PROOF and ORBDET in Sect. 4.3 and the observation scenarios in Sect. 4.4.

We consider two comparably problematic test cases, a SBO-like sensor platform orbiting in GEO and observing GEO objects, and a similar platform orbiting in LEO observing LEO objects. The possible case of a LEO sensor observing GEO is understood to be easier, due to larger distances and smaller angular velocities of the objects. This case would allow it to acquire comparably long observation arcs and would also provide observations of better astrometric accuracy. We will discuss this case in Chapter. 6.

From the known sensor position at the observation epochs and the orbital information of the object crossing the sensor’s FoV, both calculated from the PROOF settings, error-free observations are generated. A dedicated processing engine (SIMOBS) allows it to add various noise sources. A list of “true” epoch-related astrometric positions results. ORBDET is then used to determine a first orbit and to improve the orbit using the given observation file and the instrument orbit as input. ORBDET will in most cases be able to determine an orbit for the object from the simulated measurements. We may either use the RMS or the residuals of the orbit improvement step as decision criteria, whether the orbit determination was acceptable. All successful orbit determinations may be characterised and classified according to the achieved quality by comparing the estimated orbital elements with the “true” elements provided by PROOF.

The following input was used for the evaluation of the algorithm performance:

- image acquisition frequency of 1 Hz providing equally spaced observations of the same accuracy (RMS),
- astrometric accuracy with RMS of  $0''$ ,  $0.5''$ ,  $1''$ ,  $2.5''$ , and  $5''$ ,
- contribution of the sensor position to the error budget neglected (assumption that the sensor position during the processing is known better than 1 m),
- assumption that the epoch registration accuracy is contained in the assumed astrometric accuracy.

Table 4.2 lists the ten test objects (five each for the GEO and LEO cases) for which the orbit determination using the BNB2D algorithm was tested. The table provides the basic orbit characteristics and the arc

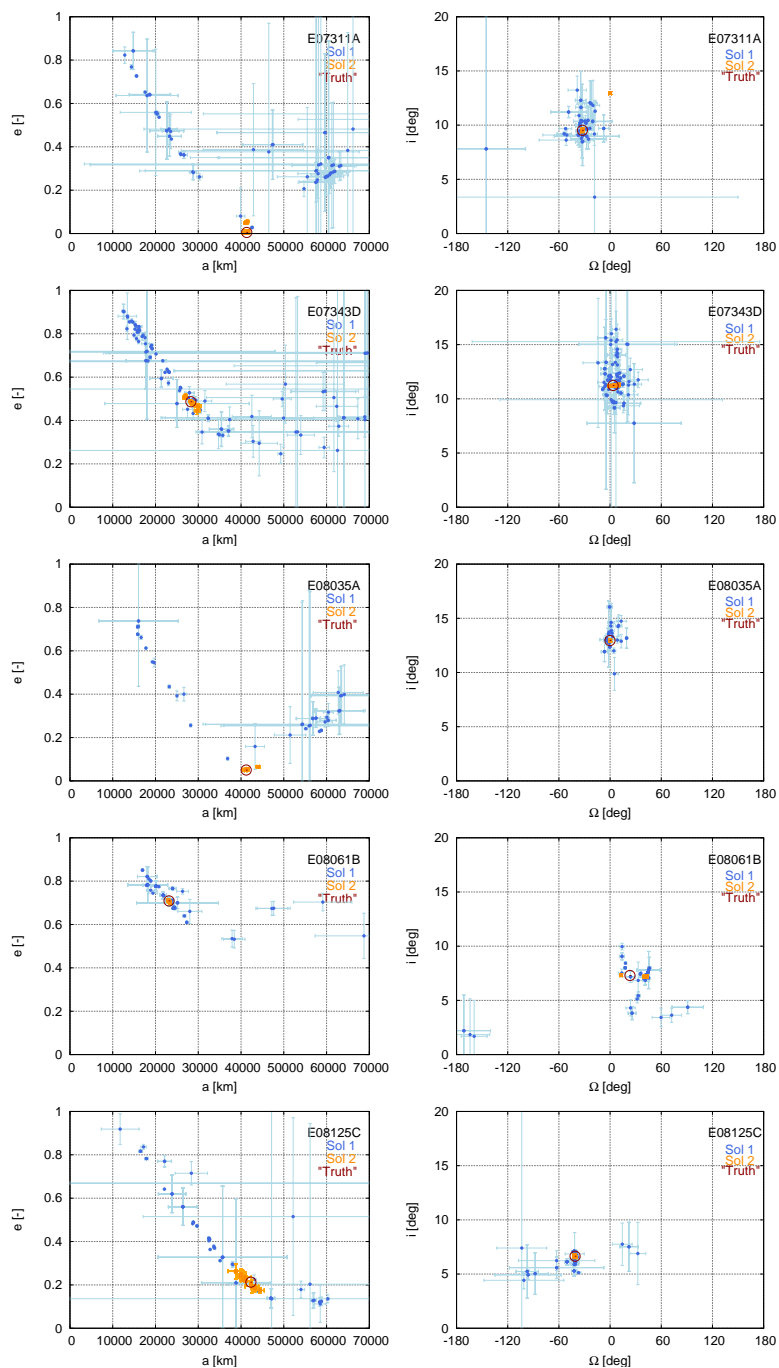


Figure 4.4: Orbit determination for single arcs (blue) and combined arcs (yellow), and best (true) solution (red circle) in the  $a$ - $e$  (left column) and  $\Omega$ - $i$  space (right column); test objects (top to bottom lines): E07311A, E07343D, E08035A, E08061B, E08125C.

Table 4.2: Test objects for the evaluation of the space-based initial orbit determination capabilities of BNB2D.

Object	$a$ [km]	$e$ [-]	$i$ [°]	$\Omega$ [°]	arc [s]
GEO1	28568	0.48	13.50	96.29	282
GEO2	26723	0.65	66.94	-101.83	120
GEO3	40950	0.03	11.14	42.34	212
GEO4	24681	0.72	6.83	105.47	210
GEO5	34060	0.22	3.93	-23.71	776
LEO1	7923	0.00	102.38	177.92	24
LEO2	8093	0.02	74.07	146.40	11
LEO3	10070	0.32	57.04	-134.30	26
LEO4	7771	0.01	101.73	150.63	48
LEO5	25085	0.72	4.24	-81.80	9

length, as well. The high angular velocities in the LEO case allow only observation arcs of several seconds, while the typical length of the arc for the GEO case is of a few minutes.

The middle epoch  $t$  was varied from  $t_A$  to  $t_B$  for each simulated observation (1 observation per second). The relevant figures for the simulated GEO and LEO test objects, which give the results for the test orbit determination are contained in Appendix A (Figs. A.4 to A.13). Each of these figures refers to one object and presents, grouped by the assumed astrometric noise, the relative frequency of the differences between the estimated and “true“ orbital elements  $a$ ,  $e$ ,  $i$ , and  $\Omega$ . Differences outside the shown interval are not covered by the figure.

GEO1 gives good results for the determination of the orientation of orbital plane, often better than  $1^\circ$  for the cases with lower noise level. In most cases with a small RMS the determination of the eccentricity is estimated close to the reference value. If the orbit determination fails, this is usually caused by a higher astrometric noise level.

The GEO2 case shows a high sensitivity to the astrometric noise level. The orbits are only acceptable

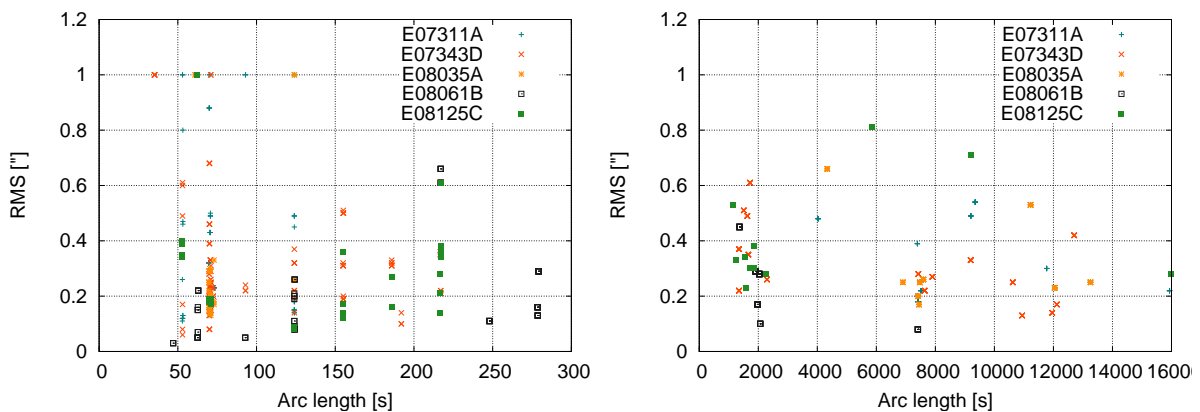


Figure 4.5: Obtained RMS as function of the arc length of the used short arc. Left: short arc formed from single observation unit; right: short arc formed from adding subsequent observation units.

for the case without noise. In all other cases for realistic noise the results show large differences to the reference values.

For GEO3 (a nearly circular drifting orbit of high inclination) the shape of the orbit ( $a$  and  $e$ ) can be determined if the astrometric noise is small. The observation geometry may cause problems when estimating the orientation of the orbital plane, independent of the noise level.

It was not possible to estimate an orbit of good quality for the object GEO4. The estimated eccentricity is about 0.98 in most "successful" orbit determinations and therefore offset by about 0.3. High-eccentricity orbits based on short arcs are difficult to be established by this algorithm.

The orbital plane for GEO5 (an eccentric sub-GEO with comparably long visibility in the FoV) maybe estimated usually better than  $1^\circ$ . A dependency from the astrometric noise is only visible for the semi-major axis. This indicates a very favourable observation geometry.

The orbit determination fails for the LEO1 and LEO5 simulations. While for LEO5 the arc is probably too short, in particular in view of the high eccentricity, the test for LEO1 probably fails because of the observation geometry. The circular orbits LEO2 and LEO4 are of better quality for comparable arc lengths.

The test for LEO2 returns very good results for the orientation of the orbital plane (mostly about  $1^\circ$ ). The determination of the shape of the orbit is difficult. The tests without astrometric noise and with  $0.5''$  noise are successful in determining of the shape in about 40% of the cases, but reveal a bad performance for higher noise levels.

For LEO3 a good performance is indicated for the determination of the orientation of the orbital plane. The results differ for the selected noise levels, but are consistent for each individual noise level, and are always within some degrees. The determination of the shape of the orbit is not successful. The eccentricity can not be determined with a high degree of confidence if there is noise added to the observations. The case for a noise level of  $5''$  could be traced to a statistical outlier, as there are only two runs that terminate with an elliptical orbit as result.

The result for LEO4 shows problems in the estimation of the shape of the orbit. The estimation of the orientation fails.

BNBN2D, as an alternative to the previously used initial orbit determination approach, has proved to be highly flexible, and easy to implement. Observations from different sites and space-based observations are supported. This is important for surveys of space debris, where potentially the combination of heterogeneous observations from different sites is required. Such observations typically differ in the astrometric accuracy due to the sensor design and due to processing issues, and are arranged in very short arcs combining very few observations. Initial orbit determination algorithms hence are important aspects in the correlation task of space surveillance.

Apart from specifying the search range, which is an efficiency-related issue, no further assumptions on the orbit are required by BNBN2D. An implementation based on three observations for the estimation of a first set of elements, with a subsequent orbit improvement step taking into account all available observations, has considerable potential for (onboard) processing of space-based observations, or as one component of a complex correlator function.

It was not surprising that the arc length matters for determining an initial orbit. For the problematic LEO case, where the observed arcs are very short, the determination of a circular orbit with subsequent orbit improvement step could be a valuable alternative. We will further study this in Sect. 4.4.

The selection of appropriate observation scenarios is crucial, as limitations set by the actual observation geometry impact the performance of all algorithms and cannot be circumvented later on by selecting different algorithms.

Let us finally point out that the discussion of the BNB2D capabilities did not take into account data processing issues (as, e.g., star occultations, extended background sources, etc.), which may degrade the astrometric accuracy. It is well known that the achievable astrometric accuracy is a function of the object brightness, implying that the selection of an observation scenario driven by the results from a simulated orbit determination also has to consider the characteristics of the target objects. Here we just assumed that any FoV crossing event would allow the full image processing and the acquisition of the necessary number of measurements for the orbit determination, which is a too optimistic assumption.

Future work on the BNB2D algorithm may include different data types, such as range or range-rate observations. There are two possible ways for an implementation. If there are only few observations, each range observation may be added as a constraint to the least squares adjustment. The other possibility is to use this additional data types to limit the search range in  $\rho_A$  and  $\rho_B$ . It is an interesting open issue, whether either the range and angular observation have to be simultaneous for a significant improvement of the solution, or a certain time difference is tolerable.

### 4.3 Simulation environment

In this section we discuss how PROOF and ORBDET can be linked to create, with the addition of a measurement simulator module SIMOBS, an end-to-end simulation environment for ground-based and space-based optical observations.

Figure 4.6 shows how PROOF may be connected to SIMOBS via a plug-in interface, which provides the topocentric observation geometry for all crossings events. The entire population of crossing objects, not only a few selected objects, is accessible. SIMOBS creates the astrometric positions expressed by the angles  $\alpha$  and  $\delta$ , and allows it to add controlled noise. The noise is Gaussian and can be either added to the astrometric place, or to the sensor positions. We assume that the epoch registration accuracy is absorbed by the astrometric accuracy. The SIMOBS output corresponds to the result after the image processing and astrometric reduction of the observations. The generated measurement file from SIMOBS is the input file for ORBDET, which will in most cases be able to determine an orbit of the object from the simulated measurement data. We may either use the RMS or the residuals provided by ORBDET to decide, whether the orbit determination was successful. All successful orbit determinations may be characterised and classified, according to the achieved quality by comparing the determined orbital elements with the input reference elements provided by PROOF.

There is one major issue for that approach. Through the PROOF plug-in the object identification is not possible. We therefore developed a very simple correlation technique selecting via observation epoch and velocity vector those observations belonging to the same object from the PROOF plug-in output.

There are limits of this tool chain that relate to the interface between PROOF and ORBDET. PROOF is fully trusted and validated for providing via the plug-in function single pixel SNR and topocentric observation geometry. A more realistic modelling of the observations makes the estimation of the associated uncertainties challenging. This task requires a model for an astrometric reduction process, which includes an image processing model, and a model for correlating observations. Such a link module must be either an existing processing software that is capable of using synthetic images, or it has at least to

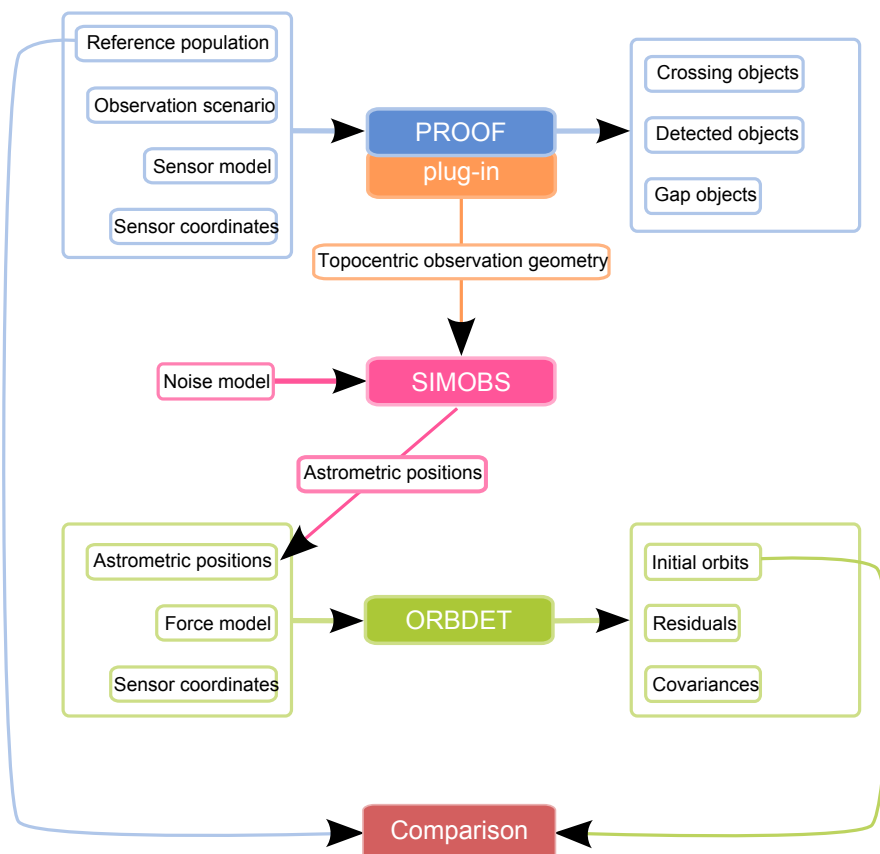


Figure 4.6: Simulator data flow.

consider realistically the detection conditions as a function of angular velocity, object brightness, detailed sensor parameters, etc. The correct parametrisation of this model is a multi-parameter exercise and rather difficult. The development of such a link is an extremely complex task and we are far from having such a tool available.

The developed simulation environment furthermore does not cover some of the more complex space surveillance tasks, which go beyond the discussion of observation strategies. These missing functionalities include the performance of catalogue correlation processes, the applicability of re-acquisition scenarios, and object identification.

The combination of observations of different accuracy from different sites is possible with this environment, and SIMOBS allows it to model the measurement accuracy of different sensor systems. Manual interaction is, however, required for such simulations.

## 4.4 Application of the simulation environment to a proposed space-based optical observation scenario

Let us now apply the simulation environment to a proposed optical space-based mission. The SBO project we briefly introduced in Sect. 2.5.2. It will also be the topic of a more extensive discussion on its space surveillance capabilities in Sect. 6. We briefly introduce the observation strategies for searching small-size space debris in Sect. 4.4.1. We present a performance evaluation including radiometry, image processing, and orbit determination aspects. The performance of the proposed system is evaluated in three steps. In a first step (Sect. 4.4.2) we discuss the observable objects using a statistical reference population from ESA's MASTER-2005 model with the help of PROOF-2005. Using the characteristics of objects crossing the FoV, we discuss the key parameters limiting the detection of objects. The next step (Sect. 4.4.3) consists of the analysis of the proposed image processing algorithm on board. Finally, in the third step, the orbit determination of the detectable space debris population is evaluated in Sect. 4.4.4. A combined performance estimation of the system is performed in Sect. 4.4.5.

### 4.4.1 Sensor baseline and proposed observation strategies

It is the goal of the SBO to improve the knowledge on small-size space debris (millimetre to centimetre objects) in LEO and GEO by passive optical means. For reasons of cost-efficiency only fixed-mounted telescopes were considered in the study, which do not require a dedicated mission. The sensor shall provide all measurements needed for orbit determination and for the estimation of the size of objects from a single crossing of a particular object through the sensor's field of view. To reduce the system requirements (mainly to limit the amount of transmitted data), data processing must be split between processing on board and on ground. Object detection of both, reference stars and debris objects (and discrimination), will be carried out on board, while the astrometric reduction, orbit determination, and size estimation are part of the processing on ground.

We found that the same instrument might be sufficient for both operating scenarios, LEO and GEO. Nevertheless, to ensure sufficient system performance the range to the small-size objects must be small. This is why space debris objects orbiting in LEO need to be observed from a sensor in LEO, while space debris in GEO must be observed from a platform in or near the GEO.

For the LEO region the study proposes a sensor mounted on a satellite orbiting in a nearly circular sun-synchronous orbit of about 800 km altitude and close to the terminator plane. The line-of-sight (LOS) shall point away from the Sun, almost perpendicular to the orbital plane, and slightly inclined in order to access densely populated regions in LEO (see Fig. 4.7).

Two concepts were studied for the GEO region. The first concept assumes use of a sensor mounted on a dedicated spacecraft in a low inclination circular orbit about 1000 km below the GEO, in a so-called subGEO orbit. In this case the sensor is proposed to point in the opposite direction to the Sun (see Fig. 4.8). In the second concept the sensor is mounted as a secondary payload onto a GEO satellite, with the instrument LOS mostly perpendicular to the orbital plane, pointing almost to the North or to the South (see Fig. 4.9). The LOS orientations in LEO and subGEO lead to optimal phase angle conditions (close to  $0^\circ$ ), while the LOS orientation in GEO results in average phase angle of about  $90^\circ$ .

The proposed instrument consists of a 20 cm aperture folded Schmidt telescope, a four megapixel, fast read-out camera using either a frame-transfer charge coupled device (CCD) or an Hybrid Visible Silicon Imager (HyViSI) sensor. With a focal length of 41 cm, the diameter of the FoV is  $6^\circ$ .

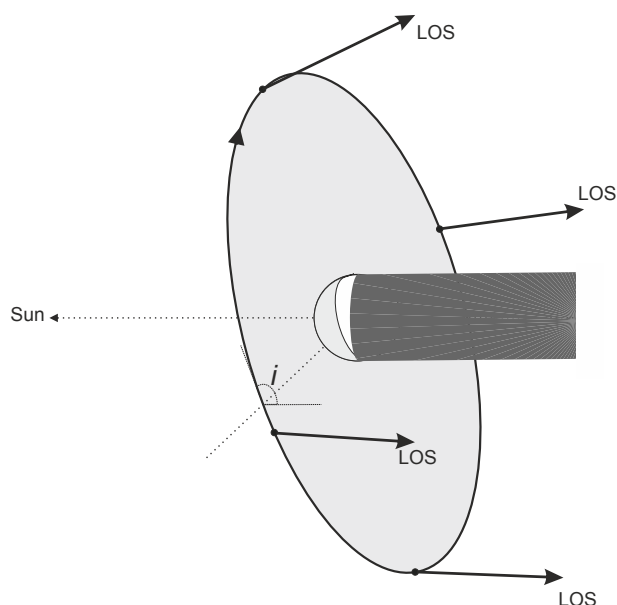


Figure 4.7: LEO operations concept: placed in a sun-synchronous orbit close to the terminator, the LOS of the sensor is slightly inclined to the normal of the orbital plane, ensuring a pointing into the densely populated regions in LEO.

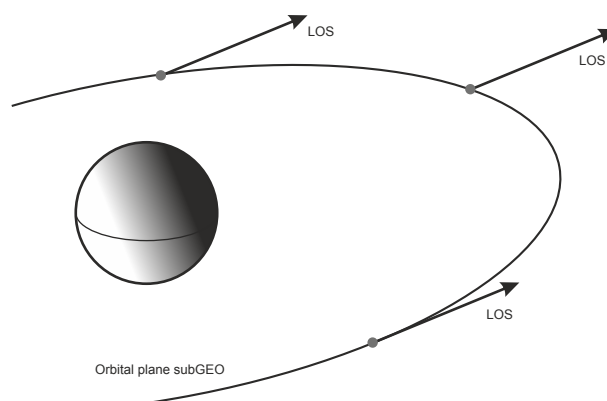


Figure 4.8: SubGEO operations concept: a dedicated spacecraft in a near-circular, slightly inclined orbit below the GEO, the LOS of the sensor is pointing away from the Sun.

#### 4.4.2 Assessment of the observable objects using PROOF

We used ESA's PROOF-tool version 2005 for the estimation of the number and the characteristics of FoV crossing events. The FoV crossing events were generated by PROOF from a statistical reference population of space debris objects, namely the ESA MASTER-2005 population. PROOF-2005 was used in the "statistic mode", and the reference epoch was 2005-05-01. To save computing time, the minimum object diameter was set to 5 mm, and the considered distances were limited to 10000 km. Furthermore, we combined the results from four Monte Carlo runs covering 24 h of observation time each, in order to improve the statistics. The PROOF-runs were executed for the 6<sup>th</sup> and 21<sup>st</sup> day of each month, over a

#### 4.4 Application of the simulation environment to a proposed space-based optical observation scenario

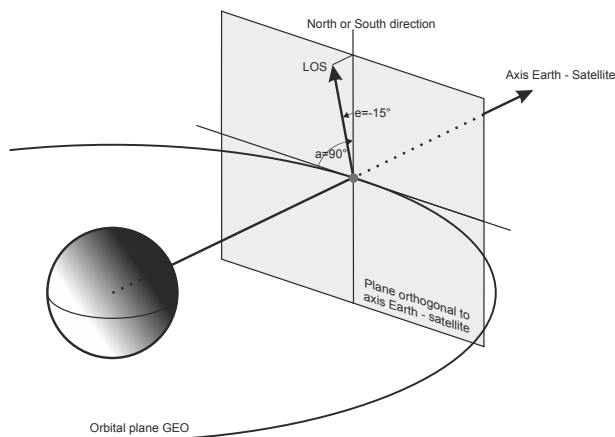


Figure 4.9: GEO operations concept: mounted as secondary payload on-board a GEO satellite, the LOS of the sensor points to the North or South, but slightly inclined towards the Earth by 15°.

one-year period starting December 2005. This altogether results in 576 h of simulated observation time. It must be kept in mind that all numbers presented are strongly dependent on the underlying space debris population model, which does not yet reflect the impact from the recent catastrophic changes to the LEO environment around 800 km altitude.

The results for CCD-detectors do not differ significantly from the HyViSI-detector results, which is why we will only present the results for the HyViSI detector. The considered observation distance is far more important for the interpretation of the simulation results. Due to CPU-time limitations only a limited band of observation distances can be simulated. The main focus of the SBO sensor is on small-size space debris. As the detection performance is expected to be better for short distances to the objects, the lower limit is 0 km, while for the upper bound we used 10000 km for all operation scenarios.

In the LEO there is, however, a significant loss in the detection sensitivity for increasing distances. Figure 4.10 shows the peak signal-to-noise ratio (SNR) as function of the object diameter for five selected distance ranges. Subsequently, we will always refer to the peak SNR per single pixel. Figure 4.10 indicates that for a reasonable  $SNR > 3$  a significant number of detectable FoV crossing events of small-size space debris objects ( $< 0.1$  m) can only be expected for distances below about 400 km.

The FoV dwell time is significantly shorter for short-distance FoV crossings, but for small objects the increase of the SNR due to the shorter distance exceeds the decrease of the SNR due to the higher FoV crossing velocity. The comparison of the FoV dwell time with the observation distance in Fig. 4.11 shows that for observation distances below 500 km the FoV dwell time is typically between 0.4 and 5 s. For the long-distance observations, dwell times of several minutes are possible. In order to acquire the required number of position measurements, dwell times below 10 s are demanding. Due to this fact, we will analyse the LEO operation concept with a distance cut-off at 400 km (subsequently called LEO400) in addition to a distance cut-off at 10000 km. For both concepts of the GEO operation, we analyse the FoV crossing characteristics with a 10000 km distance limit.

Table 4.3 and 4.4 summarise the results of the performance simulation with PROOF. The so-called unique crossings are listed in Table 4.3, which are the number of objects observed only once within the simulation period, and the number of so-called multiple crossings, which refer to objects crossing the sensor FoV at least twice during the simulation. The visible big differences between the number of LEO and

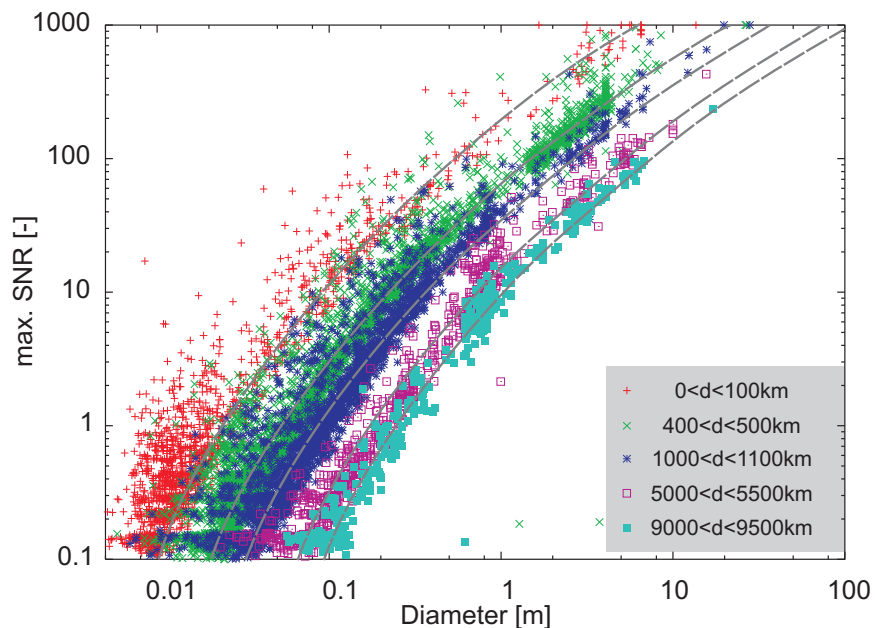


Figure 4.10: Peak SNR per pixel as a function of the object diameter in the LEO concept for five selected data subsets with different bands of the observation distance. The dashed lines indicate the average of the corresponding data subset.

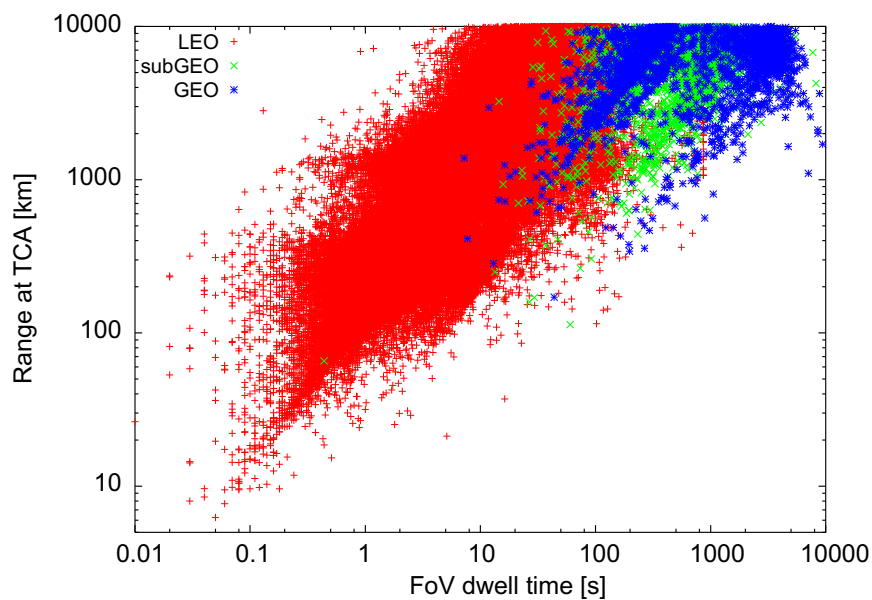


Figure 4.11: FoV dwell times in the LEO concept for five selected data subsets with different bands of the observation distance.

#### 4.4 Application of the simulation environment to a proposed space-based optical observation scenario

	<b>LEO</b>	<b>LEO400</b>	<b>subGEO</b>	<b>GEO</b>
Unique crossing events	18906	10829	2595	1619
Multiple crossing events	48765	10695	162	243

Table 4.3: Number of FoV crossing objects larger than 5 mm diameter within 576 h simulated observation time for the three considered operation concepts (LEO, subGEO, GEO).

	<b>LEO</b>		<b>LEO400</b>		<b>subGEO</b>		<b>GEO</b>	
SNR>1	43076	7	6589	7	642	9	254	12
SNR>2	33452	8	5055	8	513	9	198	30
SNR>3	28620	8	4417	8	434	23	163	34
SNR>4	27301	8	4273	8	419	23	157	34

Table 4.4: Number of FoV crossing objects larger than 5 mm diameter within 576 h simulated observation time for various simulated SNR detection thresholds (peak values per FoV crossing event), together with the related minimum object diameter (in mm) in *italic*.

GEO FoV crossing events is due to the significant differences in the density of the space debris population. Table 4.3 shows that the majority of the objects cross the FoV more than within the simulation period in the LEO case. For the subGEO and GEO most FoV crossing events are unique. The GEO case is worse than the subGEO and LEO case because of to the non-optimal phase angle conditions (the North/South pointing leads to average phase angles of 90°).

Table 4.4 shows that small-size debris objects are detected, even for the higher SNR detection threshold of four. In LEO smaller objects compared to the subGEO and GEO cases are observed for a given SNR detection threshold, due to the smaller distances to the objects. The numbers do not yet take into account a possible loss due to failed image processing or orbit determination. It is thus more interesting to assess the number of objects having crossed the FoV, for which the objects were detected, and for which the orbit determination was successful.

From Table 4.4 we calculate a rough estimate for the average detection rate. A number of 7.5 objects/hour are expected in LEO within the 400 km distance, if a SNR detection threshold of 4 is assumed. Within the 10000 km distance we calculate 47 objects/hour in LEO, 0.7 objects/hour for subGEO, and 0.3 objects/hour for GEO (North/South). The rates refer to continuous operation over a full revolution of the sensor. However, in the subGEO the Earth will be in or close to the FoV of the sensor once per revolution and thus only about half of the total mission time can be used for observations.

For optical observations the parameters that limit the detection of objects are:

- the FoV dwell time, which is equivalent to the angular velocity with respect to the FoV taking into account a path offset,
- the brightness of the background, and
- the apparent brightness of the object, determined by distance, phase angle, object diameter and albedo.

The exposure time and the instrumental noise are set to fixed values.

We first analyse the orbital elements of the objects crossing the FoV. This allows assessing the coverage of the space debris population with the proposed operation concepts. Figures 4.12 and 4.13 refer to the orbital elements output by PROOF.

The eccentricity  $e$  is shown as a function of the semi-major axis  $a$  in Fig. 4.12. A reasonable number of GEO objects are crossing the FoV in all concepts, visible as the clustered population at higher eccentricities. Both GEO concepts give similar results, the subGEO case generates additional crossings with a semi-major axis of about 40000 km– mainly objects which do not cross the FoV of the North or South pointing GEO telescope.

Fig. 4.13 shows the inclination  $i$  as a function of the right ascension of the ascending node  $\Omega$ . For the GEO concepts we may distinguish two classes of objects. The first class comprises the GEO objects with an inclination below about  $20^\circ$ . We recognise the well-known pattern in the  $i$ - $\Omega$  space (see also Fig 3.2). Due to the North- or South-pointing in the GEO operation concept, there are basically no crossing objects in very low inclination orbits. A second class of objects with  $i \approx 67^\circ$  could be traced back to MEO objects in the MASTER population with a semi-major axis between approximately 25000 and 30000 km crossing the FoV at distances below 10000 km. For LEO400 one recognises the preferred inclination bands for sun-synchronous and telecommunication satellites. This is the region where most of the small-size debris detections are expected. The graph for LEO covering long-distance observations shows a good agreement with the modeled space debris environment in LEO, the entire right ascension range is covered uniformly and selected inclination bands with higher crossing rates can be identified.

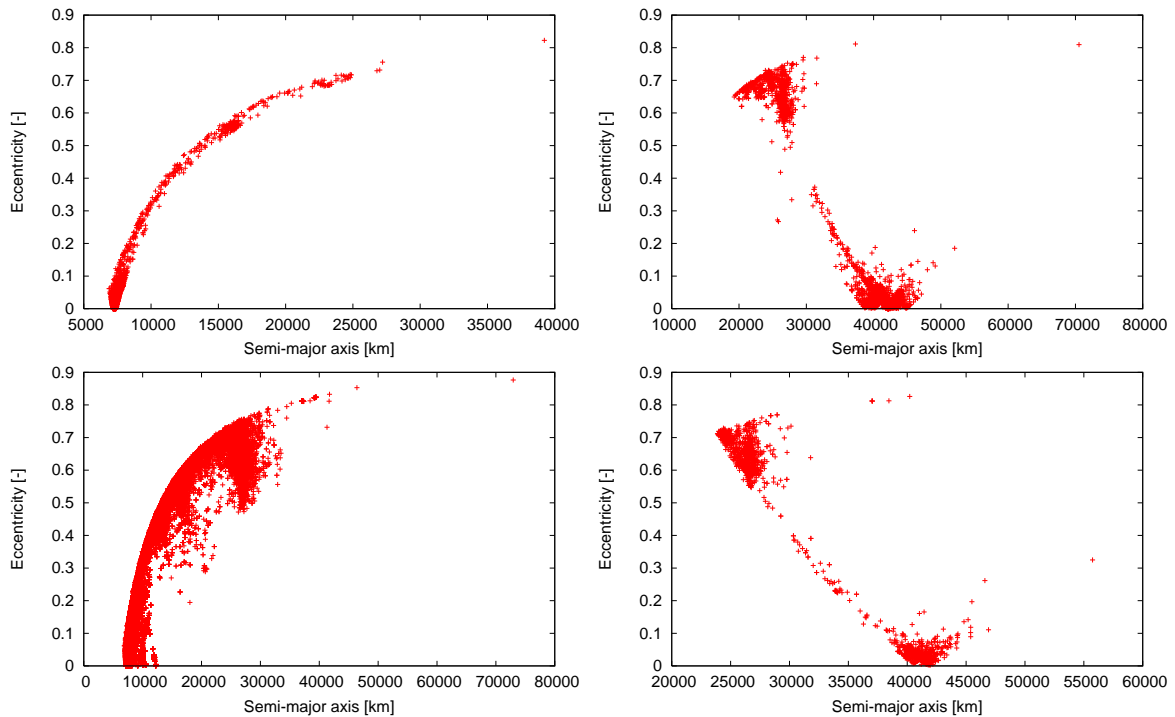


Figure 4.12: Eccentricity vs. semi-major axis for objects larger than 5 mm crossing the FoV within the 576 h simulation for LEO400 top-left, LEO bottom-left, subGEO top-right, GEO bottom-right.

#### 4.4 Application of the simulation environment to a proposed space-based optical observation scenario

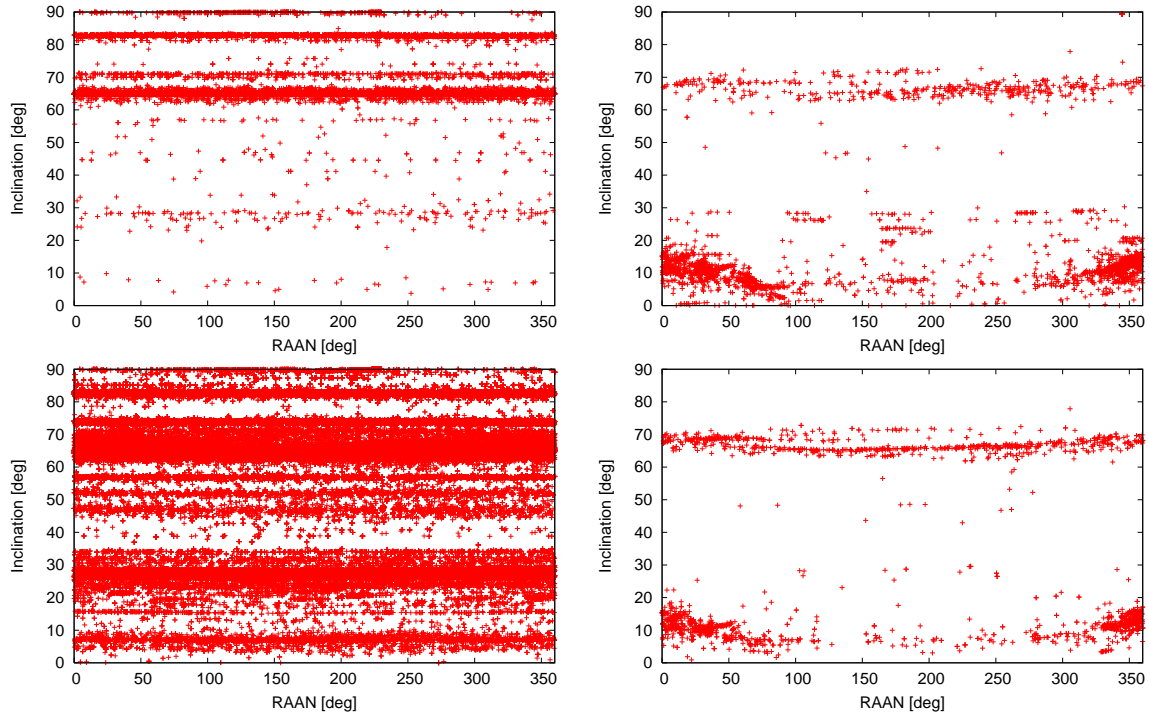


Figure 4.13: Inclination vs. right ascension for objects larger than 5 mm crossing the FoV within the 576 h simulation for LEO400 top-left, LEO bottom-left, subGEO top-right, GEO bottom-right.

Figure 4.14 compares the expected FoV dwell time for all observation concepts. This figure illustrates some of the key problems related to the orbit determination. As already pointed out, the dwell times in the LEO operation concept are very short, while in GEO dwell times of several minutes allow the observation of an arc of sufficient length. In GEO only a few short-distance FoV crossings are expected while in LEO the placement of the sensor platform into a densely populated region causes a large number of short-distance crossings. The much higher number of expected detections in LEO requires on-board data processing, and impacts the data transfer budget.

Fig. 4.15 shows the apparent brightness of the FoV-crossing objects as a function of the brightness of the sky background. We conclude that the majority of the objects are very faint. In LEO, near objects (within a distance of 400 km) are usually brighter than 15 mag, and, without limiting the distance, 5 mm objects may appear even fainter than 20 mag. The largest part of the objects in GEO appears fainter than 15 mag. Brighter objects (as bright as 0 mag in LEO or 5 mag in GEO) may cross the FoV in all cases occasionally. The instrument is designed to cope with this large dynamic range. All operation concepts allow observations where the sky background is fainter than 20 mag.

Figure 4.16 shows the phase angle variations as function of the observation epochs. A 15 day structure is due to the simulation of runs spanning 24 h. The phase angles are between  $0^\circ$  and  $60^\circ$  in LEO, irrespective of the selected distance range. In GEO the phase angle is comparably bad, always between  $50^\circ$  and  $130^\circ$ , with an average of  $90^\circ$ . Best phase angle conditions are obtained in the subGEO operation concept due to the optimum pointing in right ascension away from the Sun, keeping the phase angle below  $25^\circ$ . The phase angles show prominent seasonal variations caused by the varying declination of the Sun. In the GEO operation concepts the daily periodic variation of the phase angle is constant (about

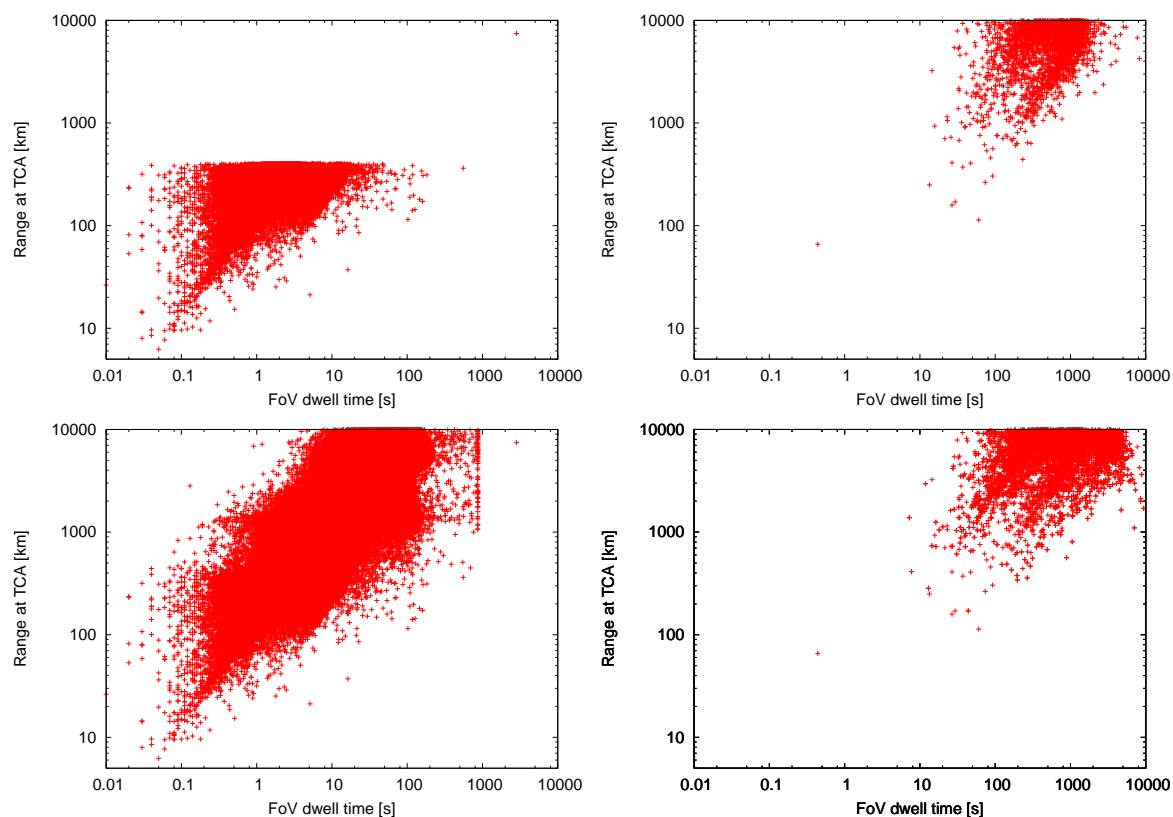


Figure 4.14: Minimum distance vs. FoV dwell time for the simulated LEO, subGEO and GEO operational concepts considering objects larger than 5 mm diameter within 576 h simulated observation time; LEO400 top-left, LEO bottom-left, subGEO top-right, GEO bottom-right.

$5^\circ$  in subGEO and  $25^\circ$  in GEO), but the 24 h average of the phase angle shows an annual variation. In LEO the daily average of the phase angle stays constant, but there is an annual variation of the daily amplitude. The variation within 24 h is narrow in spring and autumn, when the declination of the Sun is low. The largest amplitude is expected at high declinations of the Sun. The subGEO operation concept allows for optimal illumination conditions (phase angle is  $0^\circ$ ) twice a year, when the declination of the Sun equals the inclination of the SBO sensor orbit.

Finally, Fig. 4.17 gives the most important information relevant for the sensor performance – the simulated peak SNR as a function of the object diameter. The analysis reveals for a SNR detection threshold of four an average diameter of the FoV crossing objects of about 7 cm for the LEO case and about 10 cm in the two GEO operation concepts. For a given SNR detection threshold the associated diameter covers a range of about 10 cm. For a SNR of four there are detections below 1 cm in LEO and at around 2-3 cm in GEO possible, as Table 4.4 already showed.

#### 4.4.3 Performance of the image processing

A large number of test images were generated in order to evaluate the performance of the proposed SBO instrument. The images were simulated with the Image Reduction and Processing Facility (IRAF). Test

#### 4.4 Application of the simulation environment to a proposed space-based optical observation scenario

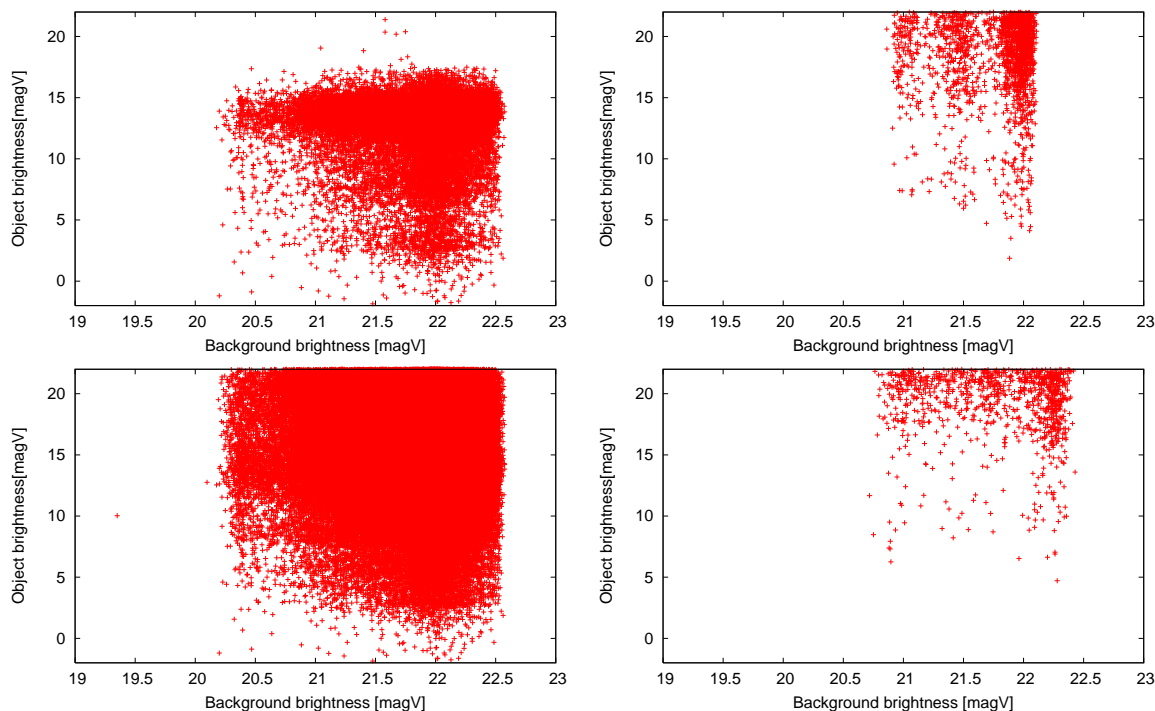


Figure 4.15: Brightness of the FoV crossing objects vs. the brightness of the sky background for all objects larger than 5 mm diameter within 576 h simulated observation time; LEO400 top-left, LEO bottom-left, subGEO top-right, GEO bottom-right.

images were simulated for the different operation concepts, the sensor architecture, and for various FoV crossing angles. The proposed algorithm for on-board object detection was applied to the test images. The SBO study concluded that the acquired images should be processed on-board using a “dynamic masking” approach with dedicated image pre-filtering processors. The resulting sub-frames containing stars and candidate debris objects (plus probably some cosmic ray events, processing artifacts, etc.) should be further processed on-ground. The necessary processing steps are centroiding, astrometric reduction, orbit determination, and estimation of the size of the objects. For the on-ground processing system it was proposed to use the border-and-fill algorithm applied in AIUB’s off-line data processing system.

A slightly modified implementation of the border-and-fill algorithm was applied in the SBO study in order to precisely discriminate object and background pixels and to determine the centroids of the star and debris objects. A comparison of the determined centroids with the input into the IRAF program system allows it to determine the SNR cut-off and to assess afterwards the accuracy of the centroiding procedure.

The astrometric error is governed by the centroiding error of star and object, and the epoch registration error. The determination of the centroid of fainter objects close to the SNR limit is of lower accuracy compared to the brighter objects. The centroiding error was therefore determined as a function of the apparent brightness. The apparent brightness is not only a function of the diameter of the objects. It also depends on the phase angle, the distance to the objects, the shape, and surface properties of the objects.

A limiting apparent brightness of the detection algorithm was found at about 15.6 mag for GEO, 15.8 mag

#### 4 Simulation environment for optical observations

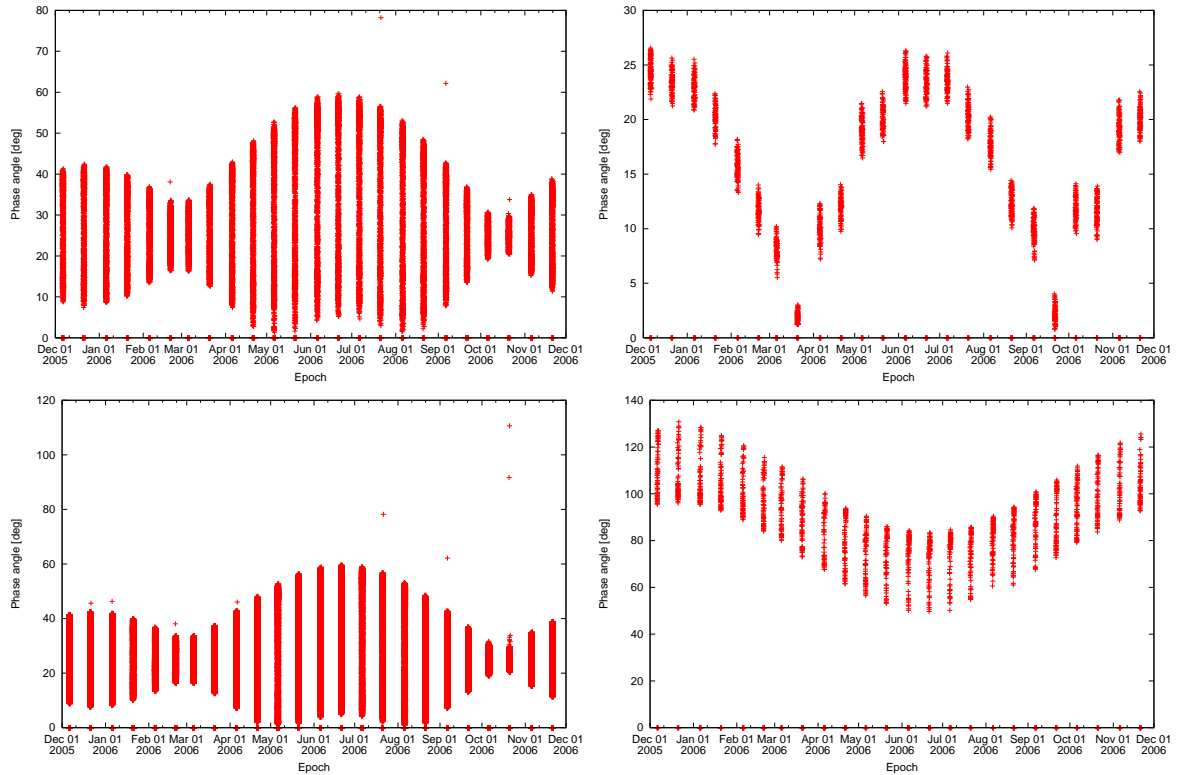


Figure 4.16: Phase angle variations as function of the observation epoch; LEO400 top-left, LEO bottom-left, subGEO top-right, GEO bottom-right.

for subGEO and 10.3 mag for LEO using the CCD detector with this approach. In the HyViSI detector, the values are 16.0 mag for GEO and subGEO and 10.6 mag for LEO. The limiting magnitude is comparable for the GEO and the subGEO operation concept; the faintest objects can be detected in these two concepts. The limiting SNR value is around four for the GEO and three for the LEO operation concepts.

Lowering the detection threshold allows the detection of fainter, and thus of smaller and more objects, but produces also a higher number of “false” detections. It is an issue of the on-board software implementation and telemetry limitations, which false detection rate may be allowed by selecting the SNR detection threshold. We assumed that 95% correct detections must be guaranteed.

Table 4.5 gives classes of the object centroiding errors in pixel coordinates ( $\Delta x$  and  $\Delta y$ ) for a wide range of apparent brightness values. The smallest errors correspond to the brightest objects, the largest errors to objects crossing the FoV at the SNR detection limit. Due to the proposed operation concepts (mainly the orbital and pointing strategies) the centroiding error covers different ranges. Table 4.5 also provides the transformation of the centroid determination error to a centroid position error using the pixel scale of the SBO. In the next section we will use the centroiding error classes while simulating position measurements as part of the orbit determination. “Error-free” position measurements are obtained from the observation geometry at the simulation epoch. The instrumental noise sources need to be addressed realistically. The centroiding accuracy derived from the image processing will be used to add normal-distributed noise to the simulated position measurements for orbit determination.

With the release of PROOF-2005 it became possible to dump the synthetic images used by PROOF in-

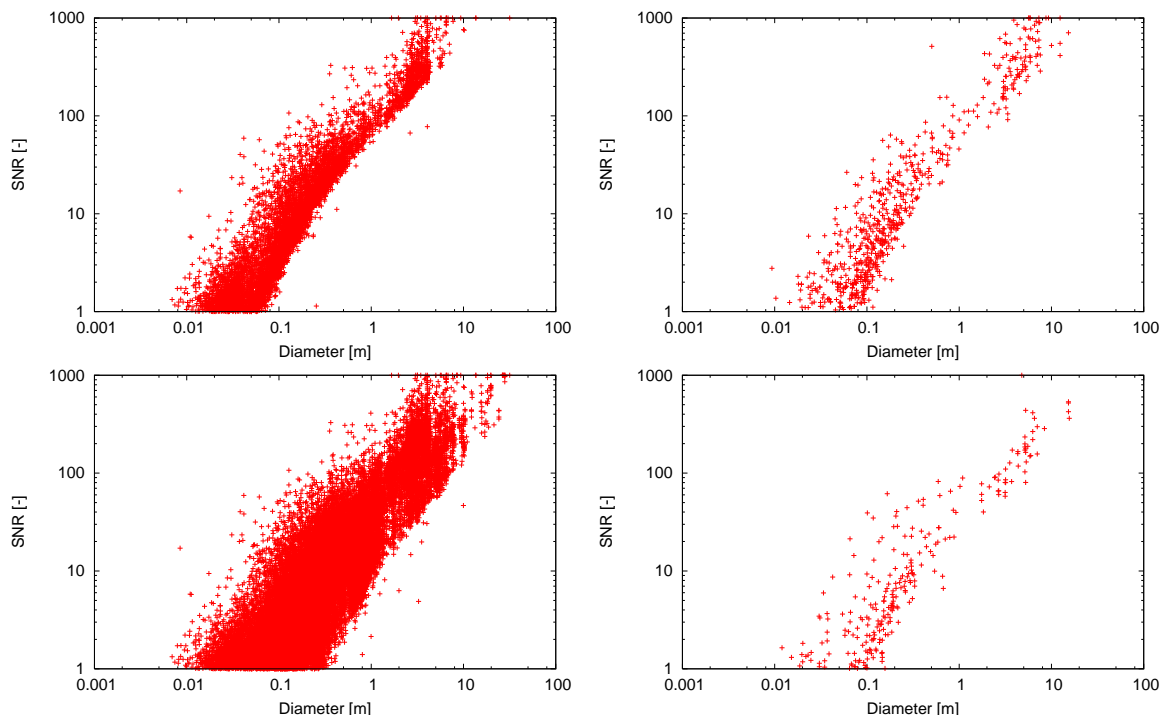


Figure 4.17: Peak SNR vs. diameter of the FoV crossing objects larger than 5 mm within the 576 h simulation for LEO400 top-left, LEO bottom-left, subGEO top-right, GEO bottom-right.

ternally. User-defined image processing algorithms may replace the PROOF built-in detection criterion, which is basically an SNR detection threshold, by means of a plug-in mechanism. As a first step we developed a conversion routine in addition to the plug-in, which exports PROOF's synthetic images in the FITS format. It is possible now to directly feed PROOF data into existing image processing facilities like IRAF or AIUB's off-line data processing system. The detailed analysis of the image processing using these synthetic PROOF images directly has to be done in the future.

#### 4.4.4 Performance of the orbit determination

To determine orbits of unknown space debris objects is the major objective of the SBO system. For the estimation of the size of the objects from the apparent brightness the distance to the objects must be known. The distance is computed from the determined orbits of the objects and the sensor orbit. Both, the (at least statistical) knowledge of the orbital elements and the size of the objects, are required as input to space debris population models.

The simulation is based on PROOF output. ORBDET was adapted to support space-based platforms and the output of the observation geometry from the PROOF tool. PROOF provides via the plug-in the observation geometry for the simulated exposure epochs, the arrays containing the pixel coordinates, the object and star signals, and the background signal. The data combines the epoch, the position of the sensor, and the position and velocity of the observed object. Unfortunately, it is not possible to trace the output observation geometry back to the simulated FoV crossing characteristics. This missing functionality of the PROOF plug-in would be needed to assign directly a specific astrometric error as

	Apparent brightness [mag]	$\Delta x, \Delta y$ [pix]	Centroiding error ["]
LEO	Brightest objects	0.15	1.98
	<8.5	0.4	5.2
	<9.5	0.6	7.9
	<10.5	1.2	16.0
subGEO	Brightest objects	0.01	0.13
	<14.5	0.1	1.3
	<15	0.2	2.6
	<15.5	0.3	3.9
	<16	0.4	5.2
GEO	Brightest objects	0.01	0.13
	<11	0.03	0.4
	<12	0.1	1.3
	<14.5	0.4	5.2
	<16	1.2	16.0

Table 4.5: Centroiding accuracies (after the astrometric reduction step in the on-ground processing) in pixel units and maximum corresponding position error in arc seconds, assuming a SBO pixel scale of  $9.041''/\text{pixel}$ .

a function of the simulated brightness and FoV crossing velocity to the orbit determination. SIMOBS processes the data from PROOF, and generates astrometric observations (pairs of right ascension and declination of the object centroids) for all epochs. Noise that reflects the astrometric error and the error in the determination of the sensor position is added.

We consider all FoV crossing objects in the simulation of the orbit determination, irrespective of their FoV crossing characteristics. We will ignore in particular, whether the SNR allows for a detection or not. This approach allows us to discuss the performance of the orbit determination with a larger number of events. We combine the results of orbit determination with the results from simulating the image processing and the characteristics of the FoV crossing.

In the IOD we make use of all available observations of a crossing event. We obtain a two-body orbit. In the simulations we use a search range of  $50 \text{ km} < \rho < 12000 \text{ km}$  with a step size of 15 km for both algorithms, BNBNDV and BBN2D.

The SBO study concluded that it is possible to use HyViSI detectors for epoch registration with millisecond accuracy. It is therefore assumed that the contributions from the epoch registration accuracy to the overall error budget are contained in the considered astrometric error. No epoch registration error was added to the simulated observations. The astrometric error was included as a function of apparent brightness (Table 4.5). Four classes in LEO, and five classes in the subGEO and GEO are considered in the simulation of the orbit determination.

The position of satellites can be determined without special means to better than 2 m in LEO, and 10 m in GEO. This is why a random normally distributed noise with a  $1-\sigma$  error of 10 m in each of the 3 axes in subGEO and GEO operation concept, and of 2 m in LEO, was added to the position of the observing platform.

Let us now discuss the results of orbit determination for the subset of the PROOF data consisting of 24 h of observations on June 12, 2006.

#### 4.4 Application of the simulation environment to a proposed space-based optical observation scenario

---

Orbits were determined from 38572 FoV crossing events in the LEO concept, 510 events in the subGEO concept and 293 events in the GEO concept. With the assumption of a 1 s image acquisition spacing about 10% of the FoV-crossing events in LEO do not give enough observations. In the case of determining a circular orbit this applies only to about 2% of the events. Circular orbit determination was only considered for the LEO. In the GEO and subGEO basically all events give a sufficient number of observations for a full orbit determination.

Orbit determination was not always successful. The determined first orbit may not be good enough as input for the orbit improvement step. The number of failures increases with the astrometric error of the position measurements. BNB2D is more successful in determining first orbits than BNBNDV. BNB2D successfully treats about 90% of the cases in all three concepts considered. This is attributed to the exclusion of hyperbolic orbits prior to orbit improvement. BNBNDV succeeds for about 50% in LEO and about 80% in subGEO and GEO.

All successful orbit determinations may be characterised and classified according to the achieved accuracy by comparing the determined orbital elements to the “true” elements provided by PROOF.

The definition of the acceptance criteria is crucial. For our simulation, we accept an orbit, if the difference between “true” and “determined” is smaller than

- 500 km in the semi-major axis  $a$ , 0.05 in eccentricity  $e$ ,  $5^\circ$  in inclination  $i$ , and  $5^\circ$  in right ascension of the ascending node  $\Omega$  (in the LEO case), or
- 1000 km in semi-major axis  $a$ , 0.1 in eccentricity  $e$ ,  $2^\circ$  in inclination  $i$ , and  $2^\circ$  in right ascension of the ascending node  $\Omega$  (in the subGEO and GEO case).

A detailed analysis of the orbits which were not accepted showed that mostly the highly eccentric orbits ( $e > 0.3$ ) were difficult to determine. As these orbits are not of primary interest for the SBO system (the focus is on small objects in LEO and GEO and thus more on low-eccentricity orbits), we may exclude these objects after orbit determination. A simple perigee/apogee height criterion using the determined perigee and apogee values turned out to be suitable for first tests.

The a posteriori filters had the following characteristics:

- Minimum perigee height of 6500 km and maximum apogee height of 15000 km in LEO,
- Minimum perigee height of 30000 km and maximum apogee height of 60000 km in subGEO and GEO.

A test was carried out to ensure that the proposed filter criteria do not exclude “poorly determined, but interesting objects”. We compared the filtering of the PROOF results (our “truth”) to the filtering of the ORBDET output. Only about 1-2% of the objects were erroneously excluded (7 out of 390 in subGEO in the worst case, 1 out of 178 in GEO in the worst case). Due to the shorter passes in LEO the number of erroneously excluded objects is much higher, up to 30%. Thus the filtering in LEO is not reliable.

The IOD from the short observed arcs must be considered as difficult. Figures A.1 to A.3 in Appendix A show the results of the comparison between “true” and determined orbital elements for the a posteriori filtered successful IODs. The value 100% refers to all successful IODs. We may conclude from the figures that in all cases, and for all used algorithms, the performance of orbit determination only

slightly degrades with an increasing astrometric error. This fact implies that orbits of faint objects can be determined with almost the same quality as orbits of bright objects.

The determination of a circular orbit is much more reliable than the determination of an orbit using either one of the boundary value approaches in the LEO. The right ascension of the ascending node  $\Omega$  is only weakly determined. The determination of  $a$ ,  $e$ , and  $i$  is acceptable in about 50% of the successful IODs.

In the subGEO case the BNBNDV algorithm fails to find the correct minima, yielding a bad performance. The BNBNDV algorithm is capable of determining the shape of the orbit ( $a$ ,  $e$ ) in about 90% of the successful IODs and the orientation of the orbital plane ( $i$ ,  $\Omega$ ) in about 70% of the successful IODs.

The results in the GEO show a comparable and good quality for both algorithms, BNBNDV and BNBNDV. The shape of the orbit ( $a$ ,  $e$ ) is better determined than the orientation of the orbit ( $i$ ,  $\Omega$ ). The determination of the shape is accepted in 70-90% of the successful IODs, while the orientation of the orbit is accepted only in 50-60%. BNBNDV gives slightly better results for the fainter objects than BNBNDV, but the total number of successful IODs is higher for the BNBNDV algorithm.

With the BNBNDV algorithm the shape of the orbit can be determined with acceptable accuracy in most of the cases where IOD was successful. The determination of the orientation of the orbital plane with the assumed accuracy of  $2^\circ$  mostly succeeds in the subGEO, and succeeds in the GEO in about 50% of the cases. The determination of a full-parameter orbit in the LEO is difficult. But with the determination of circular orbits (an assumption simplifying the IOD) the shape of an orbit can be determined meeting our acceptance criterion in more than 50% of the successful IODs. The determination of the orientation of the orbits in LEO is difficult due to the very short arcs (in the order of seconds) and is thus not very reliable.

We furthermore conclude that the RMS criterion is not sufficient to qualify the accuracy of the determined orbits. In subGEO and GEO the astrometric accuracy of the position measurements does only slightly impact the quality of the determined orbit. The determined orbits of fainter objects are of a comparable accuracy with these of the brighter objects. In LEO there are often not enough observations available for an orbit determination.

#### 4.4.5 Combination of the performance simulation results

The combination of the result from the PROOF analysis with the simulation results for image processing and orbit determination gives an estimate for the number and characteristics of objects for which we may determine orbits.

We start with the application of the detection threshold (peak SNR) as filtering criterion to the list of crossing objects for 576 h of simulated observations. Merging the resulting lists of “objects above the detection threshold” with the results of the simulated orbit determination (percentage of successful IODs and percentage of accepted IODs) leads to an approximate number of determined orbits. By adding margin to these percentages we take into account that the orbit determination of fainter objects is slightly more difficult. We do not assume a correlation between apparent brightness of a particular object and the orbit determination. We present the statistics for 24 h of observations, neglecting that in subGEO observations are not possible throughout the entire revolution of the sensor, and that in all cases probably some observation time is dedicated to calibration. The number of objects is given for different ranges of object diameters.

	<b>LEO</b>	<b>subGEO</b>	<b>GEO</b>
Accepted determination of $(a,e)$	500-600	12-13	4-6
Accepted determination of $(i,\Omega)$	200-300	10-12	3
Fraction of 'accepted' objects	1% <5 cm	3% <5 cm	1% <5 cm
	5% <10 cm	12% <5 cm	5% <5 cm
		41% <20 cm	26% <20 cm

Table 4.6: Number of objects per day for which the initial orbit determination meets the acceptance criteria.

	<b>LEO</b>	<b>subGEO</b>	<b>GEO</b>	<b>TIRA</b>	<b>ESA 1-m tel.</b>
Min. detected diameter [cm]	0.8	2.3	3.4	2.1@1000 km	$\approx 15$ @GEO
Detections 2 -10 cm per day	25-30	1.5-1.6	0.2-0.3	$\approx 400$	0
Sensor operation	24 h/d	>12 h/d	24 h/d	24 h/year	$\approx 120$ h/month
Orbit determination results	Circular	Full	Full	Circular	Circular/Full
Tracking/follow-up capability	No	No	No	Yes(*)	Yes

Table 4.7: Capabilities of the SBO compared to existing ground-based sensors ((\*): stare and chase for TIRA.)

The number of position measurements provided by the image-processing algorithms is an important assumption in the combination. The wide range of processing issues (star occultations, extended background sources, streak length, ratio between peak and average signal, selected detector readout approach, adjustment of the centroiding algorithm, etc.) is not covered here. We simply assume that, if the peak SNR is larger than our estimated value, any FoV crossing event would allow it to perform the full image processing, resulting in the acquisition of the necessary number of measurements for orbit determination. Already small improvements in the SNR detection threshold would, however, lead to a higher number of detected objects.

Table 4.6 shows the results of the combination of the performance simulation results. The estimate of the number of objects for which the orbit determination meets the acceptance criteria is provided, as well. We use these data as input to Table 4.7, where we summarise the capabilities of the SBO system and compare them to the capabilities of existing ground-based systems. In LEO ground-based radars are theoretically superior, but due to their limited availability a space-based system could still contribute significantly to the monitoring of the LEO space debris environment. At geostationary altitude (or 1000 km below) the proposed SBO system is clearly exceeding the capabilities of 1-m telescopes on ground. The SBO would improve the knowledge concerning space debris by decreasing the minimum object size from about 15 cm to below 5 cm.

## 4.5 Conclusions

In this chapter we have introduced an end-to-end simulation environment connecting ORBDET of the CelMech Program System to PROOF via a measurement simulator. Different approaches for IOD in ORBDET were discussed. The capabilities of an alternative formulation of the boundary value method are discussed in detail for ground- and space-based scenarios. This algorithm requires three astrometric observations, is highly flexible, and easy to implement, supports observations from different sites and

space-based observations, is free of assumptions, and can initialise a subsequent orbit improvement step based on all available observations. The choice of appropriate observation scenarios is crucial for IOD. The length of the arc covered by observations matters for determining an initial orbit, which is critical for LEO orbits, where a determination of a circular orbit with subsequent orbit improvement is a viable alternative.

The simulation environment is used to assess the capabilities of a proposed space-based optical observation scenario. The evaluation involves analysis of the characteristics of the FoV crossing objects, estimation of the limitations of the image processing based on simulated images, and first orbit determination and orbit improvement based on simulated orbits. The detection of small-size space debris (smaller than 10 cm in diameter) is possible using the sensor architecture and operation scenario proposed in the ESA-study “Space-Based Optical Observation of Space Debris” for the three proposed operation concepts, LEO, subGEO and GEO. In LEO the highest detection rate is expected; small-size space debris objects are mostly observed with sufficiently high SNR at short distances. The proposed operation concepts provide dark sky background conditions better than 20 mag. Seasonal variations in the detection efficiency are expected due to varying phase angles. Best phase angle conditions result for the subGEO operation concept, fair conditions for the LEO operation concept, and moderate phase angle conditions for the GEO observation concept. First orbits with an acceptable accuracy for statistical assessment of the space debris population can be determined from a single FoV crossing event in all three concepts, but not for all detections. Ranges for the number of successful orbit determinations within 24 h are given assuming different astrometric errors. From the determined orbits of unknown objects, the object diameter can be determined using the observed apparent brightness. We conclude that the proposed instrument if placed in the LEO would significantly contribute to the monitoring of the space debris environment; placed at GEO altitude the instrument could decrease the current minimum of the observed object diameter to below 5 cm. The instrument would allow it to improve the knowledge about the uncatalogued small-size space debris population in LEO and GEO by using a relatively simple and straightforward instrument design and processing strategy.

## 5. Ground-based optical observation strategies

In this chapter we will discuss and propose ground-based optical observation strategies, including well established and new ones. Based on the assessment of the GEO and MEO population in Sect. 3.2 we first analyse the evolution of the population (Sect. 5.1). This analysis is complemented by a discussion of the accessibility of the population to ground-based sensors (Sect. 5.2). Afterwards we propose and classify ground-based observation strategies for GEO and MEO in Sect. 5.3. The classification scheme considers performance related aspects, such as the achievable re-acquisition rate of a particular object, the estimated orbit determination accuracy, and the covered fraction of a population. We also estimate the minimally detectable object diameter for a particular sensor architecture, considering uncatalogued, as well as catalogued objects.

### 5.1 Population evolution

The long-term evolution of the GEO population is widely discussed in the literature (see, e.g., Beutler (2005); Hugentobler (1998)). We already revisited the key issues of the orbital dynamics in Sect. 3.2.3. The long-term evolution of the MEO population is not so well addressed, and we analyse it in more detail in this section.

For the definition of observation strategies it is interesting to know how many objects are added to a population and how many drop out in a certain time period. About 25 objects are launched into GEO each year (Flohrer et al., 2011b), which adds spacecraft, upper stages, and mission-related objects to the population. Fragmentation debris exists in GEO, as well. Two fragmentation events are known to have occurred in GEO, and more are suspected to have happened (see Sect. 3.2.3). As no natural forces remove objects from the GEO region, the population will grow. For small fragments with high area-to-mass ratio ( $A/M > 1\text{m}^2/\text{kg}$ ) the growth in eccentricity may induce a decay from GEO, because the perigee will be lowered into the LEO region where the atmospheric drag dominates. For the definition of observation strategies it is important to note that for such high-area-to-mass ratio objects the motion of the orbit pole may be more rapid. The amplitude of the periodic variations of the inclination can grow up to  $\approx 50^\circ$  (Anselmo and Pardini, 2005).

Defining efficient MEO survey strategies implies the discussion of the long-term evolution of orbits in MEO. This discussion has to take into account long periodic and short periodic variations. Both, gravitational and non-gravitational perturbations need to be considered. Resonance effects dominate the long periodic variations, mainly due to the low degree and order terms of the gravitational field.

Beutler et al. (1998) compare the effects of the various kinds of perturbations by the corresponding accelerations and by orbit determination from 1 and 3 day arcs. Relevant accelerations acting on satellites

Table 5.1: Relevant accelerations acting on a GPS-like satellite in MEO (modified from (Beutler, 2005)).

Perturbation	Acceleration [m/s <sup>2</sup> ]	Orbit error after one day (radial/along- track/out-of-plane) [m]
Main term	0.57	$\infty$
Oblateness ( $C_{20}$ )	$5.1 \times 10^{-5}$	2750 / 32000 / 15000
Moon's gravity	$4.5 \times 10^{-6}$	400 / 1800 / 30
Sun's gravity	$2 \times 10^{-6}$	200 / 1200 / 400
Earth's gravity (higher degree terms)	$4.2 \times 10^{-7}$	60 / 440 / 10
Solar radiation pressure (for GPS)	$9.7 \times 10^{-8}$	75 / 180 / 5

in MEO are contained in Table 5.1 together with the results from the orbit determination over a 1 day arc using equally spaced Cartesian coordinates of the satellite positions as pseudo observations. For MEOs the dominating perturbations apart from the oblateness and luni-solar perturbations are due to the Earth's gravity potential and solar radiation pressure. No natural forces will remove objects from the MEO region within centuries. For space surveillance strategies the short periodic variations are of lesser interest.

Table 5.1 shows for GPS-like satellites that the oblateness term  $C_{20}$  is the dominating term for short-periodic effects. The semi-major axis oscillates within periods of  $P_i = P_{sat}/i; i = 1, 2$ , where  $P_{sat}$  is the revolution period of the satellite. The eccentricity does not grow substantially, if the initial eccentricity is small. This is the case for most of the MEO objects. The ascending rotates in the clockwise direction. Only for GPS satellites the inclination grows, showing semi-annual and semi-monthly variations, as well as short-periodic variations due to resonance effects. For the same reason variations of the argument of perigee and the mean anomaly are highly correlated and show short-periodic variations in case of circular GPS orbits. These resonance effects in the GPS orbits, caused by the deep 2:1 resonance of the satellites' revolution period with Earth rotation ( $2P_{sat} = 1$  sidereal day), require frequent (about once per year) along-track manoeuvres to keep the satellites at their nominal position within the orbital plane. Hugentobler (1998) covers resonance phenomena of GPS orbits with the Earth's gravitational field and finds  $C_{32}$ ,  $C_{44}$ ,  $C_{22}$  and  $C_{52}$  to be the main contributors to resonance effects. This implies that there is a dependency on the (geographical) longitude of the satellite while passing the equator, so that not all satellites in one orbital plane see the same perturbation signals.

The stability of MEOs was assessed recently by Chao and Gick (2004); Jenkin and Gick (2001); Beutler (2005); Deleflie et al. (2011). Beutler (2005) sees an increase in eccentricity for GPS satellites of up to 0.008, but only small changes in inclination and semi-major axis within 20 years after decommissioning (without applied disposal measures). Chao and Gick (2004) looked at the long-term evolution of the eccentricity of abandoned satellites of the GPS, GLONASS and the future GALILEO constellations. For a 200-year integration, the solar radiation pressure was considered to be the dominating perturbation effect. The eccentricity may grow up to 0.7 within 150 years, an effect caused by resonance perturbations due to  $C_{20}$  and lunisolar perturbations (Deleflie et al., 2011). The effect depends on the object's altitude and inclination. This long-term eccentricity growth would make it possible that objects in MEO have their apogee in GEO and the perigee in LEO after about 50 years. GLONASS satellites will start crossing

Table 5.2: Summary of the assessed population evolution in MEO.

	Eccentricity (30 years)	Motion of node	Inclination variation
GPS	up to 0.08	-11°/year (Block-I)	60° – 66°, 35 years period (Block I)
	(in 50 years up to 0.16)	-14°/year (Block-II)	50° – 58°, 30 years period (Block II)
GLONASS	up to 0.015	-12°/year	63° – 67°, 35 years period
Galileo	0.01 (for higher A/m)	-12°/year	53° – 60°, 45 years period

GPS orbits after about 40 years.

Jenkin and Gick (2001) investigated the stability of MEO disposal orbits. Currently proposed disposal orbits are not necessarily stable, because the eccentricity may grow significantly. In consequence this leads to a collision risk with the active GNSS constellations. Finally, collisions in MEO may happen and hence the number of debris objects in MEO might rise. Up to now, despite several survey activities are ongoing (Rumyantsev et al., 2010; Dick et al., 2009; Hinze, 2011), no fragmentation events have been found in MEO.

The number of launches into the upper MEO is difficult to predict, as the dominating GNSS constellations are subject to strong political funding constraints. The recent strong variations in the launching activities reflect the (re-)building of operational GNSS constellations. In view of the concrete European and Chinese plans we may assume that the current number of about 10 launches per year might be a minimum.

In order to study the evolution of reference objects in MEO we used the orbit propagation capabilities of the program SATORB contained in the CelMech program system (Beutler, 2005). The software was slightly adapted to match the requirements of a long-term propagation. We used the initial values of real objects of the GPS and GLONASS population and simulated initial values for Galileo satellites.

Table 5.2 summarises the results of this experiment. Figure 5.1 illustrates the results for the GPS population. The analysis of the simulation results shows that (as expected from the  $C_{20}$  perturbation) the motion of the node is maximal with -14°/year for GPS-like objects. While the MEO population is still arranged in rather small nodal bands reflecting the GPS and GLONASS constellation design, uncontrolled MEO objects will start covering the entire range of ascending nodes due to small differences in the individual nodal drift rates. Therefore the definition of space surveillance strategies needs to consider the complete range of right ascension of ascending nodes. A serious issue becomes obvious in the analysis of the simulation results. All orbits in the MEO show a long-term growth of the eccentricity, with eccentricity reaching up to 0.08 within the next 30 years or 0.16 within the next 50 years. This effect has maximal effect for the oldest GPS satellites (Block I), which today already have an eccentricity of about 0.03. It needs to be noted that the considered  $A/m$ -ratio of 0.1 kg/m<sup>2</sup> is rather high for operational satellites. It is also possible that during decommissioning the  $A/m$ -ratio may become intentionally lowered. Jehn et al. (2009) show that end-of-life operations in place now move the GPS satellites out of the 2:1 resonance.

## 5.2 Accessibility of population

The possible observation time at a given site is a common constraint to all optical observations, independent of the targeted population. This quantity is subject to strong seasonal variations and varies with

latitude. Figure 5.2 gives the average night time as a function of the geographical latitude and considers different twilight conditions:

- Sun entirely below the horizon: this is the case for elevation angles of  $-0.5^\circ$
- *Civil twilight* for the Sun below the horizon and elevation angles below  $-6^\circ$
- *Nautical twilight* following the civil twilight and for elevation angles below  $-12^\circ$
- *Astronomical twilight* following the nautical twilight and for elevation angles below  $-18^\circ$

For optical observations of space objects it is sufficient to meet the nautical twilight condition. From Fig. 5.2 we see that at up to  $30^\circ$  site latitude the variation of the average nautical night is marginal compared with the maximum annual observation time of  $\approx 10$  h that can be obtained at the equator. For sites higher than  $\approx 45^\circ$  latitude the possible observation time drops drastically and reaches the minimum between about  $60^\circ$  and  $80^\circ$ .

Figure 5.3 shows the average nautical nighttime during one year as a function of the geographical latitude. For medium latitude (including European sites) at about  $50^\circ$  nautical nights can be as short as 4 h around the summer solstice, but also can be more than 13 h in the winter. For sites higher than  $55^\circ$  latitude the astronomical twilight may not be reached every night, and hence no observations will be possible during such nights. For a GEO observing site at  $30^\circ$  latitude the nautical night varies between 8 h and 12 h, which is why the annual variations of the possible observation time may set significant limitations.

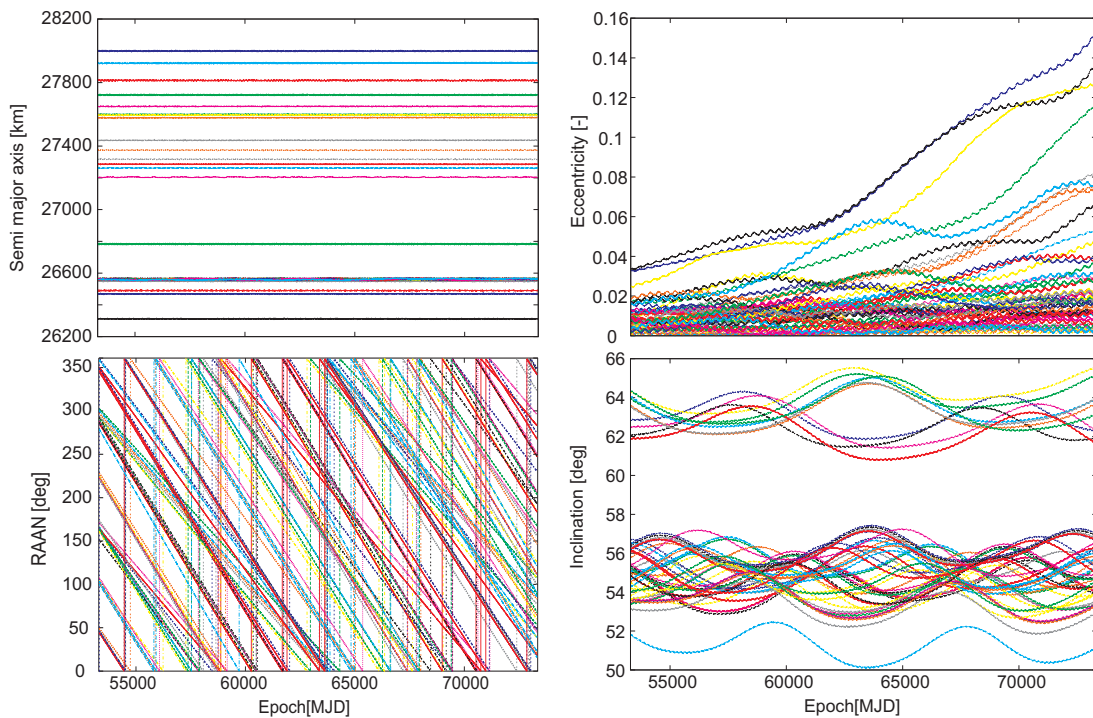


Figure 5.1: Long-term evolution of the GPS population from 2005 to 2059, from a numerical propagation considering luni-solar perturbations, the Earth's gravity field up to degree and order 30, Earth tides, general relativity, and the direct solar radiation pressure for an  $A/m$ -ratio of  $0.1 \text{ kg/m}^2$ .

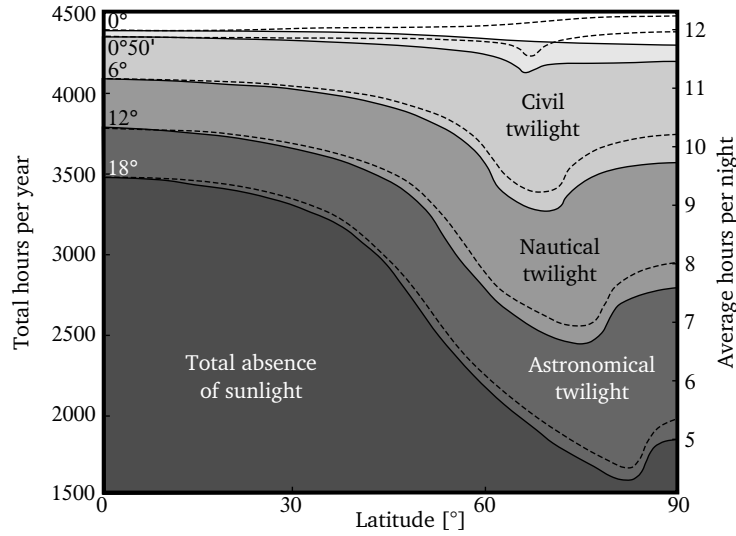


Figure 5.2: Average night time for different twilight conditions as a function of site latitude, with Northern hemisphere as solid lines and Southern hemisphere as dashed lines. Modified from (Taff, 1981).

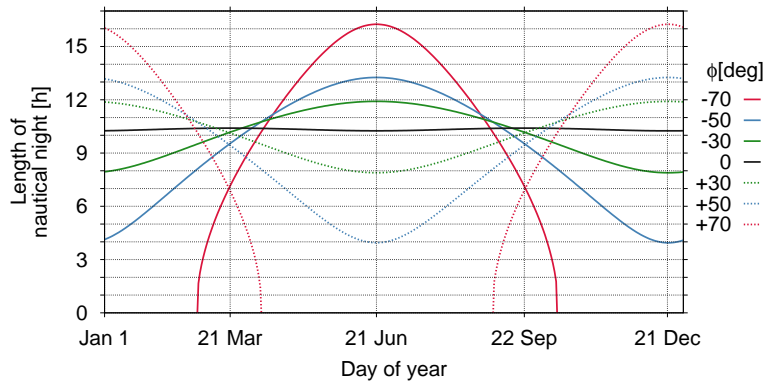


Figure 5.3: Variation of the length of the nautical night (time between nautical dusk and dawn) as function of the site's geographical latitude  $\phi$ . Solid lines refer to Northern, dashed lines to Southern latitudes. Calculations are based on Seidelmann (1992).

Apart from the available observation time, the geometrical accessibility of the objects from a given site is an issue. We discuss this separately for the GEO and MEO regime.

### 5.2.1 GEO

The accessible fraction of the GEO region is a function of the site's latitude and of the applied elevation mask. Figure 5.4 shows that at medium latitudes and low elevation masks it is possible to access a sufficient longitude range. Ignoring refraction, typically  $120^\circ$  in longitude can be covered with an elevation

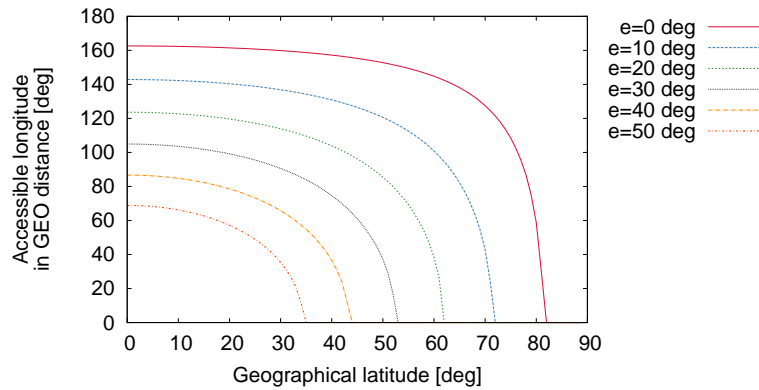


Figure 5.4: Accessible longitude range for objects at GEO distance at declination of  $0^\circ$  as a function of the geographical latitude for various elevation cut-off angles  $e$ .

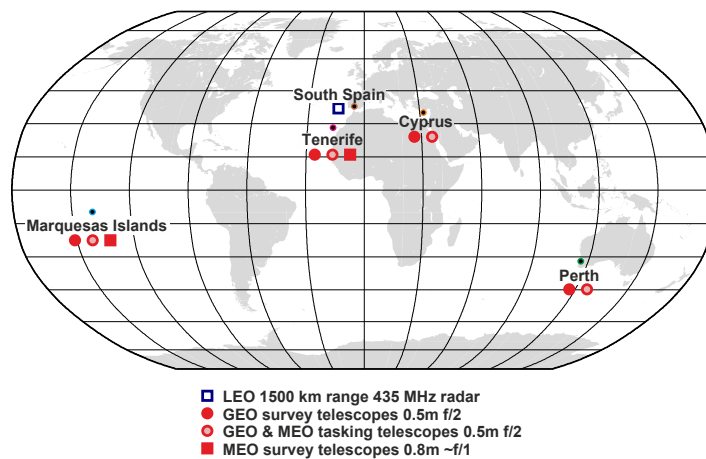


Figure 5.5: Ground-based infrastructure proposed for a European space surveillance system, modified from (Donath et al., 2005).

cut-off angle of  $20^\circ$  from latitudes below  $20^\circ$ . The elevation mask is directly proportional to longitude coverage gain. Lowering the elevation cut-off mask by  $10^\circ$  roughly relates to a gain in longitude coverage of  $20^\circ$ .

Full access to the GEO region requires a network of geographically well distributed sites. For the site selection also non-technical issues, as, e.g., accessibility, political issues, and the weather conditions are important factors. The site selection process is rather cumbersome. For our discussion we make use of the proposal for a European space surveillance system (Donath et al., 2005). Figure 5.5 presents the proposed network. Optical observation sites are proposed to be located at (approximate coordinates):

- Marquesas Islands, a French overseas collectivity in the Southern Pacific Ocean ( $\phi = -9.80^\circ$ ,  $\lambda = -139.03^\circ$ ),

- Tenerife, Canary Islands, Spain, ( $\phi = +28.18^\circ$ ,  $\lambda = -16.30^\circ$ ),
- Cyprus in the Eastern Mediterranean ( $\phi = +35.0^\circ$ ,  $\lambda = +33.0^\circ$ ),
- Perth, Western Australia ( $\phi = -32.0^\circ$ ,  $\lambda = +115.0^\circ$ ).

Figure 5.6 gives the accessibility of objects at GEO distance as function of the elevation mask for this sensor network. Zimmerwald has been added for comparison. For the low declination angles of GEO objects the proposed sensor network of 4 sites at low latitudes allows complete coverage for elevation masks below  $20^\circ$  and nearly complete coverage for higher elevation cut-off angles with only small gaps over the Americas and the Western Pacific.

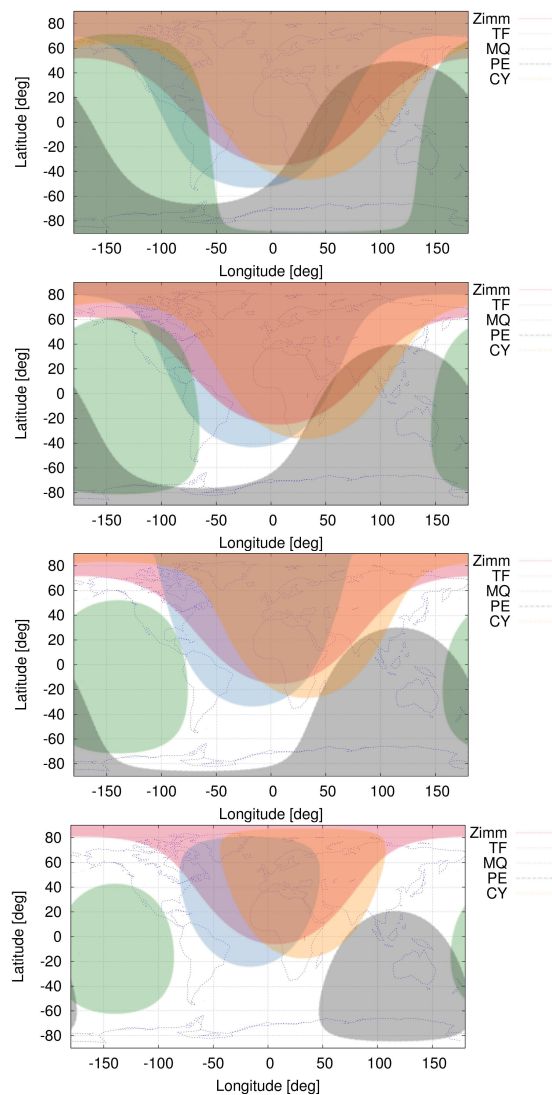


Figure 5.6: Coverage map for objects at GEO distance for different elevation angles in  $10^\circ$  steps, top:  $e = 0^\circ$  bottom:  $e = 30^\circ$ .

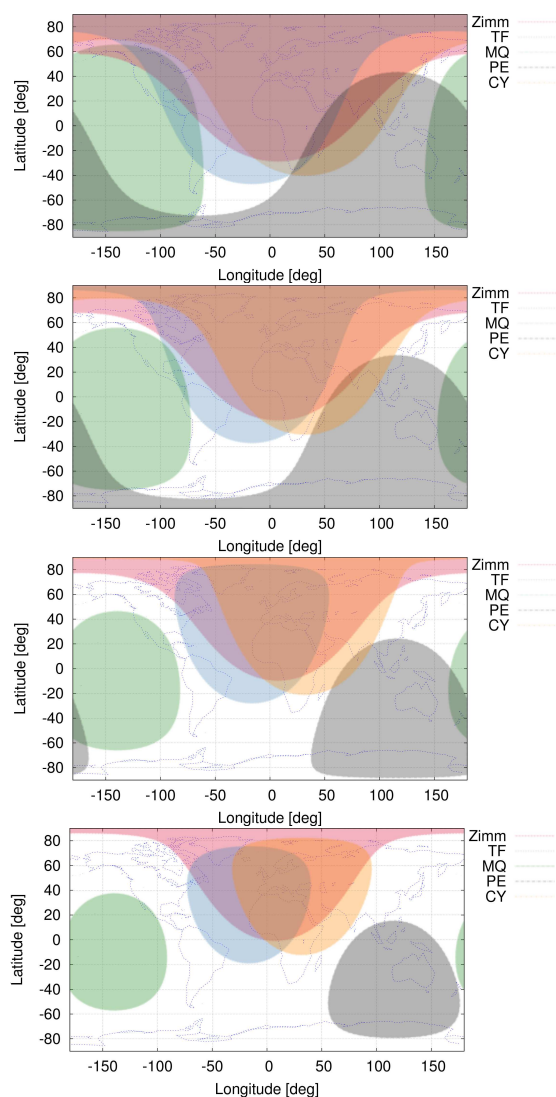


Figure 5.7: Coverage map for objects at typical MEO geocentric distance of 25000 km for different elevation angles in  $10^\circ$  steps, top:  $e = 0^\circ$  bottom:  $e = 30^\circ$ .

## 5.2.2 MEO

Due to their relatively high inclinations MEO objects are observable in wider declination bands. For the proposed sensor network the accessibility of objects at a typical distance of 25000 km is given in Fig. 5.7. Coverage gaps are visible for objects at higher latitude in a band from North America to North-East Asia, and in the Southern Atlantic Ocean.

## 5.3 Proposed observation strategies

This section is based on work and studies carried out for a proposal for an European space surveillance system (Donath et al., 2005, 2008). Special attention is at the definition of the optical part of the system (Flohrer et al., 2005b; Schildknecht et al., 2005). The proposed strategy and a performance estimation for GEO space surveillance are reported in summary by Flohrer et al. (2005b). MEO space surveillance is discussed in more detail in subsequent work by Flohrer et al. (2008b). In both cases small objects or objects with extreme area-to-mass-ratios ( $A/m$ ) in high altitudes (Schildknecht, 2007) are not considered in the proposal. The analysis considers objects larger than 1 m in diameter with a “classical” area-to-mass ratio.

We clarify the essence of observation strategies and introduce fundamentals for the classification and evaluation of optical observation strategies (Sect. 5.3.1) before we discuss observing the GEO and MEO region in Sects. 5.3.2 and 5.3.3, respectively. We use the PROOF tool as part of our simulation environment, as well as for the discussion of the sensor performance, mainly focusing on the evaluation of the minimally detectable object diameter. For the statistical mode we use the following options of PROOF (relevant options listed only, if changed from the default settings):

- No geometric prefilter, maximum of 50000 statistical objects,
- no Monte Carlo run,
- Node and perigee of object orbits left unchanged (i.e., not propagated),
- 10° elevation cut-off angle,
- 400 simulation steps per crossing,
- Diameter of objects limited to 10 cm – 100 m,
- Observation distance range 5000 – 60000 km.

For the discussion of the catalogue coverage we always assume (if not stated differently) that observations can be acquired every night for 8 hours. This in turns means that we have not taken into account any outage time, such as bad weather or sensor unavailability, during the simulation. For the image acquisition strategy we assume that initial orbit determination must be possible from consecutive observations of the same object that are linked together for the FoV dwell time.

### 5.3.1 Fundamentals for classification and evaluation of observation strategies

An observation strategy combines all relevant information for the planning and execution of data acquisition tasks. It shall therefore name the target population of objects in terms of orbital parameters and physical size. Furthermore the required network architecture and sensor system need to be specified. Finally, the strategy shall describe which data shall be acquired.

Unfortunately, there is no single “full-coverage” criterion allowing it to compare different observation strategies directly. At the first level we have to distinguish between geometric and radiometric criterion. From geometric criteria we can assess which objects of a given population are in principle accessible. By comparing with sensor locations the geometry may dictate the selection of possible sensors. The

radiometric criteria allows it to decide, which of these accessible objects a given sensor can actually detect. Only the combination of geometric plus radiometric parameters allows the complete evaluation of observation strategies. It is also important to note that the criteria are connected and show mutual dependencies. A simple top-down process for the derivation of an optimal observation strategy cannot be formulated.

From simulating the dynamics of a reference population we derive these geometric criteria a suitable observation strategy has to meet (typical values and limits):

- Angular velocity of a single object w.r.t. a sensor, and, as a derivation, the dwell time in a (normalised) FoV for possible tracking scenarios, and depending on pointing directions,
- Observation distances,
- Phase angle.

From distance and phase angle we can estimate the first radiometric criterion, and the typical, as well as minimum, and maximum object magnitudes. The angular velocity and the tracking scheme are the two central issues for the estimation of the length of the streaks in an exposure. The streak length is closely related to the achievable astrometric accuracy, and to the SNR (Sect. 3.3.2.5).

The covered population, expressed as the fraction of a reference population, can be determined by simulations considering these geometric and radiometric criteria. The covered population usually is analysed as a function of accessible orbital regimes.

From the simulations we can derive other geometric criteria, such as, most importantly, the achievable re-acquisition period, either given for a single sensor site, or applicable to the entire network. To determine the observation frequency for catalogue maintenance the achievable orbit determination accuracy results from orbit determinations based on simulations is required, among other criteria. Orbit determination and catalogue maintenance form the essential input for the evaluation of catalogue correlation and the catalogue maintenance performance. Some prototyped approaches were discussed by (Flohrer et al., 2005a; Musci et al., 2005). The robustness of an observation strategy can also be obtained from these simulations, if certain elements, such as sensors or network capabilities, are disabled, or adverse weather conditions, which do not allow it to acquire observations.

The minimal detectable object diameter, which is the final radiometric criteria is independent of the criteria reflecting the orbit determination and cataloguing processes.

We will continue the evaluation by introducing some fundamental terms describing observation strategies. If we search for objects or object parameters without having a priori information available, we denote this task with the term “survey”. Acquiring observations with having a priori orbit information is called a “follow-up” task. Follow-ups are closely related to scheduling or tasking a specific sensor resource to carry out observations. Following-up needs an active control instance to request and monitor, installed either directly at the sensor site, or remotely at a central site. Surveys not necessarily need direct control capabilities. It is possible that a sensor runs a given survey pattern autonomously without connection to a scheduler.

Typical surveys provide very short arcs, i.e., short series of consecutive observations. This is due to limits of the current sensor technology, which makes it technically impossible to have any combination of FoV and aperture diameters. In particular, the desired design of telescopes with large aperture and wide FoV is challenging, but it is the most interesting design for surveys. If the observation strategy requires a

certain minimum object diameter and the radiometry sets the aperture, the limitations of the possible FoV diameter must be accepted. The resulting short arcs are then caused by the fact that survey patterns aim to cover large areas and have to ensure frequent re-coverage of these larger areas. In addition the number of sensors is limited for budgetary and complexity reasons.

From the observed arcs acquired by surveys it is not possible to determine full six-parameter orbits with the accuracy that is needed for cataloguing. Additional observations are required to improve the accuracy of the determined orbit. Two options are at hand to achieve this: the acquisition of sufficient follow-ups (combined survey and follow-up), and the acquisition of the observations during surveys (survey only). In any case a survey is needed as an initial step.

A “survey only” ensures the acquisition of the necessary number of observations in order to improve the determined orbit. A “survey only” might be seen sufficient for all cataloguing tasks, if the observation frequency meets the requirements for catalogue maintenance, and if covariance information associated with the short arcs allows for a successful and unambiguous correlation. “Survey and follow-up”, or “survey and chase” has been introduced by Musci et al. (2005); Flohrer et al. (2008b); Abercromby et al. (2009).

In every case either surveys from co-located telescopes, surveys from distributed sites, or single telescope surveys are possible. Schildknecht et al. (2009) introduced some basics of such options for the MEO region.

We will now discuss proposals for observation strategies for the “survey only” and the “combined survey and follow-up” for both, GEO and MEO space surveillance.

## 5.3.2 GEO

### 5.3.2.1 Observational characteristics

Previous studies have extensively studied the observational characteristics of the GEO population (see Sect. 3.2.3). The next paragraphs briefly reviews the results of these studies (Schildknecht et al., 2004b).

**Angular velocities** Objects controlled in longitude and inclination do not move in an Earth-fixed frame. All other objects move with respect to the GEO with varying velocities. The minimum velocity is around the culmination. Looking at the GEO region (GEO  $\pm 2000$  km altitude) the apparent velocity for a typical site such as Tenerife reaches up to  $1.2''/s$  for objects in low inclination orbits and  $4.5''/s$  for objects in high inclination orbits when these objects cross the equator.

Correspondingly, the apparent angular velocity in the inertial frame is about  $15''/s$  for controlled GEO objects. For drifting objects this velocity is between about  $13''/s$  and  $16''/s$ . At the culmination points and for high inclination the difference to the nominal  $15''/s$  reaches a maximum.

The drift rate becomes important for the visibility assessments (Schildknecht et al., 2004b), as it is directly proportional to the difference  $\Delta a$  of the semi major axis w.r.t. the GEO with  $a=42164$  km, and is approximately  $\Delta n$  [ $^{\circ}/\text{day}$ ]= $0.0128 \Delta a$ [km]. Therefore, we expect that the most rapidly drifting objects meeting the GEO definition may return into visibility within 14 days. If  $\Delta a$  is smaller, the return interval is longer. For  $\Delta a=200$  km the interval is already 140 days, and such an object is visible during 44 consecutive days for a  $20^{\circ}$  elevation cut-off angle.

For slowly drifting or librating objects GEO catalogue maintenance with ground-based means requires geographically distributed sensors.

**Dwell times** As the orbits of objects in GEO have low inclinations, they cross a FoV more or less on a straight line (see Sect. 3.2.3). The dwell time in the FoV for observations with an Earth-fixed sensor may be infinite for controlled objects, but may drop to about 10 minutes (OGS) or about 40 minutes (for a  $3^\circ$  FoV) for maximum angular velocity. If inertial observation schemes are used, the nominal GEO object will have a dwell time of 2.8 minutes (OGS) or 12 minutes ( $3^\circ$  FoV) only. For drifting objects the dwell time lies between 2.5 and 3.2 minutes (OGS) and 10.9 and 13.3 minutes ( $3^\circ$  FoV).

**Observation distance** The possible topocentric distance of objects in the GEO region ( $\text{GEO} \pm 2000$  km altitude) mainly depends on the accessible longitude, which is a function of the applied elevation mask, the sites' latitude, and the object's declination. Figure 5.8 gives an estimate of the possible distances for the lower and upper boundary of the GEO region. The minimum distance is obviously found around the local meridian. For the lower and upper altitude limit the distance lies between 34000 km and 38000 km. For high latitudes and typical longitude coverages of  $120^\circ$  (corresponding to a typical elevation mask of  $20^\circ$ ) the maximum topocentric observation distance is up to 43000 km.

**Phase angles** For GEO observations the phase angle may differ substantially, from nearly optimal phase angles close to  $0^\circ$  to very large ones for observations close to the setting Sun. Twice per year around the equinoxes we find periods where the Earth shadow is in GEO. Schildknecht et al. (2004b) show that the parallax-corrected angular dimension of the Earth's core shadow in the GEO is roughly  $9.8^\circ$  ( $10.2^\circ$  for the penumbra), implying that for small phase angles the objects might be in the (core) shadow. For small phase angles specular reflection (flares) of controlled GEO satellites are possible, and may frequently occur around the equinoxes (the so-called eclipsing periods).

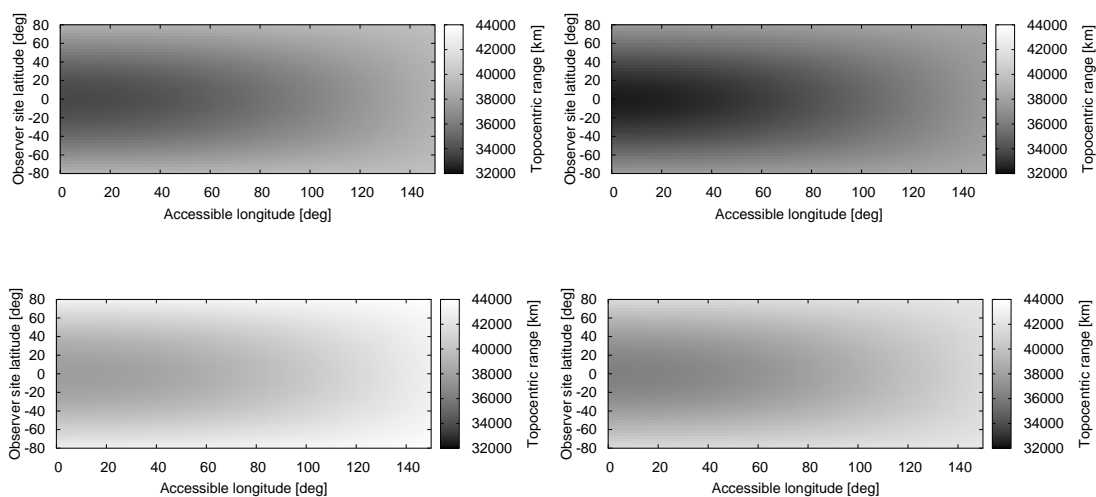


Figure 5.8: Topocentric distance to satellites as a function of the accessible longitude range, site's latitude for GEO objects at a geocentric distance of 40164 km (top) and 44164 km (bottom), with declination of  $0^\circ$  (left) and  $15^\circ$  (right).

In the case of fixed inertial pointing an observation strategy can be easily defined, which ensures an optimal phase-angle.

**Object brightness** The distribution of the apparent magnitudes of objects in Sect. 3.3.2.6 and in Fig. 3.15 shows that for a 1 m spherical object with a Bond albedo of 0.1 at the typical GEO observation distances between 34000 km and 43000 km we expect an apparent magnitude between 15.5 ( $0^\circ$  phase angle) and 17 ( $90^\circ$  phase angle).

### 5.3.2.2 Considerations for simulations of GEO observation strategies

In general, we distinguish between strategies for single and multiple telescopes, and for the multiple telescopes between strategies for single sites and distributed telescopes.

As proposed by Donath et al. (2005), we consider two types of optical sensors for the simulation of GEO operations: a 1 m aperture system and a 50 cm aperture system. The sensor network was already introduced in Sect. 5.2.1 and ensures an almost complete accessibility of the GEO region.

Four main issues describe the performance of a space surveillance system for GEO objects:

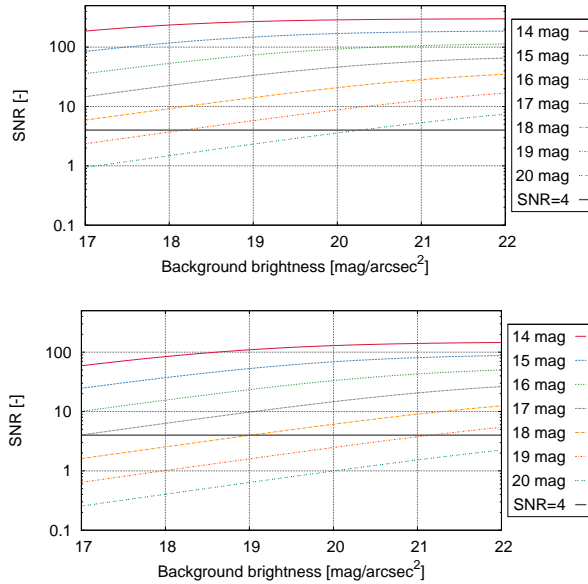
1. The performance of the optical sensors itself, ideally resulting in an estimation of the minimally detectable object diameters under various conditions. The individual sensor performance can be evaluated using the ESA PROOF tool (see Sect. 4.1), or through analytical models as introduced in Sect. 3.3.2.5.
2. For the defined survey strategy (basically the search for uncatalogued objects and for new events) the performance can be estimated using the PROOF tool, as well. For this purpose a TLE catalogue provides a reference population of objects. This approach implicitly assumes that the estimated coverage of an existing and known population of objects is also valid for the discussion of a general survey performance of any unknown population.
3. The follow-up strategy has to be discussed using the assessed survey performance. The follow-up strategy describes the necessary observations of uncatalogued objects – to allow for the determination of a first orbit, and to maintain a catalogue.
4. The correlation of observations with the catalogue and the maintenance of the catalogue need to be described and checked for feasibility.

We will assess the performance of the 1 m and 0.5 m sensor proposals using the parameters in Table 5.3. Figure 5.9 shows the SNR for various object magnitudes as a function of the background brightness. As “detected” we denote all objects crossing the FoV with a SNR above four, which allows for the object detection and centroiding. It is assumed that the velocity of the crossing object is  $5''/s$  which implies the necessity of a (blind) tracking of the objects during the exposure. Considering typical background brightness (see Sect. 3.3.2.5) and the brightness-size relations introduced in Sect. 3.3.2.6 we conclude that with each of the considered instruments the detection of 1 m objects in the GEO region is possible, even under non-optimal conditions.

The minimally detectable object diameter is also directly obtained from the PROOF simulations using the ESA MASTER population of space debris objects. The simulation is limited to objects crossing between 30,000 and 60,000km altitude in order to save computing time.

Table 5.3: Preliminary system architecture used in performance estimation.

Instrument	1 m	0.5 m
Aperture (m)	1.0	0.5
FoV ( $^{\circ}$ )	1.2	3.0
Number of pixels (-)	2048	2048
Pixel size ( $\mu\text{m}$ )	13.5	13.5
Pixel scale ( $''/\text{pixel}$ )	2.1	5.27
FWHM (pixel)	0.8	0.8
Exposure time (s)	2.0	2.0
Gap time (s)	5	5
Readout noise (e-/pixel)	10	10
Dark current noise (e-/s/pixel)	0.05	0.05
SNR threshold for detection (-)	4	4
Peak efficiency with optics	0.64	0.63

Figure 5.9: SNR as a function of the background brightness for varying object brightness for the 1 m telescope (left) and the 0.5 m telescope (right), as defined in Table 5.3, for a velocity of  $5''/\text{s}$ .

A space surveillance sensor must allow it to observe every night, if weather conditions permit. Even observations during full Moon phases and under other adverse observation conditions must be considered. This is why Fig. 5.10 gives the FoV-crossing and detected objects for observations carried out around full and new Moon. The 1 m and 0.5 m telescopes were simulated to perform a survey based on the strategy described in the next section. For the full Moon run, the start epoch was set to 2003 Sep 23, for the new Moon run to 2003 Dec 03. For each night an observation duration of 8 h, centred around local midnight, was simulated. Both telescopes were assumed to be located at Tenerife.

The results for the 0.5 m telescope confirm that detections of 1 m objects at GEO are possible. Under bad

observation conditions 1 m is the minimally detectable object diameter, while detections down to 50 cm (at some occasions down to 30 cm) are fairly possible under better conditions. For the 1 m telescope the performance is significantly better than for the 0.5 m telescope. Detections of uncatalogued objects down to 25 cm diameter would be possible.

### 5.3.2.3 Proposed strategies

In this section we will look into possible observation strategies and assess the resulting catalogue coverage, the reacquisition periods, the orbit determination accuracy, and the minimal detectable object diameter.

**Survey** Schildknecht et al. (1999) presented a strategy for the search for space debris. The work of Schildknecht et al. (1999) is also the basis for the GEO survey strategy of the Inter-Agency Space Debris Coordination Committee (IADC) (Africano et al., 2000) applied to the coordinated GEO observation campaigns. We adapt this GEO survey strategy for space surveillance to meet the specific space surveillance requirements, such as the continuous coverage of all known and new objects in the entire GEO ring (Flohrer et al., 2005b).

It is the fundamental assumption of the proposed survey strategy for observing GEO objects that – with a mean motion in the vicinity of 1 revolution/day – all objects will appear at a given right ascension once in about 24 h. It would be sufficient to observe a particular stripe in right ascension continuously. Due to the rotation of the Earth, a single site cannot observe this stripe for 24 h. A network of sites may, however, meet this condition if the sensor sites are distributed more or less equally in longitude. As GEO objects orbit in a limited inclination band, it is sufficient to cover the corresponding geocentric declination range only (as between  $-17^\circ$  and  $+17^\circ$ ). Due to the limited inclination band, all objects cross the FoV of a ground-based sensor in a more or less uniform manner in terms of both, crossing direction and crossing velocity.

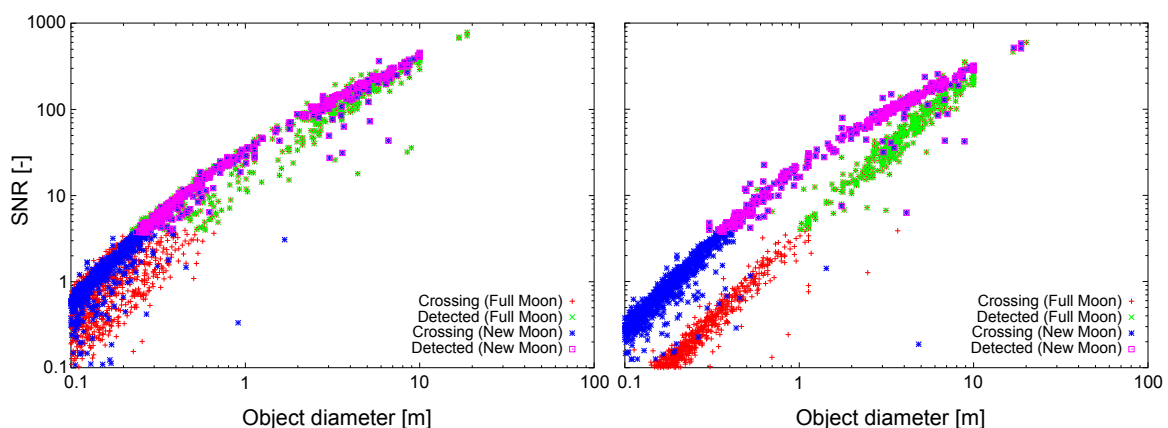


Figure 5.10: SNR of crossing and detected objects as a function of the object diameter from PROOF simulations for the 1 m telescope (left) and the 0.5 m telescope (right), as defined in Table 5.3. The one-stripe survey strategy was simulated (see Sect. 5.3.2.3).

As Fig. 3.7 suggests, we cannot expect uniform distribution of objects over the declination range. While the densest region is around  $0^\circ$  declination, where the inclination-controlled satellites are, the perturbation effects lead to a precession of the nodes of the orbital planes, which in turn yields characteristic density patterns. It would be wrong, however, to limit *ab initio* the covered declination range to a subset, as this would mean introducing a selection effect (a blind spot). It is recommended to cover the entire range.

It is not required to cover instantaneously the entire declination range. This allows to increase the efficiency of the search strategy. Musci et al. (2004) show that for maintaining the catalogue it is sufficient to observe each object once every 15 days, depending on the required orbit accuracy and on the characteristics of the used sensors. Requirements concerning the timeliness of detecting manoeuvres or fragmentation events may justify a higher re-acquisition rate. From the considerations of Musci et al. (2004) the declination band can be divided into equally sized fields along the declination range. Each of the fields has to be observed for 24 uninterrupted hours once within 15 days. Nearly all objects in the GEO ring will be observed at least once within this time span. Only objects rapidly drifting in longitude may escape detection. The size of the fields corresponds to the FoV of the telescopes, allowing for some (e.g., 10%) overlap. The right ascension of the fields is chosen so that the fields cross the meridian at local midnight, but avoid the shadow. In that way the observed objects are opposite to the Sun at an optimised phase angle, and the right ascension of the observed stripe will change during the year due to the revolution of the Earth around the Sun.

For operational considerations it is helpful to imagine that the respective field rises in the evening in the East and is observed during the entire night and sets in the West in the morning. The next telescope hopefully starts to observe the same field now.

During the observations every  $n$  seconds an exposure of the field will be acquired and will be used to form a short arc. Up to six single observations are needed to form the short arc. For initial orbit determination primarily the length of the short arc matters. This implies that in case the time span between two consecutive image acquisitions is long enough, another field may be observed in parallel. This time span depends mainly on the FoV dwell time of the objects (and therefore on the size of the FoV), the slew rate and settling times of the telescope that define the time interval between observing the parallel fields. The latter, however, is not critical, if nearby fields are selected. Even a shorter revisit time of less than 15 days is possible for larger FoV diameters. For the 0.5 m telescopes used by Flohrer et al. (2005b), the survey of two fields in parallel was proposed, leading to a stripe-scanning time of 7 days. The telescope capabilities and dwell times limit the maximum number of parallel fields. It may thus be impossible to cover the entire declination band within 15 days with a narrow FoV sensor. In such cases more telescopes need to be collocated at the site and the observation tasks need to be distributed among them in such a way that essentially a larger synthetic FoV can be formed.

Let us now estimate the number of fields, which must be observed in parallel. We assume 15-day blocks with 8 observation hours per night and site. The availability of the sensors is mainly limited by weather conditions. For the considered network we expect an availability between 51% and 74%. This leads to a total of 212 h of observation time for three sites (Tenerife, Marquesas Islands, Perth) and 301 h for four sites (Tenerife, Marquesas Islands, Perth, Cyprus). From the sensor specifications we estimate the time needed for the acquisition of one image (repositioning, settling and read-out) to 5 s. For a coarse first-level assessment, it is sufficient to assume that objects and observation sites are distributed equally in longitude.

If the FoV is smaller than  $2.3^\circ$  ( $34^\circ$  declination range divided by 15 days), more than one field has to be observed in parallel. In this case the observation strategy based on the 1 m telescope with two

Table 5.4: Catalogue coverage, number of objects crossing the FoV and being detected uniquely (one short arc generated) and several times (at least two short arcs, possibly by different sensors). Observing two fields in parallel is assumed (TF-Tenerife, PE-Perth, CY-Cyprus, MQ-Marquesas Islands).

Considered sites	Sensor type	Observation duration	Crossing/detected uniquely	Crossing/detected multiple	Crossing/detected total (%)
TF/PE/MQ	0.5 m	8 h	399 / 469	293 / 140	87.3 / 76.8
TF/PE/MQ	0.5 m	12 h	400 / 531	388 / 155	99.4 / 86.5
TF/PE/MQ	1 m	8 h	596 / 590	78 / 23	85.0 / 77.3
TF/PE/MQ	1 m	12 h	602 / 665	181 / 38	98.7 / 88.7
TF/CY/PE/MQ	0.5 m	8 h	295 / 409	463 / 299	95.6 / 89.3
TF/CY/PE/MQ	0.5 m	12 h	177 / 343	611 / 392	99.4 / 92.7
TF/CY/PE/MQ	1 m	8 h	475 / 515	273 / 197	94.3 / 89.8
TF/CY/PE/MQ	1 m	12 h	289 / 415	494 / 336	98.7 / 94.7

fields observed in parallel allows only 5% of overlap. Observing three fields in parallel is recommended to increase the overlap percentage. For the 0.5 m telescope a more comfortable overlap of 20% may be achieved without parallel field observations. With these assumptions, the survey of one stripe can be performed within 13 days, or, with two fields in parallel, within 7 days. In general, such a shorter revisit time is desirable in order to increase the repetition rate for a given field. With a higher repetition rate, a better coverage of rapidly drifting objects is possible and the redundancy is increased. The 0.5 m telescopes with the wide FoV are the preferred solution as they allow to avoid the complex observation scenarios based on parallel fields. They may return short arcs combining a higher number of single observations into a longer arc. The resulting sensor requirements concerning the slew rate are considered as not demanding.

Incorporation of already existing telescopes into the network cannot be recommended. All telescopes under European control (see Sect. 2.5.1.5) only provide a narrow FoV, resulting in a low survey efficiency. For complexity reasons identical telescopes at all sites promise synergies.

We now use the PROOF tool to validate the overall coverage of an existing GEO reference population. We use the settings introduced initially in this section. We simulate the outlined survey strategy considering two fields in parallel for December 2003. We use a TLE population extracted from ESA's DISCOS containing in total 793 objects. The simulation considers two cases: a nominal 8 h observation time per site and a maximum case of 12 h observation time per site, both centred around local midnight. Note that 12h surveys are not always possible throughout the year.

The number of crossing and detected objects for each individual sensor are listed in Table 5.4. "Multiples" are these objects, which were observed by more than one site or within more than one field. On the other hand, "uniques" refers to these objects, which were observed by only one site and within one field. The results show that, obviously, Cyprus closes a prominent coverage gap. The remaining coverage gap of 5% in the case of 8 h observation per site most likely results from the still existing smaller coverage gaps, which are closed in the case of 12 h of observation per site. Table 5.4 also allows identifying the improvements of using the wide FoV 0.5 m sensors. With these telescopes the number of multiples is significantly higher due to the better overlap between neighbouring fields. There is no significant difference in the overall catalogue coverage between the 0.5 m sensor and the 1 m telescope solutions – but the total scanning time in case of uninterrupted execution of the proposed strategy with the 0.5 m sensors

is only about half of the scanning time needed with the 1 m sensors.

Table 5.4 shows that some objects remain undetected crossing the FoV. This is mostly due to unfavourable background conditions during twilight. The distribution of missed objects in longitude must be discussed to validate the mentioned coverage gaps. The rapidly drifting objects (faster than  $5^\circ$  /day) are filtered out from the list of missed objects. Figure 5.11 shows the missed crossings and detections as a function of longitude. We conclude from this figure that indeed the missed events are highly correlated with the coverage gaps. While the coverage gaps for a 8 h observation time per site are nearly identical to these corresponding to a  $20^\circ$  elevation mask, observing 12 h per site allows it to cover a specific field from rising to setting. A  $10^\circ$  elevation limit is applied in Fig. 5.11. It is interesting to note that the Perth site has a comparatively bad detection performance, due to the short nights in December rendering it impossible to schedule 12 h observation sessions.

A more detailed analysis of the results shows that the highest crossing rates appear right in the middle of the survey cycle, when, as expected, the region around  $0^\circ$  declination is observed. As a consequence objects with a wider band of inclinations are accessible and the peak crossing rate is roughly 50 objects/h for the wide-FoV telescopes. The PROOF simulations also confirm that objects with diameters larger than 1 m are always brighter than 17 mag.

We conclude that the proposed survey strategy is sufficient for the GEO part of the proposed space surveillance system. It is important to point out that the survey uses the totally available observation time of the sensors. Consequently, there is no time left to perform any tasked observations with a dedicated survey telescope.

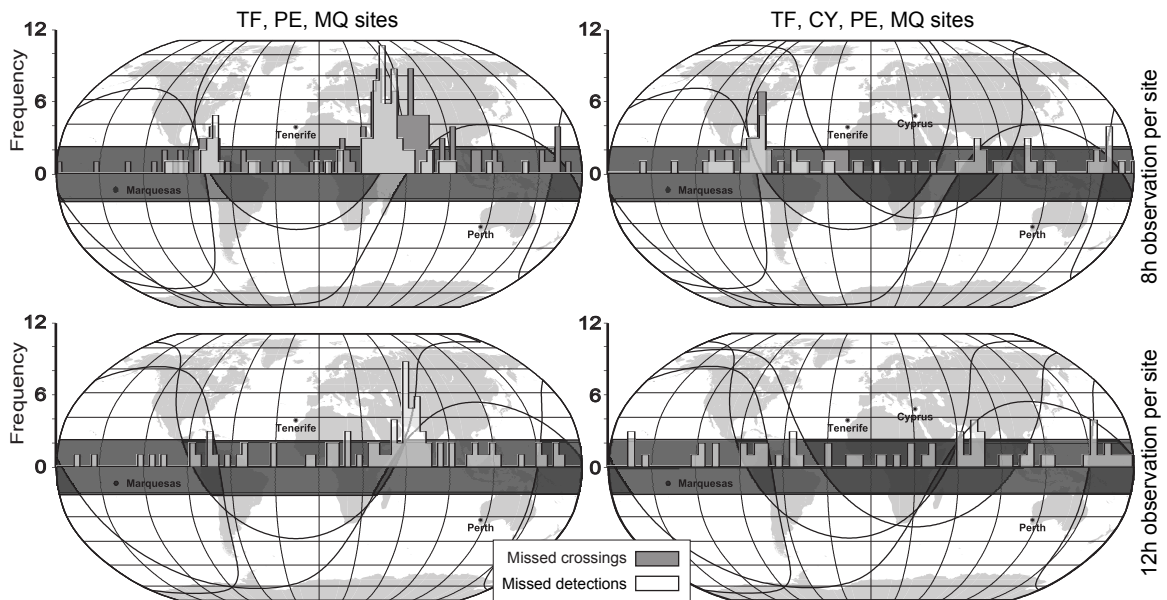


Figure 5.11: Number of missed crossings and detections per  $4^\circ$  longitude bins. The coverage map for GEO distances is included, as well. A network of 0.5 m sensors has been assumed. Fast drifters ( $>5^\circ$  /day in longitude) have been filtered out.

**Follow-up strategy** Follow-up observations are required to re-observe specific objects for catalogue maintenance and to acquire the necessary observations of newly detected objects. In the latter case newly detected objects must be observed at defined epochs to determine orbits of sufficient quality for insertion into a catalogue. After catalogue build-up catalogue maintenance is the main driver for following up objects in high altitudes.

Data requests from event monitoring, collision avoidance, or searching for lost objects are other drivers for scheduling follow-up observations. A typical follow-up request thus includes at least, for a specific site and epoch, the propagated position (right ascension and declination) of an object (Flohrer et al., 2007b). The resulting observation strategy is simple: the telescope is positioned and the necessary amount of exposures is acquired. It might be possible to observe more than one object in parallel. The covered angular distances in this case are, however, mostly larger than for the survey strategy, and longer short arcs can be generated. As the distribution of the pointing directions is random, the performance estimation for the follow-up strategy depends to a great extent on the slew rate of the telescopes.

The necessary tasking observations for maintaining the whole catalogue allows to estimate the hours needed for the tasked observations. For this short estimation of the follow-up performances we start with the operational experience at Zimmerwald, which shows for follow-up observations a mean angular distance between objects of roughly  $60^\circ$ . The minimum time period between two observations of the same object is assumed to be 30 s. This value ensures that the resulting short arc is not too short for orbit computation. A short arc should contain at least 6 observations, as for the survey observations. The total sensor time needed for the acquisition of one image is assumed to be 5 s. We assume a catalogue sizes containing 900 objects and (for future epochs) 1500 objects. Equally spaced objects and sites in the longitude are assumed.

The assessment shows that for slew rates below  $5^\circ/\text{s}$  there is no time gain if more than one follow-up request is executed in parallel. More time is spent in slewing the telescope. For a slew rate of  $1^\circ/\text{s}$  the optimum performance is achieved when only one object is observed. Then 54 h (900 objects in catalogue) or 90 h (1500 objects) are needed. For a slew rate of  $10^\circ/\text{s}$  time may be gained: 40 h, 23 h, or only 17 h are needed to cover the catalogue of 900 objects (1, 2, 3 objects in parallel). For the 1500 objects catalogue the corresponding numbers are 67 h, 38 h and 28 h.

We conclude that the necessary tasking observations could be carried out with the proposed system during within 15 days. Only if the possible slew rate of the telescopes is higher than  $5^\circ/\text{s}$ , it is beneficial to observe up to three objects in parallel. The remaining telescope time can be used to support the survey system, or for performing other tasks.

**Survey only strategy** A “survey only” strategy requires no dedicated follow-up observations for the catalogue build-up. In addition, the follow-up observations for the maintenance of the catalogue are avoided by acquiring these observations implicitly, i.e. during regular surveys. Typically, space surveillance radars observing the LEO follow this strategy. In principle, such a strategy may be chosen for GEO space surveillance based on optical sensors, too. The time needed to scan the whole GEO region must, however, be sufficiently short. The required orbit accuracy for allowing reacquisition after several days or weeks (typical period) cannot be achieved from orbits determined from a single crossing event. As a first approximation, the time needed to re-observe a specific object is a function of the FoV diameter. The FoV diameter of optical sensors is limited, and, compared to surveillance radars, very narrow. This leads to two major consequences:

1. The observed arcs of an object are very short and no full (six-parameter) orbit of the required accuracy can be determined. Using follow-ups to improve the orbits and to maintain the catalogue requires the correlation of several short arcs. It is demanding (and sometimes it proved to be impossible) to unambiguously associate these short arcs to a single object. Therefore, any “survey only” strategy requires more computational resources than the alternative scheduling of dedicated follow-up observations.
2. Detecting manoeuvres of controlled objects is more challenging, as the correlation of candidates with the catalogued orbit must take into account all possible manoeuvres. Apart from the lack of knowledge of all manoeuvres, the existing orbit must be already of a good quality, and each object must be observed at least  $m$  times in between two manoeuvres ( $m$  probably being at least three) for successful correlation. The maximum allowed number for manoeuvres would thus be one per  $m \times n$  days, i.e., of the order of one per 21 days (for  $n=7$  days).

We conclude that a “survey only” strategy may not always be useful for GEO space surveillance because of FoV limitations. The correct detection of all manoeuvres cannot be guaranteed. Therefore, the survey only strategy may not provide the full space surveillance functionality for the GEO. We further state that in the case of a wide FoV survey sensor covering the entire survey band, this survey strategy would likely be most efficient. Unfortunately, the design of such a sensor is currently not feasible, as radiometric and astrometric requirements (a small PS) must be met, as well. As an alternative to a single wide FoV sensor, several sensors might get combined, but this approach not necessarily lowers the overall number of telescopes.

**Combined survey and tasking strategy** Let us now assume that a survey based on the presented continuous scanning of a stripe of fixed right ascension is carried out. This survey generates short arcs of, up to this point unknown, objects. From these short arcs orbits of a limited accuracy can be determined. Follow-up observations with a certain frequency are needed to improve the determined orbits and to maintain the catalogue. The resulting catalogue of up-to-date orbits is in turn essential to ensure future re-acquisitions of the objects, and thus the continued maintenance of the catalogue. Dedicated telescopes have to perform these follow-up observations, as the survey telescopes do not have any spare observation time.

The tasking frequency for GEO space surveillance was obtained in previous work based on simulations using a single site (ESAs Space Debris Telescope at Tenerife, Spain). The required tools (Musci et al., 2004) were developed using components of the CelMech program system (Beutler, 2005). The following parameters for the strategy were selected and were later on validated using real observations (Musci et al., 2005): three to four observation tracks of about 2 minutes each, spanning  $\approx 3$  hours in total, are needed, plus one additional track in the following night. For catalogue maintenance each object must be re-observed at least every 30 days (Musci et al., 2005). This tasking frequency heavily depends on the astrometric accuracy of the observations, and of the diameter of the sensor FoV.

To execute this follow-up schedule, to cope with drifting objects in particular, and to circumvent difficulties related to visibility and weather conditions, a network of follow-up telescopes is needed, which covers all longitudes. Assuming elevation cut-off angles of  $20^\circ$ , we need a minimum of four sites for GEO space surveillance. The co-location with the survey sensors is obviously positive and recommended.

#### 5.3.2.4 Summary of GEO observation strategy proposals

The analysis of the proposed stripe-scanning survey with added follow-ups revealed that catalogue coverage reaches over 95% with the proposed network of four survey sites. The remaining coverage gaps result from the bad coverage of GEO between Tenerife and the Marquesas Islands over America and from some difficulties with rapidly drifting objects. The proposed 0.5 m sensor allows a repeatability of the observations of 7 days, if weather permits (Flohrer et al., 2005a). A network of follow-up telescopes is needed, which covers all longitudes. At minimum four sites are required for GEO space surveillance, preferably co-located with the survey sensors. Approaches for correlating the generated observations into short arcs and for correlating the short arcs with catalogued objects is essential for catalogue build-up and maintenance. Only prototypes exist for this task so far. We have seen that this task is very closely related to the achievable orbit determination accuracy. Musci et al. (2004) showed that cataloguing is impossible using orbits determined from a single crossing event. Depending on the sensor design about two immediate re-acquisitions within the same observation night, one additional follow-up observation during the next night, and, finally, regular follow-ups once per month are required for adding an object to the catalogue and maintaining these information. The simulations showed that 1 m is the minimally detectable object diameter under bad observation conditions, while under better conditions objects as small as 50 cm, sometimes even of 30 cm, are detectable (Flohrer et al., 2005a).

### 5.3.3 MEO

In this section we develop, in a similar manner as for GEO observations in Sect. 5.3.2, observation strategies for the MEO. We also explain why a GEO strategy is not perfectly suited for MEO space surveillance.

#### 5.3.3.1 Observational characteristics

Donath et al. (2005) state a system based on the fusion of the proposed LEO and GEO sensors is not efficient for space surveillance of MEO objects. Radars for LEO observations are unable to continuously observe objects smaller than 1 m diameter in MEO altitudes. Optical sensors in a space surveillance system, which follow only the proposed GEO space surveillance strategy, cannot guarantee the required re-acquisition periods of MEO objects for catalogue maintenance. Therefore, there is a need for a dedicated MEO observation strategy with optical means.

Information on MEO space surveillance strategies is, however, quite sparse. Few examples of possible MEO space surveillance strategies are given by Payne (2003). Two strategies proposed for the GEODSS focus on semi-synchronous orbits: an eccentric semi-synchronous orbit apogee search and a circular semi-synchronous orbit search. The strategy is a simple along-track search of already known objects. A pure survey is considered as very difficult due to the low spatial density of objects.

It is not known how and where the US Space Surveillance Network currently observes MEO objects. As there is only a limited number of MEO objects in the US catalogue, it is possible that no dedicated MEO sensors are used. Probably, no dedicated MEO search task exists today. In consequence it seems possible that MEO objects are observed with the GEODSS through a pure “tasking” strategy with initial orbits taken from the launch assessment, or from other sources.

As first analysis of the presumed current approach and of the proposal by Payne (2003) reveals two problems: (1) an initial catalogue is needed, and (2) the MEO region cannot be covered completely. The evolution of MEO orbits is not considered in the search strategy.

As opposed to the GEO regime, the IADC does not run MEO observation campaigns and hence there is no MEO observation strategy of the IADC that could serve as a starting point for space surveillance.

We will continue with the analysis of the observation characteristics of MEO objects during one night. For that purpose, we generate ephemerides for the reference population introduced in Sect. 3.2.2 for a duration of 24 hours. We assume Tenerife as an observing site and set the starting epoch to November 16, 2004. The generated ephemerides data for the main MEO constellations GPS, GLONASS, and the assumed Galileo satellites, allows it to discuss observation distance, phase angle, and object velocity in the FoV for each particular object.

**Angular velocities** Figure 5.12 shows the elevation-filtered distribution of the GPS satellites' angular velocities in the local horizon system for Tenerife. The objects move in the horizon system with angular velocities between  $26''/s$  and  $40''/s$ .

Figure 5.13 shows the angular velocities as a function of the declination. For the GPS population the maximum velocity in declination is between  $-40^\circ$  and  $20^\circ$  declination. There, the absolute value of the velocity in declination is between  $18''/s$  and  $38''/s$ . The non-symmetry in declination is because of the consideration of topocentric velocities.

The GLONASS satellites move in the horizon system with angular velocities between  $30''/s$  and  $41''/s$ , which is slightly faster compared to the GPS. The maximum velocity in declination is between  $-50^\circ$  and  $35^\circ$ , which is a wider range compared to the GPS. The absolute values are similar to those of GPS, between  $20''/s$  and  $40''/s$ .

Objects of the simulated Galileo population move in the horizon system with angular velocities between  $15''/s$  and  $25''/s$ , which is a bit smaller compared to both, GPS and GLONASS. The maximum velocities in declination are found between  $-35^\circ$  and  $15^\circ$  declination, which is a range slightly smaller than for GPS. The absolute values are smaller than for GPS and GLONASS, and lie between  $23''/s$  and  $30''/s$ .

Fernández et al. (2011) show that for high eccentricities of  $e = 0.16$  objects in near semi-synchronous orbits may reach topocentric angular velocities of  $20''/s - 60''/s$  around the perigee.

**Dwell times** The dwell times for MEO objects vary due to the non-uniform crossing directions and the larger range of possible velocities (see also Sect. 3.2.2). The dwell time in the FoV for observations with an Earth-fixed sensor can therefore reach values from about 1 minute (faster GPS objects observed from OGS) to 12 minutes (slowest Galileo objects observed from a  $3^\circ$  FoV).

In case of inertial observations with sidereal tracking the nominal GPS object may cross a FoV of  $1^\circ$  in about 300 s, if the telescope points to a low or moderate declinations. For such declinations, the objects move mainly in North-South direction (see Sect. 3.2.3). For high declinations the dwell time may be as long as 1000 s or more. Dwell times for GLONASS objects vary from around 300 s to over 1100 s at high declination, while the Galileo objects are expected to have at least a dwell time of 350 s in a FoV of  $1^\circ$ .

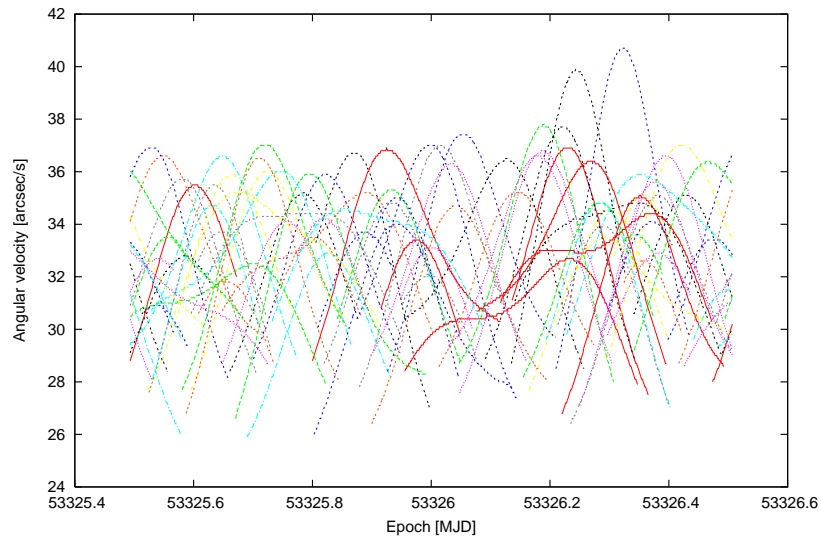


Figure 5.12: Angular velocities in the local horizon system of the OGS for GPS satellites.

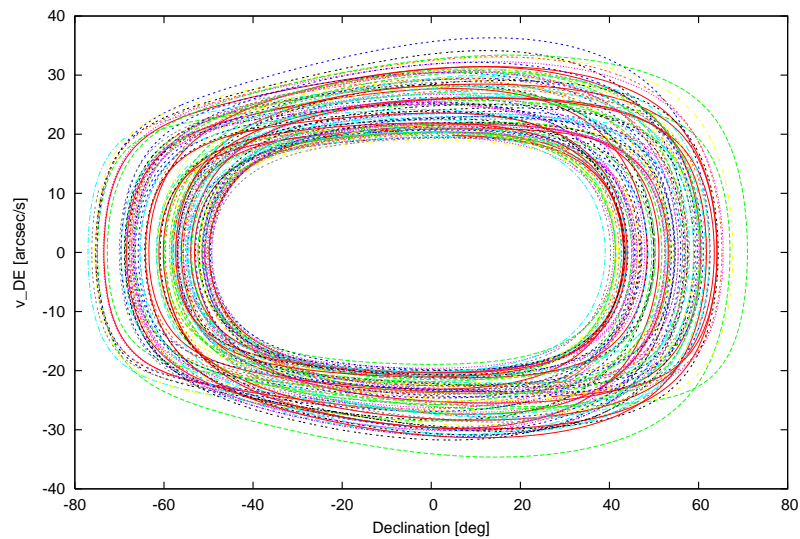


Figure 5.13: Velocity in declination vs. declination of GPS satellites.

**Observation distance** Figure 5.14 shows the topocentric distances for the GPS population visible from the OGS. GPS satellites can be observed at distances between  $\approx 20000$  km and  $\approx 27000$  km. The objects of the GLONASS population can be observed at distances between  $\approx 19000$  km and  $\approx 27000$  km, while for the Galileo population the distances range from  $\approx 23500$  km to  $\approx 29500$  km. Not all objects are observable in the entire given distance range in a particular observation night.

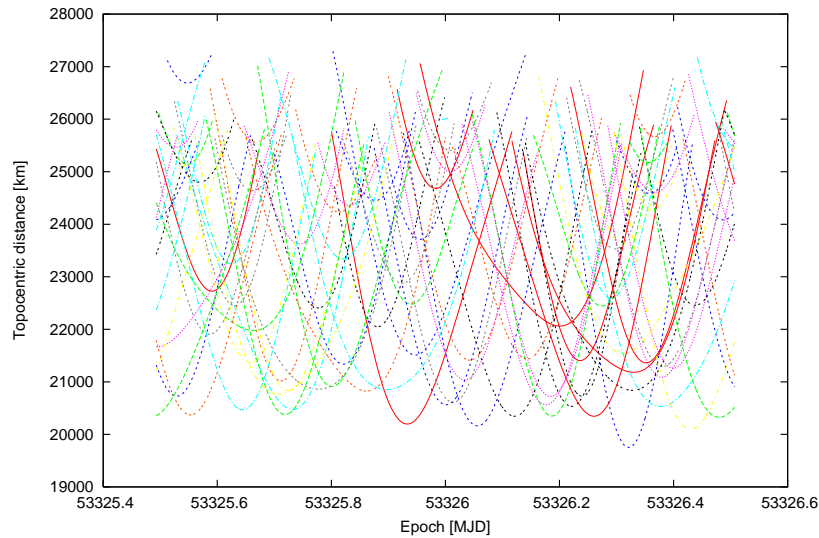


Figure 5.14: Topocentric observation distances for GPS satellites seen from the OGS for November 16, 2004.

**Phase angles** Figure 5.15 shows the analysis of the phase angles for GPS satellites above the horizon. As only nighttime observations are possible, a maximum phase angle of  $120^\circ$  may be reached. Phase angles around  $0^\circ$  are possible for certain objects. For GLONASS and Galileo similar results are obtained. This implies that, as opposed to the outlined GEO surveys, an optimum observation geometry cannot be guaranteed for MEO surveys. A phase angle close to  $120^\circ$  may rarely occur for all objects. Further investigations showed, however, that an upper limit for the phase angle of  $90^\circ$  is a sufficient upper limit.

**Object brightness** Based on the discussion in Sect. 3.3.2.6 and on Fig. 3.15 we estimate that a 1 m spherical object with a Bond albedo of 0.1, observed at typical distances for upper MEO between 10000 km and 35000 km, has an apparent brightness between 14 mag (low phase angle) and more than 18 mag ( $120^\circ$  phase angle). In GNSS-like orbits (which would typically be observed at topocentric distances of about 25000 km), we expect between 15.5 mag and 18 mag for such an object. Larger objects (payloads) can be observed with a brightness of 12 mag or brighter, even under less favourable phase angle conditions.

Donath et al. (2005) propose a suitable sensor for MEO space surveillance. The dedicated MEO survey sensors must be capable of detecting 17 mag objects, corresponding to 1 m diameter spherical objects observed at  $90^\circ$  phase angle. As the relative velocity with respect to the sensor of up to  $40''/s$  is realistic for either pointing scenario in the local or inertial system, streak losses must be incorporated in the SNR estimations. Donath et al. (2005) propose a 0.8 m aperture, wide field (Schmidt design) telescope with  $f/D=1$ , equipped with a  $4k \times 4k$  CCD, leading to an effective FoV of  $4.7^\circ \times 4.7^\circ$ . This sensor should result in an astrometric accuracy of  $1''$ . In PROOF simulations we used the corresponding settings of Table 5.5.

Using the results of the assessment of the MEO population evolution (Sect. 5.1) and the evaluated topocentric distances, phase angles, angular velocities, and apparent brightness in the previous subsection

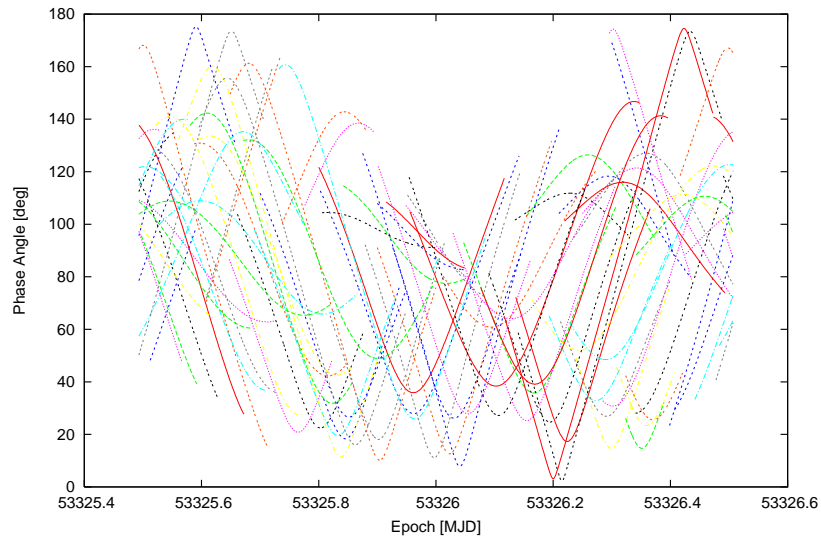


Figure 5.15: Phase angles for GPS satellites seen from the OGS for November 16, 2004.

Table 5.5: Preliminary system architecture used in performance estimation.

Instrument	MEO survey
Aperture	0.8 m
FoV	$4.7^\circ \times ^\circ$
Number of pixels	4096
Pixel size	$13.5 \mu\text{m}$
Pixel scale	$4.1''/\text{pixel}$
Gap time	variable
FWHM	1.0 pixel
Exposure time	1.0 s
CCD readout noise	$10e^-/\text{pixel}$
CCD dark noise	$0.05e^-/\text{pixel/s}$
SNR threshold for detection	4
Peak efficiency with optics	0.64

we are now in a position to develop a proposal for MEO observation strategies.

### 5.3.3.2 Survey only scenario

Basically, the same limitations have to be observed in either MEO or GEO surveys: the diameter of the FoV shall be as large as possible, but the pixel scale should still be acceptable.

The analysis of the MEO population in the inertial space shows that each object in upper MEO crosses the equator once in about 6 hours, as the mean motion is around 2 revolutions/day. For sites at low or moderate latitude this occurs at least once during an observation night. Therefore, the continuous and uninterrupted observation of a so-called fixed declination stripe would allow a complete survey of the

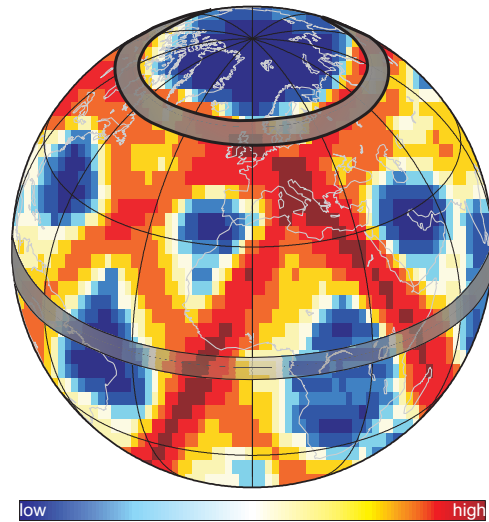


Figure 5.16: Apparent density of the upper MEO objects in the DISCOS catalogue projected onto the Earth for epoch 20 August 2004, highlighted are the declination stripe centred at  $0^\circ$  declination and a “caustic” declination stripe at  $65^\circ$ .

MEO population within very short time. Such a declination stripe denotes a region in the sky defined by the entire right ascension range (considered as stripe width) and the sensor FoV (equivalent to the stripe height). In order to be able to observe objects in low-inclination orbits, a stripe covering the declination of  $\delta=0^\circ$  is mandatory. Figure 5.16 indicates, however, that a declination close to the culmination region would be more efficient due to the higher spatial density. In this case the covered sky region is smaller compared to the  $0^\circ$  declination stripe and thus the sensor requirements could be relaxed. We will look at this optimised approach in the next subsection.

The main limitation of the “survey only” strategy is the extended time until the scan of the targeted declination stripe is finished. Thus, the sensor architecture has to guarantee that a leak-proof scan is possible and that also the necessary number of observations for each object crossing the FoV is acquired to form a short arc that allows for the initial orbit determination.

As opposed to the GEO, covering the entire longitude band is desirable, but not strictly required. The revolution of the Earth around the Sun of about  $1^\circ/\text{day}$  and the motion of the right ascension of the ascending node of the MEO objects of about  $2^\circ/\text{day}$  make, during time, different orbital planes accessible for a single site. After about three months the observation of the entire MEO population should have been possible under valid illumination conditions.

Figure 5.17 shows the accessible fields for one year for a moderate latitude site (Tenerife). Due to the revolution of the Earth around the Sun the right ascension of both (rising and setting) fields increases steadily. This in turn means that the filled area slowly moves “upwards”. We may conclude that all fields that have not yet set in the West at sunset or have just risen in the East at sunrise are in principle observable during the observation night. The right ascension range, which is in principle accessible during the part of observation night at the given epoch is highlighted in light blue colour. Not surprisingly, the observation conditions are better in winter (at the left hand side in the figure), where there are even fields, which can be observed over the entire right ascension arc. These fields are highlighted in deep blue. In winter the nautical twilight duration is long enough to allow fields to rise after sunset and set before sunrise. Such

fields do not exist in summer. About 90% of the fields in winter and about 75% of the fields in summer are accessible during the night. The figure shows that a particular right ascension cannot be accessed for about 20 to 60 consecutive days per year, for example the right ascension of  $300^\circ$  and  $100^\circ$ .

Figure 5.18 shows the accessible fields rising at given epochs after sunset (green) or setting at given epochs before sunrise (red). In summer, fields setting 8 h prior sunrise and fields rising 8 h after sunset are accessible. Consequently, the maximum observation duration of a particular field is 8 h. In winter, fields setting 11.5 h prior sunrise and fields rising 11.5 h after sunset are accessible. As the accessible arc in right ascension for an elevation mask of  $10^\circ$  in Tenerife is only about 10.4 h ( $156^\circ$ ), we have in winter fields that are accessible over the entire arc, from rising to setting. Twice a year the Earth shadow will prevent the observation of low declination angles.

To improve the performance two survey telescopes, spaced by  $90^\circ$  in longitude, are proposed. With the second survey site the gaps in Fig. 5.17 can be closed. A second site spaced  $180^\circ$  in longitude would, however, close the gaps in an optimum manner, but would not improve the MEO population coverage significantly: the same orbital planes would be accessible from both sites.

As opposed to the limitations imposed by a “survey only” in GEO, the manoeuvres detection is more relaxed if the entire longitude band is permanently covered by the MEO survey, as in this case the re-acquisition period of MEO objects is reduced to less than one day.

### 5.3.3.3 Optimised survey only scenario

A possible way to optimise the MEO survey is to focus the survey at a so-called “caustic”, a special region around the poles, visible as most dense regions (Fig. 5.16). Such a caustic survey will not allow it to observe objects in low inclination orbits.

Not the entire caustic is accessible from a low latitude site. In case of a full longitude coverage with low latitude survey telescopes, the observation of all objects should still be possible. Even if objects in the

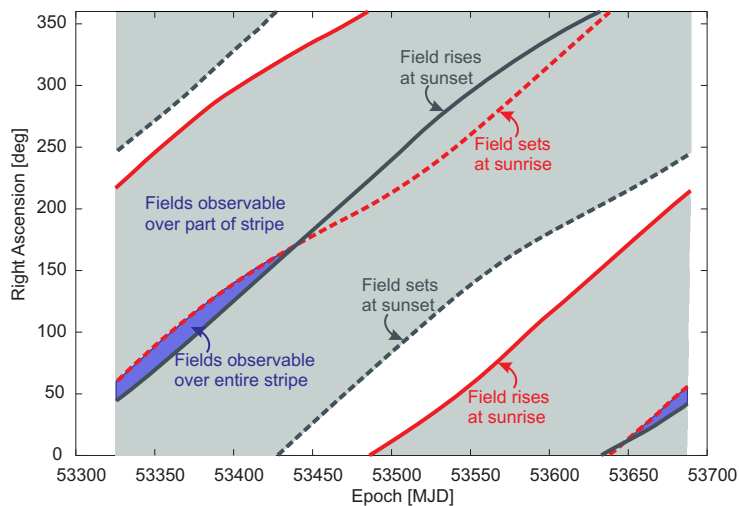


Figure 5.17: Total accessible area in right ascension of  $0^\circ$  declination fields for Tenerife with elevation mask of  $10^\circ$  and evolution of area over a one year period.

caustic are observed at low elevation angles, the next telescope will in most cases be able to observe the same objects at a higher elevation angle in the caustic.

Unfortunately, a high-latitude site in a space surveillance network does not solve these limitations without opening new issues. A single high latitude site has a poor performance, because the available observation time is limited in summer. Consequently, two sites would be optimal – one in the Northern polar and one in the Southern polar region, which is an expensive affair. A compromise would be to use sites at medium latitudes (around  $55^\circ$  latitude). The trade-off between lowering the number of needed sites as a function of the latitude and losing observation time during summer needs further studies at system level.

### 5.3.3.4 Simulations of MEO survey strategies

Both, a “survey only” strategy either by scanning a fixed declination stripe at  $0^\circ$  declination or at the culmination region may be used for MEO space surveillance. For the orbit determination of newly detected objects the survey has to provide observations at given frequencies. We will discuss this parameter using PROOF simulations.

The proposed survey strategy cannot be exactly reproduced with PROOF. PROOF does not allow it to request observation epochs containing seconds (or fractions of minutes). The proposed survey pattern assumes that a full scan of the stripe is carried out in a few minutes, which is why the individual observation epoch per right ascension/declination field requires a sub-minute spacing of observation epochs. Fortunately, it is possible to circumvent this limitation by using a modified, but equivalent survey strategy maintaining the leak-proof feature. This modified survey strategy is not feasible from the technical point of view, but could be implemented in PROOF: Instead of executing the proposed continuous scan of the declination stripe (i.e. the repetitive “acquire - reposition - acquire - reposition” pattern), a complete snapshot of the entire stripe is created with a frequency according to the achievable image acquisition

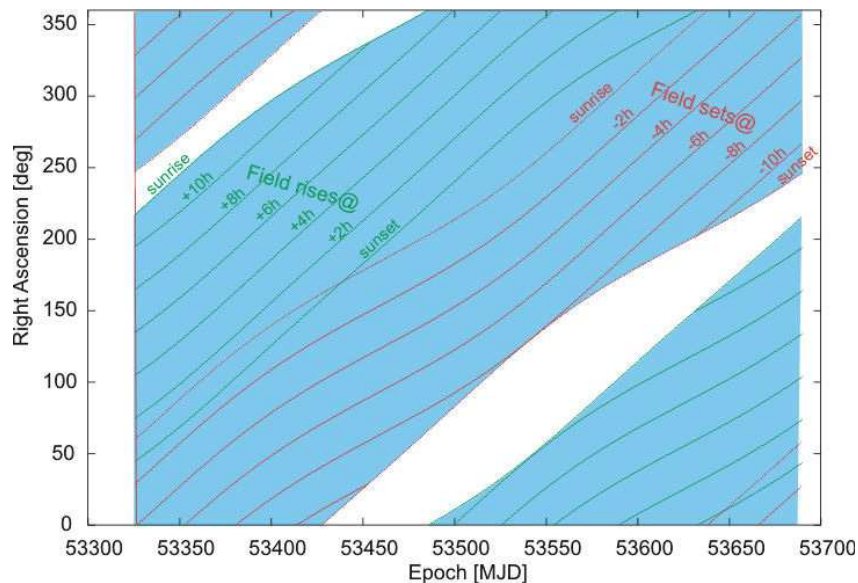


Figure 5.18: Possible observation duration of  $0^\circ$  declination fields for Tenerife with elevation mask of  $10^\circ$  and evolution over a one year period.

frequency of all the individual fields. The length of the considered stripe (in right ascension) is adapted in such a way so that the re-acquisition interval (in minutes) of the fields is an integer. For a comparison between the proposed and implemented survey strategy, we refer to Fig. 5.19.

The most important unknown parameter relevant for the assessment of the survey performance is the length of the covered arc in longitude from a single site. From the given system FoV and a certain requested longitude coverage, we may calculate the number of fields to be observed in the  $0^\circ$  declination stripe. At least two exposures are necessary to identify a moving object (the MEO satellite) in front of the star background. In order to minimise the false detection rate due to cosmic ray events and objects moving out of the FoV, three, better four, exposures should form a series of observations. Together with other parameters, the telescope slew rate and settling time, and the detector parameters, we may finally calculate how long it would take to re-observe a specific field. If this re-observation time span is shorter than the time it takes a typical MEO object to cross half the FoV, we consider the strategy as leak-proof for the given longitude range. Here, we assume a higher object velocity of  $40''/s$ . Hence, the limit is 211 s for the  $4.7^\circ \times 4.7^\circ$  FoV. It is necessary to assume a high-frequency readout of the detector, probably during the repositioning to the next field.

For the simulations we define three different arc lengths (all had to result in an integer re-acquisition time of a particular field in minutes):

- A – About  $90^\circ$  longitude coverage: with a field re-acquisition time of 2 minutes this is achieved using the case “minimum of 3 exposures per object per FoV crossing event, 5 MHz readout frequency”. This yields 21 observed fields (10% overlap).
- B – About  $100^\circ$  longitude coverage: with a field re-acquisition time of 3 minutes this is achieved using the case “minimum of 4 exposures per object per FoV crossing event, 5 MHz readout frequency”. This yields 24 observed fields (10% overlap).
- C – About  $137^\circ$  longitude coverage: with a field re-acquisition time of 3 minutes this is achieved using the case “minimum of 3 exposures per object per FoV crossing event, 5 MHz readout frequency”. This yields 32 observed fields (10% overlap).

The PROOF simulation returns for the considered time interval and the assumptions made the number of objects crossing the FoV and several characteristics of each crossing event. The data analysis allows extracting the number of objects observed once within the considered time interval (referred to as unique crossing), or being observed on several frames (referred as multiple crossing). Note that no initial orbit determination will be possible based on unique crossing events. The total number of crossing objects is, however, the sum of unique and multiple crossing objects. The ratio of the total number to the reference population size is referred as catalogue coverage. A population of 158 objects in the upper MEO was used for this simulation. The population was filtered from a DISCOS reference population.

The PROOF simulations are based on the proposed sensor network (Fig. 5.5). Two sites are considered for MEO observations (TF-Tenerife, MQ-Marquesas Islands) as well as 8 h of uninterrupted observation time per site. Observations are simulated for three nights, namely for 1 May 2005, 1 June 2005, and 1 July 2005.

Typically, the formed tracklets are shorter than 8 minutes. By dividing the total number of FoV crossing events by the total number of objects crossing the FoV during the analysed night, we estimate that on average 4.75 observations per object could be acquired while the object crosses the surveyed declination

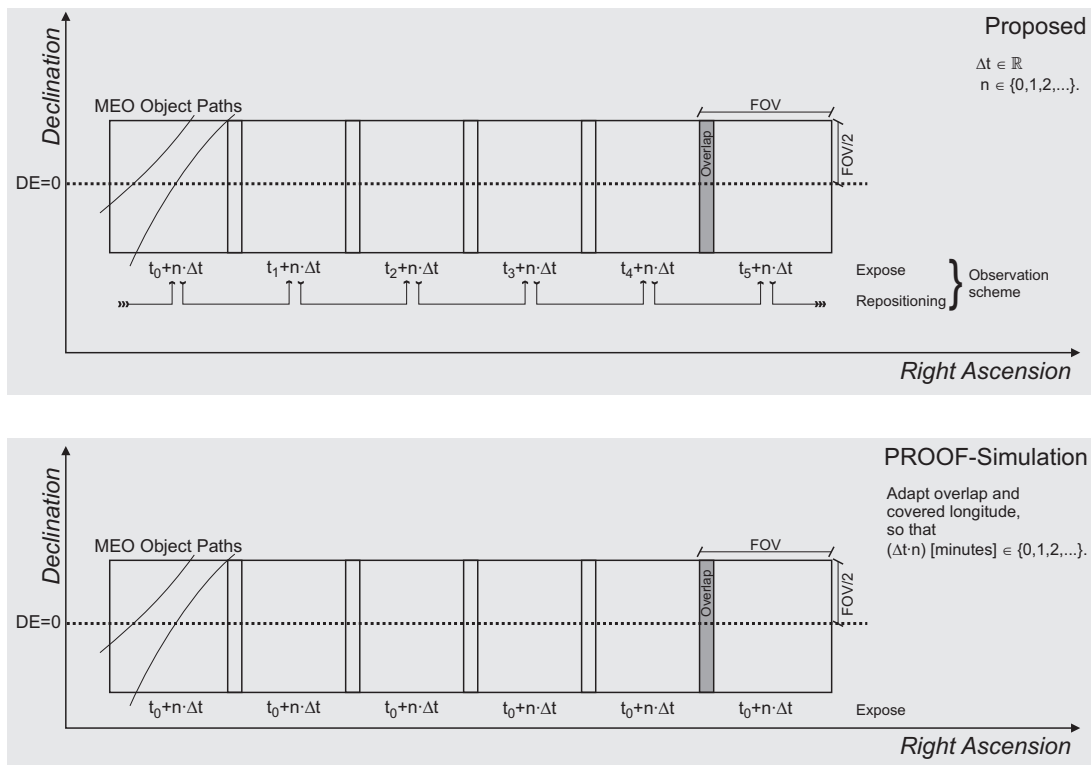


Figure 5.19: Implementation of the proposed MEO survey strategy in PROOF.

stripe, if the re-acquisition of the field occurs every 2 minutes. For a re-acquisition period of 3 minutes an average of 3.5 observations is achieved. In such cases more than 4 observations of a single object are available for the initial orbit determination, which is usually sufficient. No peak loads on the space surveillance sensor network are expected. The analysis of the observation characteristics also shows that the phase angle stays below  $90^\circ$ , and that the major orbital planes are visible in the spatial distribution of the crossing events.

Figure 5.20 shows the coverage of the MEO population after a single night, after including a second night after 30 days, and after including a third night after 60 days. The MEO observation strategy focussing at the  $0^\circ$  declination stripe is used and three implementations of the survey are shown: A)  $90^\circ$  longitude coverage, B)  $100^\circ$  longitude coverage, and C)  $137^\circ$  longitude coverage per site. Note, that a survey covering the entire longitude range would, in principle, cover 100% of the MEO population after 24 h. Here, we used the limited survey approach, using only 2 survey sites, which are expected to cover the MEO completely after about 2-3 months. A summary of the reference population coverage analysis, resulting in Fig. 5.20, is given in Table 5.6.

The analysis of Fig. 5.20 and Table 5.6 shows a small number of “unique” events, indicating that for all crossing objects a sufficiently high number of observations can be acquired allowing for an initial orbit determination. We also conclude that a single survey site may only cover a smaller fraction of the entire MEO population in one night. This is in particular true if the covered arc is short. In the case of a covered longitude of  $90^\circ$  the combination with a second site allows it to cover two thirds of a reference population in one night. The combination with the second site shows that there are only three objects

observed by both sites during that single night. There is no significant coverage overlap between the two sites if the stripe covers  $90^\circ$  in longitude and the observation duration per night is 8 h. If we consider three months of observations (represented here by combining results from the three individual nights), more than half of the reference population can be covered by one site, already 89% by combining the observations from two sites. The coverage of the reference population from a single site is increased by an average of 10% per month, depending on the accessibility of densely populated orbital planes. In turn, a single site would have accessed the entire MEO population after less than 1 year, if 8 hours per night are the average observation time, and  $90^\circ$  in longitude are covered. An additional analysis showed that by combining the results from two nights, separated by 30 days, up to half of the population can be covered by a single site, while more than 80% of the population can be covered by combining the survey results from two sites. The motion of the node of MEO objects is so slow, that observations from the nights between the two considered nights do not improve the coverage, as there are no additional objects crossing the observed stripe in that time.

Figure 5.20 and Table 5.6 also show that a coverage of  $100^\circ$  in longitude improves the single site nightly coverage only by about 3%. An overall coverage of the reference population of 90% can be achieved after three months of observation combining the observation from two sites. There is no improvement of the overlap between the two sites. As for the  $90^\circ$  case about 5% of the objects are observed by more than one site. Covering  $137^\circ$  in longitude improves the single site (nightly) coverage by 10-15%, implying that nearly half of the MEO population is accessible from a single site during one night. An overall coverage of the reference population of 84% can be accessed within one night only after combining observations from two sites. Some objects are observed by both sites during one night. About 10% of the objects are observed by more than one site. The MEO population can be covered nearly completely (95%) already after two months, if the observation results from two sites are combined. A three months arc does slightly increase the coverage further to more than 97%.

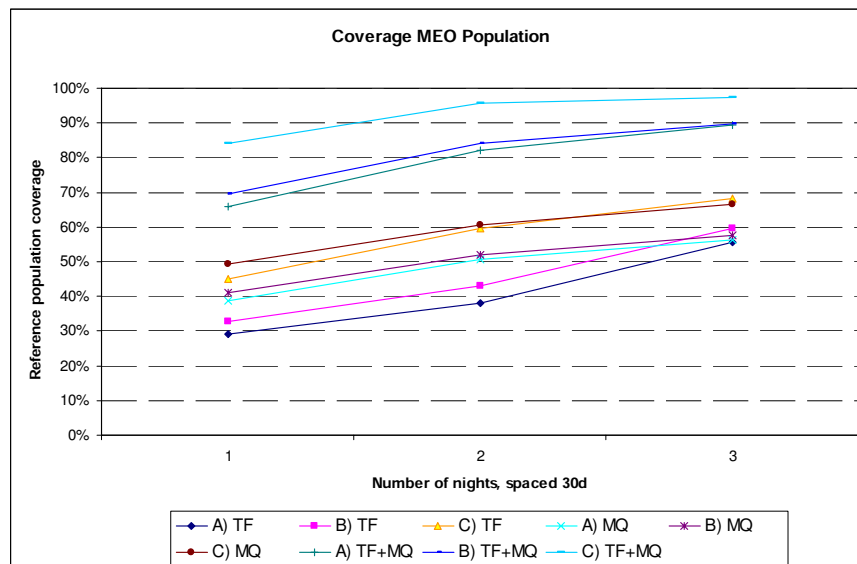


Figure 5.20: Coverage of the MEO reference population with the proposed  $0^\circ$  declination MEO survey strategy.

Table 5.6: Coverage of a reference population: Number of multiple crossing events and (in parentheses) unique crossing events, and the corresponding coverage of the reference population (TF-Tenerife, MQ-Marquesas Islands).

Scenario	1 night			2 nights			3 nights		
	TF	MQ	TF+MQ	TF	MQ	TF+MQ	TF	MQ	TF+MQ
A	46(0)	60(1)	103(1)	60(0)	78(2)	129(1)	88(0)	88(1)	140(1)
	29%	39%	66%	38%	51%	82%	56%	56%	89%
B	52(0)	62(3)	108(2)	67(1)	79(3)	132(1)	94(0)	90(1)	142(0)
	33%	41%	70%	43%	52%	84%	60%	58%	90%
C	71(0)	77(1)	132(1)	93(1)	94(2)	150(1)	107(1)	105(0)	154(1)
	45%	49%	84%	59%	61%	96%	68%	66%	98%

Comparing the coverage after three months, we conclude that even for the shorter arcs in longitude a sufficient survey coverage of the MEO population can be achieved. A longer (technically demanding) arc allows for a nearly complete coverage of the MEO using only two survey telescopes operating 8 h per night.

We continue the simulation of the MEO observation strategies by a look at the caustics survey. We use PROOF simulations and by adapting the simulation environment introduced in Sect. 4.3, we include initial orbit determination in the discussion.

As the MEO environment is sparsely populated, we need a synthetic reference population for the discussion of the performance of the caustics survey. We use the results of simulated explosions in MEO, a population containing 1000 objects (Schildknecht et al., 2009).

We select a survey target field in the caustic region in which different orbital planes populated with explosion fragments intersect. Again we use the 0.5 m, 3° FoV sensor implying that the survey area is composed of nine fields at different right ascensions. We simulate 12 h of repetitive coverage of this survey region at  $t_0$ .

In order to simulate the benefits of having a second survey sensor available that helps to immediately re-acquire the objects detected in the first survey region, we simulate a second survey region covering the area where typical MEO objects would be expected after 1 h ( $t_1$ ). Again, we simulate 12 h of observations, and we would expect that after 12 h of observations the considered orbital plane would be completely covered. Two telescopes are required to implement this version of a caustic survey. Figure 5.21 shows the orbits of six example objects and the two survey areas “survey  $t_0$ ” and “survey  $t_1$ ”. Pattern “survey  $t_0$ ” is aligned with the orbital plane containing objects 102 and 103 around the culmination. The other four objects cross the survey area much more rapidly.

The simulation reveals that 1185 objects crossing events are registered for the “survey  $t_0$ ”, which are related to 9 objects with a single (unique) crossing event and 172 objects with more than one (multiple) crossing events. For the survey pattern  $t_1$  488 crossing events result, which relate to 2 unique and 138 multiple events. This implies that the survey efficiency is 59% for first “survey  $t_0$ ” (the target is to cover the mentioned three orbital groups) and 82% for the second “survey  $t_1$ ” (assuming that 1.5 orbital groups are covered). Analysing the combined coverage of both groups shows that either for the survey pattern  $t_0$  or  $t_1$  35% of the population are covered, and about 53% are covered by both, the survey  $t_0$  and  $t_1$ .

Figure 5.22 illustrates the coverage of the reference population, clearly indicating the orbital group (South) is covered by both, “survey  $t_0$ ” and “survey  $t_1$ ”. The figure also shows that there is ample

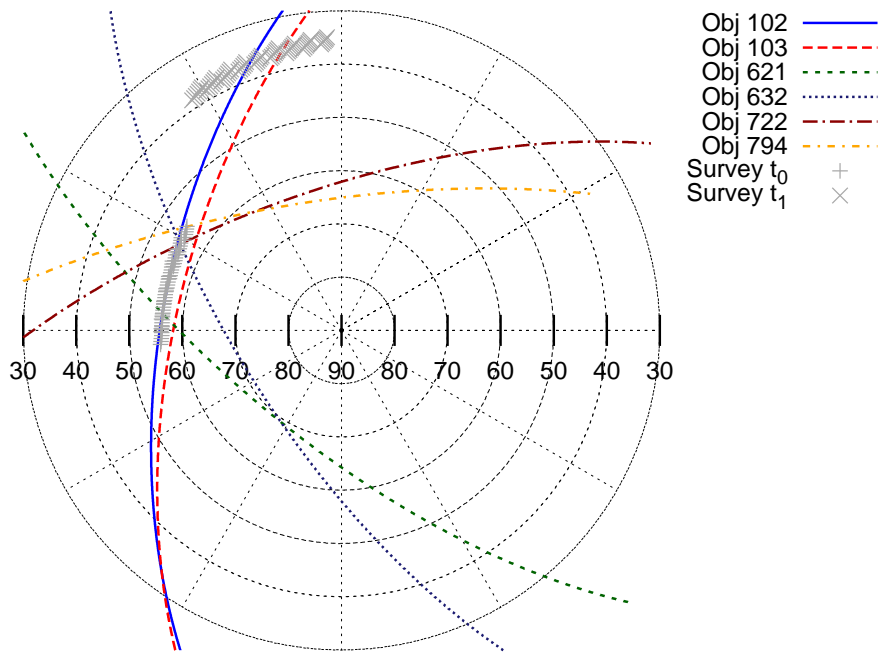


Figure 5.21: Right ascension vs. declination of the two simulated caustic survey patterns at  $t_0$  and  $t_1$  and orbits of six objects.

span for improvement, in particular if the coverage of other orbital planes is considered by flexibly modifying the observation scheduling. This could be achieved by either daily alternating schedules, or by adding more dedicated survey telescopes executing the caustic survey. Noted that even in case of a single telescope a shifted execution of the two survey patterns allows the 53% coverage of a particular orbital plane. A shifted pattern could be executing in night 1 from the beginning of the night “survey  $t_0$ ” for 1 h, followed by “survey  $t_1$ ” for 1 h, “survey  $t_0$ ” for 1 h, and so on. In the next night the first hour of observations can be dedicated to other tasks before “survey  $t_0$ ” is executed for 1 h, followed by 1 h “survey  $t_1$ ”, and so on.

For initial orbit determination we select object 107 with 13 detections in the area “survey  $t_0$ ” supplemented by 2 detections in the area “survey  $t_1$ ”. The arc covers the time interval 19h18m to 20h27m for the simulation epoch 2009 June 11. ORBDET was configured to use the boundary value method with the maximum arc length and a minimum search between 250 km and 60000 km of topocentric distance. An improvement step made use of all available observations, where the perturbations due to Earth oblateness ( $C_{20}$ ) and due to Sun and Moon were taken into account. Figures 5.23 and 5.24 show that the initial orbit determination gives good results and provides an orbit with a well determined orientation of the orbital plane at the order of some milli-degrees, and with a well determined shape of the orbit better than 50 km in semi major axis, at least for an astrometric noise better than  $1''$ .

**Minimally detectable diameter** The minimally detectable MEO object diameter can be estimated for the proposed 0.8 m sensor from the PROOF simulations if a statistical population is adapted. Figure 5.25 shows that for a SNR threshold of four a 1 m diameter object can always be detected, even under

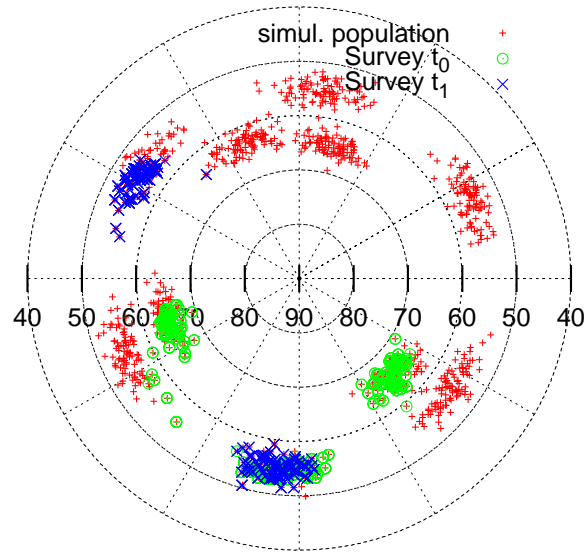


Figure 5.22: Inclination  $i$  vs. right ascension of ascending node  $\Omega$  of the synthetic reference population based on explosion models, and the fraction of the population covered by the survey patterns  $t_0$  and  $t_1$ .

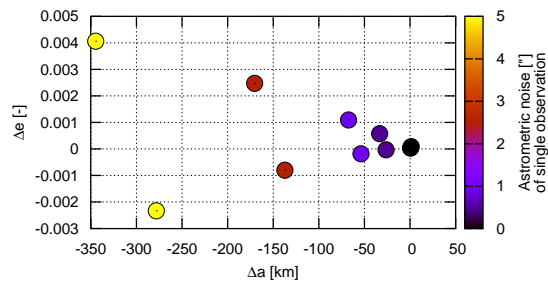


Figure 5.23: Differences in semi-major axis vs. eccentricity of the initially determined orbits w.r.t. the reference orbit as a function of the astrometric noise for test object 107.

adverse phase angle and background conditions. A minimally detectable objects diameter for worst case conditions can be extrapolated. It is of the order of 80-90 cm. In the best-case objects as small as 30 cm in diameter may be detected.

### 5.3.3.5 Follow-up strategy

As for GEO surveys, follow-up observations are required for catalogue maintenance and to initially catalogue the MEO objects. This might not be possible from “survey only” observations. In order to decide whether follow-up observations from follow-up telescopes are needed to complement the regular survey, we have to estimate the follow-up frequencies. These frequencies define the orbit improvement strategy. Here we adapt the declination stripe scanning survey at  $0^\circ$  declination for simplicity. Although

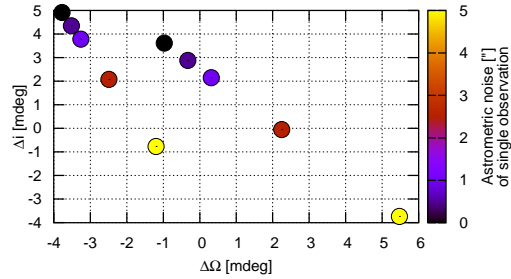


Figure 5.24: Differences in right ascension of the ascending node vs. inclination of the initially determined orbits w.r.t. the reference orbit as a function of the astrometric noise for test object 107.

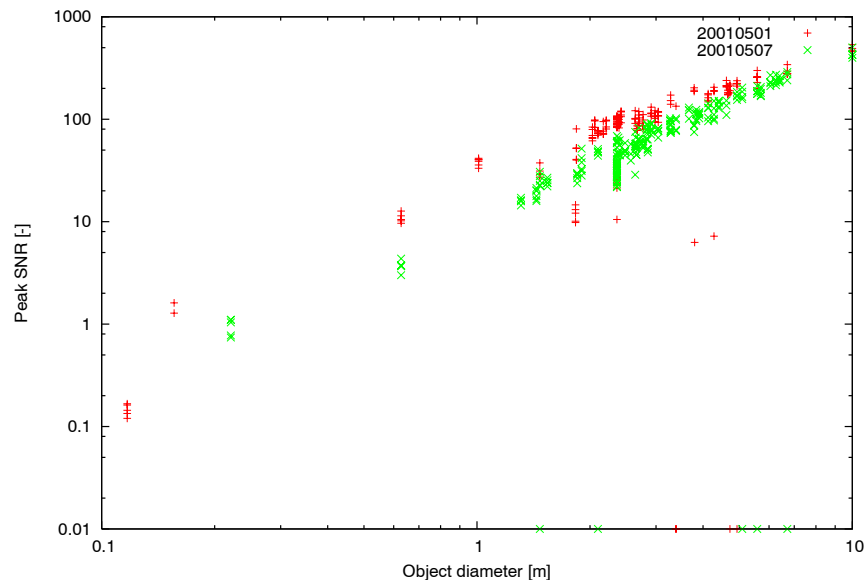


Figure 5.25: SNR as a function of MEO objects diameter during MEO survey. Red: average observing conditions. Green: worst observing conditions during full Moon.

the distance to the MEO objects is smaller compared to GEO, at least comparable radiometric conditions are expected. Therefore, the proposed GEO network of sensors could be used, consisting of the 0.5 m Schmidt-Cassegrain telescopes with a  $3^\circ$  FoV.

There is no previous work available assessing the required follow-up frequency for MEO. We modified the approach of Musci et al. (2004) to derive these quantities. The tasking strategy simulation assumes that the survey strategy provides an initial orbit at epoch  $t_0$ , determined from more than three observations forming a short arc. For simulation, the individual observations are assumed to be spaced by 2 s (1 s exposure plus 1 s sensor repositioning and readout). An astrometric error of  $1''$  (error of the object's position determination) is used in the simulation. This astrometric error results from the  $4.1''$  pixel scale of the survey telescope, which agrees well with empirical experience.

We use a synthetic population of 250 randomly distributed objects with the following characteristics:

- Semi-major axis:  $24970 \text{ km} < a < 30250 \text{ km}$  (Mean motion:  $1.65 \text{ revolutions/day} < n < 2.2 \text{ revolutions/day}$ ),
- Eccentricity:  $0 < e < 0.08$ ,
- Inclination:  $52^\circ < i < 67^\circ$ ,
- Right ascension of the ascending node:  $0^\circ < \Omega < 360^\circ$ ,
- Argument of the perigee:  $0^\circ < \omega < 360^\circ$ ,
- Longitude:  $0^\circ < \lambda < 360^\circ$ .

We assume that the survey strategy provides an initial arc of four observations from one series of consecutive exposures, denoted as the discovery. The assumption of exactly four exposures for the determination of an initial orbit in the simulation does not exactly fit with the simulation of the survey (the survey simulation of cases A and C assume only at least 3 exposures). The effect may be considered as minor. The quality of the determined initial orbit does not benefit very much from the fourth observation. The elimination of false detection, like cosmic ray events etc., is, however, much easier. This performance evaluation does also show how many exposures of a simulated reference object can be acquired on the average.

We estimate the angular differences between the positions calculated from the first orbit determination results and the “true” orbits of the synthetic population. From these differences we determine the maximum time until this angular difference reaches a limit of FoV/2 of the tasking telescope ( $1.5^\circ$ ). Assuming that all follow-up observations of the object during the estimated time could be correlated with the discovery arc, we simulate a first follow-up observation and determine the orbit. With these results we determine the time for the second follow-up observation. The analysis is repeated for the third and fourth follow-up observation. We initialise the orbit determination by assuming a circular orbits, but the subsequent orbit improvement step then returns a full-parameter orbit.

We simulate all of the follow-up observations in a similar way as the observations of the survey strategy: one series containing five observations spaced by 2 s in time. The astrometric error was again assumed to be  $1''$ . However, as we may select the observation strategy for the follow-up observations independently from the survey strategy, the selected strategy has room for improvements, in particular concerning the number and temporal spacing of observations.

Figure 5.26 shows the results of the initial orbit determination. We conclude that the first follow-up observation has to take place at least 1 h (0.042 days) after discovery (the maximum angular difference after 1 h is about  $1.5^\circ$ ).

A successful follow-up observation after 1 h was simulated and leads to the residuals in Fig. 5.27. We see that the second follow-up observation must be scheduled 2 h after the discovery in order to guarantee a successful re-acquisition.

The orbit determination taking two successful follow-ups 1 h and 2 h after the discovery was used to generate Fig. 5.28. The third follow-up should be scheduled about 12 h after the discovery, if the visibility conditions allow it. For 99% of all objects a third follow-up is feasible up to 24 h after discovery.

Figure 5.29 gives the results of the orbit determination after the third follow-up observation, 12 h after the discovery. The orbit is now good enough to include additional perturbing forces in the orbit determination, namely direct radiation pressure, as well as a better model for the gravity field of the

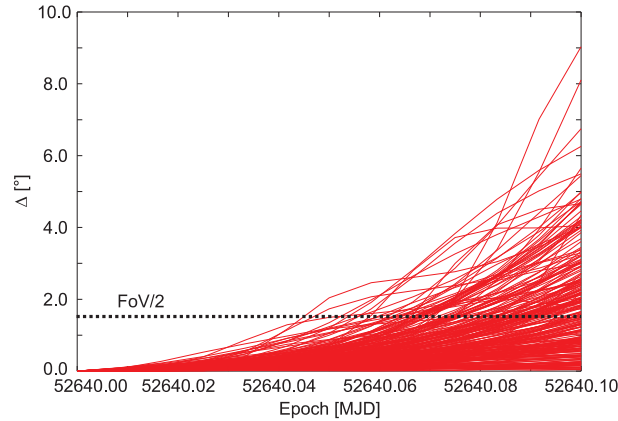


Figure 5.26: Residuals of position differences between initial orbit determination results and the original synthetic MEO population.

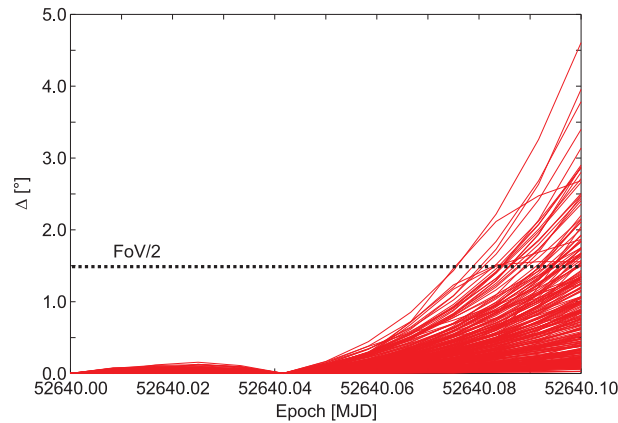


Figure 5.27: Residuals of position differences between orbit determination results after the first follow-up observation ( $t_0+1$  h) and the original synthetic MEO population.

Earth. Figure 5.30 covers the obtained position differences for 5 days. The results show that the orbit can now (after three successful follow-up observations) be considered as “secured”. This means that a re-acquisition after several weeks is sufficient. This re-acquisition can be part of the normal survey procedures not requiring additional follow-up observations using the dedicated tasking facilities.

The simulation results of a fourth follow-up observation, 24 h after the discovery (Fig. 5.31) show that there is a slight improvement achieved compared to the results after the third follow-up observations. For most of the objects the position differences calculated from the “true” and the determined orbit are below  $0.1^\circ$  over 30 days.

The proposed MEO follow-up schedule is thus  $t_0+1$  h,  $t_0+2$  h, and  $t_0+12$  h, where  $t_0$  is the epoch of discovery. All three follow-up observations must be available to “secure” the object. The survey procedure does not provide observations at these epochs, which is why follow-ups from tasked observations are required. A fourth follow-up after 24 h is expected to be part of the survey procedure.

However, even as this “orbit acquisition” period is surprisingly short, the follow-up requirements cannot be relaxed further without risking to lose the object. Allowing that only 95% of the objects are recovered

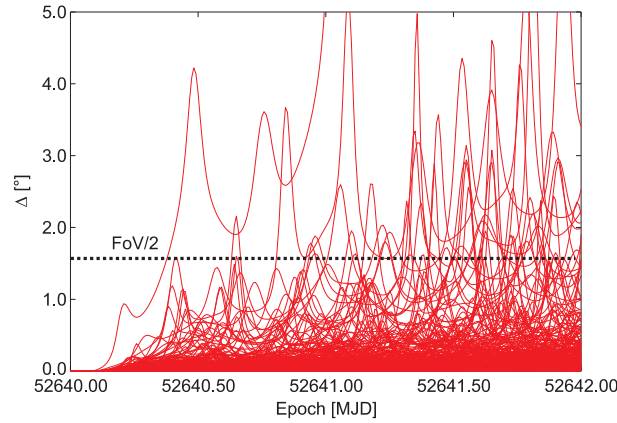


Figure 5.28: Residuals of position differences between orbit determination results after the second follow-up observation ( $t_0+2$  h) and the original synthetic MEO population.

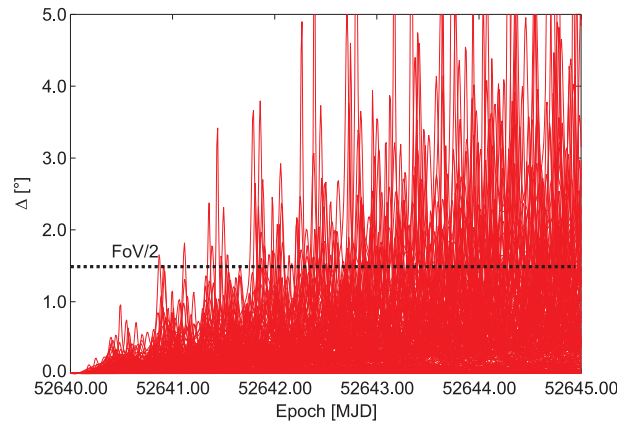


Figure 5.29: Residuals of position differences between orbit determination results after the third follow-up observation ( $t_0+12$  h) and the original synthetic MEO population, assuming a simple model of the perturbing forces.

12 h after the discovery, the first and second follow-ups may be performed earlier at  $t_0+45$  min and  $t_0+90$  min.

A successful re-acquisition after 30 days can be guaranteed with an orbit determined from the discovery, the first, second, and third follow-up. Maintenance observations are thus sufficient once in about 30 days to keep the catalogued orbit “secured”. The proposed survey strategy already provides observations, which are used for catalogue maintenance.

We conclude that for MEO space surveillance the “survey only” strategy is not able to provide the necessary follow-up observations for new discoveries. A combined survey and follow-up strategy is required, as it is already the proposed strategy for GEO space surveillance.

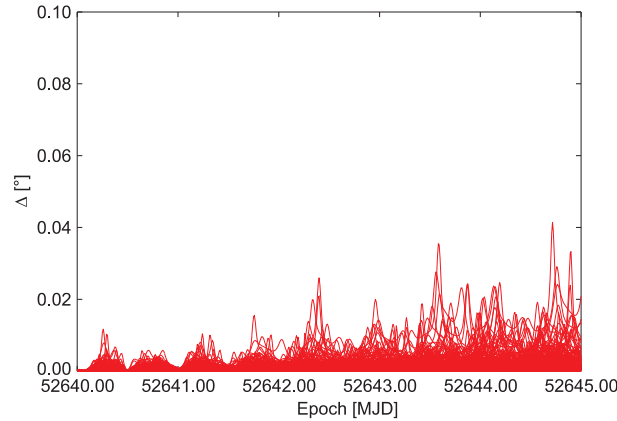


Figure 5.30: Residuals of position differences between orbit determination results after the third follow-up observation ( $t_0+12$  h) and the original synthetic MEO population, assuming a sophisticated model of the perturbing forces.

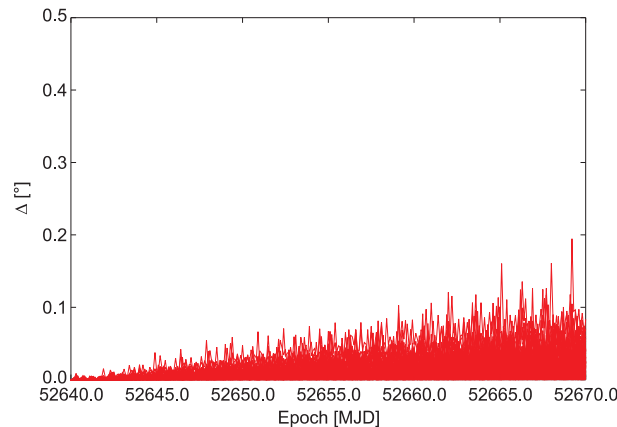


Figure 5.31: Residuals of position differences between orbit determination results after the fourth follow-up observation ( $t_0+24$  h) and the original synthetic MEO population, assuming a sophisticated model of the perturbing forces.

### 5.3.3.6 Applicability of the GEO sensor network to survey the MEO population

It is interesting whether the proposed GEO sensor network can also contribute to observe the MEO. Dedicated MEO observation strategies focussing at higher declination angles, where the apparent spatial object density is higher (Schildknecht et al., 2009), are entirely not compatible with GEO observation strategies.

Optical observations acquired for GEO space surveillance may only partly be suitable for detecting MEO objects larger than 1 m in diameter. These objects are bright enough to be detected by the GEO survey sensor, but do of course not show GEO-like FoV crossing characteristics in a GEO survey. MEO objects cross the FoV rapidly, so that likely not the minimum of three consecutive observations is available for initial orbit determination.

It is expected that during the spare time between GEO follow-ups, all necessary MEO follow-ups could

by carried out by the GEO tasking sensors. The analysis of the tasking network proposed for GEO space surveillance showed that at least 65% of the observation capacity is not used. There is enough spare sensor time available, as the expected number of MEO objects is smaller compared to the number of GEO objects.

### 5.3.4 Summary

Observation strategies for GEO and MEO space surveillance have been developed. For both cases optical observations from CCD-equipped telescopes are required. We recommend to perform a combined survey and follow-up strategy for both, the GEO and MEO region. Dedicated telescopes for survey and follow-up observations are needed. The most promising survey strategy in both cases is based on a stripe-scanning technique. For the GEO survey a stripe of fixed right ascension has to be covered continuously, whereas for the MEO survey a stripe at low declination has to be observed continuously.

Follow-up observations from a network of tasking telescopes (shared for GEO and MEO observations) are needed to perform orbit improvement prior to inserting the determined orbital elements into a catalogue. For objects in GEO three to four arcs of about 2 minutes each, spanning  $\approx 3$  h in total, are needed, plus one additional track in the following night. Candidate MEO objects require follow-up observations after 1 h, 2 h, and 12 h after their discovery in order to catalogue the detection.

For catalogue maintenance each object must be re-observed at least every 30 days if the object is in GEO. The same is true for objects in the MEO, but the proposed survey observations will implicitly provide maintenance observations more frequently. The GEO and MEO systems are proposed to use the same centralised architecture for data management and processing. In addition to the GEO system consisting of four sites each equipped with two 0.5 m telescopes for survey and tasked observations, additional survey sensors are needed for MEO space surveillance. For MEO two survey sensors, spaced by  $90^\circ$  in longitude, are proposed to carry out all necessary survey operations. The covered longitude range is set by the re-acquisition time of a particular field. The GEO follow-up network can be used for the tasked observations of the MEO, too. The network of follow-up telescopes may also be used for the acquisition of the more frequent dedicated observations for supporting conjunction analysis, and for the detection of newly launched objects, fragmentation events and manoeuvres.

The PROOF simulations of the proposed space surveillance strategies using the proposed sensors and a reference population reveal that for both regions a nearly complete coverage can be guaranteed within a short time, and that a catalogue of orbital elements can be built up from scratch and maintained in time. With the three proposed sites over 85% of the existing catalogue of the GEO region could be covered; with the fourth site the coverage is above 95%. The remaining coverage leak results from the bad coverage of the GEO ring between the Canaries and Marquesas Islands (over America), and from the problems observing rapidly drifting objects. The coverage of the MEO can be considered as nearly complete already after 30 days, if survey results from two sites are combined. The accessible population during a single night is about 50% from a single sensor, and more than 80%, if the observations from one night from two survey sites are combined.

With the proposed 0.5 m telescopes for GEO and with the proposed 0.8 m telescopes for MEO the minimally detectable object diameter is below 1 m, even for bad conditions. The wide-FoV allows 8 days repeatability of observations in GEO. For MEO up to daily repeatability is possible.

All simulations assume that a non-ambiguous correlation is possible, as no established concept for correlating the observations with the catalogue exists yet.

Observation strategies should always be implemented in a way to anticipate changes in the covered environment, and be able to react to refined requirements from the cataloguing or object characterisation processes.



## 6. A system proposal for space-based optical space surveillance

In this chapter we analyse how space-based optical observations, in particular acquired by the proposed SBO architecture, could contribute to fulfil SSA tasks. We focus on the space surveillance task surveying and tracking. This chapter is based on an analysis by Flohrer et al. (2011a).

In Sect. 2.5.2.3 we introduced the SBO sensor architecture, and briefly reviewed the performance for the observation of small-sized space debris. We discussed the SBO observation strategy, and the various aspects of the expected performance in more detail in Sect. 4.4 as an example for the capabilities of the developed simulation environment. Special aspects of initial orbit determination have already been addressed in Sect. 4.2.2.2.

Possible efficient observation strategies for space surveillance applications of the SBO shall be studied in Sect. 6.1. A detailed discussion has the focus on the SBO instrumentation as a secondary payload placed onboard an Earth-observation satellite in a circular sun-synchronous orbit (SSO) at 800 km altitude. We discuss the observation conditions for objects at higher altitude. In Sect. 6.2 the radiometric characterisation of the SBO instrument and the selected observation scenario are analysed. We derive the detectable object diameters. The coverage of a reference population, and an assessment of the covered arc lengths of individual objects is discussed in Sect. 6.3. This discussion is of particular interest for the simulation of orbit determination, correlation, and cataloguing, which are addressed in Sect. 6.4. With realistic noise levels known from the SBO design we study first orbit determination for sample objects and derive requirements for a correlation process.

### 6.1 SSA-related observation strategies with the SBO architecture

To answer the question how the SBO instrument contributes to SSA-related tasks, we first have to identify efficient operation scenarios. The SBO observation scenario (see Sect. 4.4) is not useful, because sampling a space debris population statistically while striving to detect very small objects in the cm-regime is not a primary task of space surveillance. The definition of an appropriate observation strategy is instead driven by the central need of space surveillance, the build-up and maintenance of a catalogue of orbital elements. In a given space surveillance regime the observation of an object, which is larger than a given diameter, has to be performed at least with a certain re-acquisition frequency. The related uncertainties of the observations have to allow for a successful and unambiguous correlation with other observations of the same object. In other words, the observation strategy has to be “leak-proof” (Krag et al., 2010). This is to ensure the timely detection of manoeuvres, fragmentation, or release events related to the covered objects. Furthermore, the cataloguing process sets requirements on the accuracy of the observations, which in case of optical observations may be sufficiently described by the astrometric

accuracy of the centroid determination of a single observation. This description assumes that any other sensor noise, in particular any epoch registration accuracy, is incorporated in the astrometric accuracy.

A steerable sensor requires a dedicated satellite mission, which is beyond the current European SSA objectives, mainly because of the expected costs. We assume that a flight opportunity on a three-axis stabilised platform will allow to carry the SBO instrument as a secondary payload. Only two promising pointing scenarios can be derived for the observation of satellites in higher altitudes from such a space-based platform for a fixed-mounted sensor:

- A phase-angle-optimal pointing, i.e., a pointing orthogonal to a SSO, which is “easily” obtained, if the sensor is mounted on an Earth-observation satellite orbiting close to the terminator. Remote sensing satellites carrying a radar, or photometric experiments, such as the MOST satellite, operate in such a SSO. The very good accessibility to the acquired data from high-latitude ground stations in terms of timeliness of ground contacts and duration of passages is a key advantage of the high-inclined SSOs. From the limited information available about the Canadian SAPPHERE mission we assume that such a pointing scenario has been selected for this mission, as well (Maskell and Oram, 2008).
- A pointing in flight direction from a low-inclination orbit, which would be the best choice if no ground stations at high latitudes are available. This strategy would, however, give a poor scanning performance for high altitude orbits, because only little observation time with favourable phase angles is available. This strategy complicates the observation scheduling and operation, and the sensor design, because the Sun may cross the sensor’s FoV.

Both observation strategies will face the problem of having many objects in the FoV in parallel, which is a frequent issue for larger FoV diameters. A detailed discussion of this issue is not within the scope of our work. We assume that available data processing methods, such as directly forming short arcs through the already mentioned “dynamic masking” approach (as outlined, e.g., by Schildknecht (2007)), or a probabilistic data/track association (DeMars and Jah, 2009; DeMars et al., 2010), allow it to solve this critical issue.

We assume that high-latitude ground stations are available for European missions, and that a flight opportunity onboard a “classical” Earth-observation satellite will be used. We therefore focus on the analysis of a SBO-like sensor orbiting in a circular SSO at 800 km altitude, resulting an inclination of  $98.57^\circ$ .

For selecting the optimal pointing direction of such a mission, we have to consider the following core parameters:

- expected dwell time of objects in the sensor FoV: longer observed arcs usually yield better initial orbit determination results,
- expected angular velocity of objects crossing the FoV: slower objects provide better astrometric accuracy of observations, as the objects appear point-shaped and/or the exposure time can be longer, which also increases the SNR and in turn the sensitivity,
- overall accessibility of a given population: either the inability to access low inclination orbits, and/or the short coverage of some inclination bands may have an adverse effect,
- re-acquisition time for a single object,

- avoidance of unfavourable observation conditions, such as a pointing direction into the Earth's shadow, or close to the Earth's limb, or into the Milky Way.

Fix-mounted sensors make it impossible for space-based sensors to actively track objects. Objects can only be observed while crossing the sensor's FoV. Depending on the relative angular velocity of the object with respect to the line-of-sight and the exposure rate, short observation arcs are formed from several acquired position measurements of the object. The quality of the initial orbits determined from the short arcs is primarily a function of the arc length and the astrometric accuracy of the individual measurements - the number of measurements forming the arc is only a secondary issue. Subsequent improvement of the initial orbits is required, e.g., to maintain the orbits in a catalogue (see Sect. 5.3.1). A space-based survey strategy using the SBO cannot rely on scheduled follow-up observations of given objects, because of the inability to steer the telescope. It is, however, possible to implement implicit follow-up capabilities, if the re-observation of objects is guaranteed to be frequent enough to ensure meeting the follow-up requirements.

We decided to focus on the analysis of GEO as the main application, because the few MEO objects are expected in a much larger spatial volume (Sect. 3.2.2), and because MEO observation strategies are incompatible with observing GEO.

Considering the tasks set by the SSA goals we have to keep in mind that a larger part of the GEO population will not be instantaneously accessible from a single space-based platform. A fix-mounted sensor operated according to a "survey only" observation strategy is not capable of acquiring observations of selected objects at any selected epoch, and fails to support the more challenging SSA tasks for the entire GEO population, such as timely manoeuvre and event detection, launch support and verification of orbit insertion. In addition, the avoidance of unfavourable observation conditions imposed by the position of the Earth's shadow, or pointing into the Milky Way, is not possible with a fix-mounted sensor operated as a secondary payload.

Let us now consider a pointing orthogonal to the orbital plane at 800 km altitude. This pointing ensures small phase angle conditions throughout the whole operational life for dusk-dawn orbits. To support this pointing scenario the sensor's line-of-sight shall point to an azimuth of  $90^\circ$  in the local satellite coordinate frame. Figure 6.1 shows the effect of the elevation of the pointing direction for a sensor orbit with the ascending node at  $90^\circ$  in an inertial frame, while Fig. 6.2 gives the complementary situation in an Earth-fixed frame. In both figures the projection of the  $6^\circ$  FoV at GEO distance is shown for elevation angles of  $-5^\circ$ ,  $0^\circ$ , and  $+5^\circ$ . An inclination of the sensor orbit different from  $90^\circ$  does not allow it to centre the FoV during a full sensor orbit at declination angles, namely to point to  $i = 0^\circ$  GEO objects continuously. Depending on the elevation angle the radius of the projection scanning circle at GEO distance will be different. The scanning circle is found to be minimum for  $\approx -9.6^\circ$  elevation. Obviously, low elevation pointing directions (below about  $-5^\circ$ ) cannot acquire the controlled GEO satellites at  $0^\circ$  inclination, which is, however, a densely populated and interesting sub-region. If the selected elevation angle is too large, a significant portion of the scanning volume is outside the GEO-belt, and, in addition, the intersection with the controlled GEO satellites is limited to two rather short crossings. We conclude that a positive elevation angle between  $0^\circ$  and  $+5^\circ$  is a good compromise between population coverage and dwell time of individual objects in the FoV. We will nevertheless analyse all of the three elevation angles in more detail.

Pointing into the Earth's shadow occurs for all considered pointing scenarios, but this is unavoidable because of the telescope cannot be steered. The diameter of the Earth's shadow at GEO distance is less than  $10^\circ$  and will move between the solstices from about  $-23.5^\circ$  to  $+23.5^\circ$ . Hence the Earth's shadow

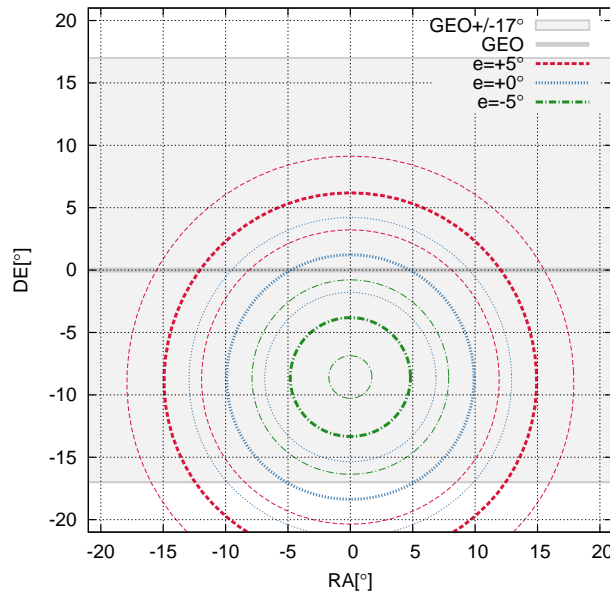


Figure 6.1: Covered regions in the GEO vicinity from a fix-mounted sensor with a  $6^\circ$  FoV onboard a platform orbiting in an 800 km circular SSO. Pointing direction is orthogonal to the orbital plane with different elevation angles. Three different of the pointing direction are colour-coded.

will affect only a fraction of the observations during a revolution of the sensor platform, and only for limited periods within the year.

## 6.2 Radiometric characteristics of the SBO observing high altitudes

The expected detection limits and, accordingly, the observation frequency depend on the SNR detection threshold of the on-board object detection algorithm (see Sect. 3.3.2.5). The SBO study concluded that a limiting magnitude of about 16 mag is required in the selected observation scenario to detect 95% of the considered small-sized space debris. The limiting (peak) SNR value to detect 95% of all objects is about 4 for the GEO case.

As the simulation of the sensor performance is closely connected to the definition of the observation strategy we need to make assumptions for phase angles and angular velocities of objects crossing the FoV. We show later on in this section that these assumptions are met.

Figure 6.3 shows that the optimum exposure time is at the order of  $t=1-2$  s. For longer exposure times no significant gain is expected in the SNR, as the sensor is operated in a sky-background dominated environment. The figure assumes the object to be of apparent magnitude  $m_v=14$  mag (which refers to a 1.9 m spherical object with Lambertian scattering and a Bond albedo of 0.1 in GEO observed from a 800 km SSO under a phase angle of  $15^\circ$ ), and assumes instrument optical efficiency  $\varepsilon=0.50$ , quantum efficiency of detector  $QE=0.80$ , sensor effective aperture  $D=0.20$  m, focal length  $f=0.35$  m, pixel size  $d=18.00$   $\mu\text{m}$ , diameter of point spread function for 80% encircled energy  $d_{PSF}=1.00$  pixel, angular velocity of object  $v_{ang}=60.00$   $''/\text{pixel}$ , read-out noise  $\rho=3.80$   $\sqrt{e^-}$ , dark current  $\delta=10.00$   $e^-/\text{pixel}/\text{s}$ , and a

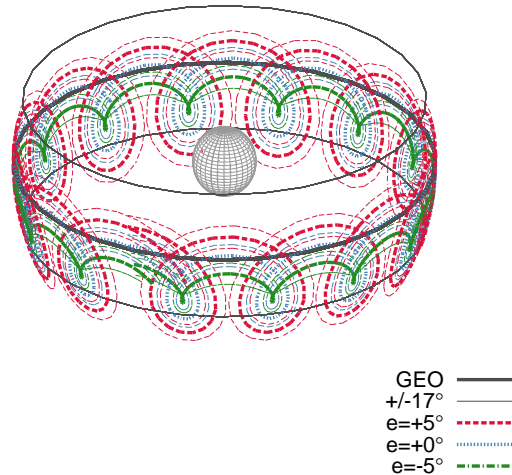


Figure 6.2: Pointing centre directions intersecting GEO distance in an Earth-fixed frame during 24 hours, assuming a fix-mounted sensor onboard a platform orbiting in a 800 km circular SSO. Pointing is orthogonal to the orbital plane.

binning factor of 1. The typical sky background for space-based observations is expected to be better than  $m_v=21$  mag/arcsec<sup>2</sup>.

Fully exploiting the SBO instruments capabilities for observing the GEO regime from a SSO will allow the detection of 16 mag objects, if the SNR detection threshold is around 4. Figure 6.4 shows the resulting SNR for a single pixel for varied sky background conditions for different object brightness. An apparent brightness of 16 mag corresponds to a 0.77 m Lambertian scattering spherical object with Bond albedo of 0.1 in GEO observed from a 800 km SSO under a phase angle of 15°.

We will now show that the assumptions made in the SNR estimation are valid. The linked simulation results will also be used to discuss the population coverage and cataloguing statistics in the next sections. The first step of the performed simulation of GEO observations uses 4 TLE snapshots, taken from the DISCOS catalogue of a certain epoch, filtered for GEO objects (mean motion between 0.9 and 1.1 rev/day). Each snapshot is used to simulate observations spanning 10 days. The selected simulation parameters are given in Table 6.1. PROOF provides the FoV crossing statistics together with estimates of the radiometric observation conditions for the selected reference population during the simulation period.

Figure 6.5 shows the angular velocity between objects and the sensor's line-of-sight as a function of the observation epoch for three elevation pointing angles. Positive elevation pointing of +5° result in angular velocities up to about 120''/s, while horizontal pointing directions result in angular velocities of typically 60''/s. The smallest angular velocities are expected from negative elevation angles, between about 20''/s and 40''/s. In all cases the object streaks can be expected to stretch only over a few pixels, if the exposure time is 1 to 2 s. The figure also indicates variable crossing rates during the year, which we will discuss later.

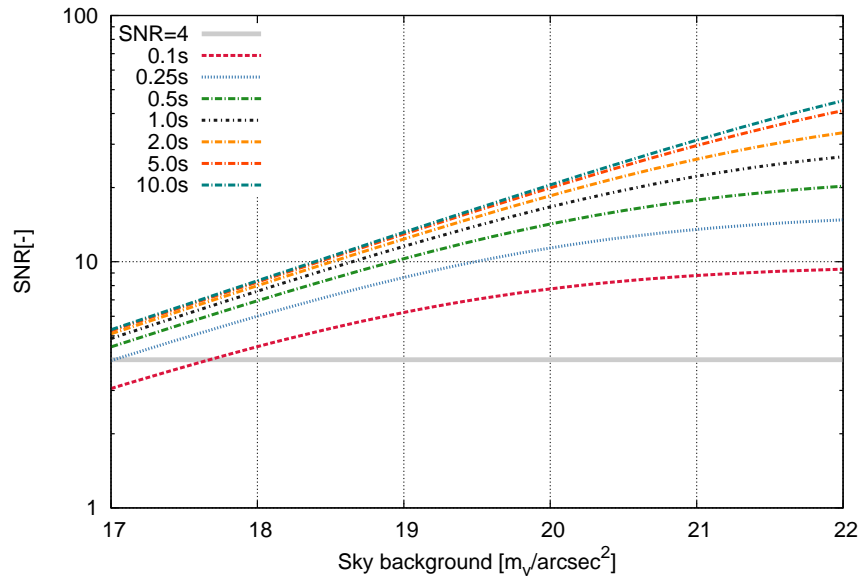


Figure 6.3: SNR of moving source with an apparent brightness of 14 mag as a function of the sky background brightness for different exposure times  $t$ .

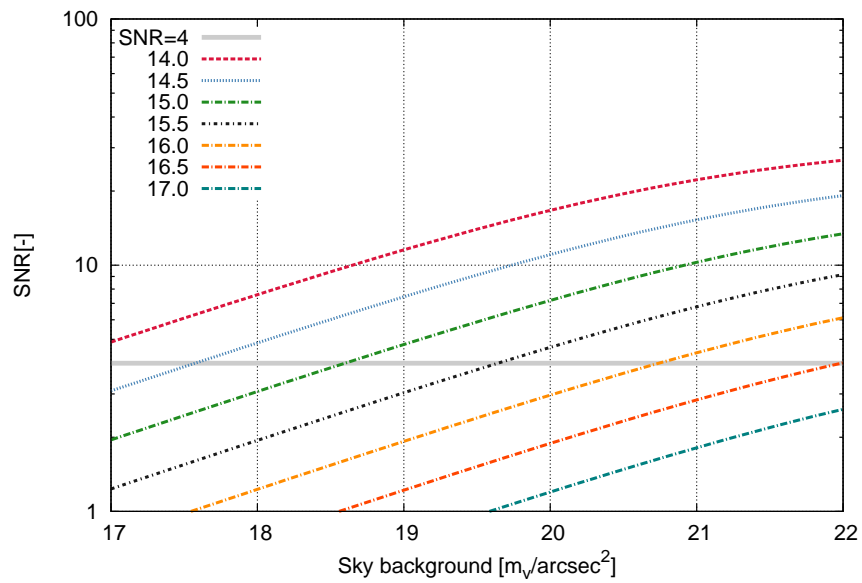


Figure 6.4: SNR of moving source of different apparent brightness as a function of the sky background brightness for exposure time  $t=1$  s.

Table 6.1: Simulation parameters using a TLE population of GEO objects.

Simulation	Jul	Oct	Jan	Apr
Simulation time (00:00 - 00:00)	2009 Jul 2 - 2009 Jul 11	2009 Oct 1 - 2009 Oct 10	2010 Jan 1 - 2010 Jan 10	2010 Apr 2 - 2010 Apr 11
Epoch of TLE snapshot	2009 Jul 16	2009 Oct 13	2010 Jan 11	2010 Apr 6
Number of objects	1014	1021	1027	1032
$\alpha$ of Sun at first epoch [h]	6.74	12.48	18.75	0.75
Orbit at first epoch	$a=7178\text{km}, e=0, i=98.57^\circ$			
$\Omega$ at first epoch [deg]	191.10	277.20	11.25	101.25

Figure 6.6 shows the range of phase angles and the angular velocities. The phase angles are small throughout the entire year, the lowest values are at  $\approx 35^\circ$  for the three pointing scenarios. Daily variations are very small, of the order of the diameter of the FoV for the horizontal pointing scenario. We advise to select  $15^\circ$  as the annual average value for the phase angle. A stable band of characteristic angular velocities of GEO objects crossing the FoV can be obtained for each pointing scenario. It is reasonable to perform the analysis for the  $e=0^\circ$  and  $e=+5^\circ$  scenarios, because these scenarios result in small phase angles throughout the year with moderate angular velocities, but also guarantee stable rates of objects crossing the FoV.

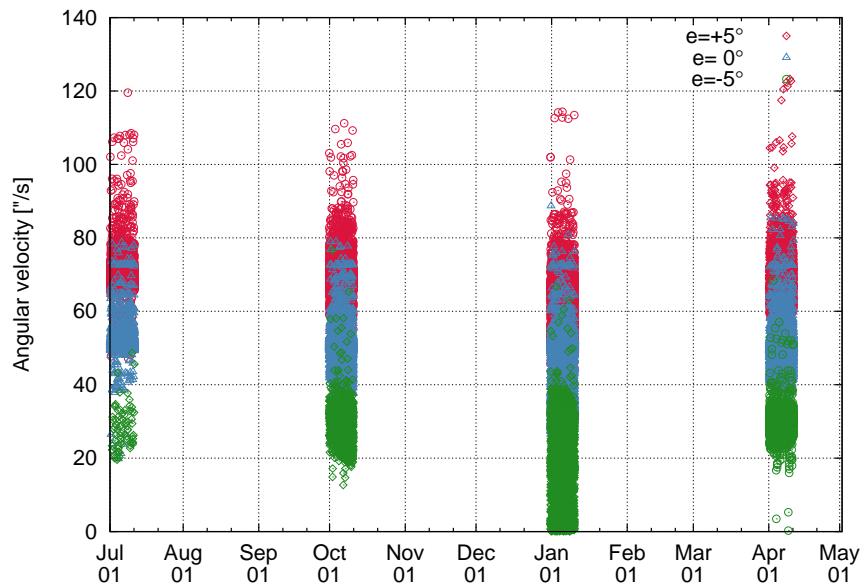


Figure 6.5: Angular velocities of TLE catalogue objects crossing the sensor's FoV as a function of the observation epoch for three elevation pointing scenarios.

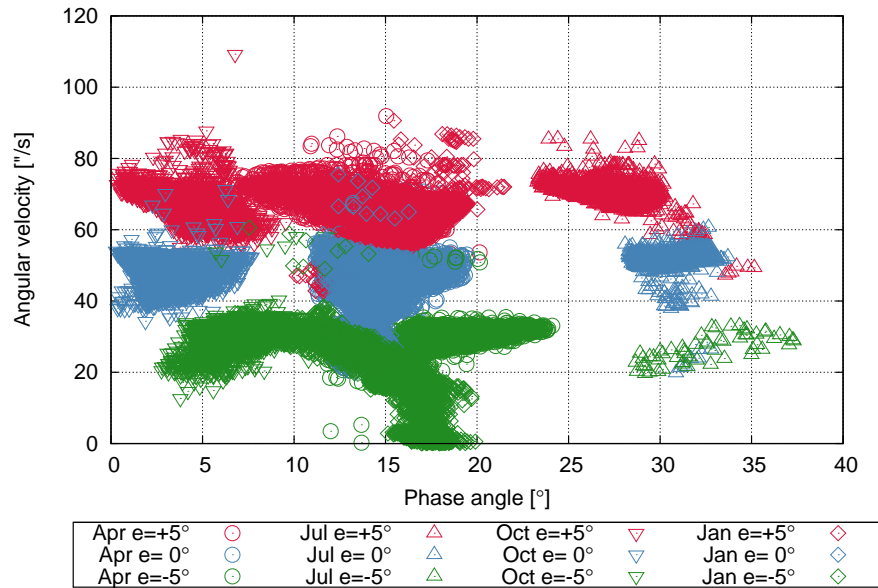


Figure 6.6: Angular velocities of TLE catalogue objects crossing the sensor’s FoV as a function of the phase angle at the observation epoch. Objects in the Earth shadow are excluded.

### 6.3 Coverage of reference populations

In this section we discuss the core performance parameters for space surveillance, i.e., the coverage of a reference population, the reacquisition period, and the covered arc lengths of individual objects. We use the simulation scenario of Table 6.1.

Table 6.2 and Fig. 6.7 give the covered catalogue fraction during the analysed observation batches of 10 days and allow it to draw a conclusion concerning the overall population coverage during the year. Nearly complete coverage of the reference population is possible at certain epochs for positive pointing angles. Pointing at negative elevation angles, on the other hand, does not lead to sufficient population coverage. During some periods (summer) the coverage is extremely poor. These results support the preliminary conclusions drawn when interpreting Fig. 6.1. The best overall coverage results are obtained for the  $e=+5^\circ$  pointing directions. The results furthermore show that only small number of objects are observed under invalid illumination conditions, the difference of the coverage ratios between covered and detected objects is usually less than 10%.

Figure 6.7 also shows that the majority of objects (for positive pointing scenarios) is at least observed every one to two days. The arc length per observation is at least half of the FoV of  $6^\circ$ . The interpretation of Fig. 6.7 is supported by Table 6.3, where we extract the average number of FoV crossing events, and the number of properly illuminated crossing events (“detections”) per object within 10 days from the simulation results. If only crossing events are considered, the differences between the three pointing scenarios are minor, as it is also the case between the four seasonal simulation scenarios. If the illumination conditions are considered, a particularly bad, but seasonally varying, coverage of the reference population is found. This is true in particular for the  $e=-5^\circ$  pointing scenario, but also partly for the  $e=0^\circ$  pointing scenario in October. The  $e=0^\circ$  pointing scenario is less sensitive to observing a larger portion of objects in the Earth’s shadow.

Table 6.2: Simulation results using deterministic (TLE) populations of the GEO regime obtained from PROOF-based analysis. Covered objects refer to objects crossing the FoV, while numbers of detected objects refer to covered objects illuminated at the observation epoch.

Simulation	1 (Jul)	2 (Oct)	3 (Jan)	4 (Apr)
Number of objects	1014	1021	1027	1032
Ignored TLEs	19	19	19	19
Covered objects $e=+5^\circ$	605 (61%)	988 (99%)	987 (98%)	992 (98%)
Covered objects $e=0^\circ$	451 (45%)	740 (74%)	986 (98%)	867 (86%)
Covered objects $e=-5^\circ$	11 (1%)	248 (25%)	629 (62%)	437 (43%)
Detected objects $e=+5^\circ$	588 (59%)	985 (98%)	982 (97%)	944 (93%)
Detected objects $e=0^\circ$	439 (44%)	682 (68%)	985 (98%)	788 (78%)
Detected objects $e=-5^\circ$	8 (1%)	4 (0%)	588 (58%)	401 (40%)

From Table 6.3 we expect that objects are detected in the FoV on average every one or two days, and the mean time between detections usually does not exceed 1.5 days, with the maximum gap of about 3 days. The smallest mean time, and also the smallest maximum time, between subsequent detections is achieved for the  $e=0^\circ$  pointing scenario. We are also able to extract the calculated mean, minimum, and maximum length of the observation arc per detection event. These numbers are important for the quality of first orbit determination. A longer observation arc leads to better initial orbit determination. We also expect that correlating well-determined short arcs will be more efficient. Table 6.3 shows that the average arc covered with detections of a single object is on average  $3^\circ$  to  $5^\circ$ , and cannot exceed  $6^\circ$ . The apparent seasonal variations are at least partly caused by the significantly different numbers of detections in the simulation run. The minimum covered arc is smallest for the  $e=-5^\circ$  pointing scenario (with about  $2^\circ$ ), and is comparable with the other two pointing scenarios with about  $2.5^\circ$  to  $3^\circ$ . These results allow it to further discuss the initial determination of orbits, and indicate that the maintenance of a catalogue of orbits with sufficient timeliness is possible.

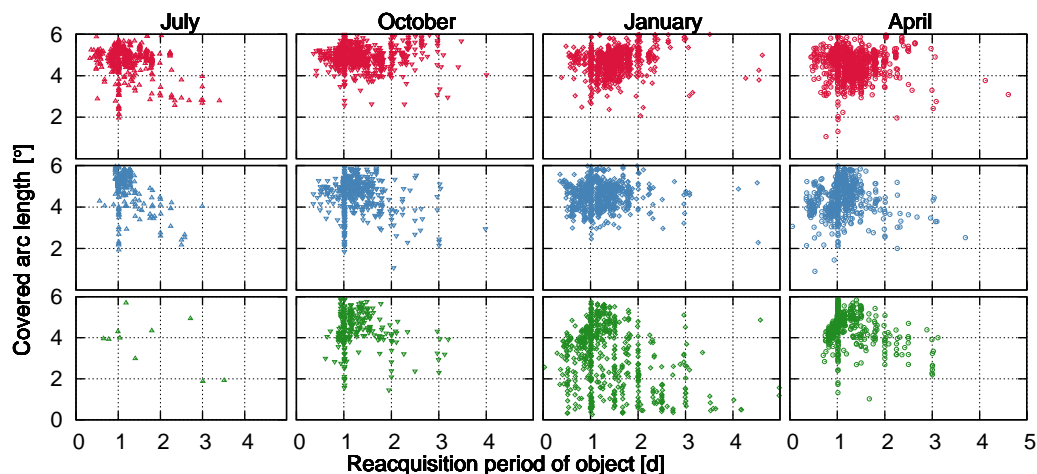


Figure 6.7: Reacquisition period compared to covered arc length, top row (red)  $e=+5^\circ$ , middle row (blue)  $e=0^\circ$ , bottom row (green)  $e=-5^\circ$ .

Table 6.3: Summary of the simulation runs: average number of FoV crossing events, properly illuminated crossing events (“detections”), object-wise calculated mean, minimum, and maximum time between re-acquisitions, and mean, minimum, and maximum observation length per short arc.

Simulation number (month)	1 (Jul)	2 (Oct)	3 (Jan)	4 (Apr)
	$e=+5^\circ$			
Crossings per object in 10d	$6.99 \pm 2.41$	$7.33 \pm 2.42$	$6.18 \pm 1.55$	$4.90 \pm 2.11$
Detections per object in 10d	$6.04 \pm 2.56$	$6.49 \pm 2.38$	$5.34 \pm 1.51$	$4.90 \pm 2.11$
Max detection gap [d]	$3.01 \pm 1.42$	$2.77 \pm 1.33$	$3.13 \pm 1.13$	$2.97 \pm 1.24$
Min detection gap [d]	$0.31 \pm 0.50$	$0.53 \pm 0.57$	$0.36 \pm 0.64$	$0.36 \pm 0.48$
Mean detection gap [d]	$1.21 \pm 0.49$	$1.30 \pm 0.48$	$1.44 \pm 0.58$	$1.32 \pm 0.44$
Max observation arc [°]	$5.71 \pm 0.80$	$5.92 \pm 0.35$	$5.89 \pm 0.41$	$5.84 \pm 0.49$
Min observation arc [°]	$2.86 \pm 0.94$	$3.08 \pm 1.11$	$2.83 \pm 1.14$	$2.50 \pm 1.17$
Mean obs arc [°]	$4.68 \pm 0.73$	$4.92 \pm 0.49$	$4.71 \pm 0.58$	$4.58 \pm 0.66$
	$e=0^\circ$			
Crossings per object in 10d	$8.48 \pm 2.04$	$7.54 \pm 2.69$	$7.84 \pm 2.38$	$5.07 \pm 2.69$
Detections per object in 10d	$7.87 \pm 2.28$	$2.85 \pm 1.63$	$6.99 \pm 2.41$	$5.07 \pm 2.69$
Max detection gap [d]	$1.65 \pm 0.88$	$2.06 \pm 1.33$	$2.39 \pm 1.50$	$2.26 \pm 1.56$
Min detection gap [d]	$0.94 \pm 0.19$	$0.74 \pm 0.55$	$0.50 \pm 0.64$	$0.60 \pm 0.50$
Mean detection gap [d]	$1.13 \pm 0.32$	$1.17 \pm 0.51$	$1.19 \pm 0.55$	$1.08 \pm 0.40$
Max obs arc [°]	$5.73 \pm 0.77$	$5.59 \pm 0.99$	$5.88 \pm 0.38$	$5.75 \pm 0.71$
Min obs arc [°]	$3.24 \pm 1.32$	$2.87 \pm 1.28$	$2.73 \pm 1.27$	$2.54 \pm 1.38$
Mean obs arc [°]	$5.05 \pm 0.82$	$4.74 \pm 0.95$	$4.74 \pm 0.68$	$4.66 \pm 0.83$
	$e=-5^\circ$			
Crossings per object in 10d	$5.83 \pm 3.56$	$6.88 \pm 2.99$	$6.01 \pm 3.43$	$6.82 \pm 3.34$
Detections per object in 10d	$4.67 \pm 3.94$	$0.02 \pm 0.13$	$5.04 \pm 3.30$	$6.82 \pm 3.34$
Max detection gap [d]	$2.86 \pm 2.01$	$2.15 \pm 1.28$	$3.00 \pm 1.90$	$1.88 \pm 1.23$
Min detection gap [d]	$0.49 \pm 0.49$	$0.80 \pm 0.60$	$0.68 \pm 1.28$	$0.80 \pm 0.66$
Mean detection gap [d]	$1.42 \pm 1.08$	$1.24 \pm 0.58$	$1.49 \pm 1.21$	$1.23 \pm 0.65$
Max obs arc [°]	$4.37 \pm 2.02$	$5.34 \pm 1.18$	$3.97 \pm 1.91$	$5.46 \pm 1.06$
Min obs arc [°]	$1.71 \pm 1.31$	$2.33 \pm 1.41$	$1.56 \pm 1.22$	$1.98 \pm 1.34$
Mean obs arc [°]	$3.32 \pm 1.55$	$4.28 \pm 1.01$	$2.93 \pm 1.57$	$4.35 \pm 0.90$

## 6.4 Orbit determination based on simulations

We use the simulation environment described in Sect. 4.3 connecting PROOF through its plug-in functionality to ORBDDET. PROOF was configured to simulate observations every second.

Five test objects were selected for initial orbit determination. The key characteristics for these objects are provided in Table 6.4. We determine initial orbits from single passes of each object on subsequent days. The initial orbits are determined for various astrometric noise levels, including a case without noise. We assume that the orbit without noise reflects the “truth”. The differences of the orbital elements to this “truth” are a measure for the quality of the determined orbit. This approach allows us to discuss the sensitivity of initial orbit determination as a function of the astrometric noise. We used BBNB2D for initial orbit determination together with a subsequent orbit improvement taking into account Earth’s

Table 6.4: Selected test objects for the simulation of the orbit determination.

Object ID	COSPAR ID	$a$ [km]	$e$ [-]	$i$ [°]	Remarks
858	1964-047A	42170	0.00015	6.3	Syncom 3, average inclination
33059	2008-022B	43548	0.05008	1.8	Zenith-3 third stage, higher eccentricity
23192	1994-047A	42631	0.00095	2.5	DirecTV-2, graveyard orbit
22563	1993-015A	42454	0.00057	17.5	USA 98 (UFO F1), high inclination
34710	2009-016A	42166	0.00044	0.0	Eutelsat W2A, controlled object

oblateness as a major perturbing force ( $C_{20}$ ) and using all simulated observations to determine the orbit in a least-squares adjustment process.

Figure 6.8 illustrates the results for the first test object. The figures for the other objects are provided in Appendix B (Figs. B.1 to B.4).

Orbit determination based on the selected observation scenario is possible. The results indicate consistent performance for the rather different orbits of the test objects, with one exception. The right ascension of the ascending node of the controlled object 34710 cannot be determined properly as it is almost singular for  $i \approx 0^\circ$ . The node is poorly determined or low-inclination orbits (see object 23192 and 33059). Non-singular elements should be used instead.

The simulation results also allow it to specify the input for a correlation algorithm trying to identify common observation arcs in the orbital element domain. Our results may enable the definition of performance requirements for a to-be-defined correlation process. From experience with ground-based sensors we know already that achieving a centroid determination below  $0.5''$  is a challenge for the wide FoV of the proposed SBO instrument. An astrometric accuracy of a single observation of at least  $1''$ – $1.5''$  should be achieved in order to keep  $\Delta a$  below a few hundred kilometres,  $\Delta e$  below 0.01, and  $\Delta i$  below  $0.1^\circ$ , which might be typical requirements of a correlation process using initial orbits. In any case, the correlation process needs to cope with outliers (large differences in the case of a poor initial orbit).

## 6.5 Conclusion

The space surveillance capabilities of the proposed passive, small, and comparably simple SBO instrumentation fix-mounted onboard an Earth observation satellite orbiting in an 800 km altitude SSO were discussed. The orbit is assumed close to the terminator plane. A pointing of the sensor nearly orthogonal to the orbital plane with an optimum elevation (between  $0^\circ$  and  $+5^\circ$ ) allows accessing the entire GEO regime within one day, implying a very good coverage of controlled objects in GEO, too.

From the simulation environment rates and properties of objects crossing the sensor FoV are obtained for four observation periods covering 10 days each for TLE snapshots from ESA's DISCOS database. The simulations reveal that the proposed pointing scenario provides low phase angles with small seasonal variations, but always below  $\approx 35^\circ$ , together with low angular velocities of  $\approx 60$ – $80''/s$ . The simulated

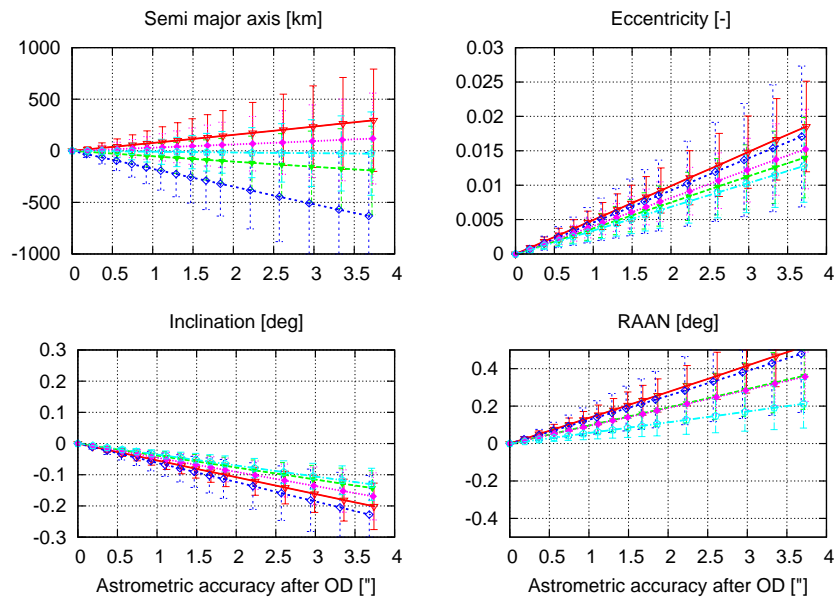


Figure 6.8: First orbit determination of object 858 for ten subsequent days. The figures show the difference for selected orbital elements (semi-major axis, eccentricity, inclination, and right ascension of the ascending node) w.r.t the “truth” (i.e., the orbit determination without astrometric noise).

brightness of objects indicate that 1 to 2 s exposure times are optimal for the assumed instrument. With these parameters the detection limit is equivalent to spherical objects in GEO with a diameter of at least 1 m in front of a dark background of  $m_v > 21$  mag/arcsec<sup>2</sup>. A nearly complete GEO population coverage can be reached under proper illumination conditions within a few days, but seasonal drops in the population coverage are possible. The mean gap between subsequent observations is usually shorter than 1.5 days and does not exceed a maximum of three days. A single observation arc spans 3° to 5° on average. The consistency of the initial orbits was checked for five selected test objects for ten subsequent days using different, but realistic astrometric noise. The initial orbit determination is possible for realistic noise levels. To ensure successful catalogue maintenance, the astrometric accuracy of a single observation should be at least 1''–1.5'', which allows to keep the consistency among the first determined orbits below a few hundred kilometres for the semi-major axis, below 0.01 for the eccentricity, and below 0.1° in inclination.

## 7. Conclusion and recommendations

We first introduced the concept of space situational awareness and the related space surveillance principles. We described the space debris problem and how the current ground-based and space-based sensors with surveillance capabilities help to tackle the challenges for a safe and sustainable operation of systems in space.

With the focus on optical systems we discussed in detail the fundamentals of observation techniques and introduced the relevant reference systems, orbital regimes, and the models for the motion and dynamics of Earth-orbiting objects.

We developed a simulation environment allowing an end-to-end assessment of optical observation strategy proposals. The simulation environment connects the tool PROOF, distributed by ESA, and the program system CelMech, developed by and maintained at the Astronomical Institute of the University of Bern. Currently, the correlation task of the toolchain is based on the assumption that a non-ambiguous correlation of the observations is possible. So far, no concept has been established for that purpose. Further research in this area is important. It should focus on correlation at the sensor level to form short arcs from survey observations, and on efficient methods for correlating short arcs among distributed sensors and for correlating short arcs with a catalogue. The handling of “no-shows” and the quick and robust detection of manoeuvres and fragmentation events should both be considered in the algorithm development. Validating the approach through the acquisition of real observations is a necessity and the related effort should not be underestimated. New developments as, e.g., by a team from the University of Pisa, should be considered that propose techniques combining correlation and initial orbit determination into a common, efficient and robust process.

Initial orbit determination is clearly one of the main challenges of space surveillance. The main limitations are due to the typically short arcs resulting from survey operations and the comparably large astrometric errors due to the large pixel scale of the used wide-FoV. We described and analysed an alternative approach for initial orbit determination that extends the boundary value search in the CelMech module ORBDET to a two-dimensional search. We find the method robust, highly flexible, and supporting observations from different sites. The method has clear benefits if the initial orbit from three observations is used to start a subsequent orbit improvement step taking into account all available observations. If the arcs are too short, the determination of a circular orbit with subsequent orbit improvement still is a viable alternative.

The developed toolchain is ready and well suited to support the on-going European studies and analyses related to space surveillance. We outlined the capabilities of the simulation chain through a study on the search for small-size (un-catalogued) space debris by passive space-based optical sensors in LEO and GEO. From the analysis of the characteristics of the FoV crossing objects we estimated the detection limits of the proposed 20 cm SBO instrument. We performed initial orbit determination and orbit improvement based on simulated observations taking into account empirical knowledge on the limits of the image processing. The system architecture developed in the framework of an ESA study on space-based

optical observations is only available in a pre-phase A state. From that proposal we found, however, that the detection of small-size space debris (smaller than 1 dm in diameter) is possible for three proposed operation concepts with the platform placed into LEO, subGEO or GEO, respectively. For all three concepts the acquisition of observations in front of a dark sky background is feasible. Seasonal variations in the detection efficiency are expected due to varying phase angle conditions. We predicted the highest detection rate for LEO, but with a sufficiently high SNR only for short distances. Initial orbits with an acceptable accuracy could be determined from a single FoV crossing event in all three concepts, but not for all detections. As initial orbits allow an estimate of the observation distance, the object diameter can be estimated using the distance- and phase-angle-corrected apparent brightness. We found that the monitoring of the un-catalogued space debris environment, in particular the validation of space debris environment models, would benefit from having in place such a comparably simple observation capability. We showed that operating the SBO instrument at GEO altitude would decrease the current (ground-based) minimum of the observed object diameter from 10–15 cm to below 5 cm.

We studied ground-based space surveillance strategies for GEO and MEO. Starting from a detailed analysis of the accessibility and observation characteristics of the relevant object populations we formulated the fundamentals for the classification and evaluation of such observation strategies. We discussed pure survey-only and combined survey and follow-up approaches for GEO and MEO. We identified the latter as the more realistic one, considering the available sensor design options and the anticipated requirements from a space situational awareness system. The main concerns ruling out the survey-only approaches, which work well for ground-based radars, are the initial cataloguing of newly found objects, and the necessity to detect manoeuvres and fragmentation events. We proposed stripe-scanning survey techniques based on CCD-equipped ground-based telescopes. For the GEO survey a stripe of fixed right ascension has to be covered continuously, whereas for the MEO survey a stripe at low declination has to be observed continuously. We showed that dedicated telescopes for survey and follow-up observations are essential. A global network of telescopes shall provide the needed follow-up observations for GEO and MEO objects after the survey detections. Specific follow-up schemes for orbit improvement prior the insertion of the object into the catalogue were described. For objects in GEO three to four observation arcs of about 2 minutes each, spanning  $\approx 3$  h in total, are needed, plus one additional track acquired in the following night. Candidate MEO objects require follow-up observations at 1 h, 2 h, and 12 h after their initial discovery. For catalogue maintenance each object must be re-observed once at least every 30 days. For objects in the MEO the proposed survey scenario may implicitly provide such maintenance observations more frequently. The proposed observation strategies are closely connected to the design of the assumed sensors, and to the network architecture. We assumed a centralised architecture for data management and processing. For the GEO observations we considered four sites, each equipped with two 0.5 m telescopes. In addition, two 0.8 m sensors, spaced by  $90^\circ$  in longitude, were proposed for the MEO observations.

We used PROOF simulations for an assessment of the proposed observation strategies. For both, GEO and MEO, a nearly complete coverage can be achieved within a short time. A catalogue of orbital elements can be built up from scratch and maintained. The catalogue coverage reaches over 95% for the GEO case, and already 85% if only three sites are available. Rapidly drifting objects are a challenge for the proposed survey strategy. For MEO the accessible population during a single night is already about 50% from a single sensor, and about 80%, if two sites are operating. The minimally detectable object diameter is below 1 m even for bad conditions, in both cases, GEO observations and MEO observations. The same objects may be observed within 8 days in the GEO proposal. A higher observation frequency is possible by adding more telescopes to the proposed sites, which increases the effective FoV by operating

---

in parallel with small pointing offsets. For MEO even a daily re-acquisition of objects is possible. Each definition and implementation of an observation strategy has to take into account possible changes in the covered environment, and hence should be ready to react to a redefinition of the requirements.

We finally applied the proposed SBO instrument to a concept of space-based space surveillance of the GEO. For that purpose the sensor is assumed to orbit as a secondary payload on-board a platform in a sun-synchronous orbit of about 800 km altitude. Such a sensor would provide a very good coverage of the GEO population in a short time and with frequent re-acquisitions. With the proposed simple continuous scanning of the GEO region the SBO instrument would be a valuable survey sensor. Due to the short revisit times, it could partly be seen as a tracking instrument, as well. The acquired data would contribute significantly to catalogue build-up and maintenance. We found that a space surveillance network would benefit from such a complementing passive space-based component.

Satellite observations by passive optical means were essential from the very beginning of the space age until the 1980s. In satellite geodesy these optical observations have now been replaced by other techniques. Only the space debris and Near-Earth Objects (NEOs) research communities, which use closely related techniques and methods, continued to work in this field. During the last decades they developed revolutionary new concepts from modern optical astronomy, such as electro-optical CCD detectors, digital image processing techniques, robotics, and sensor automation. Now, the growing interest from a wider group of stakeholders in space situational awareness and space surveillance led to a resurrection of research and technology development in the area of optical observation techniques. We are therefore confident that this new situation will, in the near future, open new opportunities for further studies on optical observations of satellites, hopefully leading to a global network of ground-based observation facilities complemented by space-based sensors. The author hopes that the work described here will stimulate future research and further developments in the field of space surveillance.



## A. Performance of initial orbit determination from space-based observations

This appendix gives in Figs. A.1 to A.3 the results of the comparison of the PROOF results to the results from the initial orbit determination for the performance assessment of a proposal for space-based observation system (see Sect. 4.4.4). As a function of the astrometric error the determined orbital elements for the a posteriori filtered successful IODs are presented for the original BNBNDV algorithm and the newly implemented BNBND2D algorithm. For the LEO cases we also report the results for the determination of a circular orbit.

Figures A.4 to A.13 give for 10 test objects (5 each for the GEO and LEO case) the results of a detailed evaluation of the BNBND2D algorithm (see Sect. 4.2.2.2). Grouped by the assumed astrometric noise, the relative frequency of the differences between the determined and input orbital elements  $a$ ,  $e$ ,  $i$ , and  $\Omega$  is presented. The middle epoch  $t$  was varied from  $t_A$  to  $t_B$  for each simulated observation. One observation per second has been simulated.

A Performance of initial orbit determination from space-based observations

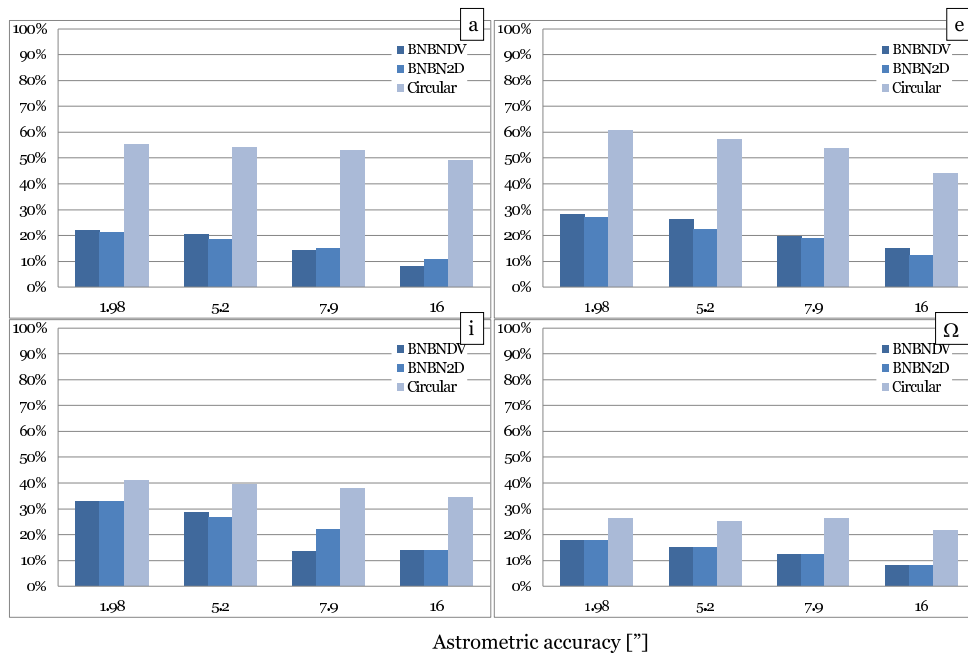


Figure A.1: LEO case, percentage of 'accepted' IODs with respect to the total number of successful IODs (after filtering).

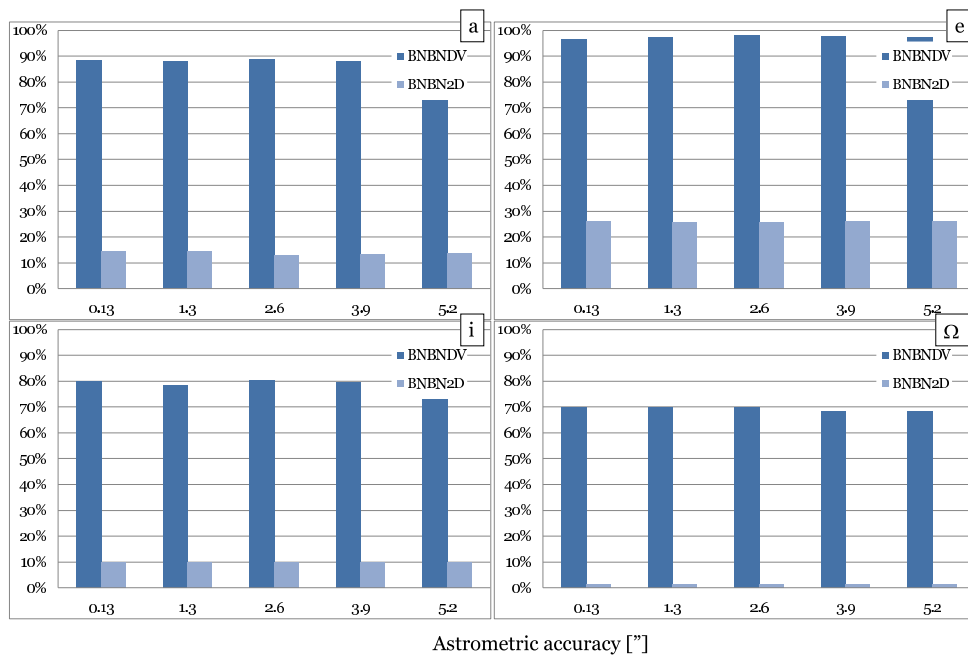


Figure A.2: SubGEO case, percentage of 'accepted' IODs with respect to the total number of successful IODs (after filtering).

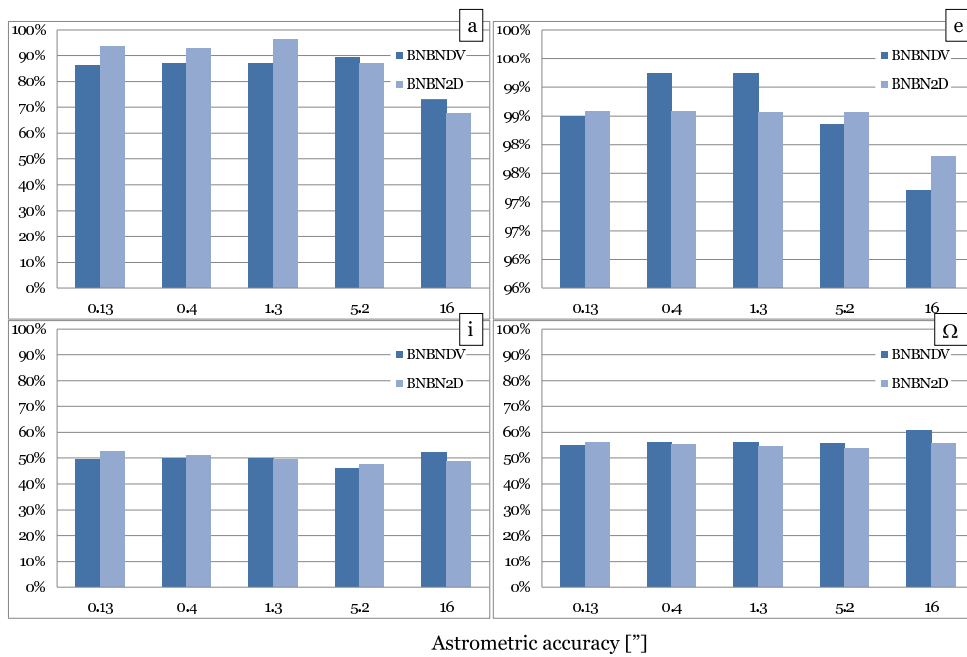


Figure A.3: GEO case, percentage of 'accepted' IODs with respect to the total number of successful IODs (after filtering).

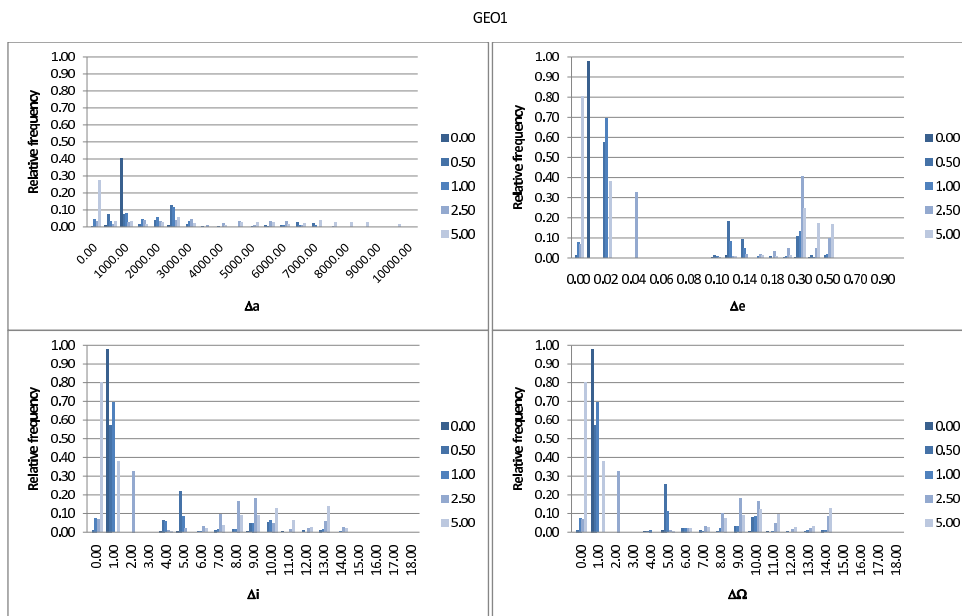


Figure A.4: Relative frequency of the differences between the determined and reference orbital elements semi-major axis  $a$  [km], eccentricity  $e$  [-], inclination  $i$  [°], and right ascension of ascending node  $\Omega$  [°], grouped by the assumed astrometric noise ["/], for the test object GEO1.

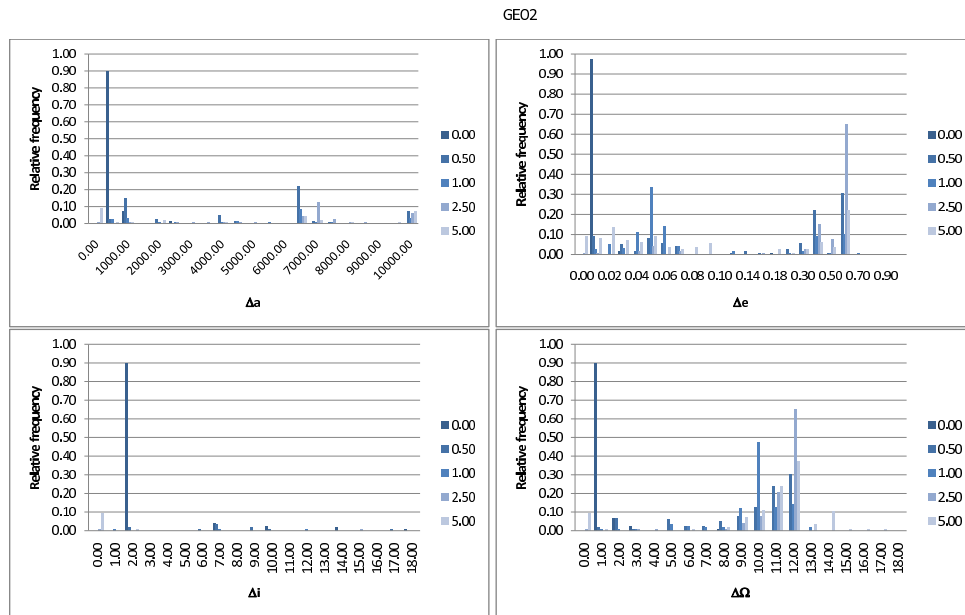


Figure A.5: Relative frequency of the differences between the determined and reference orbital elements semi-major axis  $a$  [km], eccentricity  $e$  [-], inclination  $i$  [°], and right ascension of ascending node  $\Omega$  [°], grouped by the assumed astrometric noise [″], for the test object GEO2.

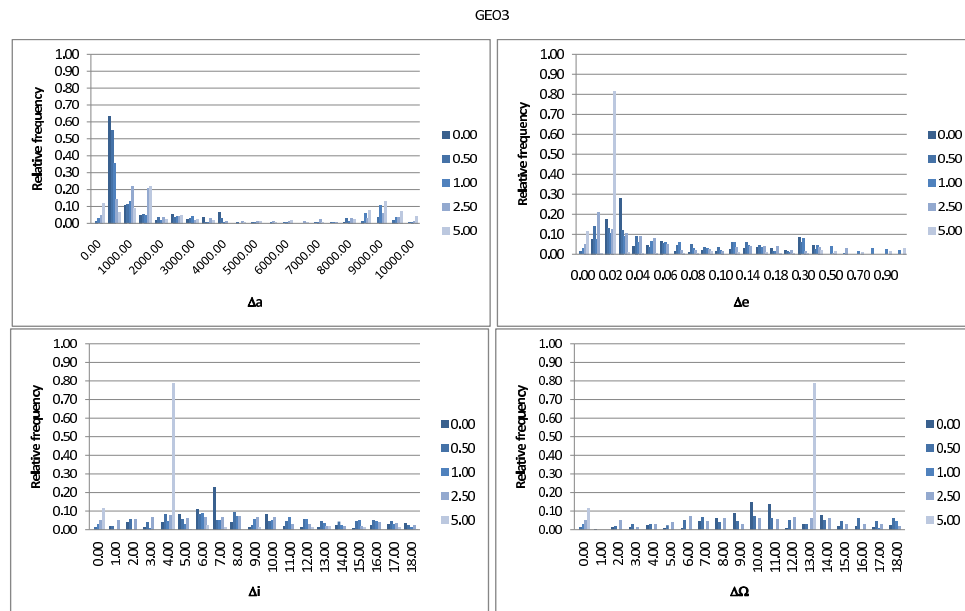


Figure A.6: Relative frequency of the differences between the determined and reference orbital elements semi-major axis  $a$  [km], eccentricity  $e$  [-], inclination  $i$  [°], and right ascension of ascending node  $\Omega$  [°], grouped by the assumed astrometric noise [″], for the test object GEO3.

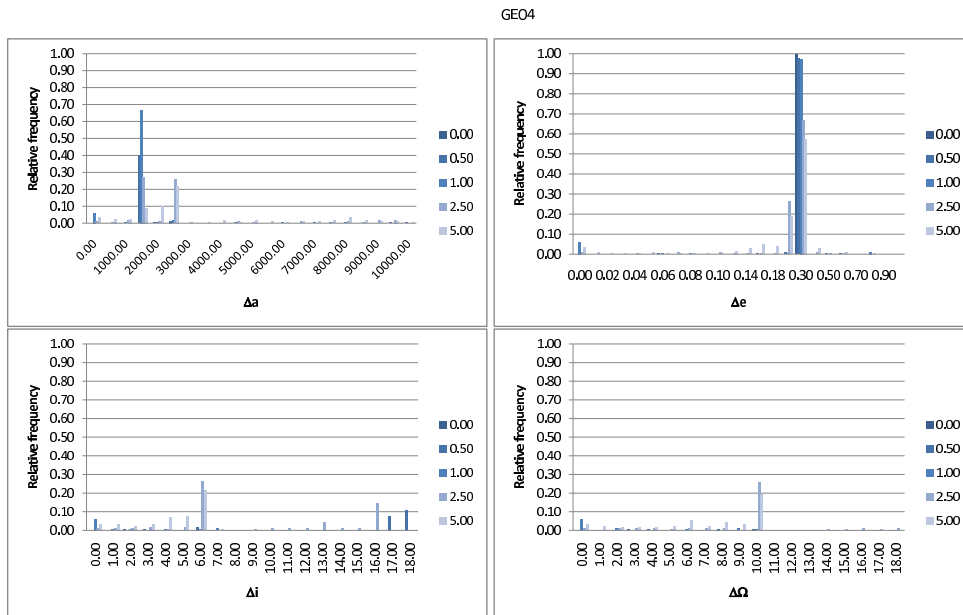


Figure A.7: Relative frequency of the differences between the determined and reference orbital elements semi-major axis  $a$  [km], eccentricity  $e$  [-], inclination  $i$  [°], and right ascension of ascending node  $\Omega$  [°], grouped by the assumed astrometric noise [″], for the test object GEO4.

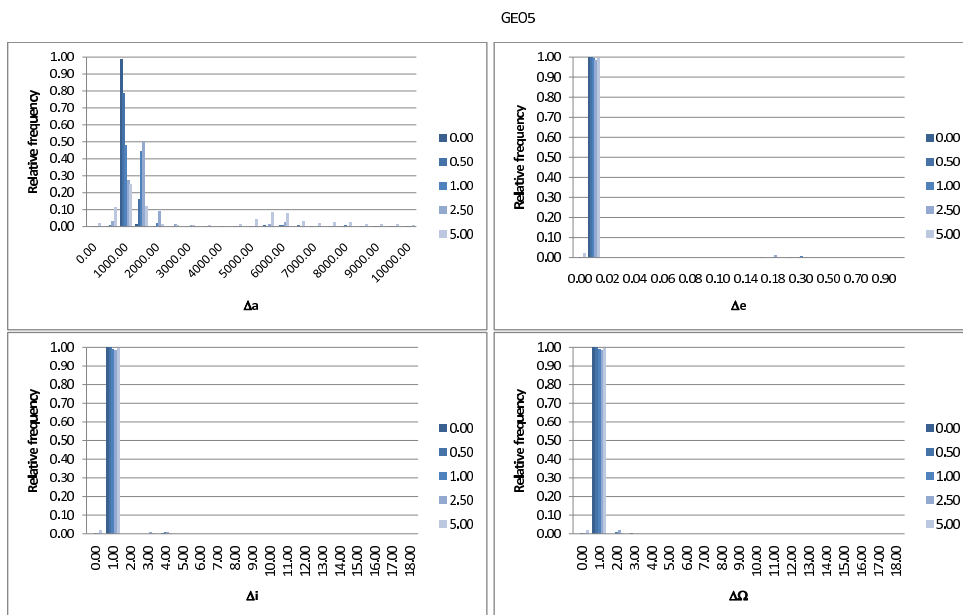


Figure A.8: Relative frequency of the differences between the determined and reference orbital elements semi-major axis  $a$  [km], eccentricity  $e$  [-], inclination  $i$  [°], and right ascension of ascending node  $\Omega$  [°], grouped by the assumed astrometric noise [″], for the test object GEO5.

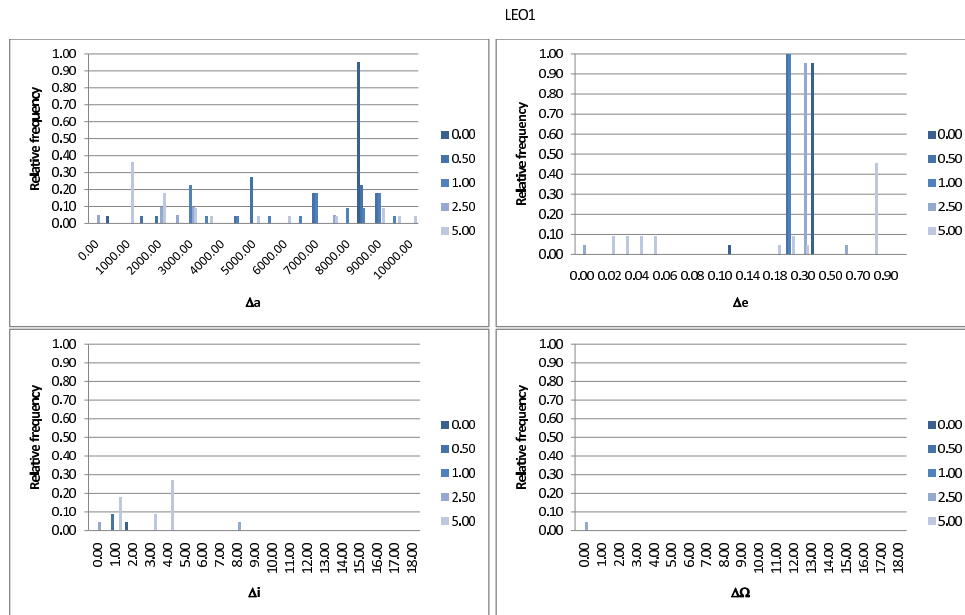


Figure A.9: Relative frequency of the differences between the determined and reference orbital elements semi-major axis  $a$  [km], eccentricity  $e$  [-], inclination  $i$  [ $^\circ$ ], and right ascension of ascending node  $\Omega$  [ $^\circ$ ], grouped by the assumed astrometric noise [ $''$ ], for the test object LEO1.

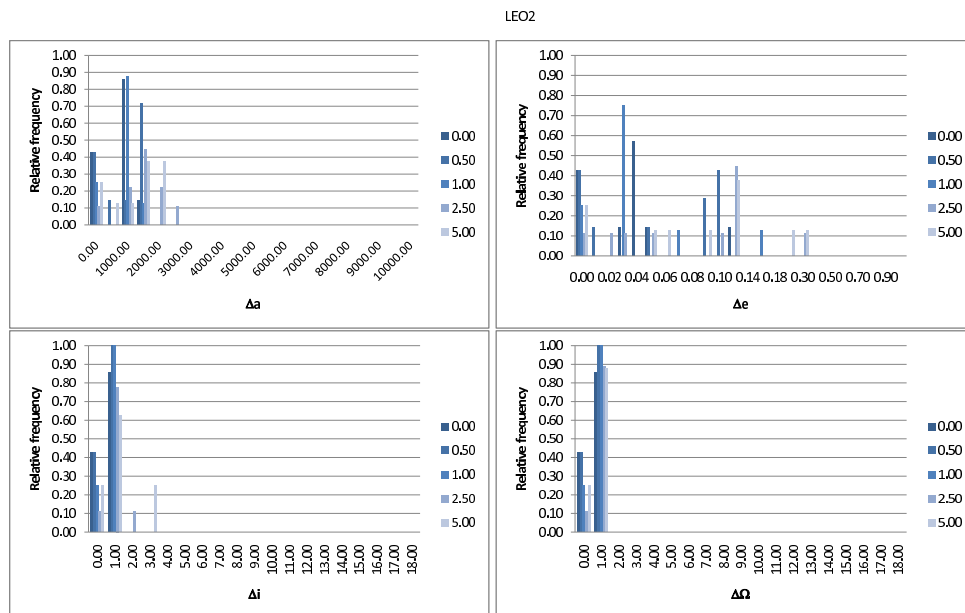


Figure A.10: Relative frequency of the differences between the determined and reference orbital elements semi-major axis  $a$  [km], eccentricity  $e$  [-], inclination  $i$  [ $^\circ$ ], and right ascension of ascending node  $\Omega$  [ $^\circ$ ], grouped by the assumed astrometric noise [ $''$ ], for the test object LEO2.

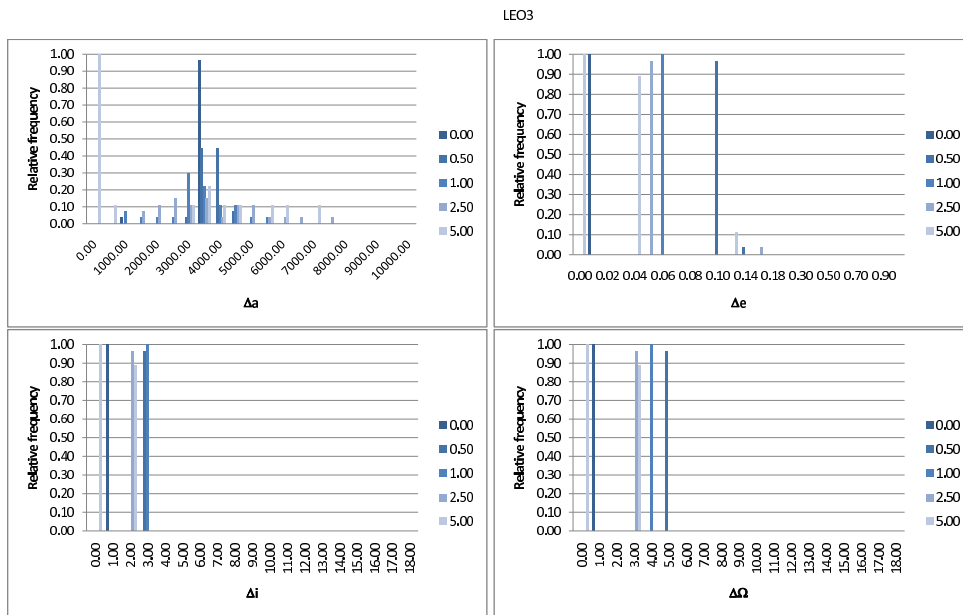


Figure A.11: Relative frequency of the differences between the determined and reference orbital elements semi-major axis  $a$  [km], eccentricity  $e$  [-], inclination  $i$  [°], and right ascension of ascending node  $\Omega$  [°], grouped by the assumed astrometric noise [″], for the test object LEO3.

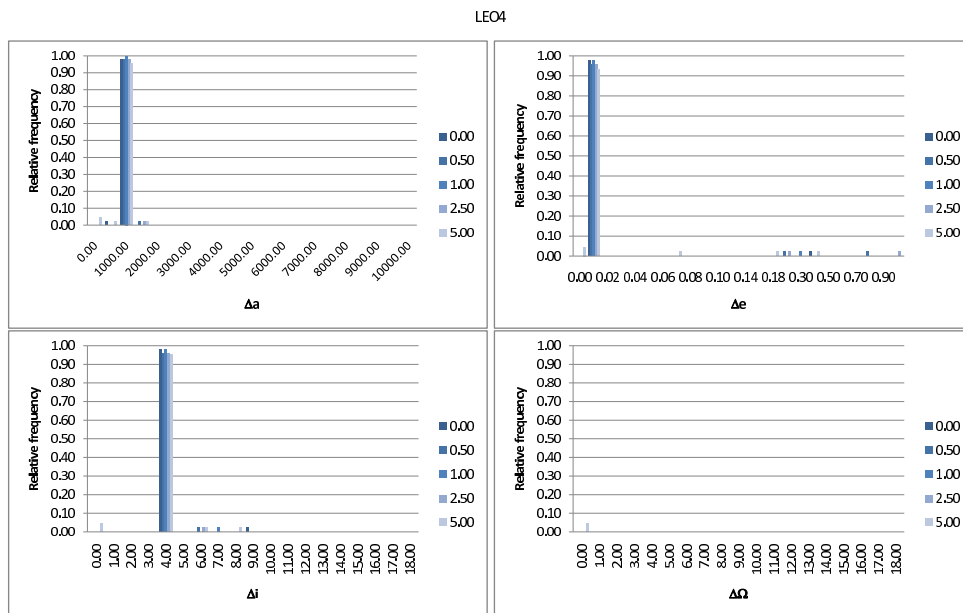


Figure A.12: Relative frequency of the differences between the determined and reference orbital elements semi-major axis  $a$  [km], eccentricity  $e$  [-], inclination  $i$  [°], and right ascension of ascending node  $\Omega$  [°], grouped by the assumed astrometric noise [″], for the test object LEO4.

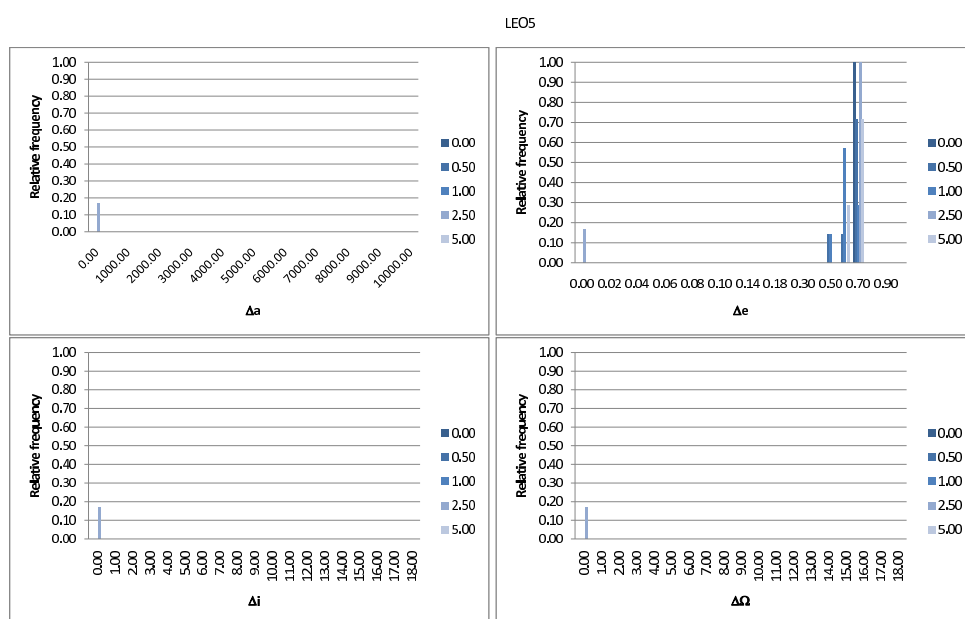


Figure A.13: Relative frequency of the differences between the determined and reference orbital elements semi-major axis  $a$  [km], eccentricity  $e$  [-], inclination  $i$  [ $^{\circ}$ ], and right ascension of ascending node  $\Omega$  [ $^{\circ}$ ], grouped by the assumed astrometric noise [ $''$ ], for the test object LEO5.

## **B. Simulated orbit determination results for a system proposal for space-based optical space surveillance**

This appendix gives in Figs. B.1 to B.4 the results of the simulation of the initial orbit determination for space-based space surveillance (see Sect. 6.4). Initial orbits from single passes are determined for subsequent days as a function of various astrometric noise levels, including a case without any noise added. The differences of the orbital elements compared to the case without added noise are displayed, together with added formal errors of the determined elements.

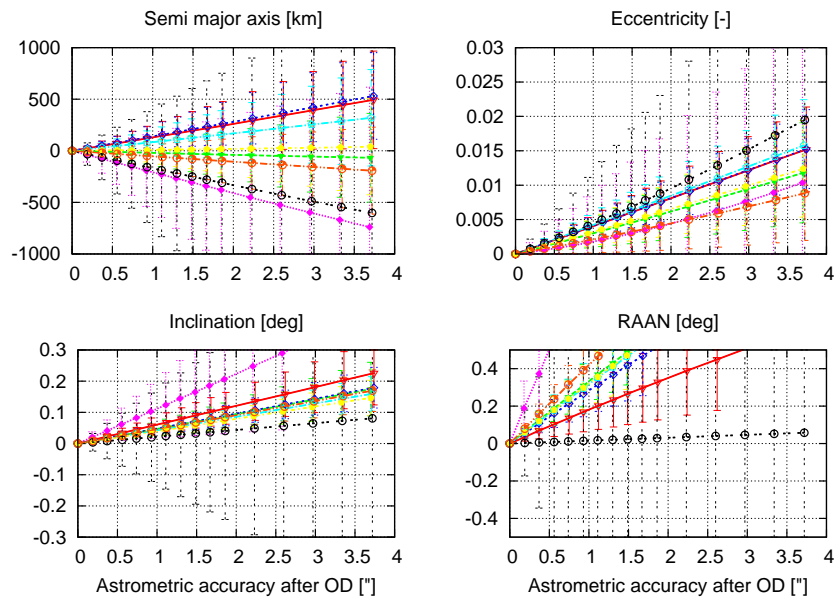


Figure B.1: First orbit determination of object 33059 for subsequent passes. The individual sub-plots show the difference for selected orbital elements (semi-major axis, eccentricity, inclination, and right ascension of the ascending node) between the "truth" (i.e., the orbit determination without astrometric noise) and the orbit determination using noised observations.

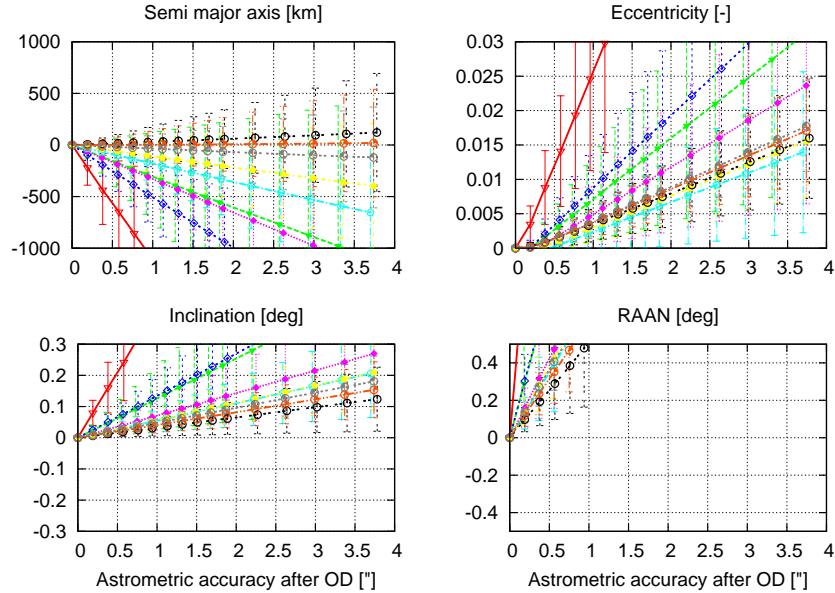


Figure B.2: First orbit determination of object 23192 for subsequent passes. The individual sub-plots show the difference for selected orbital elements (semi-major axis, eccentricity, inclination, and right ascension of the ascending node) between the "truth" (i.e., the orbit determination without astrometric noise) and the orbit determination using noised observations.

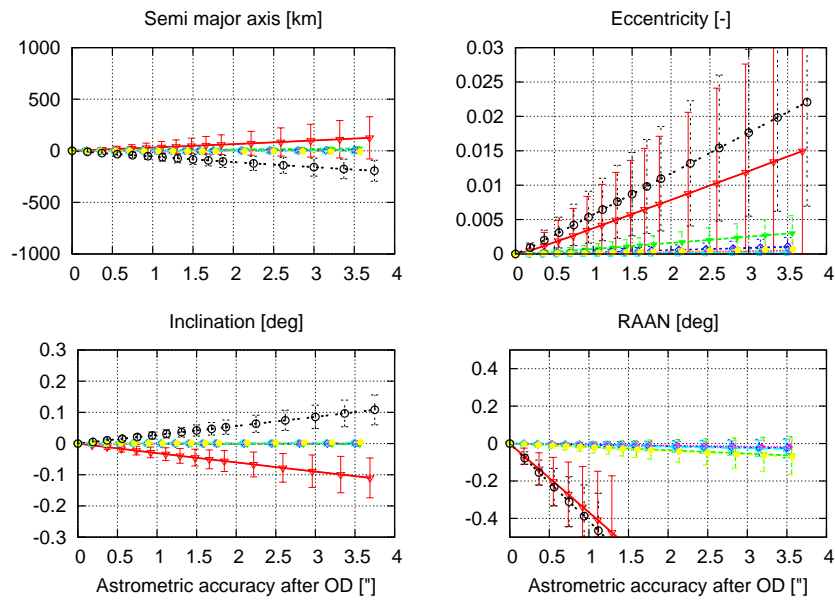


Figure B.3: First orbit determination of object 22563 for subsequent passes. The individual sub-plots show the difference for selected orbital elements (semi-major axis, eccentricity, inclination, and right ascension of the ascending node) between the "truth" (i.e., the orbit determination without astrometric noise) and the orbit determination using noised observations.

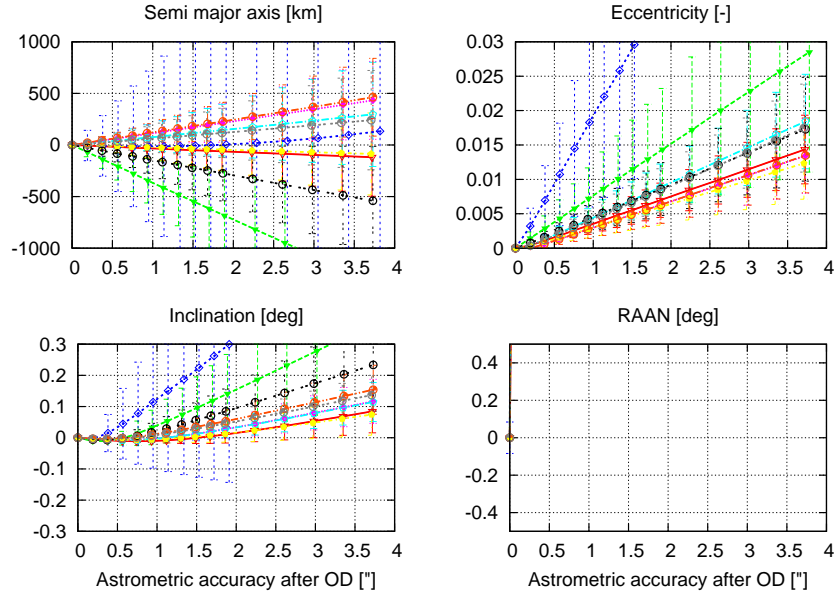


Figure B.4: First orbit determination of object 34710 for subsequent passes. The individual sub-plots show the difference for selected orbital elements (semi-major axis, eccentricity, inclination, and right ascension of the ascending node) between the "truth" (i.e., the orbit determination without astrometric noise) and the orbit determination using noised observations.

*B Simulated orbit determination results for a system proposal for space-based optical space surveillance*

# Bibliography

- Abbot, R. I., and T. P. Wallace (2007), Decision Support in Space Situational Awareness, *Lincoln Laboratory Journal*, 16, pp. 297–335.
- Abercromby, K. J., P. Seitzer, H. M. Rodriguez, E. S. Barker, and M. J. Matney (2009), Survey and Chase: A New method of Observations for the Michigan Orbital DEbris Survey Telescope (MODEST), *Acta Astronautica*, 65, pp. 103–111, July 2009.
- Africano, J., T. Schildknecht, M. Matney, P. Kervin, E. Stansbery, and W. Flury (2000), A Geosynchronous Orbit Search Strategy, *Space Debris*, 2, pp. 357–369, 10.1023/B:SDEB.0000030025.04930.08.
- Africano, J., P. Kervin, P. Sydney, K. Hamada, V. Soo Hoo, D. Nishimoto, J. Okada, J. Lambert, E. Stansbery, M. Mulrooney, and K. Jarvis (2001), AMOS Debris Observations, in *Space Debris*, Vol. 473 of *ESA Special Publication*, edited by H. Sawaya-Lacoste, pp. 107–112, October 2001.
- Africano, J. L., T. J. Setteccerri, J. V. Lambert, and E. G. Stansbery (1999), NASA/JSC Optical Orbital Debris Program: Results from the Liquid Mirror Telescope (LMT) and the CCD Debris Telescope (CDT), in *Proceedings of the 1999 Space Control Conference*, Vol. STK-254 of *MIT Lincoln Laboratory*, Lexington, MA, April 1999.
- Africano, J. L., E. G. Stansbery, and P. W. Kervin (2004), The Optical Orbital Debris Measurement Program at NASA and AMOS, *Advances in Space Research*, 34, pp. 892–900.
- Agapov, V., I. Molotov, and Z. Khutorovsky (2010), Comparison of Orbital and Physical Characteristics of Bright and Faint GEO Objects, Presentation at the 2010 AMOS Conference, Wailea, Maui, USA, 14-17 September 2010.
- Aksenov, O., O. Adreyev, V. Dicky, N. Johnson, Yu. Tretyakov, S. Veniamov, and V. Zavaliiy (2003), Dynamics of the Principal Characteristics of the US/Russian Space Object catalogs since 1995 to 2002, in *Proceedings of the 5th U.S.-Russian Space Surveillance Workshop*, edited by P. Kenneth Seidelmann, St. Petersburg, Russia, September 24–27 2003.
- Alby, F., G. Otrio, and C. Durin (2000), Space Based Observations of Orbital Debris, in *Space Debris 2000*, Vol. 103 of *AAS Science and Technologies Series*, edited by J. Bendisch, pp. 35–49, univelt publishers, San Diego, USA.
- Alby, F., M. Boer, B. Deguine, I. Escane, F. Newland, and C. Portmann (2004), Status of CNES Optical Observations of Space Debris in Geostationary Orbit, *Advances in Space Research*, 34, pp. 1143–1149.

## Bibliography

---

- Anonymous (1999a), AIAA special project report: MEO/LEO constellations: U.S. laws, policies and regulations on orbital debris mitigation, American Institute of Aeronautics and Astronautics, Inc.
- Anonymous (1999b), Position Paper on Orbital Debris, Available at <http://iaaweb.org/iaa/Studies/orbitaldebris.pdf>.
- Anonymous (1999c), Technical Report on Space Debris, Available at [http://www.oosa.unvienna.org/pdf/reports/ac105/AC105\\\_720E.pdf](http://www.oosa.unvienna.org/pdf/reports/ac105/AC105\_720E.pdf).
- Anonymous (2007), Space Debris Mitigation Guidelines (IADC-02-01), rev. 1, Available at [http://www.iadc-online.org/index.cgi?item=docs\\_pub](http://www.iadc-online.org/index.cgi?item=docs_pub).
- Anonymous (2008a), Declaration on the Space Situational Awareness (SSA) Preparatory Programme, ESA/C(2008)192, Att.: ESA/C/SSA-PP/VII/Dec. 1 (Final), December 8 2008.
- Anonymous (2008b), Sourcebook on the Okno, Krona and Krona-N Space Surveillance Sites, Version of 2008-12-30, Available at <http://www.fas.org/spp/military/program/track/okno.pdf>, December 30 2008.
- Anselmo, L., and C. Pardini (2005), Orbital Evolution of Geosynchronous Objects with High Area-To-Mass Ratios, in *4th European Conference on Space Debris*, Vol. 587 of *ESA Special Publication*, edited by D. Danesy, pp. 279–, August 2005.
- Barker, E., K. Jarvis, J. Africano, K. Jorgensen, T. Parr-Thumm, M. Matney, and G. Stansbery (2005), The Geo Environment as Determined by the CDT Between 1998 and 2002, in *4th European Conference on Space Debris*, Vol. 587 of *ESA Special Publication*, edited by D. Danesy, pp. 135–, August 2005.
- Bastida, B. (2011), personal communication.
- Bastida, B., and H. Krag (2009), Strategies for Active Removal in LEO, in *5th European Conference on Space Debris*, Vol. SP-672 of *ESA Special Publications*, edited by ESA.
- Batyr, G., S. Veniaminov, V. Dicky, V. Yurasov, A. Menshikov, and Z. Khutorovsky (1993), The Current State of Space Surveillance System and its Capability in Surveying Space Debris, in *Proc. of the 1st European Conference on Space Debris*, Vol. ESA-SD-01, edited by W. Flury, pp. 91–97, European Space Agency, Paris (France), April 5–7 1993.
- Baueršima, I. (1984), Coupled Quasar, Satellite and Star Positioning (CQSSP), *Mitteilungen der Satelliten-Beobachtungsstation Zimmerwald*, 13, pp. 15.
- Bendisch, J., J. P. Hoffmann, R. Liebscher, and F. Rollenhagen (1993), Detection of Space Debris by the use of Space Based Optical Sensors, in *Proc. of the 1st European Conference on Space Debris*, Vol. ESA-SD-01, edited by W. Flury, pp. 91–97, European Space Agency, Paris (France), April 5–7 1993.
- Beutler, G. (2005), *Methods of Celestial Mechanics*, Springer-Verlag, Berlin Heidelberg New York, 1st edition.
- Beutler, G., R. Weber, U. Hugentobler, M. Rothacher, and A. Verdun (1998), GPS Satellite Orbits, in *GPS for Geodesy*, edited by P. J. G. Teunissen and A. Kleusberg, Springer.

- Beutler, G., T. Schildknecht, U. Hugentobler, and W. Gurtner (2003), Orbit Determination in Satellite Geodesy, *Advances in Space Research*, 31, pp. 1853–1868, April 2003.
- Blagun, V., Y. Levitskiyi, and S. Kulik (2001), Activities on Space Debris in Russia, in *Space Debris*, Vol. 473 of *ESA Special Publication*, edited by H. Sawaya-Lacoste, pp. 21–23, October 2001.
- Blagun, V. P., S. V. Kulik, and V. I. Lukyashchenko (1999), Russian Space Agency Activities on the Problem of Technogenic Space Debris, *Advances in Space Research*, 23(1), pp. 271–.
- Braun, C. von (1999), Space Surveillance Operations with the Space-based Visible, in *Proc. of the 1999 Space Control Conference*, pp. 147–162, Lexington, Massachusetts.
- Braun, C. von, J. Sharma, and E. M. Gaposchkin (2000), Space-Based Visible Metric Accuracy, *Journal of Guidance Control and Dynamics*, 23(1), pp. 175–182.
- Breiter, S. Ł., and G. G. Métris (1998), Symplectic Mapping for Satellites and Space Debris Including Nongravitational Forces, *Celestial Mechanics and Dynamical Astronomy*, 71, pp. 79–94.
- Butler, A (2008), Space-Based Visible Sensor Ceases Ops, *Aviation Week*, Jun 10, 2008.
- Chao, C. C., and R. A. Gick (2004), Long-term evolution of navigation satellite orbits: GPS/GLONASS/-GALILEO, *Advances in Space Research*, 34, pp. 1221–1226.
- Chatters, Maj E. P., and Maj B. J. Crothers (2009), Space Surveillance Network, in: *Au-18 space primer*, Air Command and Staff College Space Research Electives Seminars, Air University Press Maxwell Air Force Base, Alabama.
- Deleflie, F., A. Rossi, C. Portmann, G. Métris, and F. Barlier (2011), Semi-analytical investigations of the long term evolution of the eccentricity of Galileo and GPS-like orbits, *Advances in Space Research*, 47, pp. 811–821, March 2011.
- DeMars, K., and M. Jah (2009), Passive Multi-Target Tracking with Application to Orbit Determination for Geosynchronous Objects, in *Spaceflight Mechanics 2009, Advances in the Astronautical Sciences*, Vol. 134, edited by Alan M. Segerman *et al.*, Savannah, Georgia, US, Proceedings of the 19th AAS/AIAA Space Flight Mechanics Meeting.
- DeMars, K., M. Jah, and P. W. Schumacher (2010), The Use of Short-Arc Angle and Angle-rate Data for Deep-Space Initial Orbit Determination and Track Association, in *Proceedings of the 8th U.S.-Russian Space Surveillance Workshop*, edited by P. Kenneth Seidelmann, Wailea Beach, Maui, Hawaii, United States, April 18–23 2010.
- Dick, J., P. Herridge, R. Tremayne-Smith, J. Davey, and R. Crowther (2009), Surveying for Debris in MEO with Optical Sensors, in *5th European Conference on Space Debris*, Vol. SP-672 of *ESA Special Publications*, edited by ESA.
- Dicky, V., Z. Khutorovsky, A. Kuricshah, A. Menshikov, R. Nazirov, A. Pitsyck, S. Veniaminov, and V. Yurasov (1993), The Russian space surveillance system and some aspects of spaceflight safety, *Advances in Space Research*, 13, pp. 21–31, August 1993.

- Donath, T., T. Schildknecht, P. Brousse, J. Laycock, T. Michal, P. Ameline, and L. Leushacke (2005), Proposal for a European Space Surveillance System, in *Proc. of the 4th European Conference on Space Debris*, Vol. ESA SP-587, edited by D. Danesy, pp. 31–37, ESA Publications Division, The Netherlands, September 10–14 2005.
- Donath, T., T. Schildknecht, V. Martinot, and L. del Monte (2008), Possible European Systems for Space Situational Awareness, in *Proc. of the 59th International Astronautical Congress*, Glasgow, Scotland, September 20–October 3 2008, IAC-08-A6.5.3.
- Donath, T., C. Saunders, V. Martinot, E. Elluin, and J. Rey Benayas (2009), Architectures Analysis for the Future European SSA system, in *5th European Conference on Space Debris*, Vol. SP-672 of *ESA Special Publications*, edited by ESA.
- Donath, Th., T. Michal, X. Vanwijck, B. Dugrosprez, M. Menelle, T. Flohrer, T. Schildknecht, V. Martinot, J. M. Leveau, P. Ameline, C. Walker, L. Leushacke, I. Zozaya, and M. Morgenstern (2005), Detailed Assessment of a European Space Surveillance System, *Final report*, ESA/ESOC Contract 18574/04/D/HK, ONERA, Chitillon, France.
- Faccenda, W. J. (2000), GEODSS: Past and Future Improvements, The MITRE Corporation, available online at [http://www.mitre.org/work/tech\\_papers/tech\\_papers\\_00/faccenda\\_geodss/geodss\\_faccenda.pdf](http://www.mitre.org/work/tech_papers/tech_papers_00/faccenda_geodss/geodss_faccenda.pdf).
- Farnocchia, D., G. Tommei, A. Milani, and A. A. Rossi (2010), Innovative Methods of Correlation and Orbit Determination for Space Debris, *Celestial Mechanics and Dynamical Astronomy*, 107, pp. 169–185.
- Fernández, J., L. Aivar, A. Águeda, J. Dick, P. Herridge, H. Krag, and T. Flohrer (2011), Operational Survey and Catalogue Maintenance in MEO, in *Proc. of the 1st European Space Surveillance Conference*, ESA, Madrid, Spain, 7–9 June 2011.
- Ferrazzani, M. (2010), Preliminary Considerations on the European Preparatory Programme on Space Situational Awareness, in *Proc. of the 61st International Astronautical Congress*, Prague, Czech Republic, September 27–October 1 2010, IAC-10-E7.3.
- Flohrer, C. (2008), *Mutual Validation of Satellite-Geodetic Techniques and its Impact on GNSS Orbit Modeling*, Geodätisch-geophysikalische Arbeiten in der Schweiz, Schweizerische Geodätische Kommission, Institut für Geodäsie und Photogrammetrie, Eidg. Technische Hochschule Zürich, Zürich, Switzerland.
- Flohrer, T., J. Peltonen, A. Kramer, T. Eronen, J. Kuusela, E. Riihonen, T. Schildknecht, E. Stöveken, E. Valtonen, F. Wokke, and W. Flury (2005a), Space-Based Optical Observations of Space Debris, in *4th European Conference on Space Debris*, Vol. 587 of *ESA Special Publication*, edited by D. Danesy, pp. 165–, August 2005.
- Flohrer, T., T. Schildknecht, R. Musci, and E. Stöveken (2005b), Performance estimation for GEO space surveillance, *Advances in Space Research*, 35, pp. 1226–1235.
- Flohrer, T., T. Schildknecht, R. Jehn, and M. Oswald (2006), Performance of a Proposed Instrument for Space-based Optical Observation of Space Debris, in *Proc. of the 57th International Astronautical Congress*, Valencia, Spain, IAC-06-B6.1.01.

- Flohre, T., T. Schildknecht, C. Früh, R. Musci, and M. Ploner (2007a), Optical Observations at the Zimmerwald Observatory, in *Proc. of the 58th International Astronautical Congress*, Hyderabad, India, September 24–28 2007, IAC-07-A6.I.11.
- Flohre, T., T. Schildknecht, and R. Musci (2007b), A possible way of exchanging follow-up data, in *Proc. of the 58th International Astronautical Congress*, Hyderabad, India, September 24–28 2007, IAC-07-A6.I.10.
- Flohre, T., H. Krag, and H. Klinkrad (2008a), Assessment and Categorization of TLE Orbit Errors for the US SSN Catalogue, in *Advanced Maui Optical and Space Surveillance Technologies Conference*.
- Flohre, T., T. Schildknecht, and R. Musci (2008b), Proposed Strategies for Optical Observations in a Future European Space Surveillance Network, *Advances in Space Research*, 41, pp. 1010–1021.
- Flohre, T., H. Krag, and H. Klinkrad (2009), ESA's Process for the Identification and Assessment of High-risk Conjunction Events, *Advances in Space Research*, 44, pp. 355–363, August 2009.
- Flohre, T., H. Krag, H. Klinkrad, and T. Schildknecht (2011a), Feasibility of Performing Space Surveillance Tasks with a Proposed Space-based Optical Architecture, *Advances in Space Research*, 47, pp. 1029–1042.
- Flohre, T., R. Choc, and B. Bastida (2011b), Classification of Geosynchronous Objects, *GEN-DB-LOG-00074-OPS-GR*, ESA.
- Flury, W., A. Massart, T. Schildknecht, U. Hugentobler, J. Kuusela, and Z. Sodnik (2000), Searching for Small Debris in the Geostationary Ring, *ESA bulletin*, 104, pp. 92–100.
- Früh, C., R. Musci, and T. Schildknecht (2008), Improved Method for Recognizing Unknown Space Debris Objects on Series of CCD-Frames, in *Proc. of the 59th International Astronautical Congress*, Glasgow, Scotland, September 20–October 3 2008, IAC-08-A6.5.2.
- Früh, C., T. Schildknecht, R. Musci, and M. Ploner (2009a), Catalogue Correlation of Space Debris Objects, in *5th European Conference on Space Debris*, Vol. SP-672 of *ESA Special Publications*, edited by ESA.
- Früh, C., T. Schildknecht, and M. Ploner (2009b), Comparison of Different Methods of Ephemeris Retrieval for Correlation of Observations, in *Advanced Maui Optical and Space Surveillance Technologies Conference*.
- Fujimoto, K., and D. Scheeres (2010), Correlation and Initial Orbit Determination for Short-Arc Optical Observations, in *Advanced Maui Optical and Space Surveillance Technologies Conference*.
- Gaposchkin, E. M., C. von Braun, and J. Sharma (2000), Space-Based Space Surveillance with the Space-Based Visible, *Journal of Guidance Control and Dynamics*, 23(1), pp. 148–152.
- Harrison, D. C., and J. C. Chow (1996), The Space-Based Visible Sensor, *John Hopkins APL Technical Digest*, 17, pp. 226–236.
- Hebert, T. J., J. L. Africano, E. G. Stansbery, M. J. Matney, D. T. Hall, J. F. Pawlowski, T. Hanada, P. D. Anz-Meador, K. S. Jarvis, N. Hartsough, and M. K. Mulrooney (2001), Optical Observations of the Orbital Debris Environment at NASA, *Advances in Space Research*, 28(9), pp. 1283–1290.

- Hejduk, M. (2007), Phase Functions of Deep-Space Orbital Debris, in *Advanced Maui Optical and Space Surveillance Technologies Conference*.
- Herzog, J., T. Schildknecht, and C. Früh (2010), Build-up and Maintenance of a Catalogue of GEO Objects With ZimSMART, in *Proc. of the 61st International Astronautical Congress*, Prague, Czech Republic, September 27–October 1 2010, IAC-10-A6.5.2.
- Hinze, A. (2011), personal communication.
- Hoots, F., and R. L. Roehrich (1980), Models for Propagation of NORAD Element Sets, Spacetrack Report No. 3, U.S. Air Force: Aerospace Defense Command.
- Hugentobler, U. (1998), *Astrometry and Satellite Orbits: Theoretical Considerations and Typical Applications*, Geodätisch-geophysikalische Arbeiten in der Schweiz, Schweizerische Geodätische Kommission, Institut für Geodäsie und Photogrammetrie, Eidg. Technische Hochschule Zürich, Zürich, Switzerland.
- Jarvis, K. S., T. L. Thumm, K. Jorgensen, M. Matney, J. L. Africano, T. Hebert, M. Mulrooney, M. Baugh, and E. G. Stansbery (2001a), Observational Results of NASA's Liquid Mirror Telescope, in *Space Debris 2001*, Vol. 105 of *AAS Science and Technologies Series*, edited by J. Bendisch, pp. 3–8, univelt publishers, San Diego, USA.
- Jarvis, K. S., J. L. Africano, P. F. Sydney, E. G. Stansbery, T. L. Tumm, K. Jorgensen, and M. Mulrooney (2001b), Observations of the Geosynchronous Earth Orbital Debris Environment using NASA's CCD Debris Telescope, in *ESA Special Publication*, Vol. 473 of *ESA Special Publication*, edited by H. Sawaya-Lacoste, pp. 95–99, October 2001.
- Jedicke, R. (2006), The Pan-STARRS Moving Object Processing System, in *The Advanced Maui Optical and Space Surveillance Technologies Conference*.
- Jehn, R. (2001), Comparison of the 1999 Beam-park Experiment Results with Space Debris Models, *Advances in Space Research*, 28(9), pp. 1367–1375.
- Jehn, R., A. Rossi, T. Flohrer, and D. Navarro (2009), Reorbiting of Satellites in High Altitudes, in *5th European Conference on Space Debris*, Vol. SP-672 of *ESA Special Publications*, edited by ESA.
- Jenkin, A. B., and R. A. Gick (2001), Collision Risk associated with Instability of MEO Disposal Orbits, in *Space Debris*, Vol. 473 of *ESA Special Publication*, edited by H. Sawaya-Lacoste, pp. 471–476, October 2001.
- Johnson, N. L. (2001), Activities on Space Debris in U.S., in *Space Debris*, Vol. 473 of *ESA Special Publication*, edited by H. Sawaya-Lacoste, pp. 13–19, October 2001.
- Johnson, N. L. (2010), Medium Earth Orbits: Is there a Need for a Third Protected Region?, in *Proc. of the 61st International Astronautical Congress*, Prague, Czech Republic, September 27–October 1 2010, IAC-10-A6.4.1.
- Johnson, N. L., E. Stansbery, D. O. Whitlock, K. J. Abercromby, and D. Shoots (2008), History of On-orbit Satellite Fragmentations, *Nasa/tm2008214779*, NASA Orbital Debris Program Office, National Aeronautics and Space Administration, Lyndon B. Johnson Space Center, Houston, Texas 77058.

- Kaiser, N. (2006), Pan-STARRS - A New Generation Survey Telescope System, in *The Advanced Maui Optical and Space Surveillance Technologies Conference*.
- Kessler, D. J., and B. G. Cour-Palais (1978), Collision Frequency of Artificial Satellites: The Creation of a Debris Belt, *JGR*, 83, pp. 2637–2646, June 1978.
- Khutorovsky, Z. N., V. F. Boikov, and A. V. Testov (2001), Monitoring of GEO satellites, in *Space Debris*, Vol. 473 of *ESA Special Publication*, edited by H. Sawaya-Lacoste, pp. 117–124, October 2001.
- King-Hele, D. (1983), *Observing Earth Satellites*, Van Nostrand Reinhold, New York, 1st edition.
- Klinkrad, H. (2006), *Space Debris Models and Risk Analysis*, Springer, Berlin, Heidelberg, New York, 1st edition.
- Klinkrad, H. (2011), personal communication.
- Klinkrad, H., R. Tremayne-Smith, F. Alby, and D. Alwes (2008), Europe’s Eyes on the Skies: The Proposal for a European Space Surveillance System, *ESA Bulletin*, 133, pp. 42–48, February 2008.
- Kouprianov, V. (2008), Distinguishing Features of CCD Astrometry of Faint GEO Objects, *Advances in Space Research*, 41(7), pp. 1029–1038.
- Kouprianov, V. (2010), Advanced Image Processing Techniques for Automatic Reduction of GEO Survey Data, in *Proceedings of the 8th U.S.-Russian Space Surveillance Workshop*, edited by P. Kenneth Seidelmann, Wailea Beach, Maui, Hawaii, United States, April 18–23 2010.
- Krag, H. (2003), *A Method for the Validation of Space Debris Models and for the Analysis and Planning of Radar and Optical Surveys*, Berichte aus der Luft- und Raumfahrttechnik, Shaker Verlag, Aachen, Germany.
- Krag, H., and H. Klinkrad (2009), SSA Surveillance and Tracking Customer Requirements Document, *SSA-S&T-CRD-00060-OPS-GR*, ESA.
- Krag, H., P. Beltrami-Karlezi, J. Bendisch, H. Klinkrad, D. Rex, J. Rosebrock, and T. Schildknecht (2000), PROOF – The Extension of ESA’s MASTER Model to Predict Debris Detections, *Acta Astronautica*, 47(2–9), pp. 687–697, Space an Integral Part of the Information Age.
- Krag, H., M. Kahl, J. Bendisch, H. Klinkrad, and T. Schildknecht (2001), Space Based Optical Observation of Small Debris Objects, in *Space Debris*, Vol. 473 of *ESA Special Publication*, edited by H. Sawaya-Lacoste, pp. 147–152, October 2001.
- Krag, H., H. Klinkrad, T. Flohrer, and E. Fletcher (2010), The European Surveillance and Tracking System Services and Design Drivers, in *Proceedings of the SpaceOps 2010 Conference*, Huntsville, Alabama, AIAA-2010-1927.
- Laas-Bourez, M., D. Coward, A. Klotz, and M. Boër (2011), A Robotic Telescope Network for Space Debris Identification and Tracking, *Advances in Space Research*, 47(3), pp. 402–410.
- Landgraf, M., R. Jehn, and W. Flury (2004), Comparison of EISCAT Radar Data on Space Debris with Model Predictions by the MASTER Model of ESA, *Advances in Space Research*, 34(5), pp. 872–877, Space Debris.

- Laporte, F., and E. Sasot (2008), Operational Management of Collision Risks for LEO Satellites at CNES, in *Proc. of the SpaceOps 2008 Conference*, Heidelberg, Germany, May 12–16 2008, AIAA-2008-3409.
- Levit, C., and W. Marshall (2010), Improved Orbit Predictions Using Two-line Elements, *ArXiv e-prints*, February 2010.
- Lewis, H. G., G. G. Swinerd, and R. J. Newland (2009), The Space Debris Environment: Future Evolution, in *Proc. of the CEAS 2009 European Air and Space Conference*, Royal Aeronautical Society, Manchester, UK, October 26–29 2009.
- Liou, J.-C., D. T. Hall, P. H. Krisko, and J. N. Opiela (2004), LEGEND - a Three-dimensional LEO-to-GEO Debris Evolutionary Model, *Advances in Space Research*, 34, pp. 981–986.
- Lobb, D. R. (1992), Study on Optical Sensors for Space Debris Observation, *Final Report ESTEC Contract 9267/90/D/MD*, SIRA Research and Development.
- Markkanen, J. (2005), Towards Routine Real-Time Space Debris Measurements with EISCAT, in *4th European Conference on Space Debris*, Vol. 587 of *ESA Special Publication*, edited by D. Danesy, pp. 67–, August 2005.
- Maruskin, J. M., D. J. Scheeres, and K. T. Alfriend (2009), Correlation of Optical Observations of Objects in Earth Orbit, *Journal of Guidance Control and Dynamics*, 32(1), pp. 194–209.
- Maskell, P., and L. Oram (2008), Sapphire: Canada’s Answer to Space-Based Surveillance of Orbital Objects, in *Advanced Maui Optical and Space Surveillance Technologies Conference*.
- Matney, M., R. Goldstein, D. Kessler, and E. Stansbery (1999), Recent Results from Goldstone Orbital Debris Radar, *Advances in Space Research*, 23, pp. 5–12.
- Matney, M. J., E. Stansbery, J. Africano, K. Jarvis, K. K. Jorgensen, and T. Thumm (2004), Extracting GEO Orbit Populations from Optical Surveys, *Advances in Space Research*, 34, pp. 1160–1165.
- Mehrholz, D., L. Leushacke, W. Flury, R. Jehn, H. Klinkrad, and M. Landgraf (2002), Detecting, Tracking and Imaging Space Debris, *ESA bulletin*, 109, pp. 128–134.
- Michal, T., J. P. Eglizeaud, and J. Bouchard (2005), Graves: the New French System for Space Surveillance, in *4th European Conference on Space Debris*, Vol. 587 of *ESA Special Publication*, edited by D. Danesy, pp. 61–, August 2005.
- Milani, A., G. Tommei, D. Farnocchia, A. Rossi, T. Schildknecht, and R. Jehn (2010), Orbit Determination of Space Objects Based on Sparse Optical Data, *ArXiv e-prints*, December 2010.
- Miller, J. G., and W. G. Schick (1999), Contributions of the Space-Based Visible Sensor to Catalog Maintenance, The MITRE Corporation, available online at [http://www.mitre.org/work/tech\\_papers/](http://www.mitre.org/work/tech_papers/).
- Molotov, I., and V. Agapov (2009), Faint High Orbit Debris Observations with ISON Optical Network, in *Advanced Maui Optical and Space Surveillance Technologies Conference*.

- Molotov, I., V. Agapov, V. Titenko, Z. Khutorovsky, Yu. Burtsev, I. Guseva, V. Rumyantsev, M. Ibrahimov, G. Kornienko, A. Erofeeva, V. Biryukov, V. Vlasjuk, R. Kiladze, R. Zalles, P. Sukhov, R. Inasaridze, G. Abdullaeva, V. Rychalsky, V. Kouprianov, O. Rusakov, E. Litvinenko, and E. Filippov (2008), International Scientific Optical Network for Space Debris Research, *Advances in Space Research*, 41(7), pp. 1022–1028.
- Montejo, F.J., T. López Moratalla, and C. Abad (2010), Astrometric Positioning and Orbit Determination of Geostationary Satellites, *Advances in Space Research*, *In Press*, *Corrected Proof*.
- Mottola, S., A. Börner, J. T. Grundmann, G. Hahn, B. Kazeminejad, E. Kührt, H. Michaelis, S. Montenegro, N. Schmitz, and P. Spietz (2008), AsteroidFinder: Unveiling the Population of Inner Earth Objects, in *Proc. of the 59th International Astronautical Congress*, Glasgow, Scotland, September 20–October 3 2008, IAC-08-A3.5.6.
- Musci, R. (2006), *Identification and Recovery of Objects in GEO and GTO to Maintain a Catalogue of Orbits*, Phd thesis, University of Bern, Astronomical Institute, Druckerei der Universität Bern.
- Musci, R., T. Schildknecht, and M. Ploner (2004), Orbit improvement for GEO objects using follow-up observations, *Advances in Space Research*, 34, pp. 912–916.
- Musci, R., T. Schildknecht, M. Ploner, and G. Beutler (2005), Orbit improvement for GTO objects using follow-up observations, *Advances in Space Research*, 35, pp. 1236–1242.
- Musci, R., T. Schildknecht, and M. Ploner M. (2010), Analyzing Long Observation Arcs for Objects with High Area-to-mass Ratios in Geostationary Orbits, *Acta Astronautica*, 66, pp. 693–703, March 2010.
- Nakajima, A., and H. Kurosaki (2007), Space Debris Observations Programs in JAXA, in *Advanced Maui Optical and Space Surveillance Technologies Conference*.
- Nalezty, M., A. Majczyna, R. Wawrzaszek, and M. Sokolowski (2010), Estimation of Space Debris Detection Possibility by Pi of the Sky Telescopes, in *Society of Photo-Optical Instrumentation Engineers (SPIE) Conference Series*, Vol. 7745, June 2010.
- Newsam, G. N. (2008), Surveillance of Space in Australia, in *Advanced Maui Optical and Space Surveillance Technologies Conference*.
- Olmedo, E., N. Sánchez-Ortiz, M. R. Lerate, M. Belló-Mora, H. Klinkrad, and F. Pina (2008), Initial Orbit Determination Algorithms for Cataloguing Optical Measurements of Space Debris, *Monthly Notices of the Royal Astronomical Society*, 391, pp. 1259–1272, December 2008.
- Olmedo, E., N. Sánchez Ortiz, M. Lerate, M. Belló-Mora, and H. Klinkrad (2009), Design and Development of Correlation Techniques to Maintain a Space Surveillance System Catalogue, *Acta Astronautica*, 65(7–8), pp. 1133–1148.
- Oswald, M., C. Wiedemann, P. Wegener, S. Stabroth, and P. Vrsmann (2004a), Accuracy of Space Debris Orbit Determination Using Space-Based Optical Sensors, in *Space Debris 2003*, Vol. 109 of *AAS Science and Technologies Series*, edited by J. Bendisch, pp. 77–95, univelt publishers, San Diego, USA.

- Oswald, M., H. Krag, P. Wegener, and B. Bischof (2004b), Concept for an Orbital Telescope Observing the Debris Environment in GEO, *Advances in Space Research*, 34, pp. 1155–1159.
- Oswald, M., P. Wegener, S. Stabroth, C. Wiedemann, J. Rosebrock, C. Martin, H. Klinkrad, and P. Vörsmann (2005), The Master 2005 Model, in *4th European Conference on Space Debris*, Vol. 587 of *ESA Special Publication*, edited by D. Danesy, pp. 235–, August 2005.
- Payne, T. (2003), New deep space optical search strategy, in *Proceedings of the 5th U.S.-Russian Space Surveillance Workshop*, edited by P. Kenneth Seidelmann, pp. 259–266, St. Petersburg, Russia, September 24–27 2003.
- Petit, G., and B. Luzum (2010), IERS Conventions (2010), *International Earth Rotation and Reference Systems Service (IERS) Technical Note 36*, Verlag des Bundesamtes für Kartographie und Geodäsie, Frankfurt am Main.
- Porfilio, M., F. Piergentili, and F. Graziani (2002), First Space Debris Optical Detection Campaign in Italy, in *34th COSPAR Scientific Assembly*, Vol. 34 of *COSPAR, Plenary Meeting*.
- Porfilio, Manfredi, Fabrizio Piergentili, and Filippo Graziani (2006), Two-site Orbit Determination: The 2003 GEO Observation Campaign from Collepardo and Mallorca, *Advances in Space Research*, 38(9), pp. 2084–2092, Small Bodies in the Solar System; Space Debris.
- Potter, A. E., and M. Mulrooney (1997), Liquid Metal Mirror for Optical Measurements of Orbital Debris, *Advances in Space Research*, 19(2), pp. 213–219.
- Price, S. D., M. P. Egan, S. J. Carey, D. R. Mizuno, and T. A. Kuchar (2001), Midcourse Space Experiment Survey of the Galactic Plane, *The Astronomical Journal*, 121, pp. 2819–2842.
- Reynolds, R. C., D. L. Talent, and F. Vilas (1989), Observing Orbital Debris Using Space-Based Telescopes: I. Mission Control Considerations, *Publications of the Astronomical Society of the Pacific*, 101, pp. 1055–, November 1989.
- Rumyantsev, V., V. Biryukov, V. Agapov, and I. Molotov (2010), MEO and LEO space debris optical observations at Crimean Observatory: first experience and future perspectives., in *38th COSPAR Scientific Assembly*, Vol. 38 of *COSPAR, Plenary Meeting*, pp. 3952–.
- Schefter, J. (1982), Satellite Trackers Spot Ultra-dim Stars, too, *Popular Science*, pp. 86–88, September 1982.
- Schildknecht, T. (1994), *Optical Astrometry of Fast Moving Objects Using CCD Detectors*, Geodätisch-geophysikalische Arbeiten in der Schweiz, Schweizerische Geodätische Kommission, Institut für Geodäsie und Photogrammetrie, Eidg. Technische Hochschule Zürich, Zürich, Switzerland.
- Schildknecht, T. (2003), Wiedergeburt der traditionellen Himmelsüberwachung und Astrometrie dank moderner Techniken, *Orion*, 3, pp. 30–35.
- Schildknecht, T. (2007), Optical Surveys for Space Debris, *Astronomy and Astrophysics Review*, 14, pp. 41–111.
- Schildknecht, T., I. Baueršima, U. Hugentobler, A. Verdun, and G. Beutler (1991), CQSSP: a New Technique for Establishing the Tie Between the Stellar and Quasar Celestial Reference Frames, in *IAU Colloq. 127: Reference Systems*, edited by J. A. Hughes, C. A. Smith, & G. H. Kaplan, pp. 341–.

- Schildknecht, T., U. Hugentobler, and A. Verdun (1995), Algorithms for Ground Based Optical Detection of Space Debris, *Advances in Space Research*, 16(11), pp. 47–50, Space Debris.
- Schildknecht, T., U. Hugentobler, and G. Beutler (1997), Techniques for Optical Observations of Space Debris - Performance Tests with the New 1 Meter Zimmerwald Telescope, in *Second European Conference on Space Debris*, Vol. 393 of *ESA Special Publication*, edited by B. Kaldeich-Schuermann, pp. 93–.
- Schildknecht, T., U. Hugentobler, and M. Ploner (1999), Optical Surveys of Space Debris in GEO, *Advances in Space Research*, 23(1), pp. 45–54.
- Schildknecht, T., M. Ploner, and U. Hugentobler (2001), The Search for Debris in GEO, *Advances in Space Research*, 28(9), pp. 1291–1299.
- Schildknecht, T., R. Musci, M. Ploner, G. Beutler, W. Flury, J. Kuusela, J. de Leon Cruz, and L. de Fatima Dominguez Palmero (2004a), Optical Observations of Space Debris in GEO and in Highly-eccentric Orbits, *Advances in Space Research*, 34(5), pp. 901–911, Space Debris.
- Schildknecht, T., R. Musci, M. Ploner, U. Hugentobler, M. Serra Ricart, J. de León Cruz, and L. Domínguez Palmero (2004b), Geostationary Orbit Objects Survey, *Final report*, ESA/ESOC Contract 11914/96/D/IM.
- Schildknecht, T., T. Flohrer, and R. Musci (2005), Optical Observations in a Proposed European Space Surveillance Network, in *Proceedings of the 6th U.S.-Russian Space Surveillance Workshop*, edited by P. Kenneth Seidelmann and Victor K. Abalakin, pp. 9–21, Pulkovo Observatory, Russia, 22–26 August 2005.
- Schildknecht, T., R. Musci, and T. Flohrer (2007), Challenges Related to Discovery, Follow-up, and Study of Small High Area-to-mass Ratio Objects at GEO, in *Advanced Maui Optical and Space Surveillance Technologies Conference*.
- Schildknecht, T., T. Flohrer, R. Musci, and R. Jehn (2008), Statistical Analysis of the ESA Optical Space Debris Surveys, *Acta Astronautica*, 63(1–4), pp. 119–127, Touching Humanity - Space for Improving Quality of Life. Selected Proceedings of the 58th International Astronautical Federation Congress, Hyderabad, India, 24-28 September 2007.
- Schildknecht, T., T. Flohrer, and A. Vananti (2009), Optical Surveys for Space Debris in MEO - Simulations and First Results, in *Proc. of the 60th International Astronautical Congress*, Daejeon, Republic of Korea, IAC-09-A6.1.04.
- Schumacher, P. W. (2009), US Naval Space Surveillance Upgrade Program, in *5th European Conference on Space Debris*, Vol. SP-672 of *ESA Special Publications*, edited by ESA.
- Scott, R. L., B. Wallace, and D. Bedard (2006), Space-Based Observations of Satellites from the MOST Microsatellite, *Technical memorandum 2006-199*, Defence Research and Development Canada, available online at <http://handle.dtic.mil/100.2/ADA462866>.
- Seidelmann, P. K. (ed.) (1992), *Explanatory Supplement to the Astronomical Almanac*, University Science Books, Mill Valley, California.

- Seitzer, P., R. Smith, J. Africano, K. Jorgensen, E. Stansbery, and D. Monet (2004), MODEST Observations of Space Debris at Geosynchronous Orbit, *Advances in Space Research*, 34(5), pp. 1139–1142, Space Debris.
- Sharma, J. (2000), Orbit Determination Applications with the Space-based Visible Space Surveillance, *Publications of the American Astronautical Society - Advances in the Astronautical Sciences, Space-flight Mechanics volumes*, 105(1), pp. 275–286.
- Sharma, J., A. Wiseman, and G. Zollinger (2001), Improving Space Surveillance with Space-Based Visible Sensor, in *Proc. of the 2001 Space Control Conference*, pp. 57–69, Lexington, Massachusetts.
- Spencer, D. B., C. B. Hogge, W. S. Campbell, M. E. Sorge, and S. R. Mewaters (2000), Some Technical Issues of an Optically Focused Small Space Debris Tracking and Cataloging System, *Space Debris*, 2, pp. 137–160, 10.1023/A:1022990214830.
- Stansbery, E. (2010), Characterizing the Space Debris Environment with a Variety of SSA Sensors, Presentation at the 38th COSPAR General Assembly, 18-25 July 2010, Bremen, Germany, in “Space Situational Awareness and its Relationship with Science (PSW2)”, NASA ID: JSC-CN-19974; JSC-CN-21122.
- Stansberry, G., P. Kervin, and M. Mulrooney (2010), Plans for the Meter Class Autonomous Telescope and Potential Coordinated Measurements with Kwajalein Radars, in *Proceedings of the 8th U.S.-Russian Space Surveillance Workshop*, edited by P. Kenneth Seidelmann, Wailea Beach, Maui, Hawaii, United States, April 18–23 2010.
- Stansbery, G., and J. L. Foster (2005), Completeness of Measurements of the Orbital Debris Environment, in *4th European Conference on Space Debris*, Vol. 587 of *ESA Special Publication*, edited by D. Danesy, pp. 95–, August 2005.
- Stokes, G., C. von Braun, R. Sridharan, D. Harrison, and J. Sharma (1998), The Space-Based Visible Program, *MIT LL Journal*, 11(2), pp. 205–238.
- Taff, L. G. (1981), *Computational Spherical Astronomy*, John Wiley & Sons.
- Tajima, T., and A. Takano (2001), Trajectory Design for the GEO Debris Observation Satellite, in *Space Debris*, Vol. 473 of *ESA Special Publication*, edited by H. Sawaya-Lacoste, pp. 133–138, October 2001.
- Takano, A., and K. Imagawa (1997), Space Debris Related Activities in Nasda, in *Second European Conference on Space Debris*, Vol. 393 of *ESA Special Publication*, edited by B. Kaldeich-Schuermann, pp. 31–.
- Talent, D., A. Potter, and K. Henize (1997), A Search for Debris in GEO, in *Second European Conference on Space Debris*, Vol. 393 of *ESA Special Publication*, edited by B. Kaldeich-Schuermann, pp. 99–.
- Thillot, M., X. Brenière, and T. Midavaine (2001), Micro-satellite for Space Debris Observation by Optical Sensors, in *Space Debris*, Vol. 473 of *ESA Special Publication*, edited by H. Sawaya-Lacoste, pp. 169–173, October 2001.
- Tommei, G., A. Milani, and A. Rossi (2007), Orbit Determination of Space Debris: Admissible Regions, *Celestial Mechanics and Dynamical Astronomy*, 97, pp. 289–304, April 2007.

- Vanwijck, X., and T. Flohrer (2008), Possible Contribution of Space-based Assets for Space Situational Awareness, in *Proc. of the 59th International Astronautical Congress*, Glasgow, Scotland, September 20–October 3 2008, IAC-08-A6.5.5.
- Walker, J. G. (1971), Some Circular Orbit Patterns Providing Continuous Whole Earth Coverage, *Journal of the British Interplanetary Society*, 24, pp. 369–384.
- Wallace, B., F. Pinkney, R. Scott, D. Bedard, J. Rody, A. Spaans, M. Levesque, S. Buteau, T. Racey, D. Burrell, and A. Hildebrand (2004), The Near Earth Orbit Surveillance Satellite (NEOSSat), in *Proc. of the 55th International Astronautical Congress*, Vancouver, Canada, IAC-04-IAA-5.12.1.02.
- Wang, D., L. R. Gardner, W. K. Wong, and P. Hadfield (1991), Space-based Visible All-reflective Stray Light Telescope, in *Proc. of SPIE Surveillance Technologies*, Vol. 1479, edited by Sankaran Gowrinathan *et al.*, SPIE, August 1991.
- Weeden, B. C., and T. S. Kelso (2009), Analysis of the Technical Feasibility of Building an International Civil Space Situational Awareness System, in *Proc. of the 60th International Astronautical Congress*, Daejeon, Republic of Korea, IAC-09-A6.5.2.
- Wokke, F. J. P., A. J. Kramer, R. van Benthem, R. B. Annes, T. Flohrer, T. Schildknecht, E. Stveken, E. Valtonen, J. Peltonen, E. Riihonen, T. Eronen, J. Kuusela, W. Flury, and R. Jehn (2006), An Instrumental Design for Space-based Optical Observation of Space Debris, in *Space Debris and Space Traffic Management Symposium 2005*, Vol. 112 of *AAS Science and Technologies Series*, edited by J. Bendisch, pp. 73–84, Univelt publishers, San Diego, USA.
- Yanagisawa, T., A. Nakajima, and H. Kurosaki (2005), Detection of Small Geo Debris Using Automatic Detection Algorithm, in *4th European Conference on Space Debris*, Vol. 587 of *ESA Special Publication*, edited by D. Danesy, pp. 147–, August 2005.
- Zacharias, N., C. Finch, T. Girard, N. Hambly, G. Wycoff, M. I. Zacharias, D. Castillo, T. Corbin, M. Di-Vittorio, S. Dutta, R. Gaume, S. Gauss, M. Germain, D. Hall, W. Hartkopf, D. Hsu, E. Holdenried, V. Makarov, M. Martines, B. Mason, D. Monet, T. Rafferty, A. Rhodes, T. Siemers, D. Smith, T. Tilleman, S. Urban, G. Wieder, L. Winter, and A. Young (2010), The Third US Naval Observatory CCD Astrograph Catalog (UCAC3), *The Astronomical Journal*, 139(6), pp. 2184.
- Zhang, X. (2002), The Telescopes for Space Debris, Presentation at the 20th IADC meeting, Surrey, UK.
- Zhao, C., W. Zhang, Z. Han, and H. Wang (2010), Progress in Space Debris Research, *Chinese Journal of Space Science*, 30, pp. 516–518.

*Bibliography*

---